Reconciling Paleomagnetism and Pangea

by

Mathew M. Domeier

A dissertation submitted in partial fulfillment
of the requirements for the degree of
Doctor of Philosophy
(Geology)
in The University of Michigan
2012

Doctoral Committee:

Professor Rob Van der Voo, Chair
Professor Ben A. van der Pluijm
Associate Professor Christopher J. Poulsen
Assistant Professor Nathan A. Niemi
Professor Trond H. Torsvik, University of Oslo

...the Earth speaks of its internal workings through the silent voice of the magnetic needle.
- Christopher Hansteen, *Untersuchungen über den Magnetismus der Erde*, 1819

To my family

ACKNOWLEDGEMENTS

To start off this tectonic-themed dissertation, I'd like to direct a veritable mountain of gratitude toward my advisor, Rob Van der Voo. I arrived to Michigan with a suspicion that my acceptance was due to a clerical error, and leave with a profound sense of accomplishment, much due to his patient guidance. Always helping to focus my efforts and ever-willing to let me stand on his shoulders, he steps aside with the arrival of the credit and the limelight; the mark of a truly great and selfless mentor. His seemingly bottomless resevoir of knowledge and enthusiam have also proven a source of lasting inspiration. I am truly honored to have been granted the opportunity to work with him, my only parting complaint is that he provided me with nothing to gripe about amidst my peers. I am similarly indebted to Trond Torsvik, who, with Rob, set me apace on this covetable project, which is, in large part, the fruit of many years of their own hard work. They have also both been more-than-generous in keeping me and my academic pursuits comfortably afloat, so to speak.

Ben van der Pluijm, Chris Poulsen, and Nathan Niemi are thanked for serving on my committee, and for providing me with valuable feedback that has improved this dissertation. I am appreciative of the time, effort, and invaluable insights provided to me by Eric Tohver, Renata Tomezzoli, Haroldo Vizan, and Bart Hendriks, all of whom contributed significantly to this work, and to ongoing projects stemming from it. Renata and Haroldo are especially thanked for weaving field supplies, doc-

uments, and people through the sometimes byzantine web of the Argentine world. Eric and Bart are especially thanked for explaining, re-stating, clarifying, and then re-explaining the details of the U-Pb and Ar-Ar geochronologic methods. Some of it got through. Ada Dominguez and Jordan Kirshner should be awarded civilian medals for completing an entire field-season with me as assistants; I'd like to thank both of them for acting as the better half. More broadly, my research endeavors have benefited from innumerable conversations with fellow students of paleomagnetism; Fatim Hankard, Sasha Abrazhevich, Jim Hnat, and Josep Parés.

Many other graduate students, post-docs, and undergraduates have made my time here worth more than its weight in publications, for which I am most grateful. I'd like to extend a special thanks to those that have cohabited the PaSTeL lab over the last five years, most notably my past and current office-mates, who are lucky to be able to find their own desks under my ever-encroaching mass of papers. Special thanks also to those similarly-screw-loose students who shared my interest in climbing up and falling down rock walls, among other pointless and reckless outdoor pursuits, but saw to it that I remained largely intact.

Finally, I owe a great deal to my loved ones. My parents have been unwaveringly supportive, and even regularly inquire about what the magnetic field has told me of late, despite never having any use for the answers I provide them. I also admire and appreciate Gillian's steadfast tolerance of my late-nights and prolonged absences, which are particularly difficult given the quality of her company (and cooking).

TABLE OF CONTENTS

LIST OF FIGURES

Figure

LIST OF TABLES

Table

LIST OF APPENDICES

Appendix

CHAPTER I

Introduction

Supercontinents are widely recognized as the striking archetypal imagery of tectonic mobilism, the awe-inspiring notion that the continents are, in a sense, "adrift". Several intervals of the geologic past have witnessed these global agglomerations of land, most recently in the late Paleozoic (∼325 Ma) with the formation of Pangea. Supercontinents are an especially fertile subject of study because their evolution instigates considerable change to a wide range of natural systems. On the broadest scale, mantle dynamics are affected by the reorganized interaction of tectonic plates, and by the construction of expansive landmasses with broad orogenic belts. Global climate is altered by modifications to atmospheric and oceanic circulation systems, and by changing land-sea distributions. During the amalgamation and dissemination of Pangea, the biosphere was profoundly influenced by a rapidly evolving ecological framework and changing migratory pathways. By improving on our limited understanding of the role that supercontinents have played in these dynamic changes, as observed in records of the past, we can come to a fuller understanding of our—considerably different—modern-day world. For such work, one first needs to establish the time-dependant paleogeography of these landmasses. The focus of this dissertation is on the paleogeography of Pangea, which, by virtue of its relative

youth, should afford the richest and most reliable geologic and geophysical records for study. Yet, remarkably, the configuration of this most recent supercontinent remains contested, despite decades of scrupulous study.

The concept of the supercontinent Pangea originated with the earliest ideas of continental drift, and the recognition of comparably-shaped peri-Atlantic coastlines. Unsurprisingly, nascent drafts of Pangea resemble a re-assembled puzzle, with the shape and position of the continents so-adjusted as to create a visually-inspiring fit between the present-day coastlines (Snider-Pellegrini, 1858; Wegener, 1915, 1922)(Fig. 1.1). On the heels of the discovery of seafloor spreading (Hess, 1960; Vine and Matthews, 1963), and amidst the "tectonic revolution" in geoscience, the first quantitative paleogeographic reconstruction of Pangea was computed by Bullard et al. (1965)(Fig. 1.2). Based on a least-squares fitting of the 500 fathom bathymetric contours of the Atlantic margins, this reconstruction was a landmark achievement that has been widely adopted by the scientific community. Also known as Pangea "A", this continental geometry places northwestern Africa against the eastern North American seaboard, a configuration that essentially results from simple closure of the Atlantic—and not so different from the earlier conceptual drafts. There is widespread geologic and geophysical support for this reconstruction just prior to the breakup of the supercontinent in the Early Jurassic, but what about earlier time? It is commonly assumed that Pangea amalgamated into this same general form, remaining internally rigid across the ∼130 million years that it existed (∼325-195 Ma). A wealth of information has since been gleaned from studies adopting this assumption—which allows the conventional "A-type" reconstruction to be used as a Carboniferous-Triassic paleogeographic base-map—and many well-accepted interpretations of late Paleozoic–early Mesozoic geology have been derived from this continental configuration. But is

this reconstruction really accurate for pre-Jurassic time? This question has been the fundamental motivation for numerous late Paleozoic–early Mesozoic paleomagnetic studies (including this dissertation), ultimately designed to allow paleogeographic reconstructions of Pangea to be tested at various points in time.

Figure 1.1: The earliest known paleogeographic reconstruction of the peri-Atlantic continents, by Antonio Snider-Pelligrini in *La Création et ses mystères dévoilés* (1858). Courtesy of the Earth Sciences and Map Library, University of California, Berkeley.

Paleomagnetism is the study of the ancient geomagnetic field, the record of which is preserved in a variety of remanence-carrying (magnetized) minerals. Importantly, these paleomagnetic records are vectorial, meaning that they chronicle not only the intensity of the ambient geomagnetic field (at the time of magnetization), but also its local orientation. Because the magnetic field of the Earth largely resembles a giant dipole, not unlike the field of a bar-magnet, aligned (on average) with the planet's axis of rotation, the directional component of the field changes as a function of latitude. In fact, paleomagnetic directions are uniquely correlated with latitude, allowing the original latitude at which a rock formed to be calculated from the pa-

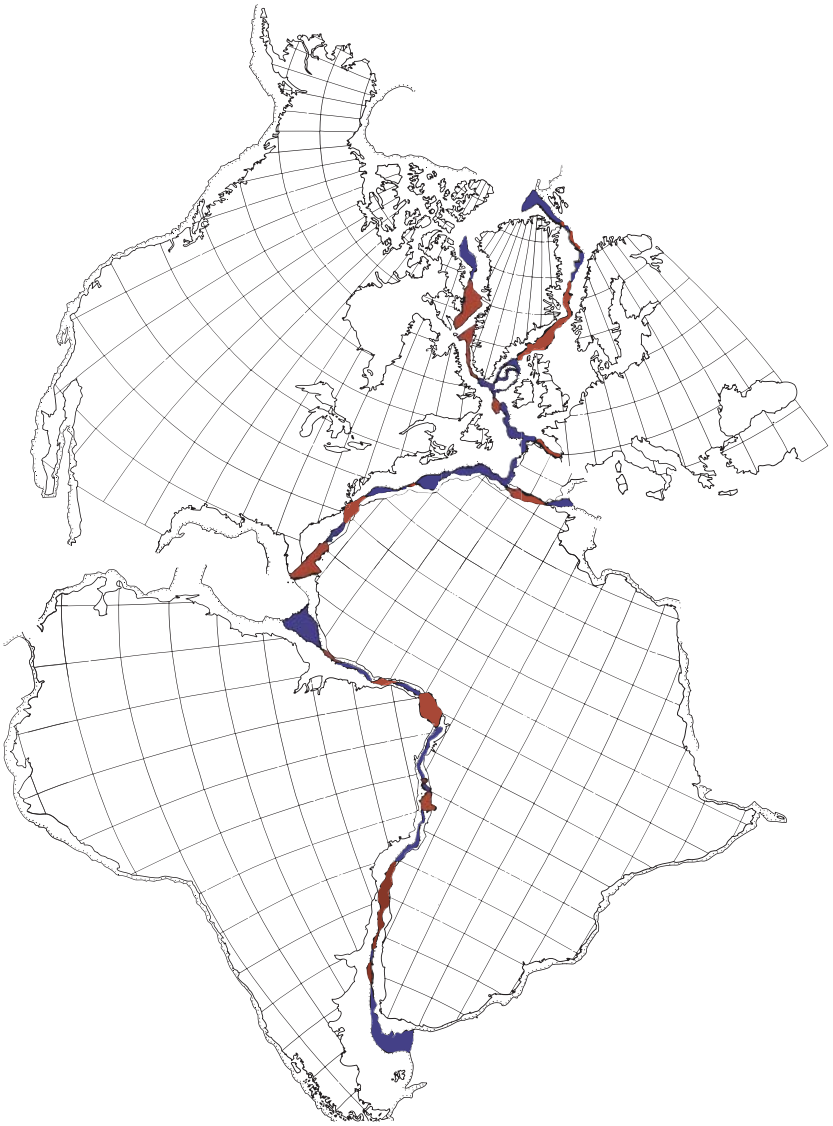

Figure 1.2: The first quantitative reconstruction of Pangea, by Bullard et al. (1965). This fit was achieved by finding the least-squares fit of the 500 fathom bathymetric contours of the Atlantic margins. Continental overlaps (gaps) are highlighted in red (blue).

leomagnetic direction that it has preserved. Furthermore, by establishing the age of paleomagnetic records, the past motions of a continent can be resolved in both space *and* time. By extracting paleomagnetic records and age-data from rocks on different continents, the global distribution of landmasses can be known through geologic time. Such exercises have resulted in a virtual continuum of Phanerozoic paleogeographic reconstructions, often with great interdisciplinary agreement. Yet, the Carboniferous-Early Triassic paleomagnetic data appear to conflict with the conventional reconstruction of Bullard et al. (1965), as repeatedly shown by various groups across the last half-century (Jaeger and Irving, 1957; Carey, 1958; Van der Voo and French, 1974; Irving, 1977; Morel and Irving, 1981; Smith and Livermore, 1991; Van der Voo, 1993; Muttoni et al., 1996; Torcq et al., 1997; Bachtadse et al., 2002; Muttoni et al., 2003; Irving, 2004; Rakotosolofo et al., 2006; Torsvik et al., 2008)(Fig. 3).

The conflict stems from a large disparity between the paleomagnetic data of the southern half of Pangea (i.e. Gondwana; includes South America, Africa, Antarctica, Australia, India, Arabia, and Madagascar) and the northern half (i.e. Laurussia; includes North America, Stable Europe, Greenland, and, after $\sim$250 Ma, Siberia) when the two landmasses are re-assembled according to the model of Pangea A. The conventional fit prevents the landmasses from simultaneously occupying the paleolatitudes required by their respective paleomagnetic data; either Gondwana is too far south or Laurussia is too far north. If the continents are instead allowed to occupy the paleolatitudes stipulated by their paleomagnetic data, but held to the relative longitudinal constraints of the conventional model, a substantial crustal misfit results; an impossible continental overlap of $\sim$10° latitude ($>$ 1000 km) occurs between the landmasses.

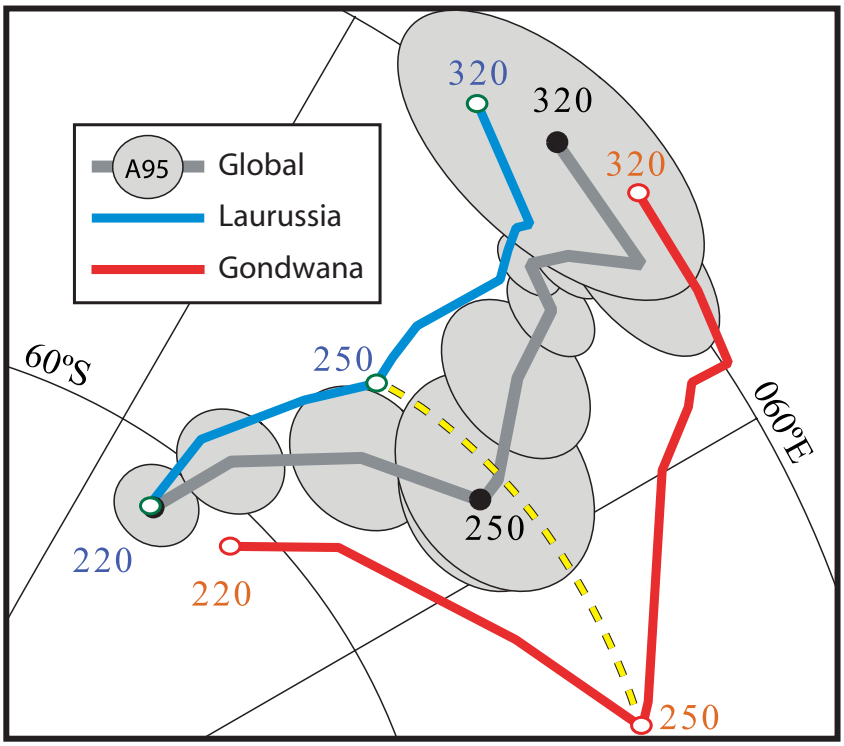

Figure 1.3: The late Paleozoic–early Mesozoic apparent polar wander paths (APWPs) of Laurussia (blue) and Gondwana (red) in an "A-type" Pangea reconstruction (all poles are in southern African coordinates). Ages of depicted mean poles are listed in Ma. Note the prominent separation of the paths at the Permian–Triassic boundary (250 Ma)(shown by the dashed yellow line). The gray path results from the combined data. From Torsvik et al. (2008).

To resolve this prominent model-data discord, several attempts have been made to reconstruct Pangea in a different way, specifically to accommodate the continental positioning required by the paleomagnetic data. The first (and only persisting) alternative paleogeographic model, Pangea "B", places Gondwana farther east than its position in Pangea A, thereby allowing it to occupy more northerly latitudes without overlapping Laurussia (Fig. 1.4). Although rectifying the paleomagnetic discrepancy between Laurussia and Gondwana, this reconstruction introduces serious geologic problems. The broad support for Pangea A in the Late Triassic/Early Jurassic implies that Pangea B, if existent in pre-Late Triassic time, must have experienced a massive internal re-structuring event to ultimately arrive at an A-type geometry by the Late Triassic. The simplest manner of transformation would necessarily involve highly unlikely plate motions between Laurussia and Gondwana, along a dextral megashear on the order of ∼3,500 km. This imperative challenges the long-held assumption of an internally rigid Pangea and, moreover, critically lacks geologic evidence. The "absence of evidence" is not a commutable statement, but in light of the sheer magnitude of the hypothetical structure, the sparsity of geologic support renders the alternative reconstruction seemingly indefensible.

To distill the essence of this conundrum: an array of geological and geophysical data support the conventional paleogeographic model of Pangea (Fig. 1.2) during the Late Triassic/Early Jurassic, but this geometry is demonstrably incongruent with the paleomagnetic data in pre-Late Triassic time (Fig. 1.3). Yet, alternative reconstructions, built to accomodate the paleomagnetic data (Fig. 1.4), require incredible tectonic transformations, and are widely considered untenable by the scientific community. This is a first-order problem in late Paleozoic–early Mesozoic tectonics and paleomagnetism. On one hand, the alternative reconstructions challenge the widely

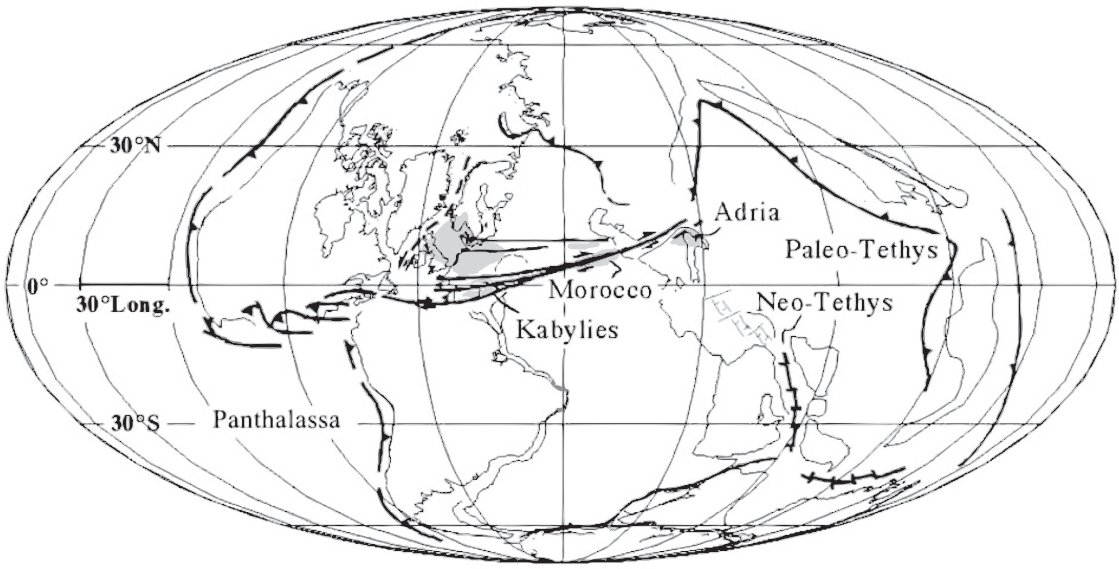

Figure 1.4: Early Permian Pangea B, from Muttoni et al. (2003). The inferred dextral megashearzone (required to reach Pangea A) is depicted between Laurussia and Gondwana.

accepted kinematic model of Alleghenian-Variscan orogenesis, as well as many meticulously constructed late Paleozoic–early Mesozoic regional geologic models along the Laurussia-Gondwana interface. On the other hand, paleomagnetism offers the only quantitative means for making continental reconstructions prior to the Cretaceous, so dismissal of the paleomagnetic data would undermine the conclusions drawn from innumerable studies predicated on pre-Jurassic paleogeography.

In lieu of substantially modifying the conventional reconstruction or abandoning paleomagnetism, this dissertation explores the possibility that the model-data discrepancy can be explained by widespread bias in the data. Specifically, the following questions are considered: (1) Is there any indication of systemic bias in the present paleomagnetic data? (2) Do new, high-fidelity data significantly differ from older, lower-quality results? (3) What effect do these findings (1,2) have on the apparent configuration of Pangea? (4) What time-dependent paleogeography is derived from

the highest-quality results?

1.1 Dissertation Outline

The succeeding 3 chapters (II-IV) have a regional scope, and are focused on new, high-quality paleomagnetic contributions and the evaluation of existing data. Both North and South America were selected as study areas so as to consider complementary paleomagnetic datasets from both Laurussia and Gondwana.

Chapters II and III present three new igneous rock-based Late Permian and Early–Middle Triassic paleomagnetic poles ("paleopoles") from western and central Argentina. Chapter III also discusses a new Early–Middle Triassic sedimentary rock-based paleopole that illustrates the effect of what is likely a widespread shallow inclination bias. Chapter II further considers the existing Permian–Triassic paleomagnetic data from South America, and demonstrates the effect of quality-filtering on its apparent polar wander path (APWP). These results collectively indicate that the APWP of South America (and, by extension, Gondwana) is biased by low-fidelity data, and that its separation from the APWP of Laurussia is due, at least in part, to data-artifacts.

Chapter IV reports on a new paleomagnetic result from Middle Permian shallow intrusive rocks in southern Illinois (USA), and its relation to the reference APWP of North America. An observed disparity between this new igneous rock-based result and the reference APWP prompts a virtual geomagnetic pole (VGP) distribution analysis of the data comprising the latter. This analysis substantiates the argument that the APWP is pervasively affected by a magnetic recording bias (inclination shallowing in sedimentary rocks), implying that previous Permian–Triassic global APWP comparisons may have been compromised.

Chapter V is a synthesis of global scope that examines the time-dependent paleogeography of Pangea with data from the previous chapters, as well as the most up-to-date compilation of data from Laurussia and West Gondwana. The chapter begins with a comprehensive review of the historical development of the intra-Pangean paleomagnetic problem and proceeds with a new analysis that offers resolution. The fruit of the work is a new series of Pangea reconstructions that are compatible with both conventional geologic models and the paleomagnetic data.

This dissertation concludes with chapter VI, which offers a brief summary of the principal contributions of this work, reflects on the aforementioned motivating questions, and considers avenues for future research.

1.2 Publications Resulting from this Dissertation

Domeier, M., Van der Voo, R., Tohver, E., Tomezzoli, R. N., Vizan, H., Torsvik, T. H., & Kirshner, J. (2011) New Late Permian paleomagnetic data from Argentina: Refinement of the apparent polar wander path of Gondwana. *Geochemistry, Geophysics, Geosystems*, 12, Q07002, doi:10.1029/2011GC003616. (**Chapter 2**)

Domeier, M., Van der Voo, R., Tomezzoli, R. N., Tohver, E., Hendriks, B. W. H., Torsvik, T. H., Vizan, H., Dominguez, A. R. (2012) Support for an "A-type" Pangea reconstruction from high-fidelity Late Permian and Early–Middle Triassic paleomagnetic data from Argentina. *Journal of Geophysical Research*, in press. (**Chapter 3**)

Domeier, M., Van der Voo, R., & Denny, F. B. (2011) Widespread inclination shallowing in Permian and Triassic paleomagnetic data from Laurentia: Support from new paleomagnetic data from Middle Permian shallow intrusions in southern Illinois (USA) and virtual geomagnetic pole distributions. *Tectonophysics*, 511, 38-52, doi:10.1016/j.tecto.2011.08.016. (**Chapter 4**)

Domeier, M., Van der Voo, R., Torsvik, T. H. (2012) Paleomagnetism and Pangea: the road to reconciliation. *Tectonophysics*, in press. (**Chapter 5**)

References

Bullard, E., Everett, J. E., & Smith, A. G. (1965) The fit of continents around the Atlantic. *Philosophical Transactions of the Royal Society of London*, 258, 41-51.

Bachtadse, V., Zaenglein, R., Tait, J., & Soffel, H. C. (2002) Palaeomagnetism of the Permo/Carboniferous (280 Ma) Jebel Nehoud ring complex, Kordofan, Central Sudan. *Journal of African Earth Sciences*, 35, 89-97.

Carey, S. W. (1958) The tectonic approach to continental drift, in Continental drift, a symposium, 1956. University of Tasmania, 177-358.

Hess, H. H. (1960) Evolution of ocean basins. Report to Office of Naval Research. Contract No. 1858(10), NR 081-067. 38 pp.

Irving, E. (1977) Drift of the major continental blocks since the Devonian. *Nature*, 270, 304-309.

Irving, E. (2004) The case for Pangea B, and the Intra-Pangean Megashear. Timescales of the paleomagnetic field. *American Geophysical Union - Geophysical Monograph*, 145, 13-27.

Jeager, J. C., & Irving, E. (1957) Paleomagnetism and reconstruction of Gondwanaland. *C. R. 3^{rd} Congr. Pacific and Indian Ocean Sciences*, 233-242, Imprimerie Officielle, Tananarive, Madagascar.

Morel, P., & Irving, E. (1981) Paleomagnetism and the evolution of Pangea. *Journal of Geophysical Research*, 86, 1858-1872.

Muttoni, G., Kent, D. V., & Channell, J. E. T. (1996) Evolution of Pangea: Paleomagnetic constraints from the Southern Alps, Italy. *Earth and Planetary Science Letters*, 140, 97-112.

Muttoni, G., Kent, D. V., Garzanti, E., Brack, P., Abrahamsen, N., & Gaetani, M. (2003) Early Permian Pangea "B" to Late Permian Pangea "A". *Earth and Planetary Science Letters*, 215, 379-394.

Rakotosolofo, N. A., Tait, J. A., Carlotto, V., & Cardenas, J. (2006) Palaeomagnetic results from the Early Permian Copacabana Group, Southern Peru: Implication for Pangaea palaeogeography. *Tectonophysics*, 413, 287-299.

Smith, A. G., & Livermore, R. A. (1991) Pangea in Permian to Jurassic time. *Tectonophysics*, 187, 135-179.

Snider-Pellegrini, A. (1858) La Création et ses mystères dévoilés. Frank and Dentu, Paris.

Torcq, F., Besse, J., Vaslet, D., Marcoux, J., Ricou, L. E., Halawani, M., et al. (1997) Paleomagnetic results from Saudi Arabia and the Permo-Triassic Pangea configuration. *Earth and Planetary Science Letters*, 148, 553-567.

Torsvik, T. H., Muller, R. D., Van der Voo, R., Steinberger, B., & Gaina, C. (2008) Global plate motion frames: Toward a unified model. *Reviews of Geophysics*, 46, 1-44.

Van der Voo, R. (1993) Paleomagnetism of the Atlantic, Tethys and Iapetus oceans. Cambridge University Press, Cambridge, U.K.

Van der Voo, R., & French, R. B. (1974) Apparent polar wandering for the Atlantic-bordering continents: Late Carboniferous to Eocene. *Earth-Science Reviews*, 10, 99-119.

Vine, F. J., & Matthews, D. H. (1963) Magnetic anomalies over oceanic ridges. *Nature*, 199, 947-949.

Wegener, A. (1915; 1922) Die Entstehung der Kontinente und Ozeane. On the Origin of Continents and Oceans, English translation of 3rd edition by J.G.A. Skerl (1924), Methuen, London. 212 pp.

CHAPTER II

New Late Permian paleomagnetic data from Argentina: Refinement of the apparent polar wander path of Gondwana

2.1 Abstract

The late Paleozoic–early Mesozoic apparent polar wander path of Gondwana is largely constructed from relatively old paleomagnetic results, many of which are considered unreliable by modern standards. Paleomagnetic results derived from sedimentary sequences, which are generally poorly dated and prone to inclination shallowing, are especially common. Here we report the results of a joint paleomagnetic/geochronologic study of a volcanic complex in central Argentina. U-Pb dating of zircons has yielded a robust age estimate of 263.0 +1.6/-2.0 Ma for the complex. Paleomagnetic analysis has revealed a pre-tilting (primary Permian) magnetization with dual-polarities. Rock magnetic experiments have identified pseudo-single domain (titano)magnetite and hematite as the mineralogic carriers of the magnetization. Lightning-induced isothermal remagnetizations are widespread in the low-coercivity magnetic carriers. The resulting paleomagnetic pole is 80.1° S, 349.0° E, A_{95}: 3.3°, N: 35, and it improves a Late Permian mean pole calculated from a filtered South American paleomagnetic dataset. More broadly, this new, high-quality,

Citation:
Domeier, M., Van der Voo, R., Tohver, E., Tomezzoli, R. N., Vizan, H., Torsvik, T. H., & Kirshner, J. (2011). New Late Permian paleomagnetic data from Argentina: Refinement of the apparent polar wander path of Gondwana. *Geochemistry Geophysics Geosystems*, 12, Q07002, doi:10.1029/2011GC003616.

igneous-based paleomagnetic pole falls between the previously distinct Late Permian segments of the Laurussian and Gondwanan apparent polar wander paths, suggesting that the long-recognized disparity between these large paleomagnetic datasets may be primarily due to the inclusion of low-quality or systemically biased data.

2.2 Introduction

The late Paleozoic–early Mesozoic apparent polar wander path (APWP) for Gondwana is poorly defined, being largely constructed from vintage paleomagnetic results, many of which are derived from sedimentary units which may suffer from known magnetic recording biases (inclination shallowing). Recent paleomagnetic work in western-central Argentina has begun to address the paucity of reliable results, by focusing on a belt of late Paleozoic–early Mesozoic volcano-plutonic complexes (Terrizzano, 2005; Tomezzoli et al., 2008; Domeier et al., 2009). However, the published data are mostly preliminary, necessitating additional work to reinforce and validate these initial studies. Continued paleomagnetic and geochronologic work along this belt also has the potential to answer questions about the nature and timing of volcanism and deformation in southwestern Gondwana during the late Paleozoic. These questions remain critical to understanding the paleogeographic and geologic evolution of this paleo-margin (see, for example, Tomezzoli, 2001).

Here we present new results from a continued investigation of volcanic rocks at the Sierra Chica, La Pampa, Argentina. This complex was elected for further study because preliminary paleomagnetic results (10 sites) suggested that a stable, late Paleozoic magnetization could be isolated, Middle Triassic isotopic age data conflict with an inferred Early Permian (Kiaman) age of magnetization, and structural restorations, applied to only two of the 10 sites in the preliminary study, did not

allow a rigorous tilt-test to be conducted (Tomezzoli et al., 2008). Additional sites were collected to evaluate and augment the existing paleomagnetic dataset and U-Pb dating was carried out to better define the age of these rocks.

2.3 Geologic Setting

The Sierra Chica is one of a series of local topographic highs, formed by a resistant sequence of silicic volcanic rocks, located in La Pampa province, Argentina (Fig. 2.1). Together these high elements delineate a discontinuous NW-SE trending belt of late Paleozoic–early Mesozoic volcano-plutonic complexes that are considered to be generally correlative with the larger, more continuous belt of the Choiyoi Group, a chain of intermediate to silicic volcanic and shallow plutonic rocks that runs from the San Rafael Block in Mendoza province, Argentina, to the High Andes of northern-central Chile (Kay et al., 1989; Sruoga and Llambías, 1992; Llambías et al., 1993; Llambías et al., 2003). The Choiyoi Group displays an evolving geochemistry that suggests a change from arc-related volcanism in the Early Permian to a transitional-intraplate setting in the Late Permian–Triassic (Mpodozis and Kay, 1992; Llambías and Sato, 1995; Martin et al., 1999; Heredia et al., 2002; Kleiman and Japas, 2009). A temporally protracted and geographically widespread deformation episode, the San Rafael Orogenic Phase (SROP), is associated with this changing geochemistry, and has been variously attributed to terrane accretion, oblique and/or flat-slab subduction, and intra-plate tectonic adjustments, either from proximal activity or via transmitted stresses (Lock, 1980; Forsythe, 1982; Dalziel and Grunow, 1992; Visser and Praekelt, 1998; Trouw and De Wit, 1999; Pankhurst et al., 2006; Ramos, 2008; Kleiman and Japas, 2009). Evidence of this deformation is pronounced in the Choiyoi Group to the west of the Sierra Chica, to the east in the fold and thrust belt of the Sierras Aus-

trales (Tomezzoli, 2001), and to the south in Northern Patagonia (Fig. 2.1). In La Pampa province, however, the effects of this deformation episode are shown only by the gently folded sedimentary rocks of the Permian-age Carapacha Basin and by the spatially-diminutive Cerro de Los Viejos mylonitic shear belt (Tickyj et al., 1997; Tomezzoli et al., 2006). This distinction in tectonic setting between the Choiyoi Group proper and volcanic rocks of La Pampa has been recognized geochemically (Llambías et al., 2003).

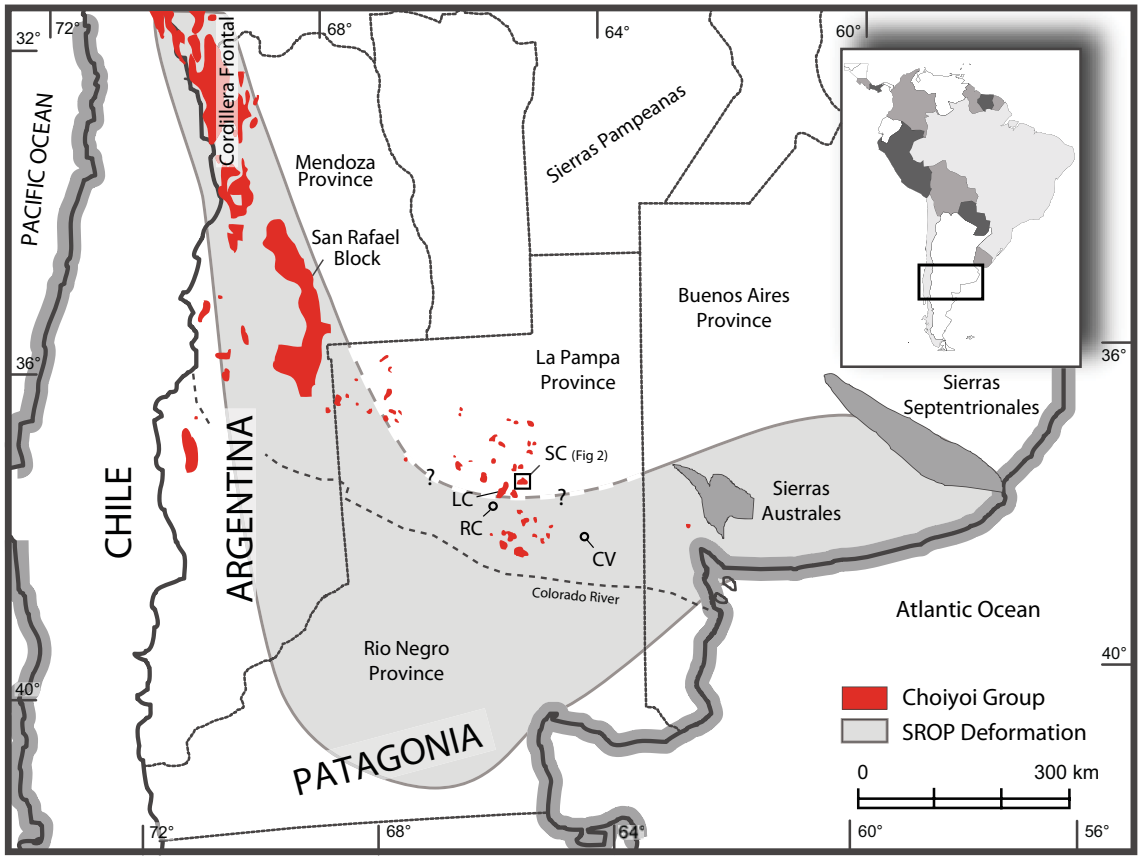

Figure 2.1: Regional map of the study area, showing the distribution of Choiyoi Group igneous rocks and structures associated with the San Rafael Orogenic Phase (SROP) of deformation. Abbreviated place names discussed in the text: CV: Cerro de Los Viejos, LC: Lihue Calel, RC: Rio Curaco, SC: Sierra Chica. The small box in the center of the figure highlights the area illustrated in Fig. 2.2. Adapted from Tomezzoli et al. (2008) and Kleiman and Japas (2009).

The Sierra Chica has been subdivided into three distinct petrologic sequences;

a lower unit, with a very limited exposure, of trachyandesitic pyroclastic flows, a middle rhyolitic unit comprised of thin (< 5 m) pyroclastic flows containing abundant lithic fragments, and interspersed with tuffs, and an upper rhyolitic unit with thick (> 5 m) lava flows and ignimbrites exhibiting rheomorphic features (Fig. 2.2; Quenardelle and Llambías, 1997; Tomezzoli et al., 2008). The changing lithologic character of the mid-to-upper units reflects an evolution of eruptive style, which may be the consequence of a primarily stratified magma chamber with a volatile-rich upper horizon. The thickness and composition of the upper unit suggest that the rocks are proximal to the effusive center, and Sierra Chica itself may be a dissected volcanic edifice (Llambías, 1973). Geochemically, all sequences are identical and exhibit high-K calc-alkaline signatures with metaluminous to slightly peraluminous trends (Quenardelle and Llambías, 1997). The similar structure of the lower and middle units (both dipping 25° S) is well determined from clearly defined flow horizons and fiamme, whereas the more massive and rheomorphic upper unit rarely yields discernable contacts or consistent fiamme orientation. An average of the measurements from several locations within the upper unit suggests that it is horizontal to very shallowly dipping (≤ 5° S). Tomezzoli et al. (2008) speculated that the lower and middle units may have been tilted by the SROP prior to emplacement of the upper unit.

Assuming that the volcanic rocks of the Sierra Chica and Lihue Calel, a sequence of rhyolitic ignimbrites 15 km to the southwest of the Sierra Chica, are co-genetic, Rapela et al. (1996) combined samples from both locations to yield a Rb-Sr whole-rock isochron age estimate of 240 ±2 Ma. However, differences in structure, stratigraphy, geochemistry, and petrology lend little credence to the premise of a common source for Lihue Calel and the Sierra Chica (Tomezzoli et al., 2008). Additionally,

this age estimate, if valid, only pertains to the lower unit of the Sierra Chica, and can therefore only act as a maximum age for the middle and upper units. Noting an absence of normal polarity magnetic directions, Tomezzoli et al. (2008) proposed that the volcanic rocks were magnetized during the Kiaman Reversed Superchron (∼318-265 Ma, Opdyke et al., 2000; Gradstein et al., 2004), which would require that the sequence be older than 265 Ma.

2.4 Methods

Sampling was conducted during two successive field seasons, during which 38 paleomagnetic sites were collected from five principal localities (A–E; Fig. 2.2) distributed along a transect through the stratigraphic section. Localities A and B are in the upper unit, locality C is located at the contact between the upper and middle units, locality D is in the middle unit, and E is in the lower unit. A collection of field-drilled cores (SC collection) was complemented by a collection of hand-samples (RS collection). Each site contains a minimum of five independently oriented samples. A solar compass was used to prevent any local magnetic anomalies from affecting orientation readings. Hand-samples for isotopic age determinations were collected from each of the three stratigraphic sequences.

Paleomagnetic samples were stored and processed in a magnetically shielded room at the University of Michigan with a residual field of $\leq$ 200 nT. Measurements of remanent magnetization were made with a three-axis 2G cryogenic magnetometer. A pilot demagnetization scheme subjected sister-specimens to both alternating field (AF) and thermal demagnetization techniques to determine the most effective approach to demagnetization for each site. AF demagnetization was carried out according to a static 3-position procedure. Thermal demagnetization was conducted in

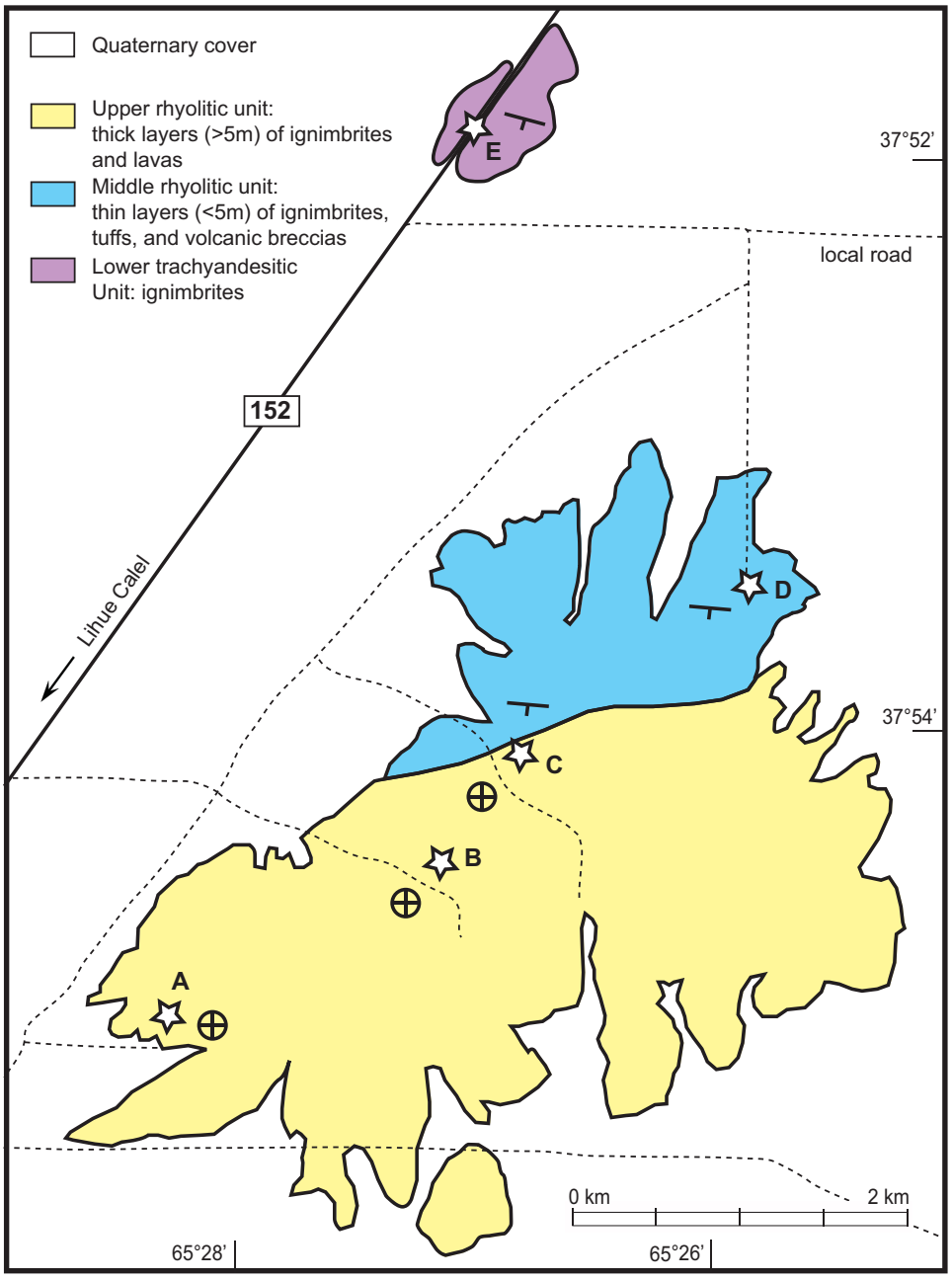

Figure 2.2: Simplified geologic map of the Sierra Chica, showing the three petrologic units and sampling localities (stars). Adapted from Tomezzoli et al. (2008).

air; samples were cooled in a magnetically shielded chamber with a typical DC field of ≤ 5 nT. Magnetic susceptibility was routinely monitored during pilot thermal demagnetizations to detect any mineralogic changes at high temperatures. Progressive demagnetization was carried out with a minimum of 12 steps, up to 200 mT or 680 °C. Demagnetization data were analyzed with orthogonal vector diagrams and stereographic projections (Zijderveld, 1967; Cogné, 2003). Principal component analysis was used to quantitatively define magnetization vectors; where persistent and random remagnetizations were observed (i.e. lightning-induced isothermal overprints), converging great circles were used to define the common magnetization direction (Halls, 1978; Kirschvink, 1980). Fisher (1953) statistics were used to compute site-level mean directions from purely vectorial (stable end point) populations; where remagnetization circles defined some samples, the statistical approach of McFadden and McElhinny (1988) was applied.

Rock magnetic experiments were conducted at the Institute for Rock Magnetism in order to identify and characterize the magnetic carriers. Hysteresis measurements and first order reversal curves (FORCs) were generated with a vibrating sample magnetometer operating at room temperature. Low temperature remanence experiments were performed with a magnetic properties measurement system (MPMS); samples were cooled to 20 K in either a field-cooled (FC) or zero-field cooled (ZFC) environment, given an isothermal remanence, and then warmed to room temperature in zero-field. Thermomagnetic curves (κ vs. T) were measured in an argon atmosphere with a high-temperature susceptibility bridge.

Three samples were collected for analysis using SHRIMP U-Pb geochronology. Zircons were separated by crushing and sieving of samples, followed by Wilfley table and heavy liquid separation. Grains were picked using a binocular microscope

and scanning electron microscope (SEM) images of zircon grains were taken prior to mounting in epoxy resin and polishing for SEM and cathodoluminescence imaging. Subsequently, SHRIMP analysis was conducted with the SHRIMP II housed at Curtin University. The epoxy mounts were cleaned and gold-coated to have a uniform electrical conductivity during the SHRIMP analyses. Samples were measured over two separate analytical sessions, during which the external error calculated from analysis of standards was 0.61% (SC-D01, SC-D03) and 1.4% (SC-D04). The zircon standard used was BR266 zircon (559 Ma, 903 ppm U). Prior to spot analysis, rastering of the ion beam was carried out for 120–150 s to remove the gold coating and reduce the common Pb contaminant within the gold coating. A primary ion beam of 2.5–3 nA with a diameter of $\sim$25 μm was focused onto the polished surface. Common Pb corrections were carried out using the measured amount of ^{204}Pb. Isotopic data are reduced using SQUID2 (Ludwig, 2003). Data were plotted on concordia diagrams using Isoplot 3 software (Ludwig, 2003), in which error ellipses on concordia plots are shown at the 2σ confidence level. All specific dates reported in the text are U-Pb concordia ages calculated from concordant analyses and include decay constant errors, with age uncertainty reported at the 95% confidence level.

2.5 Paleomagnetic Results

Sites from locality E, in the lower unit, exhibit very straightforward demagnetization behavior, characterized by a univectorial decay to the origin (Fig. 2.3a); occasionally a very minor overprint is removed in the initial demagnetization steps. All samples from these sites were thermally treated, as a pervasive high-coercivity phase makes AF demagnetization ineffective. The laboratory unblocking temperature spectrum suggests the presence of two phases in sites SC04, SC05, and RS17,

as the remanence is principally removed within two discrete intervals separated by a stable plateau. The initial unblocking of remanence generally falls between 550 °C and 585 °C, whereas the second (terminal) unblocking occurs above 650 °C. The minerals that produce such behavior are interpreted to be magnetite and hematite, respectively. Directions derived from the linear segments of the different unblocking temperature intervals are not statistically different, thus the decay is truly univectorial. Samples from site SC20 exhibit a strongly "shouldered" spectrum with a very narrow unblocking temperature interval above 650 °C, suggesting it contains only the hematite component. The directions of the characteristic remanent magnetizations (ChRMs) from all four sites at Locality E are WNW and steeply up (Table 2.1).

Sites from the D locality, from the middle unit of the sequence, yield broadly similar demagnetization behavior characterized by converging great circle trajectories. A randomly-oriented, low-coercivity/temperature component (component A) is superimposed on a more stable component (component B) with a direction that is consistently of steep positive inclination. Multiple samples from a given site yield great circle demagnetization trajectories that track from the random direction toward a common intersection point, parallel to the B-component that is isolated to varying success (e.g., Fig. 2.3d). Because the components have a strong coercivity distinction, AF demagnetization is the most effective technique for separating them, but thermal demagnetization yields comparable results (Fig. 2.3b). Component A is interpreted to be an overprint, perhaps an isothermal remagnetization acquired due to lightning. This is supported by the random nature of the directions, as well as the observation that the samples/sites with the most pervasive A-components are associated with the highest NRM intensities. Samples from site SC12, for example, have NRM intensities 10–1,000x greater than those from neighboring sites with

Figure 2.3: Characteristic demagnetization behavior of Sierra Chica samples. All results are presented in geographic coordinates. In the orthogonal vector diagrams the solid (open) symbols are projections onto the horizontal (vertical) plane. For the stereonets, the solid (open) symbols are projections onto the lower (upper) hemisphere. (a) Locality E, univectorial decay of a component held by two phases with distinct unblocking temperatures. (b) Locality D, two components of magnetization are recognized in both AF and thermal demagnetization diagrams. (c) Locality D, the presence of three phases is suggested by thermal demagnetization spectra; the two lower-temperature phases preserve a parallel direction. (d) Locality D, converging remagnetization circles demonstrate that the less stable components are randomly directed at the site level (overprints), and the components of higher-stability are consistent in direction (star). All samples were AF demagnetized. (e) Locality C, comparable results from AF and thermal demagnetization, revealing the presence of two components of magnetization, although there is no strong evidence for the high-coercive phase. (f) Locality C, two magnetization components are evident in the orthogonal vector diagram, and the thermal demagnetization spectrum suggests that the higher-temperature component is carried by more than one phase. (g) Locality C, converging remagnetization circles again demonstrate the presence of a randomly-directed overprint superimposed on a stable direction (star). However, samples from this site do not exhibit evidence of the high-coercive phases, suggesting the stable component partly resides in the low-coercive phase. All samples were AF demagnetized.

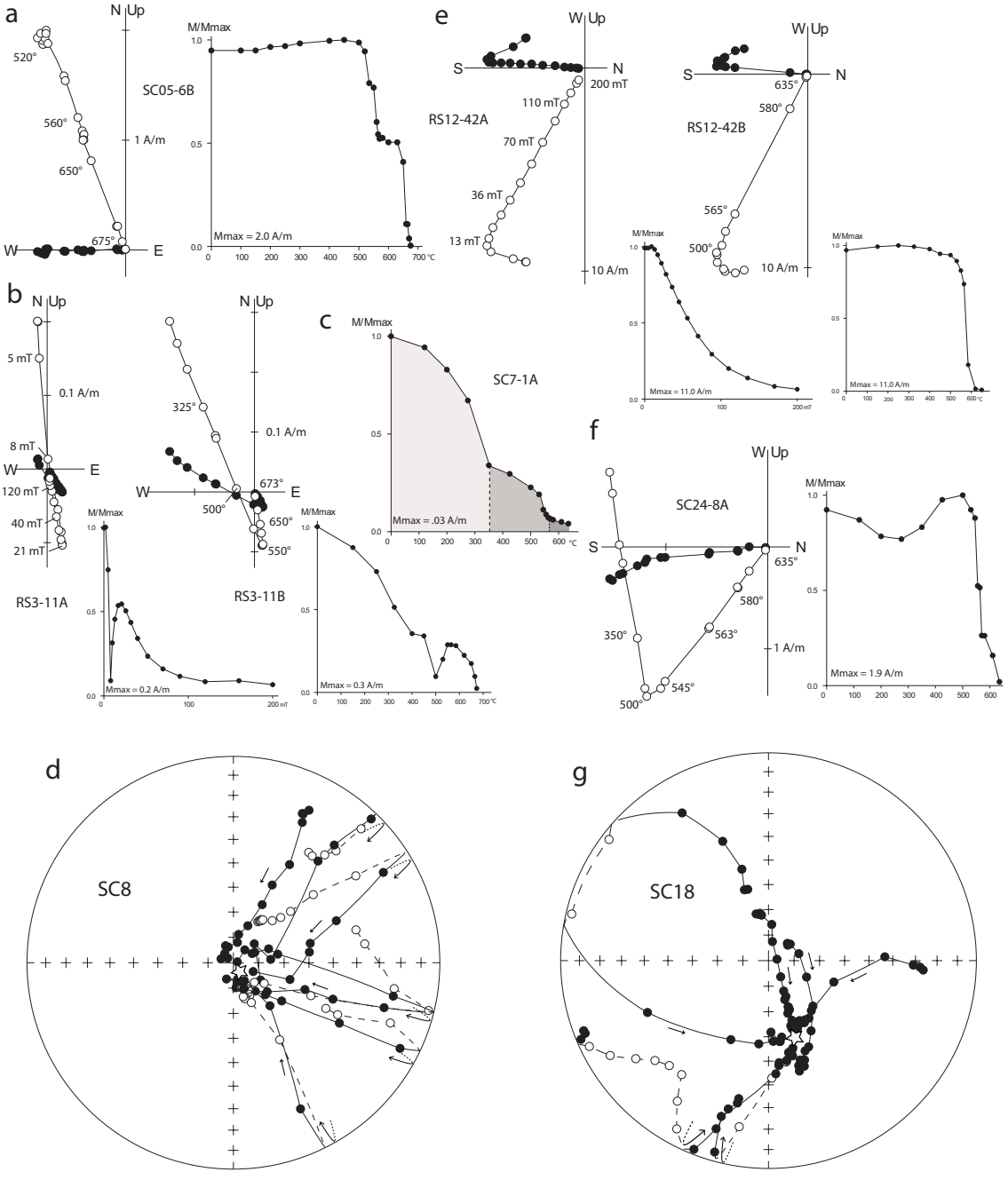
a
N Up
520°
560°
650°
675°
W
E
1 A/m
SC05-6B
M/Mmax
Mmax = 2.0 A/m
b
N Up
5 mT
0.1 A/m
8 mT
W
E
120 mT
40 mT
21 mT
RS3-11A
M/Mmax
Mmax = 0.2 A/m
N Up
325°
0.1 A/m
673°
W
E
500°
650°
550°
RS3-11B
M/Mmax
Mmax = 0.3 A/m
c
M/Mmax
SC7-1A
Mmax = .03 A/m
e
W Up
S
N
200 mT
110 mT
RS12-42A
70 mT
36 mT
13 mT
10 A/m
W Up
S
N
635°
580°
RS12-42B
565°
500°
10 A/m
M/Mmax
Mmax = 11.0 A/m
M/Mmax
Mmax = 11.0 A/m
f
W Up
SC24-8A
S
N
635°
580°
350°
563°
1 A/m
545°
500°
M/Mmax
Mmax = 1.9 A/m
d
SC8
g
SC18

similar lithologies, and these samples yield a single, randomly directed component, suggesting they have been completely overprinted. Site SC12 has therefore been discarded. Site RS01 is also rejected because the mean is ill-defined due to sub-parallel great circles resulting from sub-parallel overprint directions. Samples from SC09 exhibit univectorial demagnetization behavior with corresponding directions that resemble the B-component from neighboring sites. However, AF demagnetization demonstrates that these samples contain a low-coercivity fraction, suggesting that they may have escaped partial remagnetization. Expectedly, these samples have some of the lowest NRM intensities at this locality. In most sites, thermal demagnetization demonstrates that the phase carrying component A is unblocked between 300 °C and 585 °C, and the B-component is not unblocked until 600 °C, or above. In some instances, the A-carrying phase is removed over two discrete intervals at about 350 °C and 550 °C, indicating that two distinct mineralogic components may constitute this low-coercivity/temperature fraction (Fig. 2.3c). This phase is interpreted to be titanomagnetite, perhaps occurring as two populations that differ in titanium content, oxygen parameter, or grain size. Hematite is interpreted to be the principal carrier of the B-component, which we have assigned the ChRM (Table 2.1).

Due to limited exposure, the contact between the upper and middle units is poorly defined, but locality C was selected so as to be proximal to the interpolated contact. Demagnetization behavior of rocks from this locality is comparable to that observed in locality D, in that most sites exhibit a minor, randomly-directed, low-coercivity/temperature component (A) that is removed prior to a component of higher-stability (B) that possesses a magnetization with a consistent direction (Fig. 2.3g). As before, the randomly-directed A component is assumed to be a secondary magnetization. AF demagnetization is more successful at component separation, but

thermal demagnetization also shows comparable results (Fig. 2.3e). Thermal demagnetization reveals that the A-component is completely unblocked by 585 °C, whereas the B-component is largely unblocked above 600 °C (Fig. 2.3f). As before, these components are interpreted to be typically carried by titanomagnetite and hematite, respectively. In some sites, a high-coercivity phase is not explicitly present, but great-circle demagnetization trajectories still track toward a common direction resembling component B, which may be held by a sub-population of the low-coercivity fraction with a relatively high coercivity (Figs. 2.3e,g). Similarly, in some sites that possess both phases, a fraction of the lower-coercivity phase carries a magnetization parallel to the high-coercivity phase (component B), suggesting that remagnetization did not entirely overprint the low-coercivity phase in these sites (Fig. 2.3f). Most of the ChRMs from this locality are south-directed with inclinations of about +60° (Table 2.1). The one exception, SC23, the lowest site at the locality, has a ChRM direction oriented steeply down, parallel to those observed in the D locality of the middle unit. Correspondingly, this site has a structural orientation identical to those exposed at the D locality, suggesting that SC23 is part of the middle unit. SC22, which directly overlies SC23, yields a mean direction parallel to the rest of the sites from the C locality, thus the contact between the middle and upper units may lie between sites SC23 and SC22.

Other sites from the upper section, taken from localities A and B, have demagnetization behavior similar to that observed in locality C. Site SC17, from locality A, has been discarded because all specimens yielded statistically random yet univectorial magnetizations, indicating that it has been completely remagnetized. Consistently high NRM intensities from this site are compatible with the interpretation of lightning-induced contamination. All remaining ChRMs from sites at these localities

are south-directed with inclinations of about +60°, parallel to the magnetizations observed in locality C (excepting site SC23) (Table 2.1).

Our overall rejection rate for sites is 8% (3 of 38), and 5% for specimens (11 of 214) (Table 2.1). Of the retained specimen directions, 70% are defined by vectors and 30% by great-circles. The 35 retained site means were subjected to the bootstrap foldtest, in which tilt-corrections are applied to randomly sampled sub-sets of the original data and directional coaxiality is measured as a function of unfolding (Tauxe and Watson, 1994). After 2000 iterations, the mean degree of unfolding that maximizes directional clustering can be calculated from the collected sub-set determinations, along with 95% confidence bounds. Field observations show that the upper unit is essentially horizontal, while the middle and lower units may be restored to the paleo-horizontal by tilting ∼25° around horizontal axes trending 095° and 105°, respectively. This 10° distinction in strike does not appreciably affect the outcome of the foldtest. The optimal degree of untilting is 121.5%, with 95% confidence limits extending from 105 to 138% (Figs. 2.4a,b). This result suggests that if the site mean directions from rocks in the upper and middle/lower sections are from the same population and are reasonably well determined, the magnetization is pre-tilting, but that the structural dip may be underestimated by 1-9°. Site means were also subjected to the bootstrap reversal test, which evaluates the antipodality of the mean direction of the normal and reverse populations (Tauxe et al., 1991). Prior to tilt-correction, the mean normal direction and inverted mean reverse direction are statistically distinct (95% conf.), but after unfolding the null hypothesis of a common mean cannot be rejected. The tilt-corrected population of site-level virtual geomagnetic poles (VGPs) cannot be distinguished from a Fisher distribution at the 95% confidence level (Fig. 2.4c).

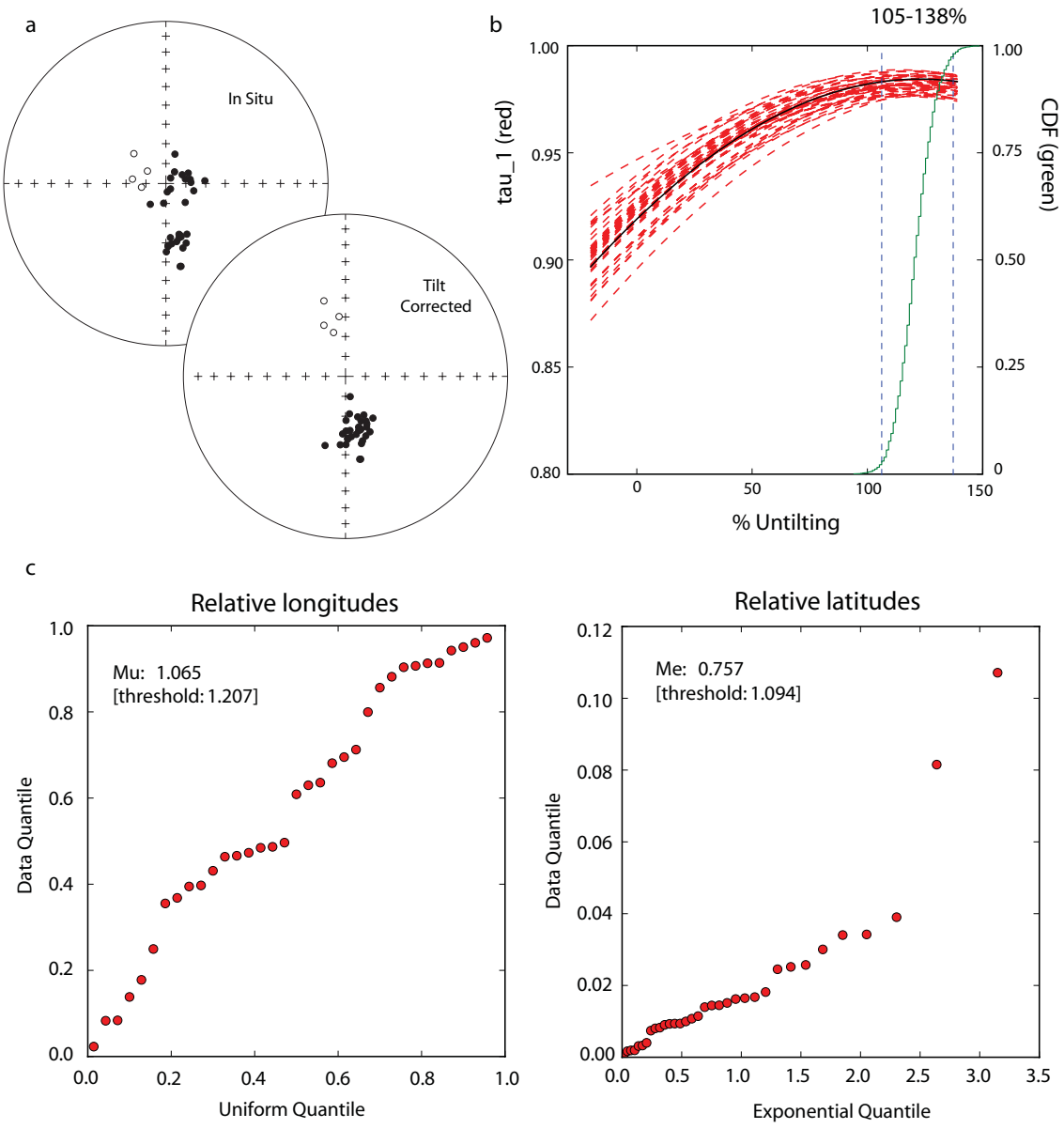

Figure 2.4: Sierra Chica site-mean paleomagnetic directions and fold-test results. (a) Mean directions before and after tilt-correction. α_{95} of the means are removed for clarity. (b) Results of the bootstrap fold-test. Red dashed lines are example bootstrap results, showing the change in directional clustering (higher τ_1 values = tighter clustering) as a function of unfolding. Cumulative distribution function (green curve) of 2000 bootstrap results shows 95% confidence bounds that extend from 105-138% untilting; the optimal value is 121.5%. (c) Quantile-Quantile plots of tilt-corrected site-level virtual geomagnetic poles (VGPs) (Lewis and Fisher, 1982). The plots graphically illustrate the fit of a dataset to a theoretical distribution (in this case a Fisher distribution) by the linearity of the data; a perfect fit would result in perfect linearity. The left panel compares VGP longitudes (relative to the mean VGP) against a uniform distribution, the right panel compares VGP latitudes (relative to the mean VGP) against an exponential distribution, according to Fisher (1953). The values of Mu and Me do not exceed the theoretical thresholds (in brackets) that would permit rejection of the hypothesis that the VGPs are Fisher distributed at the 95% confidence level (see Tauxe, 2010).

The mean direction from the upper unit of this study is statistically different from the mean direction of the upper unit from Tomezzoli et al. (2008) (see their Table 1). The directions are distinct in both declination and inclination and, being from the upper unit, are uncomplicated by tilt corrections. The in situ mean directions from the middle units sampled in the two studies are more similar, but the previous collection includes only two sites from this section, so a rigorous statistical test of a common mean cannot be applied. Because the populations of directions from these two studies do not statistically share a common mean, the datasets have not been combined. The resulting site and unit-level VGPs are listed in Table 2.1. The study-wide Sierra Chica paleopole, after tilt-correction, is: 80.1° S, 349.0° E, A_{95}: 3.3°, K: 53.4, and N: 35. If tilt-corrections are optimized by increasing the dip by 5°, the alternative paleopole (SCalt) is: 82.4° S, 6.4° E, A_{95}: 3.0°, K: 68.2.

2.6 Magnetic Mineralogy

Hysteresis measurements of representative samples throughout the stratigraphic section substantiate the presence of at least two magnetic mineral phases with distinct coercivities (Fig. 2.5), as suggested by AF demagnetizations. Two samples from the upper unit, one from a site with only the low-coercivity phase (SC18-3) and one with both low- and high-coercivity components (SC14-7), were selected for low-temperature remanence and high-temperature susceptibility experiments to further characterize the magnetic carriers. In the FC/ZFC low-temperature experiments, both SC14-7 and SC18-3 experienced a change in the rate of remanence loss during warming through the interval 110-120 K, which is diagnostic of the Verwey transition in magnetite (Figs. 2.6a,b) (Muxworthy and McClelland, 2000). In sample SC18-3, this transition appears protracted, perhaps even bimodal, initiating at ∼100

K. Such a lowered transition temperature can be a consequence of magnetite non-stoichiometry, either due to impurities or an oxygen deficiency (Özdemir et al., 1993; Brabers et al., 1998). The suppressed appearance of the transition in sample SC14-7, as well as the gradual remanence loss with warming exhibited by both samples, could also be indicative of Ti-substitution and/or oxidation of magnetite (Özdemir et al., 1993; Moskowitz et al., 1998). While the remanence of SC18-3 continues to decay monotonically from 120-300 K, SC14-7 exhibits a broad peak, centered at ∼250-260 K, which we interpret to be the expression of the Morin transition in hematite (Özdemir et al., 2008).

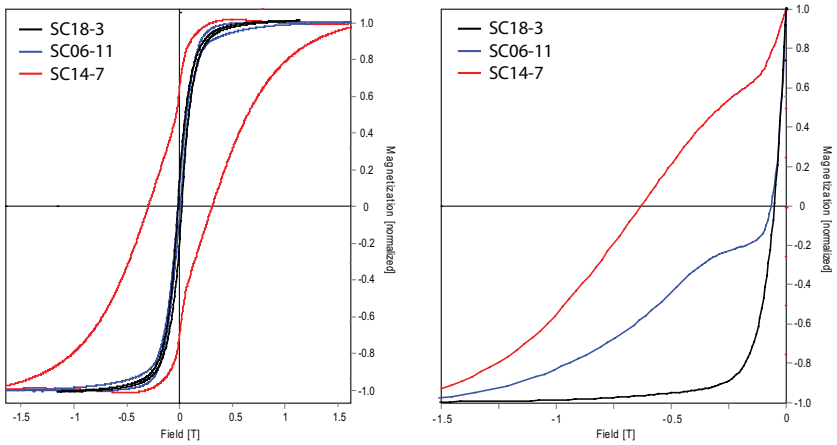

Figure 2.5: Hysteresis behavior of Sierra Chica samples. Hysteresis loops after paramagnetic correction (left panel) and back-field curves (right panel) of representative samples that exhibit: one magnetic phase with a low-coercivity (black curves), two magnetic phases with low and high coercivities (blue curves), and dominance by a phase with a high coercivity, but a minor contribution from a phase with a low-coercivity (red curves).

Sub-samples of SC14-7 and SC18-3 (not used in MPMS experiments) were subjected to thermomagnetic (κ vs. T) cycling to identify high-temperature magnetic critical points (Figs. 2.6 c,d). In SC14-7, inflection points are found at 550 °C and 680 °C, which are consistent with the Curie temperature of Ti-poor titanomagnetite and the Néel temperature of hematite (Dunlop and Özdemir, 1997). Sample SC18-3

also exhibits a pair of inflection points; at 345 °C and 575 °C, the latter likely being the Curie point of low-Ti titanomagnetite. The lower temperature critical point is not represented in the cooling curve, implying that it represents a meta-stable mineralogic phase destroyed during the heating cycle. We interpret this to be the expression of a thermally-driven inversion of maghemite to hematite. Maghemite is known to form on the surfaces of magnetite either during primary (deuteric) or secondary low-temperature oxidation (Dunlop and Özdemir, 1997). The lowered total susceptibility exhibited by the cooling curve is consistent with such a transformation.

FORC diagrams from samples SC14-7 and SC18-3, and sample SC05-4 from the lower unit all exhibit a pattern indicative of pseudo-single domain (PSD) magnetite: self-closing inner contours and outer contours which diverge toward Hc = 0, with a general asymmetry about the axis Hu = 0 (Fig. 2.7a; Roberts et al., 2000; Carvallo et al., 2006). A profile along the axis Hu = 0 demonstrates that the coercivity distribution is very similar between these samples, perhaps reflecting a broad constancy of PSD grain dominance in the magnetite population, as implied by bulk hysteresis data for magnetite dominated samples (Figs. 2.7b,c).

2.7 Geochronology

Three samples were collected for analysis by SHRIMP U-Pb geochronology; SC-D04 (lowest unit), SC-D03 (middle unit), and SC-D01 (upper unit) (Fig. 2.8, Table A.1). Zircon was least abundant in the sample from the lowest trachyandesitic unit, and individual grains showed a greater size variation, ranging from 150 to 500 μm. Zircons from SC-D04 also have a more homogeneous internal structure exhibited by the cathodoluminescent images, with grains displaying a more uniformly bright pattern (Fig. 2.8b). Zircons in the samples from the middle and upper rhyolitic units

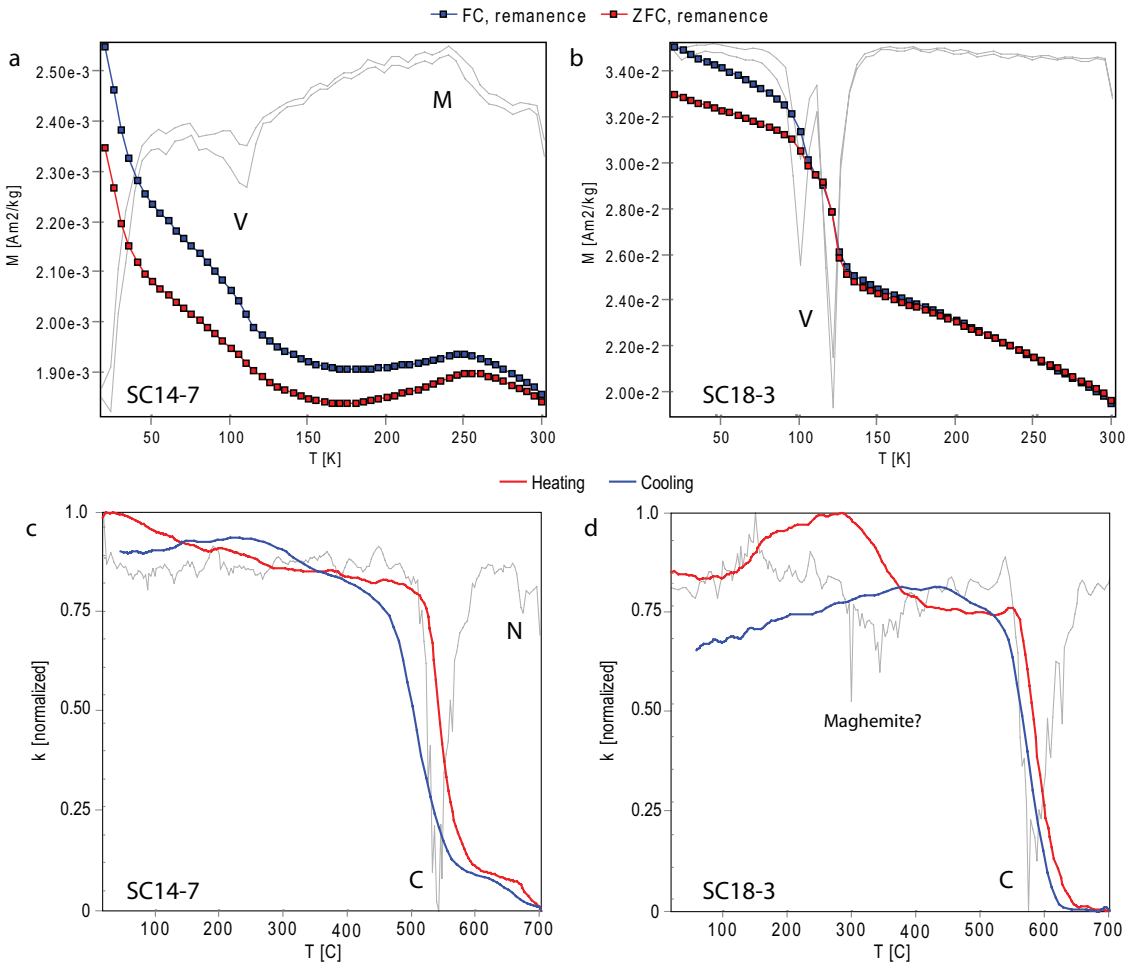

Figure 2.6: Results of low-temperature remanence (a,b) and high-temperature susceptibility (c,d) experiments on Sierra Chica samples. In (a) and (b) the light gray curves are the first derivatives of the remanence curves. V (Verwey) and M (Morin) denote interpreted transitions discussed in the text. In (c) and (d) the light gray curves are the first derivatives of the heating curve. C and N denote the interpreted Curie and Néel points discussed in the text. (a) and (c) are measurements on a sample possessing both low and high coercivity phases (as determined from demagnetization results), while (b) and (d) are measurements on a sample with only the low coercivity phase.

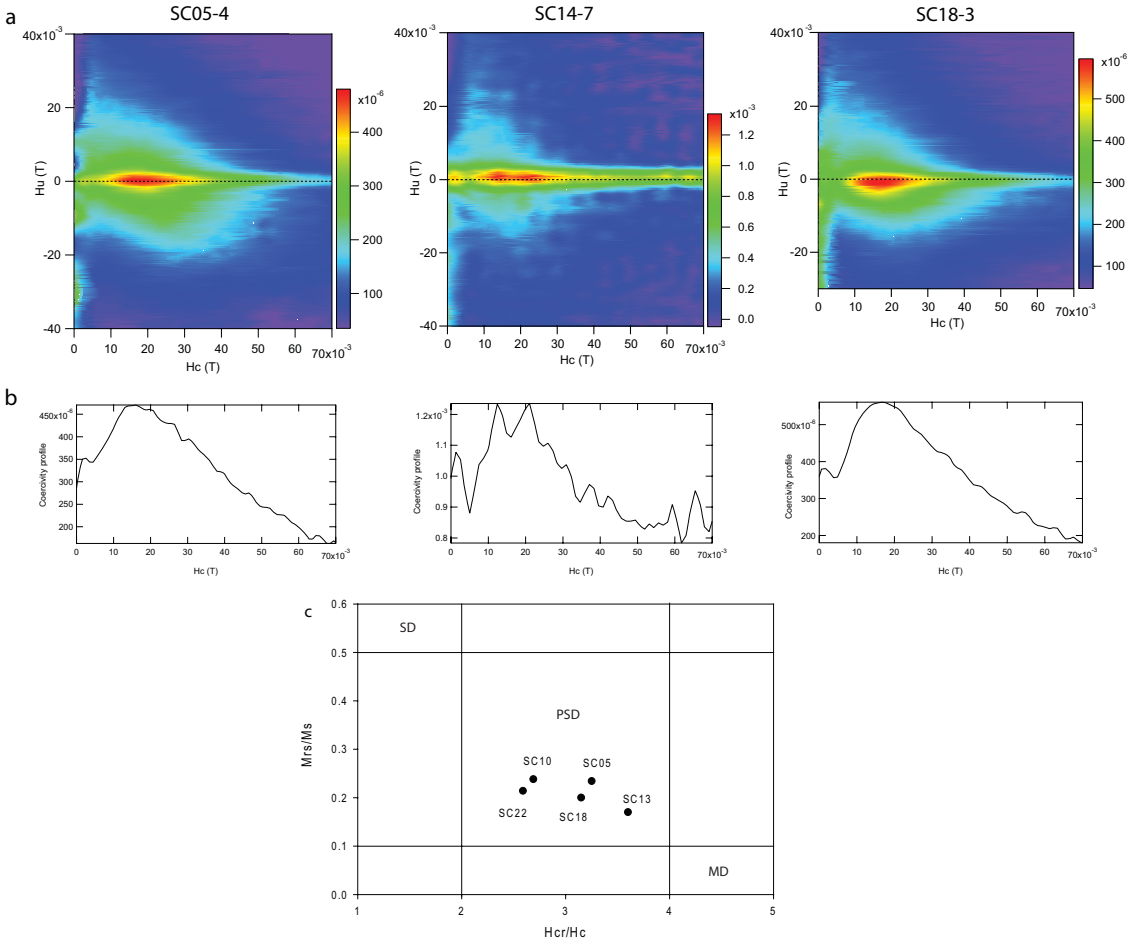

Figure 2.7: Further experiments on the low-coercivity phase (magnetite). (a) First order reversal curve (FORC) diagrams, showing typical PSD behavior. A smoothing factor of 3 was used in the production of the FORC diagrams. (b) Coercivity profiles taken across the axis Hu = 0. Again, all three samples exhibit very similar PSD behavior. (c) "Day" plot of bulk hysteresis properties of samples dominated by magnetite. All samples fall in the PSD range.

are more abundant and show a homogeneous grain size distribution (about 300 μm). These differences between the trachyandesite sample and the rhyolite samples are mirrored by differences in zircon chemistry; the rhyolitic samples are richer in U (average of 150-180 ppm) and have lower average Th/U ratios of about 1.6 (Table A.1). Zircon grains from sample SC-D04 present lower average U contents of 70 ppm, and somewhat elevated Th/U ratios > 2. Overall, zircon morphologies (euhedral), internal structure (oscillatory zoning, absence of overgrowths) and chemistry (relatively high Th/U ratios) are diagnostic of an igneous origin.

The zircon age populations are relatively homogeneous within each of the samples, and very similar between them (Figs. 2.8a,c). Only one zircon xenocryst was observed, in sample SC-D03 (which provides a U-Pb date of 690 $\pm$18 Ma; 2σ error); it was likely inherited from underlying Precambrian basement during magma ascent and emplacement. Zircons from SC-D03 display the most uniform distribution of age estimates, with 15 of the 16 grains yielding a U-Pb "concordia" date of 263.0 $\pm$5.7 Ma with a low MSWD of 0.47. A slightly older date of 268.1 $\pm$7.7 Ma is calculated for sample SC-D01, with a higher MSWD of 2.4. These age estimates are equivalent at the 2σ error level. SC-D04 yields the youngest date of 257.0 $\pm$2.8 Ma, calculated from a line intercepting the concordia curve in the Tera-Wasserberg plot. This age estimate is significantly younger than those calculated from the samples from overlying units. However, the lower U abundances in this sample signify a higher proportion of common Pb, as indicated by the presence of ^{204}Pb. We regard the data from the two rhyolitic samples as the most robust.

For paleomagnetic purposes, these three units are interpreted to represent closely spaced magmatic episodes that reflect emplacement over a million-year timescale, which should be sufficiently long to average effects of secular variation, but certainly

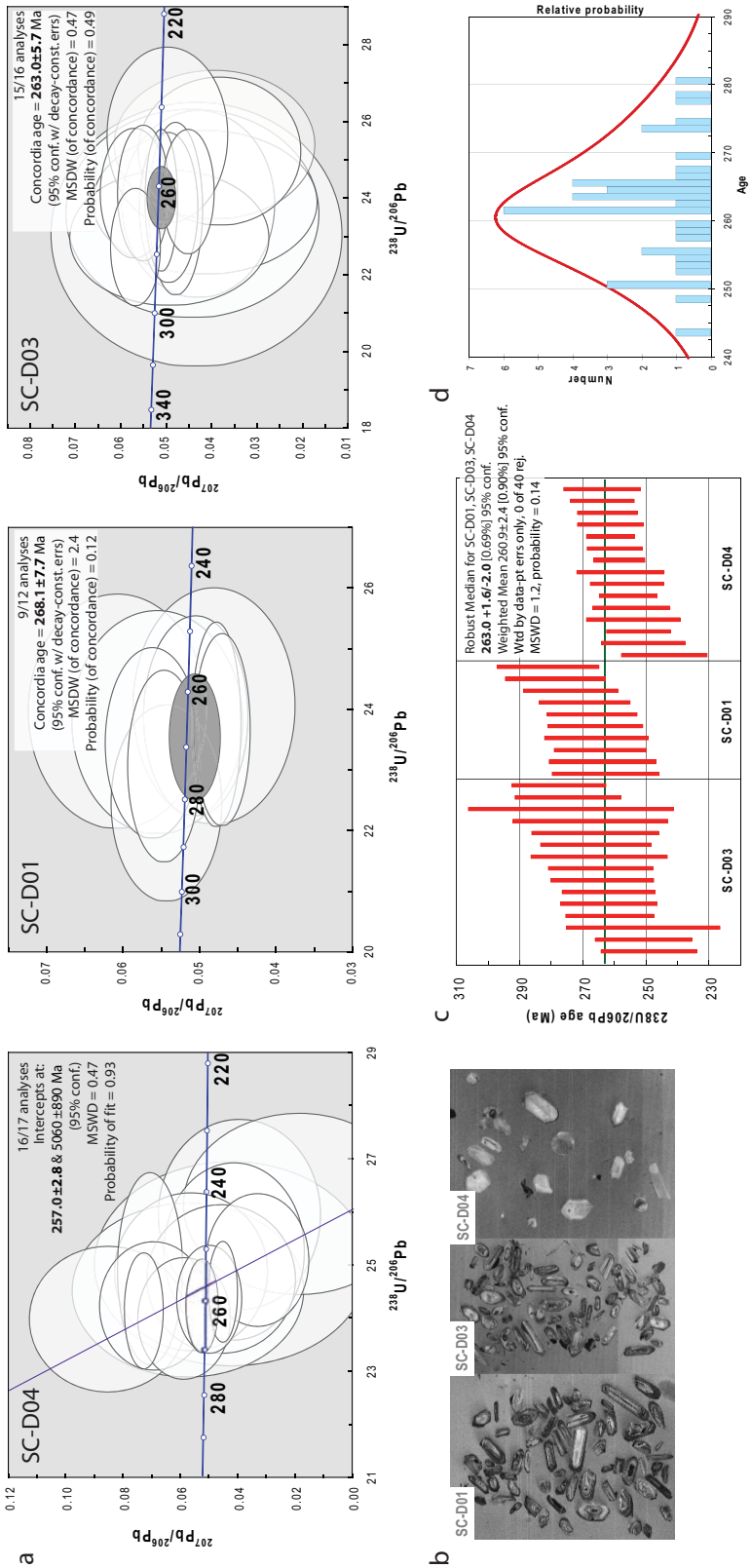

Figure 2.8: Sierra Chica U-Pb geochronology results. (a) Tera-Wasserberg plots of sample results. All data point error ellipses are 2σ. (b) Cathodoluminescent images of zircon grains used in SHRIMP analysis. (c) Plot of all retained zircon dates with 2σ error (red lines), yielding a robust median age estimate of 263.0 Ma (thick black line). (d) Histogram of all zircon dates showing the mean age estimate of 260.9 Ma.

not long enough to record appreciable plate motion. We therefore treat these samples as a single magmatic episode and pool the geochronologic data from the three samples. The median date calculated from the three samples (263.0 +1.6/-2.0 Ma, 95% conf) is statistically indistinguishable from the well-determined age estimate of sample SC-D03.

2.8 Discussion

2.8.1 Interpretation of Paleomagnetic Results

The presence of normal polarity magnetizations in the lower unit suggests that the Sierra Chica is younger than the Kiaman Reversed Superchron, which has an upper age of about 265 Ma (Gradstein et al., 2004). This is compatible with our new U-Pb age estimate of 263.0 +1.6/-2.0 Ma for the Sierra Chica. However, if the rocks were not magnetized during a protracted interval of reverse polarity, the dominance of reverse polarity magnetizations in the middle and upper units suggests that secular variation may not have been adequately averaged. The upper unit is notable in this regard; the 15 site-level VGPs are very well-clustered with an A_{95} of 3.5° and a K of 122. Using the mean value of K (at latitude $\approx 42°$) determined from a compilation of volcanic rock paleomagnetic records from the last 5 Myr (Harrison, 2009), and the χ^2 test of McFadden (1980), a VGP-set of N = 15 is expected to yield a K of 20.3 to 49.6 (95% confidence limits), if secular variation has been adequately averaged. The tight clustering of the upper unit VGPs can be attributed to rapid flow emplacement, and may suggest that the upper unit represents one large eruptive event. This is further supported by the thick and featureless character of the upper unit, and the scarcity of identified cooling contacts within it. The lower and middle units, with thinner flows, abruptly changing characteristics, and distinct cooling contacts, are more likely to represent a prolonged series of eruptions. This is reflected in a higher

A_{95} (5.2° after tilt correction), a smaller K (40.7) and dual polarity magnetizations. The expected range for K (determined as above with N = 20) is 21.3 to 45.7 (95% confidence limits).

If the upper unit was largely emplaced during one eruptive event, it is plausible that the tilting of the middle/lower units could have been a consequence of local subsidence or caldera collapse, due to the rapid evacuation of large quantities of magma. In a multicyclic eruptive center, it is likely that early eruptive phases become structurally modified by later eruptive events (Lipman, 1997). An alternative interpretation involving tilting driven by regional deformation seems less likely, given the short time span between emplacement of the lower/middle and upper units, based on the U-Pb dates.

It was previously noted that the optimal degree of unfolding is greater than 100% and possibly indicates an underestimate of the true tectonic tilt of the lower/middle units. It is important to note that original horizontality cannot always be assumed with silicic volcanic rocks, due to their relatively high viscosity. Although we are unable to unequivocally eliminate this possibility, we recognize that the character (thinner, lithic-rich) of the dipping lower/middle units is indicative of volatile-charged (fluidized) flow, which is unlikely to assume steep gradients during emplacement. An on-going magnetic fabrics study may be able to confirm this assumption in the future.

The bootstrap foldtest seeks to maximize the co-axiality of a population of directions, but this expectation is only exactly appropriate if two populations of directions are of the same age (and, technically, error-free). Our U-Pb dates indicate that the lower, middle, and upper units are approximately the same age, having been emplaced over a million-year timescale. Thus, the condition of age-equivalence seems to be met; however, the results of the secular variation averaging χ^2 test suggest

that the upper unit was magnetized over a relatively brief interval of time, and so its population of magnetization directions may more closely represent an instantaneous paleomagnetic field rather than a time-averaged one. In this case, maximizing the co-axiality of the population of directions from the lower/middle and upper units is unlikely to be exactly appropriate, as the lower/middle units have collectively averaged secular variation, while the upper unit has not. Therefore, we do not necessarily consider the optimal foldtest result (SC_{alt}) to be the most reliable estimate of the true paleomagnetic pole.

The positive reversal test based on the complete dataset supports our contention that the collection as a whole reflects a sufficiently time-averaged sampling of the paleomagnetic field, and that the populations are directionally similar. The recognition of PSD magnetite and hematite as the carriers of the ChRM, which are capable of acting as high-fidelity magnetic recorders across geologic timescales, is consistent with the interpretation of a primary magnetization (Dunlop and Özdemir, 1997). Ultimately, the Sierra Chica paleopole meets 6 of the 7 reliability criteria as proposed by Van der Voo (1990); it does not meet criterion #7, as it resembles Late Cretaceous South American paleopoles (Somoza and Zaffarana, 2008).

2.8.2 Implications

Most paleomagnetic poles that constitute the late Paleozoic–early Mesozoic APWP of South America are derived either from relatively old studies, which do not meet modern reliability criteria, or sedimentary rocks, which are prone to misrepresenting the paleomagnetic field via inclination shallowing, and are often associated with poor absolute age-control. A total of 27 South American paleomagnetic poles with inferred ages of 300 to 200 Ma meet reliability criteria #2 (sufficient number of samples: $N \geq 6$, $n \geq 30$) and #3 (adequate demagnetization) (Van der Voo, 1990)

(Table 2.2). Of the 27 compiled poles, seven are derived from post-folding magnetizations with no upper age-constraints, and are instead dated by the relative position of the pole with respect to previously published results. The use of such poles in the construction of an APWP or as reference poles involves circular reasoning, and these poles will not be considered further. We discard four additional poles due to poor structural control, in that they are suspected to have been subjected to vertical axis rotations or the structural restorations are either unknown or complex. Of the remaining 16 poles, three are defined by syn-folding magnetizations from sedimentary sequences that were deformed during the SROP. Because the timing of SROP deformation is poorly established, the age-constraints on these magnetizations are relatively limited. Only seven of the 16 filtered results include data derived from igneous rocks, and of the nine studies conducted entirely on sedimentary rocks, only two were explicitly checked/corrected for the effects of inclination shallowing. Furthermore, none of the igneous rocks examined have been recently or reliably dated by modern geochronologic methods, the few existing isotopic age estimates having been obtained by the demonstrably inferior K-Ar technique. Thus, our new data provide a well-dated, high-quality paleomagnetic pole for this critically data-deficient segment of the South American APWP.

Our new paleopole (SC) is proximal to the Late Permian mean pole calculated from the filtered compilation (Fig. 2.9, Table 2.2). Because of the sparsity of poles and the poor chronologic resolution on several sequences, only three mean paleopoles were calculated from the filtered compilation (for the Early Permian, Late Permian, and Triassic), and several results were included in two mean pole calculations, so the estimates are not strictly independent. To allow for a meaningful comparison, SC was not included in the calculation of the Late Permian mean pole (Fig. 2.9).

We note that SC is observed to fall within the A_{95} of this Late Permian mean pole, whereas SC_{alt}, the pole obtained by alternatively adopting the structural correction that optimizes directional clustering, lies outside this A_{95}. SC is significantly different from the previous pole from the Sierra Chica (pSC), which appears to fall closer to the Early Permian mean pole, but with a notably different longitude (Fig. 2.9).

Despite the overall scatter of poles in this filtered compilation, there is a clear change in pole position as a function of inferred pole age (path A, Fig. 2.10), which is consistent with the combined late Paleozoic–early Mesozoic APWPs of other Gondwana blocks rotated into a common reference frame (path B, Fig. 2.10; data from the compilation of Torsvik et al., 2008). The trajectory of Path B corroborates the mid-to-Late Permian curvature evident in path A, which SC seems to further support (see also, Tomezzoli, 2009). It is important to note that paths A and B, although similar in trend, are not coincident for mid-to-Late Permian time. In the same way, the combined APWPs of Baltica and Laurentia, rotated into the same South American reference frame (path C, Fig. 2.10; data from the compilation of Torsvik et al., 2008), show a similar form to path A, but diverge from it most obviously in the mid-to-Late Permian. Yet, the most pronounced disparity in the mid-to-Late Permian is between paths B and C, a discrepancy that has been long-recognized and enduring (Irving, 2004). The fact that the filtered South American dataset and the SC result "bisect" the separation of the B and C paths would suggest that the disparity is in part a consequence of inclusion of poor-quality results, rather than a reconstruction problem or a geomagnetic field aberration. Indeed, within the South American dataset, the poles that fall the closest to the Permian segment of path B are those derived from sedimentary rocks (and uncorrected for inclination shallowing). Similarly, late Paleozoic–early Mesozoic South American paleopoles rejected on the basis of fail-

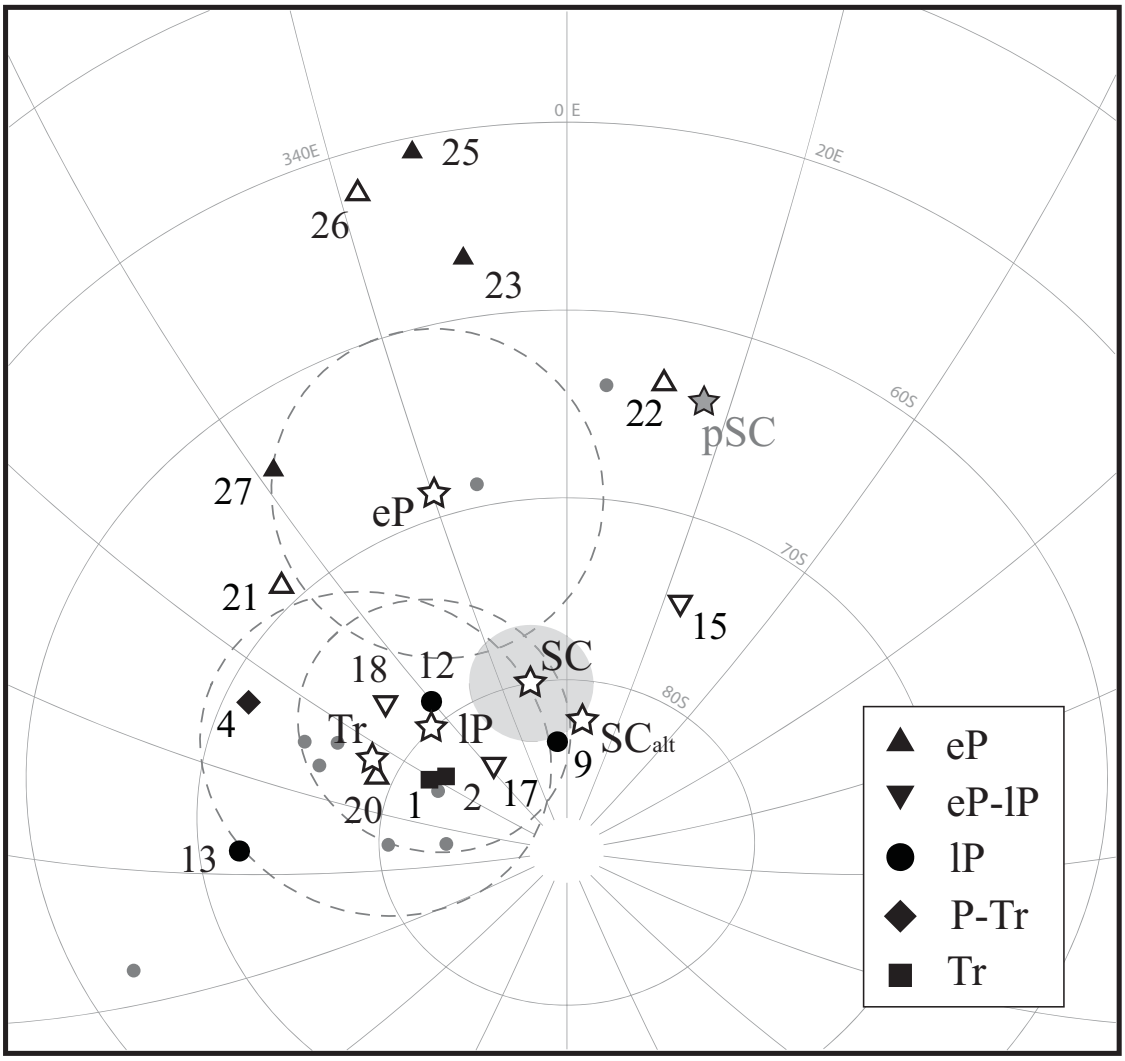

Figure 2.9: 300–200 Ma paleopoles from South America. Numbers correspond to pole numbers in Table 2.2. Symbol shapes correspond to age as follows: upright triangles = Early Permian, inverted triangles = mid-Permian, circles = Late Permian, diamonds = Permo-Triassic, squares = Triassic. Solid symbols are poles that are at least partly derived from igneous rocks, or from sedimentary rocks that have been checked/corrected for inclination shallowing; open symbols are therefore considered to be "less-reliable" results. Small gray dots are the poles listed in Table 2.2 that were rejected according to notes 1 or 2. SC = Sierra Chica result (this work), SC_{alt} = Sierra Chica result with optimal untilting. pSC = Sierra Chica result of Tomezzoli et al. (2008). Open stars correspond to mean poles in Table 2.2: eP = Early Permian, lP = Late Permian, and Tr = Triassic. A_{95} from all but SC and the mean poles have been removed for clarity.

ing to meet reliability criterion #2 or #3 (and therefore not shown) are generally closer to path B than high-quality age-equivalent poles. This may suggest that path B (and perhaps path C) is contaminated by systematic data-pathologies, such as unrecognized or incompletely removed overprints, inclination shallowing, structural complexities, or erroneous age assignments. Although an in-depth analysis of these larger pole-sets is beyond the limitations of this paper, we note that vintage paleomagnetic results and poles derived from sedimentary rocks constitute a significant part of the collections, as in the South American dataset. Although errors in Euler rotations undoubtedly remain and contribute to these APWP discrepancies, we posit that paleomagnetic data of relatively poor quality are the principal source of the problem. This hypothesis implies that controversial Late Permian–Early Triassic paleogeographic reconstructions built to accommodate the paleomagnetic data (Irving, 1977, 2004; Torcq et al., 1997) are not necessary, but additional work is required to demonstrate this unequivocally. For times before the mid-to-late Early Permian ($\gtrsim$ 280 Ma), a Pangea "B-type" configuration remains a possibility (Muttoni et al., 1996; 2003).

2.9 Conclusions

A joint paleomagnetic and geochronologic re-examination of the Sierra Chica has resulted in a new high-quality late Paleozoic paleomagnetic pole for Gondwana. New U-Pb age determinations indicate that the Sierra Chica was emplaced at 263.0 +1.6/-2.0 Ma. Positive fold and reversal tests reveal the magnetization to be primary, and rock magnetic tests indicate that the carriers of magnetization are PSD magnetite and hematite, which are capable of preserving a primary Late Permian remanence. The position of the Sierra Chica pole (80.1° S, 349.0° E, A_{95}: 3.3°) is proximal to

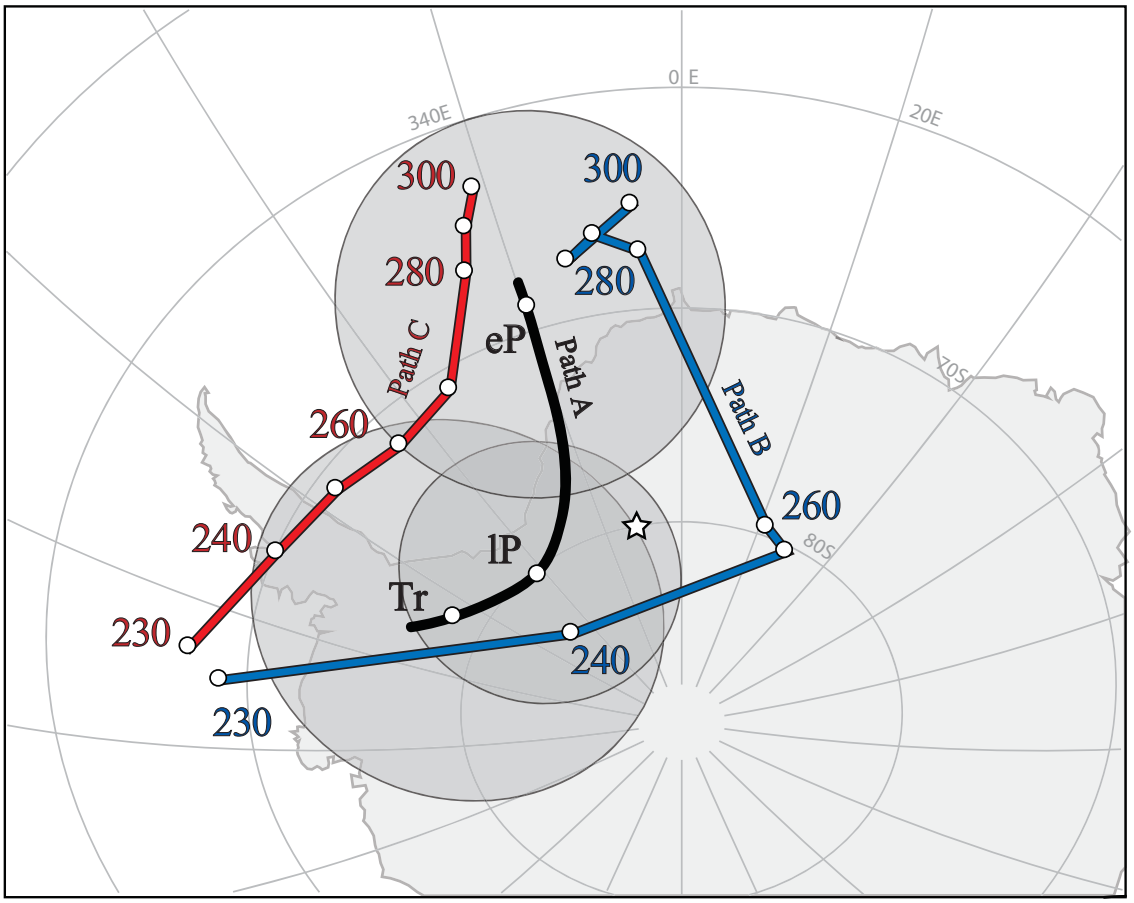

Figure 2.10: Comparison of apparent polar wander paths in a Pangea A-type reconstruction (see Torsvik et al., 2008). Path A is defined by three mean poles from Table 2.2: eP = Early Permian, lP = Late Permian (with SC result included), and Tr = Triassic. The black line connects the poles, assuming a simple path. Path B (combined data from India-Pakistan, Madagascar, and Africa; Torsvik et al., 2008) and Path C (combined data from Baltica and Laurentia; Torsvik et al., 2008) have been rotated into the Colorado (Central Argentina) Plate reference frame (Torsvik et al., 2009). Baltica and Laurentia data have been combined via the Euler pole of Alvey (2009). Paths B and C are moving averages, constructed by a moving 20-Myr window, with 10-Myr steps. Ages (Ma) are listed adjacent to select poles. A_{95} from these paths have been removed for clarity. The star is the new SC pole.

the Late Permian mean pole for South America, calculated from a filtered paleopole dataset that yielded few, but moderately reliable records. The Sierra Chica pole, therefore, corroborates the position of this Late Permian mean pole, as well as the curvature of the late Paleozoic segment of the APWP of Gondwana. The position of this new high-quality paleomagnetic pole between the previously distinct Late Permian segments of the Laurussian and Gondwanan APWPs suggests that the long-observed separation between the paths is due to systemic data pathologies.

2.10 Acknowledgements

H. Tickyj and M. E. Woroszylo are thanked for discussions about the area and assistance in the field. Mike Jackson and the staff at the IRM are thanked for their assistance with the rock magnetic experiments. Use of the following freeware is acknowledged: Paleomac, PmagPy, Gmap, and FORCinel. Financial support for this research was provided by the Norwegian Geological Survey (NGU) and the U.S. National Science Foundation, Division of Earth Sciences (Tectonics Program), and NSF's Office of International Science and Engineering (Americas Program), grant EAR-0634807, and is gratefully acknowledged. Additional funding was provided by PIP-CONICET 11220080102828, UBACYT X220, and an IRM visiting fellowship granted to M. Domeier. E. Tohver acknowledges funding from the Australian Research Council (LP0991834) and use of the UWA-Curtin joint facilities for imaging (Centre for Microscopy, Characterization and Analysis) and U-Pb SHRIMP II facility at the John de Laeter Centre for Geochronology. Comments from John Geissman and an anonymous reviewer improved the quality of the chapter.

Table 2.1: Sierra Chica site-mean paleomagnetic data

Site	**N/n/v**	**Dg**	**Ig**	**Ds**	**Is**	**k**	α_{95}	**PLat**	**Plon**	$\mathbf{A_{95}}$
A								−37.92	294.53	
RS16	5/5/5	165.2	56.2	165.2	56.2	50.8	10.8	−78.2	25.7	15.6
SC19	7/6/1	170.3	47.0	170.3	47.0	698.2	3.0	−77.3	71.8	3.9
RS15	5/5/2	174.5	59.4	174.5	59.4	110.9	8.3	−85.2	354.8	12.5
RS13	8/8/8	161.2	58.2	161.2	58.2	160.1	4.4	−75.2	15.1	6.5
SC18	7/6/3	157.4	62.3	157.4	62.3	118.7	6.6	−72.0	358.9	10.3
SC17	-	-	-	-	-	-	-	-	-	
B								−37.91	294.55	
SC25	7/7/5	164.1	62.0	164.1	62.0	89.9	6.6	−76.8	355.6	10.2
RS12	5/5/5	164.6	63.0	164.6	63.0	39.1	12.4	−76.8	350.2	19.5
SC16	6/6/5	178.0	58.1	178.0	58.1	876.7	2.3	−88.2	353.7	3.4
C								−37.90	294.55	
SC24	7/7/4	175.2	62.6	175.2	62.6	505.5	2.8	−82.9	323.7	4.4
SC13	7/6/3	179.6	55.3	179.6	55.3	770.1	2.6	−88.0	106.1	3.7
RS11	5/5/3	169.6	46.9	169.6	46.9	231.6	5.4	−76.9	70.0	7.0
SC15	5/5/4	178.0	58.6	178.0	58.6	278.0	4.7	−87.9	340.6	7.0
SC14	7/7/5	169.5	60.2	169.5	60.2	320.5	3.5	−81.3	359.8	5.3
RS10	6/6/5	166.4	61.8	166.4	61.8	82.7	6.8	−78.5	354.2	10.4
SC22	7/4/0	164.1	−62.2	164.1	−62.2	–	12.5	−76.7	354.7	–
SC23	7/7/6	85.9	70.4	146.7	64.8	158.4	4.9	−64.1	353.8	7.8
D								−37.89	294.57	
SC12	-	-	-	-	-	-	-	-	-	
RS09	4/4/2	216.9	77.0	196.5	53.4	561.9	4.5	−76.1	192.9	6.3
SC11	7/7/0	165.2	85.9	182.1	61.1	–	9.7	−85.4	274.5	–
RS08	4/4/0	35.0	82.7	173.8	71.0	–	12.2	−72.0	305.9	–
SC21	7/5/4	61.7	80.7	163.2	68.7	168.3	6.1	−71.6	328.7	10.3
RS07	5/5/5	80.3	77.6	155.3	65.3	74.7	8.9	−69.7	349.0	14.4
RS06	3/3/2	77.1	80.0	160.8	66.2	85.7	11.6	−72.5	340.8	19.0
RS05	5/4/3	87.4	77.4	155.9	63.7	41.0	15.4	−70.6	354.3	24.4
SC08	6/6/4	139.3	86.4	179.5	62.4	113.2	6.6	−84.1	298.1	10.3
SC10	7/7/4	170.7	85.8	182.9	60.9	29.2	11.9	−85.4	266.9	18.1
RS03	4/4/4	104.6	75.6	156.2	59.3	74.1	10.7	−71.4	10.2	16.1
SC09	7/7/7	41.1	86.4	179.3	67.8	159.6	4.8	−77.0	296.5	8.0
RS04	4/4/2	17.1	74.6	167.0	79.6	121.7	9.7	−57.3	302.8	18.5
SC07	7/5/0	183.2	80.2	184.5	55.2	–	5.4	−85.8	174.3	–
SC06	8/7/6	134.3	76.5	166.6	54.9	122.2	5.1	−79.0	33.3	7.2
RS02	5/5/5	65.0	77.6	154.6	68.5	38.3	12.5	−67.4	338.3	21.1
RS01	-	-	-	-	-	-	-	-	-	-
E								−37.87	294.54	
RS17	6/6/6	261.4	−77.7	344.7	−67.2	41.5	6.8	73.8	151.9	11.3
SC05	8/8/8	277.6	−73.1	337.1	−62.0	183.6	2.7	71.8	180.1	4.2
SC20	6/6/6	304.1	−78.9	353.8	−59.6	188.7	4.9	84.6	174.3	7.4
SC04	10/10/10	313.0	−68.0	344.0	−50.0	122.9	3.0	75.1	228.2	3.9
Mean	N=35	152.9	74.2	169.2	61.4	95.5	2.5	−80.1	349.0	3.3

N/n/v:(N)umber of specimens measured/(n)umber of specimens used/(v)number of vectors
Dg(s)/Ig(s): declination/inclination in geographic (stratigraphic) coordinates
k: Estimate of the Fisher (1953) precision parameter
$\alpha(A)_{95}$: the semi-angle of the 95% cone of confidence about the site mean direction (VGP)
VGP lat/long: virtual geomagnetic pole latitude/longitude; bold entries are sector lat/lon

Table 2.2: 300–200 Ma paleopoles from South America

Pole#	Rock Unit	Type	Age	$Plat_{co}$	$Plon_{co}$	N	A_{95}	Notes	Reference
1	Dolerites, Suriname	I	∼200 Ma[a]	-82.5	295.8	10	10		Veldkamp et al., 1971
2	Rio Blanco, Uspallata, Arg.	S,E	lTr	-81.8	298.3	12	7.6		Vizan et al., 2004
3	Rio Curaco, Carapacha Basin, Arg.	S,I	242 ± 10 Ma (K-Ar)	-64	5	13	5	1	Tomezzoli et al., 2006
4	Mitu Group, Peru	S,E	lP-eTr	-71.4	293.5	6	5.7		Gilder et al., 2003
5	Pavon Fm., SRB, Arg.	S,I	260-240 Ma (K-Ar)	-83.7	271	11	7.9	1	Rapalini and Cingolani, 2004
6	Cerro Victoria, Rio de la Plata, Arg.	S	lP-eTr	-82.4	303.3	13	3.9	1	Rapalini and Snchez Bettucci, 2008
7	Yerbal, Rio de la Plata, Arg.	S	lP-eTr	-76.6	294.9	6	5.9	1	Rapalini and Snchez Bettucci, 2008
8	Rocha, Rio de lat Plata, Arg.	S	lP-eTr	-76.2	287.7	18	4.2	1	Rapalini and Snchez Bettucci, 2008
9	Independencia Grp., Paraguay	S	lP (post-Kiaman)	-83.6	355.8	10	6.6	[b]	Rapalini et el., 2006
10	Quebrada del Pimiento Fm., SRB, Arg.	I	260 Ma (K-Ar)	-65.9	189.8	7	11.8	2	Terrizano et al., 2005
11	La Flecha, Precordillera, Arg.	S	lP? (post-Kiaman)	-63.8	244.6	7	18	1	Rapalini and Astini, 2005
12	Tambillos, Uspallata Basin, Arg.	E	late eP-lP (Kiaman)	-78.9	319.6	16	6.5		Rapalini and Vilas, 1991
13	Horcajo Fm., Uspallata Basin, Arg.	E	lP (Kiaman)	-72.4	264.8	26	12		Rapalini and Vilas, 1991
14	La Colina Fm. - Paganzo Village, Arg.	S	266 ± 7 Ma (K-Ar)	-80.6	268.8	162	2.8	2	Geuna and Escosteguy, 2004
15	Tunas II, Sierra Australes, Arg.	S	eP-lP (Kiaman)	-74.7	23.6	24	5.2	3	Tomezzoli, 2001
16	Choiyoi, Cerro Chachil, Arg.	E	eP-lP (Kiaman)	-21	232	n=33	8	2	Rapalini et al., 1989
17	Multiple Fms., E. Cordillera, Bolivia	S	eP-lP (Kiaman)	-83.7	322.7	57	3.5		Libarkin et al., 1998[c]
18	Sierra Grande - San Carlos Mem., Arg.	S	eP-lP (Kiaman)	-77.3	310.7	13	7	3	Rapalini , 1998
19	Zonda and San Juan Fms., Argentina	S	P? (Kiaman)	-68.9	346.9	11	17.8	1	Rapalini and Tarling, 1993

... Table 2.2 continued

Pole#	Rock Unit	Type	Age	$Plat_{co}$	$Plon_{co}$	N	A_{95}	Notes	Reference
20	Cerro Colorado, Paganzo Basin, Arg.	S	lCr-lP (Kiaman)	-79.3	290.6	6	11		Geuna and Escosteguy, 2004
21	Copacabana Group, Peru	S	eP	-69.1	312.7	9	5.2		Rakotosolofo et al., 2006
22	Tunas I, Sierra Australes, Arg.	S	eP (Kiaman)	-63.6	12	19	5.1	3	Tomezzoli and Vilas, 1999
23	Pular/Cas Fms., Chile	E	290 ± 7 Ma (K-Ar)	-57	350	10	9.6		Jesinkey et al., 1987
24	Rincon Blanco, Arg.	S,E	295-287 Ma (K-Ar)	-75	291.5	19	6.7	2	Geuna and Escosteguy, 2004
25	La Tabla Fm., Chile	E	lCr-eP	-51	347	10	5.7		Jesinkey et al., 1987
26	La Colina Fm. - Las Mellizas, Arg.	S	295 +/- 5 Ma (K-Ar)	-52.4	341.6	63	4.9		Geuna and Escosteguy, 2004
27	Santa Fe Grp., Brazil	S	lCr-eP (Kiaman)	-64	322.1	60	4.1	[b]	Brandt et al., 2009
pSC	Sierra Chica, La Pampa, Arg.	E	263 +1.6/-2.0 Ma	-64	17	10	15		Tomezzoli et al., 2008
SC	Sierra Chica, La Pampa, Arg.	E	263 +1.6/-2.0 Ma	-80.1	349	35	3.3		This Study
SC_{alt}	Sierra Chica, La Pampa, Arg.	E	263 +1.6/-2.0 Ma	-82.4	6.4	35	3		This Study

Means	Poles used	Label	Age	$Plat_{co}$	$Plon_{co}$	Np	A_{95}
Triassic	1, 2, 4	Tr	250-200 Ma	-78.6	295.2	3	9.5
Late Perm.	4, 9, 12, 13, 15, 17, 18	lP	275-250 Ma	-80.1	314.2	7	7.3
	lP w/ SC			-80.3	318.4	8	6.4
Early Perm.	15, 17, 18, 20-23, 25-27	eP	300-275 Ma	-68.9	340.4	10	8.9

Type: (S)edimentary, (I)ntrusive, (E)xtrusive rocks

$Plat_{co}$/$Plon_{co}$: paleopole lat/lon rotated into Colorado Plate coordinates, see Torsvik et al., 2009

N: number of sites (or n=samples)

Notes: 1: no robust age constraints, 2: poor structural control, 3: syntectonic magnetization

[a]Estimate from Nomade et al. (2007)

[b]Checked/corrected for inclination shallowing

[c]Re-interpreted by Gilder et al. (2003)

References

Alvey, A. D., (2009). Using crustal thickness and continental lithosphere thinning factors from gravity inversion to refine plate reconstruction models for the Arctic and North Atlantic, Ph.D. thesis, University of Liverpool, U.K., 189 pp.

Brabers, V. A. M., Walz, F., & Kronmüller, H. (1998). Impurity effects upon the Verwey transition in magnetite. *Physical Review B*, 58, 14163-14166.

Brandt, D., Ernesto, M., Rocha-Campos, A. C., & dos Santos, P. R. (2009) Paleomagnetism of the Santa Fé Group, central Brazil: Implications for the late Paleozoic apparent polar wander path for South America. *Journal of Geophysical Research* 114, B02101, doi:10.1029/2008JB005735.

Carvallo, C., Muxworthy, A. R., & Dunlop, D. J. (2006) First-order reversal curve (FORC) diagrams of magnetic mixtures: Micromagnetic models and measurements. *Physics of the Earth and Planetary Interiors*, 154, 308-322.

Cogné, J. P. (2003) PaleoMac: A Macintosh ^{TM} application for treating paleomagnetic data and making plate reconstructions. *Geochemistry, Geophysics, Geosystems*, 4, 1-8.

Dalziel, I. W. D., & Grunow, A. M. (1992) Late Gondwanide tectonic rotations within Gondwanaland. *Tectonics*, 11, 603-606.

Domeier, M., Van der Voo, R., Tomezzoli, R. N., Torsvik, T. H., Vizan, H., Dominguez, A., & Kirshner, J. (2009) Alternative Pangea Reconstructions: A Matter of Flawed Data? Implications of a new Early Triassic Paleopole from Argentina. *American Geophysical Union Abstracts*, Abstract GP11A-05.

Dunlop, D. J., & Özdemir, Ö. (1997) Rock Magnetism: Fundamentals and Frontiers, Cambridge University Press. 596 pp.

Fisher, R. A. (1953) Dispersion on a sphere. *Proceedings of the Royal Society of London, Series A*, 217, 295-305.

Forsythe, R. (1982) The Late Paleozoic to Early Mesozoic evolution of Southern South America: a plate tectonic interpretation. *Journal of the Geological Society*, 139, 671-682.

Geuna, S., & Escosteguy, L. D. (2004) Paleomagnetism of the Upper Carboniferous-Lower Permian transition from Paganzo basin, Argentina. *Geophysical Journal International*, 157, 1071-1089.

Gilder, S., Rousse, S., Farber, D., McNulty, B., Sempere, T., Torres, V., & Palacios, O. (2003) Post-middle Oligocene origin of paleomagnetic rotations in upper Permian to lower Jurassic rocks from northern and southern Peru. *Earth and Planetary Science Letters*, 210, 233-248.

Gradstein, F. M., Ogg, J. G., Smith, A. G., et al. (2004) A Geologic Time Scale 2004. Cambridge University Press, Cambridge, 610 pp.

Halls, H. C. (1978) The use of converging remagnetization circles in palaeomagnetism. *Physics of the Earth and Planetary Interiors*, 16, 1-11.

Harrison, C. G. A. (2009) Latitudinal signature of Earth's magnetic field variation over the last 5 million years. *Geochemistry, Geophysics, Geosystems*, 10, Q02012.

Heredia, N., Rodríguez Fernández, L. R., Gallastegui, G., Busquets, P., & Colombo, F. (2002) Geological setting of the Argentine Frontal Cordillera in the flat-slab segment (30°00'-31°30'S latitude). *Journal of South American Earth Sciences*, 15, 79-99.

Irving, E. (1977) Drift of the major continental blocks since the Devonian. *Nature*, 270, 304-309.

Irving, E. (2004) The Case for Pangea B, and the Intra-Pangean Megashear. In: Timescales of the paleomagnetic field, J. E. T. Channell, D. V. Kent, W. Lowrie and J. G. Meert, Editors, *American Geophysical Union - Geophysical Monograph*, 145, 13-27.

Jesinkey, C., Forsythe, R. D., Mpodozis, C., & Davidson, J. (1987) Concordant late Paleozoic paleomagnetizations from the Atacama Desert: Implications for tectonic models of the Chilean Andes, *Earth and Planetary Science Letters*, 85, 461-472.

Kay, S. M., Ramos, V. A., Mpodozis, C., & Sruoga, P. (1989) Late Paleozoic to Jurassic silicic magmatism at the Gondwana margin: analogy to middle Proterozoic in North America? *Geology*, 17, 324-328.

Kirschvink, J. L. (1980) The least squares line and plane and the analysis of paleomagnetic data. *Geophysical Journal of the Royal Astronomical Society*, 62, 699-718.

Kleiman, L. E., & Japas, M. S. (2009) The Choiyoi volcanic province at 34°S-36°S (San Rafael, Mendoza, Argentina): Implications for the Late Palaeozoic evolution of the southwestern margin of Gondwana. *Tectonophysics*, 473, 283-299.

Lewis, T., & Fisher, N. I. (1982) Graphical methods for investigating the fit of a Fisher distribution for spherical data. *Geophysical Journal of the Royal Astronomical Society*, 69, 1-13.

Libarkin, J., Butler, R., Richards, D., & Sempere, T. (1998) Tertiary remagnetization of Paleozoic rocks from the Eastern Cordillera and sub-Andean belt of Bolivia. *Journal of Geophysical Research*, 103, 30417-30429.

Lipman, P. W. (1997) Subsidence of ash-flow calderas: relation to caldera size and magma-chamber geometry. *Bulletin of Volcanology*, 59, 198-218.

Llambías, E. J. (1973) Las ignimbritas de la Sierra de Lihue-Calel, provincia de La Pampa. *V Congreso Geológico Argentino Actas*, 4, 55-67.

Llambías, E. J., & Sato, A. M. (1995) El Batolito de Colangüil: transición entre orognesis y anorognesis. *Revista de la Asociación Geológica Argentina*, 50, 111-131.

Llambías, E. J., Kleiman, L. E., & Salvarredi, J. A. (1993) Magmatismo gondwánico de Mendoza. In: V. A. Ramos, Editor, Geología y Recursos Naturales de Mendoza. *Relatorio XII Congreso Geológico Argentino*, 53-64.

Llambías, E. J., Quenardelle, S., & Montenegro, T. (2003) The Choiyoi Group from Central Argentina: a subalkaline transitional to alkaline association in the craton adjacent to the active margin of Gondwana continent. *Journal of South American Earth Sciences*, 16, 243-257.

Lock, B. E. (1980) Flat-plate subduction and the Cape Fold Belt of South Africa. *Geology*, 8, 35-39.

Ludwig, K. R. (2003) Using Isoplot/Ex, Version 2.01: A Geochronological Toolkit for Microsoft Excel, *Berkeley Geochronology Center Special Publication*, 4. Berkeley Geochronology Center, Berkeley, California. 47 pp.

Martin, M. W., Clavero, J. R., & Mpodozis, C. M. (1999) Late Paleozoic to Early Jurassic tectonic development of the high Andean Principal Cordillera, El Indio Region, Chile (29-30°S). *Journal of South American Earth Sciences*, 12, 33-49.

McFadden, P. L. (1980) Testing a palaeomagnetic study for the averaging of secular variation. *Geophysical Journal of the Royal Astronomical Society*, 61, 183-192.

McFadden, P. L., & McElhinny, M. W. (1988) The combined analysis of remagnetization circles and direct observations in paleomagnetism. *Earth and Planetary Science Letters*, 87, 161-172.

Moskowitz, B. M., Jackson, M., & Kissel, C. (1998) Low-temperature magnetic behavior of titanomagnetites. *Earth Planetary Science Letters*, 157, 141-149.

Mpodozis, C., & Kay, S. M. (1992) Late Paleozoic to Triassic evolution of the Gondwana margin: evidence from Chilean Frontal Cordilleran batholiths (28° to 31° S).

Geological Society of America Bulletin, 104, 999-1014.

Muttoni, G., Kent, D. V., & Channell, J. E. T. (1996) Evolution of Pangea: paleomagnetic constraints from the Southern Alps, Italy. *Earth and Planetary Science Letters*, 140, 97-112.

Muttoni, G., Kent, D. V., Garzanti, E., Brack, P., Abrahamsen, N., & Gaetani, M. (2003) Early Permian Pangea 'B' to Late Permian Pangea 'A'. *Earth and Planetary Science Letters*, 215, 379-394.

Muxworthy, A. R., & McClelland, E. (2000) Review of the low-temperature magnetic properties of magnetite from a rock magnetic perspective. *Geophysical Journal International*, 140, 101-114.

Nomade, S., Knight, K. B., Beutel, E., Renne, P. R., Verati, C., Feraud, ,G., Marzoli, A., Youbi, N., & Bertrand, H. (2007) Chronology of the Central Atlantic Magmatic Province: Implications for the Central Atlantic rifting processes and the Triassic–Jurassic biotic crisis. *Palaeogeography, Palaeoclimatology, Palaeoecology*, 244, 326-344.

Opdyke, N. D., Roberts, J., Claoue-Long, J., Irving, E., & Jones, P. J. (2000) Base of the Kiaman: its definition and global stratigraphic significance. *Geological Society of America Bulletin*, 112, 1315-1341.

Özdemir, Ö., Dunlop, D. J., & Moskowitz, B. M. (1993) The effect of oxidation on the Verwey transition in magnetite. *Geophysical Research Letters*, 20, 1671-1674.

Özdemir, Ö., Dunlop, D. J., & Berquó, T. S. (2008) Morin transition in hematite: Size dependence and thermal hysteresis. *Geochemistry, Geophysics, Geosystems*, 9, Q10Z01.

Pankhurst, R. J., Rapela, C. W., Fanning, C. M., & Márquez, M. (2006) Gondwanide continental collision and the origin of Patagonia. *Earth-Science Reviews*, 76, 235-257.

Quenardelle, S. M., & Llambías, E. J. (1997) Las riolitas de Sierra Chica (37°S, 65°O): un centro eruptivo gondwánico en el bloque del Chadileuv, provincia de La Pampa, Argentina. *Revista de la Asociación Geológica Argentina*, 52, 549-558.

Rakotosolofo, N. A., Tait, J. A., Carlotto, V., & Cárdenas, J. (2006) Paleomagnetic results from the Early Permian Copacabana Group, southern Peru: Implication for Pangea palaeogeography. *Tectonophysics*, 413, 287-299.

Ramos, V. A. (2008) Patagonia: A Paleozoic continent adrift? *Journal of South American Earth Sciences*, 26, 235-251.

Rapalini, A. E. (1998) Syntectonic magnetization of the mid-Paleozoic Sierra Grande formation: further constraints for the tectonic evolution of Patagonia. *Journal of the Geological Society*, 155, 105-114.

Rapalini, A. E., Fazzito, S., and & Orué, D. (2006) A new Late Permian paleomagnetic pole for stable South America: The Independencia group, eastern Paraguay. *Earth, Planets, and Space*, 58, 1247-1253.

Rapalini, A. E., & Astini, R. (2005) La remagnetización Sanrafalica de la Precordillera en el Prmico: nuevas evidencias. *Revista de la Asociación Geológica Argentina*, 60, 290-300.

Rapalini, A. E., & Cingolani, C. A. (2004) First Late Ordovician paleomagnetic pole for the Cuyania (Precordillera) terrane of Western Argentina: a microcontinent or a Laurentian Plateau. *Gondwana Research*, 7, 1089-1104.

Rapalini, A. E., & Sánchez Bettucci, L. (2008) Widespread remagnetization of late Proterozoic sedimentary units of Uruguay and the apparent polar wander path for the Rio de La Plata Craton. *Geophysical Journal International*, 174, 55-74.

Rapalini, A. E., & Tarling, D. H. (1993) Multiple magnetizations in the Cambrian-Ordovician carbonate platform of the Argentine Precordillera and their tectonic implications. *Tectonophysics*, 227, 49-62.

Rapalini, A. E., & Vilas, J. F. (1991) Tectonic rotations in the Late Palaeozoic continental margin of southern South America determined and dated by palaeomagnetism. *Geophysical Journal International*, 107, 333-351.

Rapalini, A. E., Vilas, J. F., Bobbio, M. L., & Valencio, D. A. (1989) Geodynamic interpretations from paleomagnetic data of Late Paleozoic rocks in the Southern Andes. In: Hillhouse, J. W. (ed.) Deep Structure and Past Kinematics of Accreted Terranes. *American Geophysical Union - Geophysical Monograph*, 50, 41-57.

Rapela, C. W., Pankhurst, R. J., Llambías, E. J., Labudía, C., & Artabe, A. (1996) "Gondwana" magmatism of Patagonia: Inner cordilleran calc-alkaline batholiths and bimodal volcanic provinces. *Proceedings Third International Symposium on Andean Geodynamics*, 791-794.

Roberts, A. P., Pike, C. R., & Verosub, K. L. (2000) First-order reversal curve diagrams: a new tool for characterizing the magnetic properties of natural samples. *Journal of Geophysical Research*, 105, 28461-28475.

Somoza, R., & Zaffarana, C. B. (2008) Mid-Cretaceous polar standstill of South America, motion of the Atlantic hotspots and the birth of the Andean cordillera. *Earth and Planetary Science Letters*, 271, 267-277.

Sruoga, P., & Llambías, E. J. (1992) Permo-Triassic leucorhyolitic ignimbrites at Sierra de Lihue Calel, La Pampa Province, Argentina. *Journal of South American Earth Sciences*, 5, 141-152.

Tauxe, L. (2010) Essentials of paleomagnetism. University of California Press. 489 pp.

Tauxe, L., Kylstra, N., & Constable, C. (1991) Bootstrap statistics for paleomagnetic data. *Journal Geophysical Research*, 96, 11723-11740.

Tauxe, L., & Watson, G. S. (1994) The fold test: an eigen analysis approach. *Earth and Planetary Science Letters*, 122, 331-341.

Terrizzano, C. M. (2005) Nuevos estudios paleomagnéticos en el Bloque de San Rafael, provincia de Mendoza. Departamento de Geología, Master Thesis. Universidad de Buenos Aires, 118 pp.

Tickyj, H., Dimieri, L. V., Llambías, E. J., & Sato, A. M. (1997) Cerro de Los Viejos (38° 28' S-64° 26' O): cizallamiento dúctil en el sudeste de La Pampa. *Revista de la Asociación Geológica Argentina*, 52, 311-321.

Tomezzoli, R. N. (2001) Further paleomagnetic results from the Sierras Australes fold and thrust belt, Argentina. *Geophysical Journal International*, 147, 356-366.

Tomezzoli, R. N. (2009) The apparent polar wander path for South America during the Permian–Triassic. *Gondwana Research*, 15, 209-215.

Tomezzoli, R. N., & Vilas, J. F. (1999) Paleomagnetic constraints on age of deformation of the Sierras Australes thrust and fold belt. *Geophysical Journal International*, 138, 857-870.

Tomezzoli, R. N., Melchor, R., & MacDonald, W. D. (2006) Tectonic implications of post-folding Permian magnetizations, Carapacha basin, Argentina. *Earth Planets, and Space*, 58, 1235-1246.

Tomezzoli, R. N., Saint Pierre, T., & Valenzuela, C. (2008) New palaeomagnetic results from Late Paleozoic volcanic units along the western Gondwana margin in La Pampa, Argentina. *Earth, Planets and Space*, 60, 1-7.

Torcq, F., Besse, J., Vaslet, D., Marcoux, J., Ricou, L. E., Halawani, M., & Basahel, M. (1997) Paleomagnetic results from Saudi Arabia and the Permo-Triassic Pangea configuration. *Earth and Planetary Science Letters*, 148, 553-567.

Torsvik T. H., Muller R. D., Van der Voo R., Steinberger B., & Gaina C. (2008) Global plate motion frames: Toward a unified model. *Reviews of Geophysics*, 46, 1-44.

Torsvik, T. H., Rousse, S., Labails, C., & Smethurst, M. (2009) A new scheme for the opening of the South Atlantic Ocean and the dissection of an Aptian salt basin. *Geophysical Journal International*, 177, 1,315-1,333.

Trouw, R. A. J., & De Wit, M. J. (1999) Relation between the Gondwanide Orogen and contemporaneous intracratonic deformation. *Journal of African Earth Sciences*, 28, 203-213.

Van der Voo, R. (1990) The reliability of paleomagnetic data. *Tectonophysics*, 184, 1-9.

Veldkamp, J., Mulder, F. G., & Zijderveld, J. D. A. (1971) Palaeomagnetism of Suriname dolerites. *Physics of the Earth and Planetary Interiors*, 4, 370-380.

Visser, J. N. J., & Praekelt, H. E. (1998) Late Palaeozoic crustal block rotations within the Gondwana sector of Pangea. *Tectonophysics*, 287, 210-212.

Vizan, H., Ixer, R., Turner, P., Cortes, J. M., & Cladera, G. (2004) Paleomagnetism of Upper Triassic rocks in the Los Colorados hill section, Mendoza province, Argentina. *Journal of South American Earth Sciences*, 18, 41-59.

Zijderveld, J. D. A. (1967) A.C. demagnetization of rocks: analysis of results. In: D. W. Collinson, K. M. Creer and S. K. Runcorn, Editors, *Methods in Paleomagnetism*, Elsevier, Amsterdam. 254 pp.

CHAPTER III

Support for an "A-type" Pangea reconstruction from high-fidelity Late Permian and Early-Middle Triassic paleomagnetic data from Argentina

3.1 Abstract

A major disparity is observed between the late Paleozoic–early Mesozoic apparent polar wander paths of Laurussia and Gondwana when the landmasses are reconstructed in a conventional "A-type" Pangea. This discrepancy has endured from the earliest paleomagnetic reconstructions of the supercontinent, and has prompted discussions of non-dipole paleomagnetic fields and alternative paleogeographic models. Here we report on a joint paleomagnetic/geochronologic study of Late Permian and Early–Middle Triassic volcanic and volcaniclastic rocks from Argentina, which demonstrates support for an A-type model, without requiring modification to the geocentric axial dipole hypothesis. New SHRIMP U-Pb and ^{40}Ar-^{39}Ar isotopic dating has reinforced the inferred age of the sequences, which we estimate at ∼264 Ma (Upper Choiyoi Group) and ∼245 Ma (Puesto Viejo Group). Field-stability tests demonstrate that the volcanic rocks are carrying early/primary magnetizations that yield paleopoles: 73.7° S, 315.6° E, A_{95}: 4.1°, N: 40 (Upper Choiyoi) and 76.7°

Citation:
Domeier, M., Van der Voo, R., Tomezzoli, R. N., Tohver, E., Hendriks, B. W. H., Torsvik, T. H., Vizan, H., & Dominguez, A. R. (2012). Support for an "A-type" Pangea reconstruction from high-fidelity Late Permian and Early–Middle Triassic paleomagnetic data from Argentina. *Journal of Geophysical Research*, in press.

S, 312.4° E, A_{95}: 7.3°, N: 14 (Puesto Viejo). A comprehensive magnetic fabric analysis is used to evaluate structural restorations and to correct for magnetization anisotropy. Paleomagnetic results derived from volcaniclastic rocks are interpreted to be affected by inclination shallowing, and corrections are discussed. A comparison of these new results with the existing Permian–Triassic paleomagnetic data from Gondwana suggests the presence of widespread bias in the latter. We contend that such bias can explain the observed apparent polar wander path disparity, at least for Late Permian–Middle Triassic time, and that alternative paleogeographic reconstructions or non-dipole paleomagnetic fields do not need to be invoked to resolve the discrepancy.

3.2 Introduction

It has long been recognized that the apparent polar wander paths (APWPs) of Laurussia and Gondwana are not coincident during the late Paleozoic–early Mesozoic, if a conventional reconstruction of Pangea ("Pangea A") is assumed (Irving, 1977; Torsvik et al., 2008). This paleomagnetic discrepancy has previously been attributed to a fundamental problem with the conventional paleogeographic model (Irving, 1977; Morel and Irving, 1981; Smith and Livermore, 1991; Torcq et al., 1997; Muttoni et al., 2003; Irving, 2004; Muttoni et al., 2009) or to atypical behavior of the paleomagnetic field (Briden et al., 1971; Van der Voo and Torsvik, 2001; Torsvik and Van der Voo, 2002). Although these explanations are theoretically viable, they require an unsettling break with widely adopted models: Pangea A and the uniformitarian geocentric axial dipole hypothesis, respectively. It is therefore prudent to consider the possibility that the APWP disparity is simply an artifact of magnetic recording biases in low-fidelity paleomagnetic data (Rochette and Vandamme, 2001).

Supportingly, a data-filtering exercise conducted on paleomagnetic data from Baltica has demonstrated that the use of only high-quality results improves the agreement between the Permian–Triassic APWPs of Baltica and Gondwana in a conventional reconstruction (Van der Voo and Torsvik, 2004). Similarly, Domeier et al. (2011a) have shown that Permian–Triassic paleomagnetic data from Laurentia may be widely biased by too-shallow inclinations, and demonstrated that a correction for this bias improves the agreement between the APWPs of Laurentia and Gondwana. The remaining difference between the APWPs in both of these studies can be plausibly attributed to the lingering presence of low-fidelity data in the paleomagnetic record of Gondwana.

Indeed, a review of the Permian–Triassic data from the global paleomagnetic database reveals a dearth of high-quality results from Gondwana. The majority of the paleomagnetic results have been derived from sedimentary rocks, which are prone to a shallow inclination bias (Tauxe et al., 2008), and generally associated with poor age-constraints. Many other results fail to meet modern reliability criteria, lacking either a sufficient number of samples or sites, field-stability tests, or adequate demagnetization. Domeier et al. (2011b) explicitly discussed the quality of Permian–Triassic paleomagnetic data from South America, and showed that by removing the data of lowest quality, the South American APWP moved closer to the APWP of Laurussia. Unfortunately, the filtering exercise left few results, so the APWP was defined only by three mean paleopoles with large uncertainties. Moreover, the limited number of high-quality igneous-based paleomagnetic results precluded a comparative test for a shallow inclination bias in the sedimentary-based paleomagnetic data.

To improve the quality of the Permian–Triassic paleomagnetic dataset of Gondwana, and to further test the hypothesis that its incongruity with the corresponding

Laurussian data (within a conventional Pangea reconstruction) could be an artifact of low-fidelity data, we present new, high-quality paleomagnetic results from Late Permian and Early–Middle Triassic rocks from Argentina. Our study has largely focused on volcanic rocks to avoid the complications of inclination shallowing in sedimentary rocks, although we present a sub-set of results that illustrate the effects of this bias. Our targeting of volcanic rocks also permits direct-dating of the sampled units, and we present results from a joint SHRIMP U-Pb and ^{40}Ar-^{39}Ar isotopic dating effort that accompanies our paleomagnetic study. A magnetic fabric analysis has been conducted on the paleomagnetic sampling sites to determine the nature of local structures and to evaluate the influence of magnetic anisotropy on the remanent magnetizations.

3.3 Geologic Background and Previous Paleomagnetic Studies

In western and central Argentina, exposures of late Paleozoic–early Mesozoic volcano-plutonic rocks form part of a large curvilinear belt of magmatism and deformation that loosely traces the paleo-margin of southern South America (Fig. 3.1a). Although the origin of this belt is not yet entirely clear, most studies have identified it as an inboard magmatic arc (Kleiman, 2002; Kleiman and Japas, 2005; 2009). In the province of Mendoza, the late Paleozoic volcano-plutonic rocks are assigned to the Choiyoi Group, which is divided into lower (Early Permian) and upper (mid to Late Permian) subgroups (Fig 3.2). In the San Rafael Block (SRB) of southern Mendoza, the Choiyoi Group lies unconformably on Late Carboniferous–Early Permian glaciomarine and fluvial sedimentary rocks of the El Imperial Formation. The Lower Choiyoi Group (called the Cochicó Group in the SRB) is a sequence of andesitic breccias and lavas, dacitic to rhyodacitic ignimbrites, and continental

sedimentary rocks. The volcanic rocks follow a calc-alkaline trend and exhibit elemental distributions suggestive of an arc-affinity and derivation from a thickened crust (Kleiman, 2002; Kleiman and Japas, 2009). Unconformably overlying the Cochicó Gr. is the Upper Choiyoi Gr., which is subdivided into three formations in the SRB: the Agua de los Burros Formation, the Quebrada del Pimiento Formation, and the Cerro Carrizalito Formation (Rocha-Campos et al., 2011). The Agua de los Burros Fm. is a volcano-sedimentary rock sequence composed of basal conglomerates and continental sedimentary rocks that yield to tuffaceous sedimentary rocks, volcanic breccias, and dacitic to rhyolitic ignimbrites and lavas that become increasingly acidic up-section. The Quebrada del Pimiento Fm. is a minor suite of shallow intrusive andesites that intrude both the Cochicó Gr. and the Agua de los Burros Fm. The Cerro Carrizalito Fm. is characterized by high-silica ignimbrites and lavas, but includes subvolcanic rhyolitic porphyries. The volcanic rocks of the Agua de los Burros and Cerro Carrizalito fms. exhibit a geochemical signature that is transitional between a subduction-related calc-alkaline trend and an alkaline suite indicative of an intraplate setting, whereas the intrusive andesites of the Quebrada del Pimiento Fm. have a geochemistry more similar to that of the Cochicó Gr. (Kleiman, 2002; Kleiman and Japas, 2009).

In the SRB, the Upper Choiyoi Gr. is unconformably overlain by the Puesto Viejo Group, a Triassic sequence of continental sedimentary rocks intercalated with volcaniclastic rocks, tuffs, basalts, and rhyolitic ignimbrites (Kleiman and Salvarredi, 2001). The geochemistry of the volcanic rocks is indicative of a tensional, intra-plate regime; the mildly alkaline mafic series exhibits characteristics of an enriched source, contaminated by relict arc or crustal components (Kleiman and Salvarredi, 1999; 2001). The genetically distinct high-silica ignimbrites of the Puesto Viejo Gr. ap-

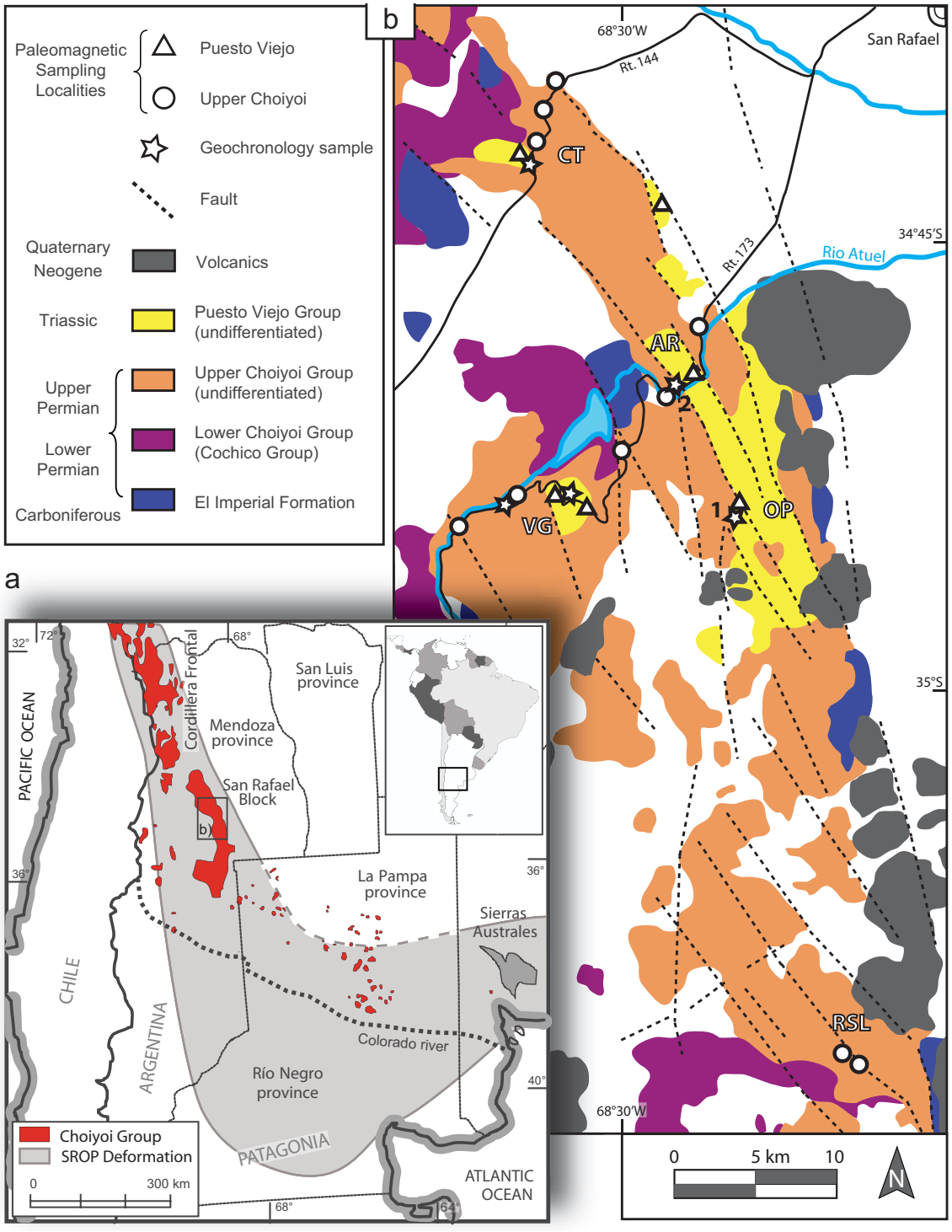

Figure 3.1: Maps of the San Rafael Block study area. (a) Regional map showing the distribution of Choiyoi Group magmatism and San Rafael Orogenic Phase (SROP) deformation in central Argentina. (b) Simplified geologic map of the central San Rafael Block showing the discussed petrologic units and major paleomagnetic and geochronologic sampling localities. CT = Cuesta de los Terneros, AR = Atuel River area, VG = Valle Grande area, OP = Old Puesto area, RSL = Rio Seco los Leones. 1, 2 = location of Upper Choiyoi Gr. geochronology samples "PV01d" and CCH, respectively. Simplified from Kleiman and Japas (2009).

pear to be extensively fractionated melts derived from a youthful crust, likely heated by a basaltic underplate from which the mafic series was derived. The sedimentary rocks of the Puesto Viejo Gr. are syn-rift alluvial and fluvial sandstones, siltstones, and claystones, floored by a thick clastic conglomerate containing fragments of the underlying Permian volcanic rocks. The volcaniclastic rocks, interbedded with tuffs, also contain fragments of volcanic rocks that were likely derived from the Permian substrate, as well as from re-worked pyroclastic material from contemporaneous volcanism. González Díaz (1972) originally defined the Puesto Viejo sequence as a formation, dividing it into lower and upper members based on a coloration change in the sedimentary sequence that was attributed to a changing sediment source and/or depositional environment. Stipanicic et al. (2007) interpreted this poorly defined boundary as a paraconformity and elevated Diaz's Puesto Viejo Formation to the rank of group; the lower and upper members were redefined as the Quebrada de los Fósiles Formation and the Río Seco de la Quebrada Formation, respectively. The Quebrada de los Fósiles Fm. has been assigned an Early to Middle Triassic age according to the identification of kannemeyeriid dicynodonts (Bonaparte, 1982; De Fauw, 1993; Domnanovich and Marsicano, 2009), an archosauriform (*Koilamasuchus gonzalezdiazi*; Ezcurra et al., 2010), lycophytes of the genus Pleuromeia (Bonaparte, 1982; Artabe et al., 2007), and palynoflora (Ottone and Garcia, 1991; Zavattieri and Batten, 1996). The overlying Río Seco de la Quebrada Fm. is generally regarded as Middle Triassic in age, according to the identification of cynodonts (Bonaparte, 1982; Martinelli, 2010), including *Diademodon tetragonus* (Martinelli et al., 2009), and kannemeyeriid dicynodonts (Bonaparte, 1982; Lucas, 1998).

Younger Mesozoic and Paleogene rocks are not known in the SRB; the Puesto Viejo Gr. is unconformably overlain by a mid-Miocene sedimentary rock sequence,

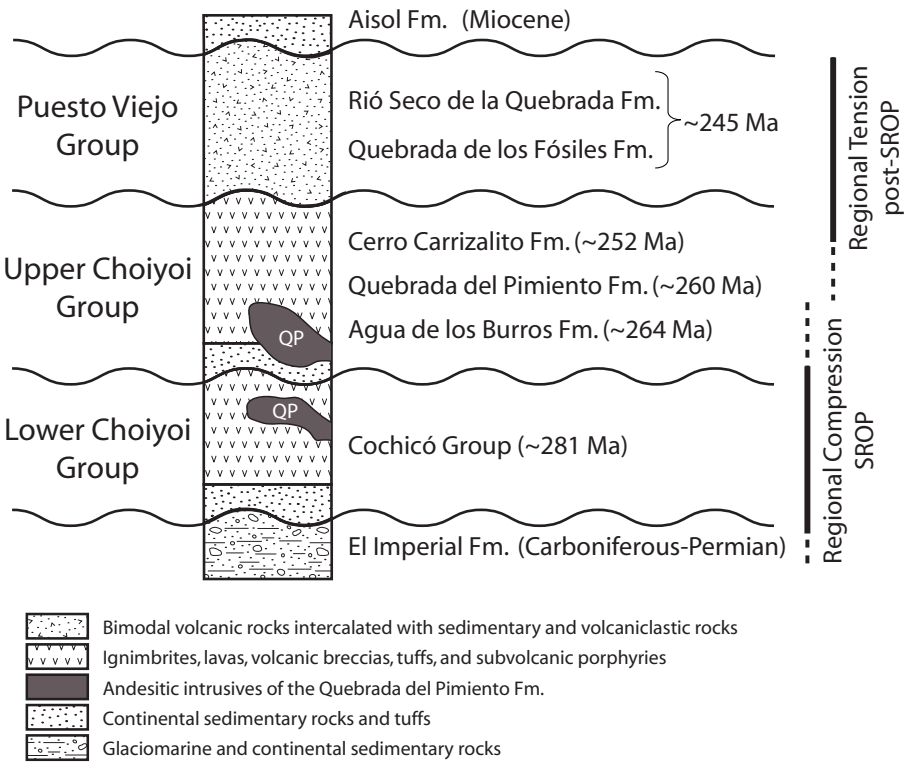

Figure 3.2: Schematic stratigraphy of the central San Rafael Block.

the Aisol Formation (Sepúlveda et al., 2007). In addition to the age-progressive compositional and geochemical changes observed in the late Paleozoic–early Mesozoic volcanic rocks, a co-evolving change in the regional paleo-stress (Fig. 3.2) can be discerned from their variable deformation. In Mendoza, late Paleozoic regional shortening is assigned to the San Rafael Orogenic Phase (SROP), and is typified by NNW to NW striking faults and folds, NNE-directed thrusting, and NNE to NE trending fractures (Kleiman and Japas, 2009). The earliest indication of SROP activity in the SRB may be the paleocurrent reversal observed in the late depositional stages of the El Imperial Fm. (Espejo, 1990 in Kleiman and Japas, 2009). More definitive evidence of Permian shortening is found in the Cochicó Gr., where growth folds and faults have been recognized, indicating that volcanism and deformation were at least partly coeval (Cortés and Kleiman, 1999). Weaker deformation of the Agua de los Burros

Fm. suggests that the SROP was waning during emplacement of this sequence; regional shortening is inferred to have ended prior to the emplacement of the Cerro Carrizalito Fm. by the absence of contraction features (Kleiman and Japas, 2009). Subsequent to the SROP, a post-orogenic relaxation occurred and many SROP structures were reactivated and structurally inverted through regional extension (Japas et al., 2005). Onset of this tensional phase is recognized in the Upper Choiyoi Gr. by injections of the Quebrada del Pimiento Fm. that exploit fracture and fault planes of post-SROP extensional structures (Kleiman and Japas, 2009). NE-SW tension continued into the Triassic, evident by the syn-rift deposits of the Puesto Viejo Gr., which are largely confined to narrow, NE-SW elongated fault-bound basins (Spalletti et al., 1996; Kleiman and Japas, 2009). Although later Mesozoic extension and Andean orogenesis occurred along the western South American margin, the SRB has remained structurally stable since the Triassic.

The paleomagnetism of the Permian and Triassic sequences in the SRB were first studied by Creer et al. (1970; 1971), Valencio and Mitchell (1972), Valencio et al. (1975), and Vilas and Valencio (1982). Notably, these early studies documented magnetizations of both normal and reverse polarity, and so provided early age constraints on the Kiaman Reversed Superchron (see, for example, Creer et al., 1971). However, only blanket alternating field (AF) demagnetization treatments were routinely applied in these studies, so the resulting paleomagnetic poles must be regarded as dubious. Moreover, field stability tests were not conducted to constrain the age of the magnetizations, so the possibility of remagnetization cannot be excluded. More recently, Tomezzoli et al. (2005) have reported paleomagnetic results from the Cochicó Gr., and Terrizzano et al. (2005) have reported preliminary findings from a paleomagnetic study of the Quebrada del Pimiento Fm.

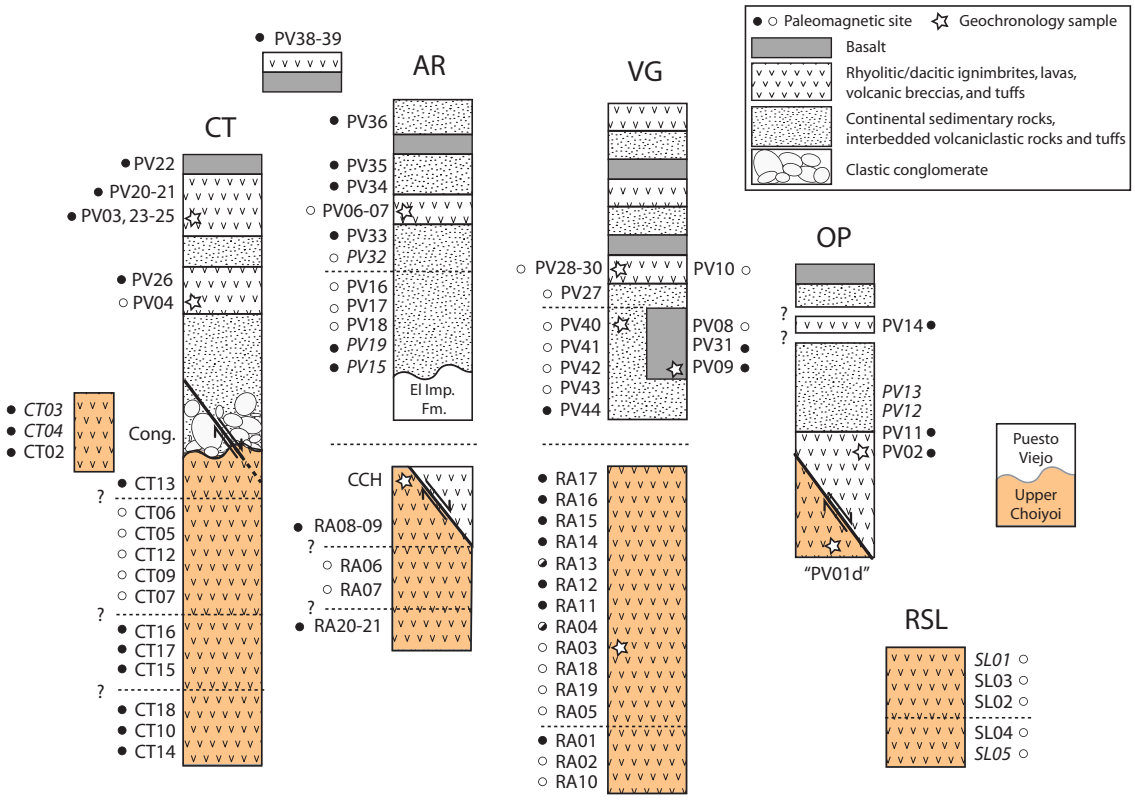

Figure 3.3: Simplified stratigraphy of paleomagnetic and geochronology sampling sites. CT = Cuesta de los Terneros, AR = Atuel River area, VG = Valle Grande area, OP = Old Puesto area, RSL = Rio Seco los Leones. Stratigraphic correlations have not been made between areas, so the lateral relationships between columns are not indicative of a true stratigraphic relationship (excepting the superposition of the Puesto Viejo Gr. on the Upper Choiyoi Gr.). The vertical scale is variable. Dashed lines indicate a significant break in the sequence (vertically and/or laterally). Question marks denote stratigraphic relationships that are only inferred. The filled (open) circles represent normal (reversed) polarity of the associated paleomagnetic site.

3.4 Sampling and Methodology

Sampling of both the Puesto Viejo Gr. and the Upper Choiyoi Gr. was conducted in several areas in the SRB, mostly along routes 144 and 173, southwest of San Rafael, Mendoza (Fig. 3.1). A supplementary set of Upper Choiyoi Gr. samples was collected from Rio Seco los Leones, ∼70 km to the south of San Rafael. Paleomagnetic samples from the Puesto Viejo Gr. were taken from rhyolitic ignimbrites, basalts, interbedded volcaniclastic rocks and tuffs, and from clasts in the basal conglomerate (Table 3.2; Fig. 3.3). Paleomagnetic samples from the Upper Choiyoi Gr. were taken from dacitic to rhyolitic ignimbrites, volcanic breccias, and tuffs (Table 3.3; Fig. 3.3). We targeted rocks of the Agua de los Burros Fm., but acknowledge that the complexity of the local stratigraphy and the similarity of the Agua de los Burros and Cerro Carrizalito fms. prevent us from discounting the possibility that some samples of the latter may be included in our collection. Paleomagnetic samples were collected as cores with a gasoline-powered drill, or as hand-samples; both magnetic and solar compasses were used to orient the samples. A minimum of 5 paleomagnetic samples were collected per site. Multiple horizons within a thick cooling unit were occasionally sampled and assigned independent paleomagnetic site labels; where the resulting magnetization directions were found to be indistinct the data were combined (discussed below). Samples for isotopic age determinations were mostly collected alongside paleomagnetic samples and the naming scheme conveys the paired paleomagnetic site (samples "PV01d" and CCH are the exceptions, the locations of these are shown in Figs. 3.1 and 3.3).

Samples selected for SHRIMP U-Pb geochronologic analysis were crushed, sieved, and washed in acetone and distilled water. Minerals were separated by standard tech-

niques, and mineral grains were handpicked under a binocular microscope. Scanning electron microscope (SEM) photomicrographs were taken of zircon grains selected for SHRIMP U-Pb analysis prior to mounting the grains in epoxy resin and polishing for SEM and cathodoluminescence imaging (Fig. A.1). Subsequently, SHRIMP analysis was conducted with the SHRIMP II housed at Curtin University. The epoxy mounts were cleaned and gold-coated to have a uniform electrical conductivity during the SHRIMP analyses. Samples were measured over two separate analytical sessions, during which the external error calculated from analysis of standards was 0.18-0.76%. The zircon standard used was BR266 zircon (559 Ma, 903 ppm U). Prior to spot analysis, rastering of the ion beam was carried out for 120–150 s to remove the gold coating and reduce the common Pb contaminant within the gold coating. A primary ion beam of 2.5–3 nA with a diameter of $\sim$25 μm was focused onto the polished surface. Common Pb corrections were carried out using the measured amount of ^{204}Pb. Isotopic data are reduced using SQUID2 (Ludwig, 2003). Data were plotted on concordia diagrams using Isoplot 3 software (Ludwig, 2003), in which error ellipses on Concordia plots are shown at the 2σ confidence level. All dates reported in the text are U-Pb concordia dates calculated from concordant analyses and include decay constant errors, with date uncertainty reported at the 95% confidence level.

For ^{40}Ar-^{39}Ar geochronologic analysis, fresh inclusion-free mineral-grains were selected. The transformation ^{39}K(n, p)^{39}Ar was performed during irradiation at the McMaster reactor in Canada (1st batch) and at the IFE Kjeller reactor in Norway (2nd batch). The Tinto biotite standard was used as a flux monitor (410.3 Ma; Rex and Guise 1995). Samples were step heated in the ^{40}Ar-^{39}Ar lab at the Geological Survey of Norway using a Heine type double-vacuum oven (McMaster samples) and a Merchantek MIR-10 CO_2 laser (IFE samples). The extracted gases were swiped over

getters (SAES AP-10) for 2 minutes, and then for 9 minutes in a separate part of the extraction line. The peaks were determined by peak hopping (at least 8 cycles) on masses ^{41}Ar to ^{35}Ar on a Balzers electron multiplier on a MAP 215-50 mass spectrometer. Data from unknowns were corrected for blanks (every 4th analysis on the CO_2 laser) prior to being reduced with the IAAA software package (Interactive Ar-Ar Analysis, written by TH Torsvik, now maintained by M. Ganerød, NGU Trondheim, Norway) that implements the equations in McDougall and Harrison (1999) using the decay constants of Renne et al. (2010) and the trapped ^{40}Ar/^{36}Ar ratio of 298.56 ±0.31 of Lee et al. (2006). Data reduction in IAAA incorporates corrections for interfering isotopes (based on K_2SO_4 and CaF_2 salts included in the irradiation packages), mass discrimination, error in blanks and decay of ^{37}Ar and ^{39}Ar. We define a plateau according to the following requirements: at least three consecutive steps, overlapping at the 95% confidence level, together comprising at least 50% of total ^{39}Ar and mean square of weighted deviates (MSWD) less than the two tailed Student T critical value. We use the weighted York-2 method to calculate the inverse isochron results, with statistically valid isochrons having a MSWD value less than the two tailed F-test critical value.

Paleomagnetic samples were stored and processed in a magnetically shielded room with a rest field of $\leq$ 200 nT. Measurements of remanent magnetization were made with a three-axis 2G cryogenic magnetometer at the University of Michigan. A pilot demagnetization scheme subjected sister-specimens to both alternating field (AF) and thermal demagnetization techniques in order to determine the most effective method of demagnetization for each site. AF demagnetization was carried out according to a static 3-position procedure. Thermal demagnetization was conducted in air; samples were cooled in a magnetically shielded chamber with a typical DC

field of $\leq$ 5 nT. Magnetic susceptibility was routinely monitored during pilot demagnetizations to detect any mineralogic changes at high temperature. Detailed demagnetizations were carried out with a typical minimum of 12 steps, up to 200 mT or 700 °C. Demagnetization data were analyzed with orthogonal vector diagrams and stereographic projections (Zijderveld, 1967; Cogné, 2003). Principal component analysis was used to quantitatively define magnetization vectors; where persistent and random remagnetizations were observed (i.e. lightning-induced isothermal overprints), converging great circles were used to define the common magnetization direction (Halls, 1978; Kirshvink, 1980). Fisher (1953) statistics were used to compute site-level mean directions from purely vectorial populations; where remagnetization circles defined some samples, the statistical approach of McFadden and McElhinny (1998) was applied.

Rock magnetic experiments were conducted at the Institute for Rock Magnetism, University of Minnesota, in order to identify and characterize the magnetic carriers. Hysteresis measurements and first-order reversal curves (FORCs) were generated with a vibrating sample magnetometer operating at room temperature. Low temperature remanence experiments were performed with a magnetic properties measurement system. Thermomagnetic curves (κ vs. T) were measured in an argon atmosphere with a high-temperature susceptibility bridge.

The anisotropy of magnetic susceptibility (AMS) was measured on a susceptibility bridge, following a static, 15-position measurement procedure. The anisotropy of anhysteretic remanent magnetization (AARM) was measured following a 9-position measurement scheme and a DC field of 0.05 mT. The anisotropy of thermal remanent magnetization (ATRM) and the anisotropy of high-field magnetic susceptibility (HF-AMS) were measured at the Institute for Rock Magnetism. TRMs were applied by

heating samples to 700 °C and allowing them to cool in a 0.05 mT field oriented along the axis of the oven. Both air and argon environments were used during TRM application, in accordance with the behavior of pilot specimens. ATRMs were determined after application and measurement of TRMs in 3 to 6 positions. HF-AMS was determined by the orientation-dependence of the high-field slope in hysteresis measurements on a VSM. A 24-position scheme was employed. Statistical analysis of the anisotropy data followed the bootstrap approach of Constable and Tauxe (1990).

3.5 Geochronology

3.5.1 Previous Work

Previous K-Ar geochronologic results from late Paleozoic volcanic rocks of the SRB have been compiled by Linares (2007) and summarized by Rocha-Campos et al. (2011). Averaged results suggest that the Cochicó Gr. was emplaced at ∼268 Ma, and the Quebrada del Pimiento Fm., of similar intermediate composition, was emplaced at ∼260 Ma. The high-silica porphyries of the Cerro Carrizalito Fm. were assigned an age estimate of ∼253 Ma. Melchor (2000) also calculated a date for the Cerro Carrizalito Fm. from a collection of published K-Ar results, but determined a date of 261 ±4 Ma.

Rocha-Campos et al. (2011) presented SHRIMP U-Pb age estimates of 281.4 ±2.5 Ma for the Cochicó Gr., 264.8 ±2.3 Ma for the Agua de los Burros Fm., and 251.9 ±2.7 Ma for the Cerro Carrizalito Fm. An additional date of 264.7 ±2.9 Ma was determined from a sample initially identified as of the Cerro Carrizalito Fm., but speculatively re-assigned to the Agua de los Burros Fm. in light of the older date determined.

Five whole-rock K-Ar age estimates from ignimbrites and basalts of the Puesto Viejo Gr., recalculated after the decay constants of Renne et al. (2010), range from

240 ±10 to 232 ±10 Ma, with an average of 235 ±4 Ma (Valencio et al., 1975).

3.5.2 New Results

One Upper Choiyoi Gr. sample (labeled "PV01d") and two Puesto Viejo Gr. samples have yielded similar mid-to-Late Permian SHRIMP U-Pb zircon dates that range from 269.0 ±3.2 to 260.8 ±3.2 Ma (Fig. 3.4; Appendix A).

^{40}Ar-^{39}Ar dating of eleven separates from nine samples has yielded three dates from the Upper Choiyoi Gr. and eight from the Puesto Viejo Gr. (Table 3.1; Appendix A). Plateau dates from volcanic rock samples of the two groups are statistically distinct (95% conf.): the Upper Choiyoi Gr. age estimates are Late Permian and the Puesto Viejo Gr. age estimates are Middle Triassic (Fig. 3.5). Plateau dates from samples of the Puesto Viejo Gr. volcaniclastic rocks, however, are Late Permian and Early Triassic. Three geochronology samples exhibit discordant date spectra (step date variation exceeds analytical uncertainty) and we report weighted-mean dates for these samples. The weighted-mean dates are significantly younger than the plateau dates, ranging from Middle Triassic to Early Cretaceous (Table 3.1). We will return to these new results in the discussion section.

3.6 Paleomagnetic Results

3.6.1 Puesto Viejo Gr.

Demagnetization of the ignimbrite samples typically results in removal of a low-temperature/coercivity component of magnetization, followed by univectorial decay to the origin (Fig. 3.6a). This indicates that only one high-stability component of magnetization (A) is present. The magnetization direction of the low-stability component is generally sub-parallel to the present day dipole (PDD) or present day field (PDF). Some sites are pervaded by a randomly-oriented component of magnetiza-

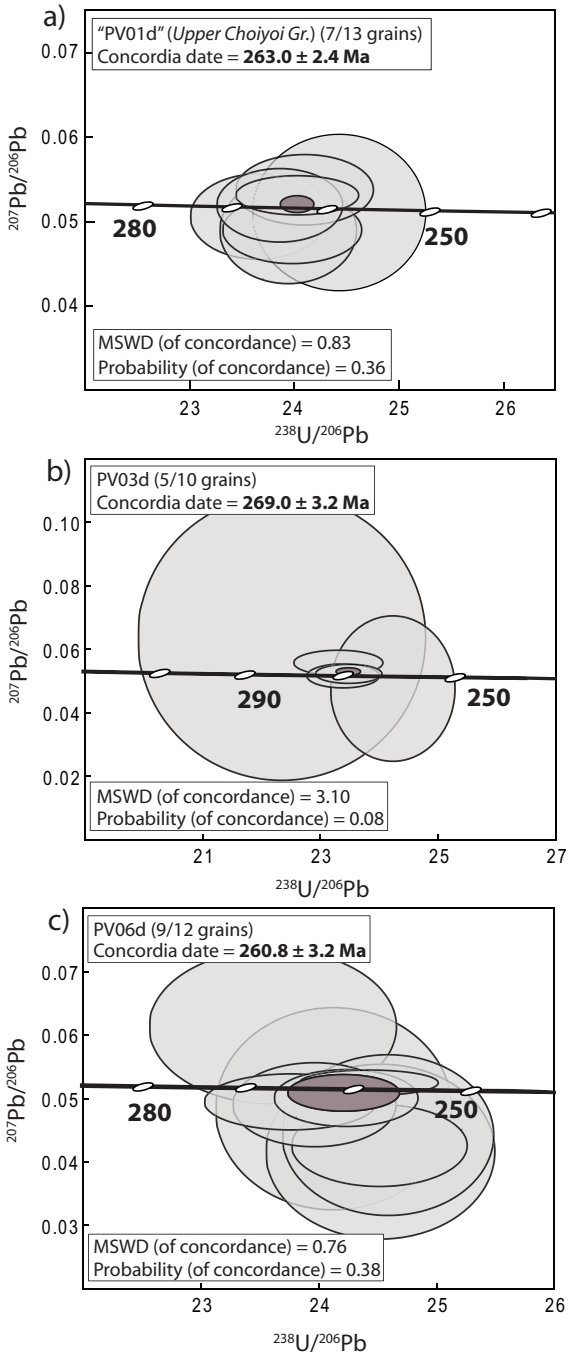

Figure 3.4: San Rafael Block SHRIMP U-Pb geochronology results. All data point error ellipses are 2σ, and include decay constant error. Dark gray ellipses depict mean results. Results from: (a) an Upper Choiyoi Gr. volcanic porphyry, and (b,c) Puesto Viejo Gr. ignimbrites. The associated data is listed in table A.2.

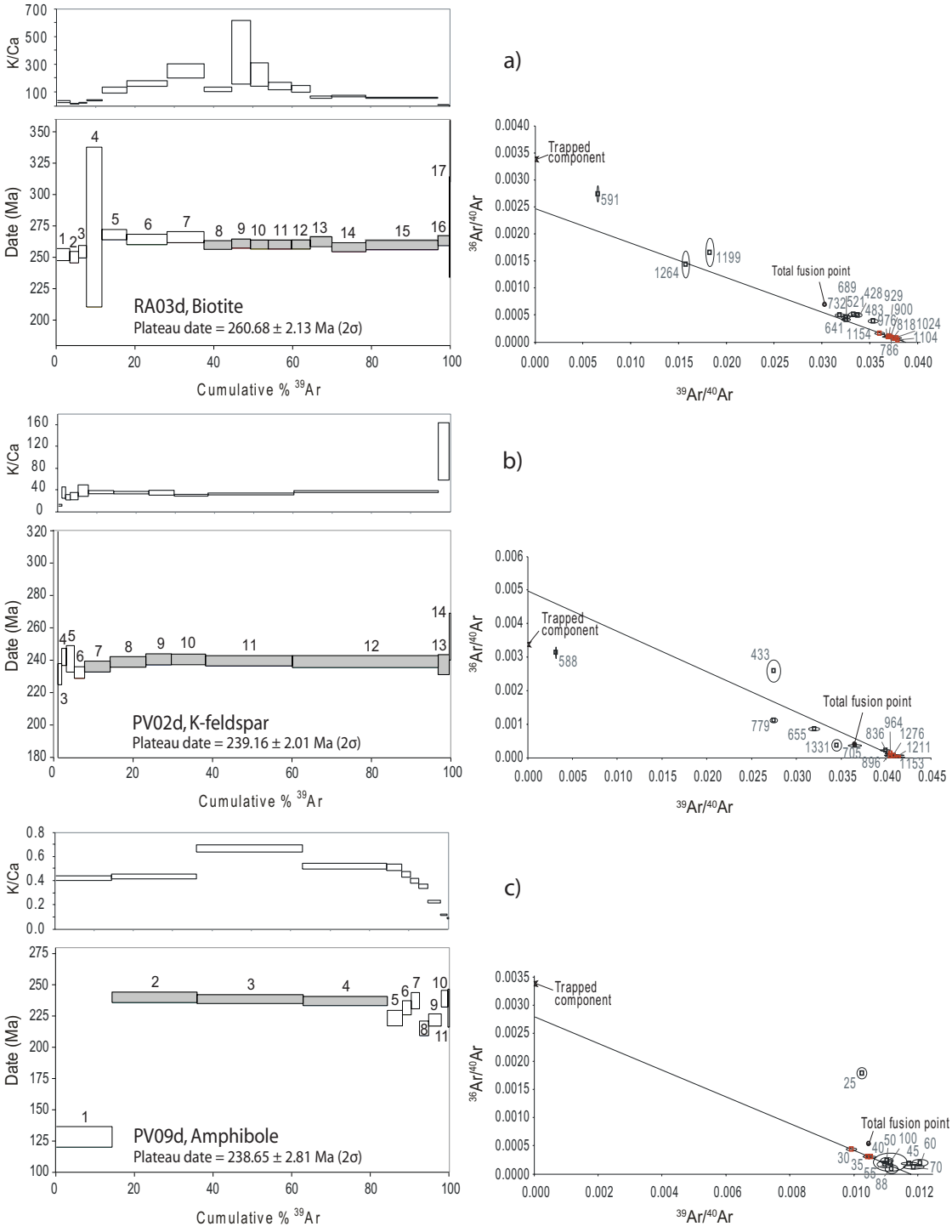

Figure 3.5: San Rafael Block ^{40}Ar-^{39}Ar geochronology results (examples). The left panels show K-Ca ratios (top) and calculated date (bottom) as a function of released ^{39}Ar during stepwise heating (bars are plotted at 2σ error). The numbers in the date spectrum plot indicate the heating step; the filled bars were used in the calculation of the plateau date. The right panels show inverse isochron diagrams. Red symbols indicate the steps used in the inverse isochron calculation. Results from: (a) an Upper Choiyoi Gr. ignimbrite, (b) a Puesto Viejo Gr. ignimbrite, and (c) a Puesto Viejo Gr. basalt. See Appendix A for the complete results.

tion (B) with a distributed unblocking temperature that causes the demagnetization trajectory to follow a great circle path. The great circles generally converge at a direction resembling that of the A-component (Fig. 3.6c). AF demagnetization is found to be more effective at removing the B-component, indicating that it predominantly resides in low-coercivity grains. The random orientation of this component, its confined coercivity, and its relatively high intensity are consistent with a lightning-induced partial-remagnetization, and we do not consider it further. Laboratory unblocking temperature spectra reveal that remanence is principally lost between ∼500 °C and 580 °C. In instances where remanence persists above 600 °C, the high-temperature (> 580 °C) fraction rarely exceeds 20% of the total remanence, and its associated direction is almost invariably parallel to that of the lower-temperature fraction (i.e. decay is univectorial) (Fig. 3.6a). Samples from sites PV28-30 are unique in possessing a high-temperature component of magnetization (C) that is of opposite polarity (but not antipodal) to the A-component in the same samples (Fig. 3.6b). This C-component is sub-parallel to the low-temperature components and the PDD. Following from its stability and directional consistency, we designate the A-component the characteristic remanent magnetization (ChRM) of the ignimbrites (Table 3.2). In a few instances, a group of sites that were collected from a thick sequence of ignimbrites present statistically indistinguishable (95% conf.) site-means; these groups likely represent single cooling units. To prevent a weighting bias in the directional dataset, we have averaged these sites at the sample-level (Table 3.2).

The results of basaltic sample demagnetization are similar to those of the ignimbrites, but without a component of remanence that persists above 580 °C (Fig. 3.6d). Sites PV22 and 31 exhibit univectorial decay (component A), after removal of a low-stability component of magnetization. Remanence is lost by ∼560 °C in

Figure 3.6: Characteristic demagnetization behavior of samples from the Puesto Viejo Gr. All directions are presented in geographic coordinates. In the orthogonal vector diagrams the solid (open) symbols are projections onto the horizontal (vertical) plane. For the stereonets the solid (open) symbols are projections onto the lower (upper) hemisphere. (a) Typical ignimbrite samples. (b) Ignimbrite sample showing the high-stability C component. (c) Example of converging great circle demagnetization trajectories; the star represents the common high-stability component. (d) Typical basalt samples. (e) Typical volcaniclastic rock samples. (f) AF demagnetization of a volcaniclastic sample. (g) Typical conglomerate clast samples. (h) Sample-level component directions from the conglomerate clast samples: diamonds (circles) denote the low- (high-)temperature components. The triangles represent the high-temperature components of two independent samples collected from the same clast, indicating that the randomness of the high-temperature component is not due to viscous behavior. The "x" (star) denotes the direction of the present day field (present day dipole).

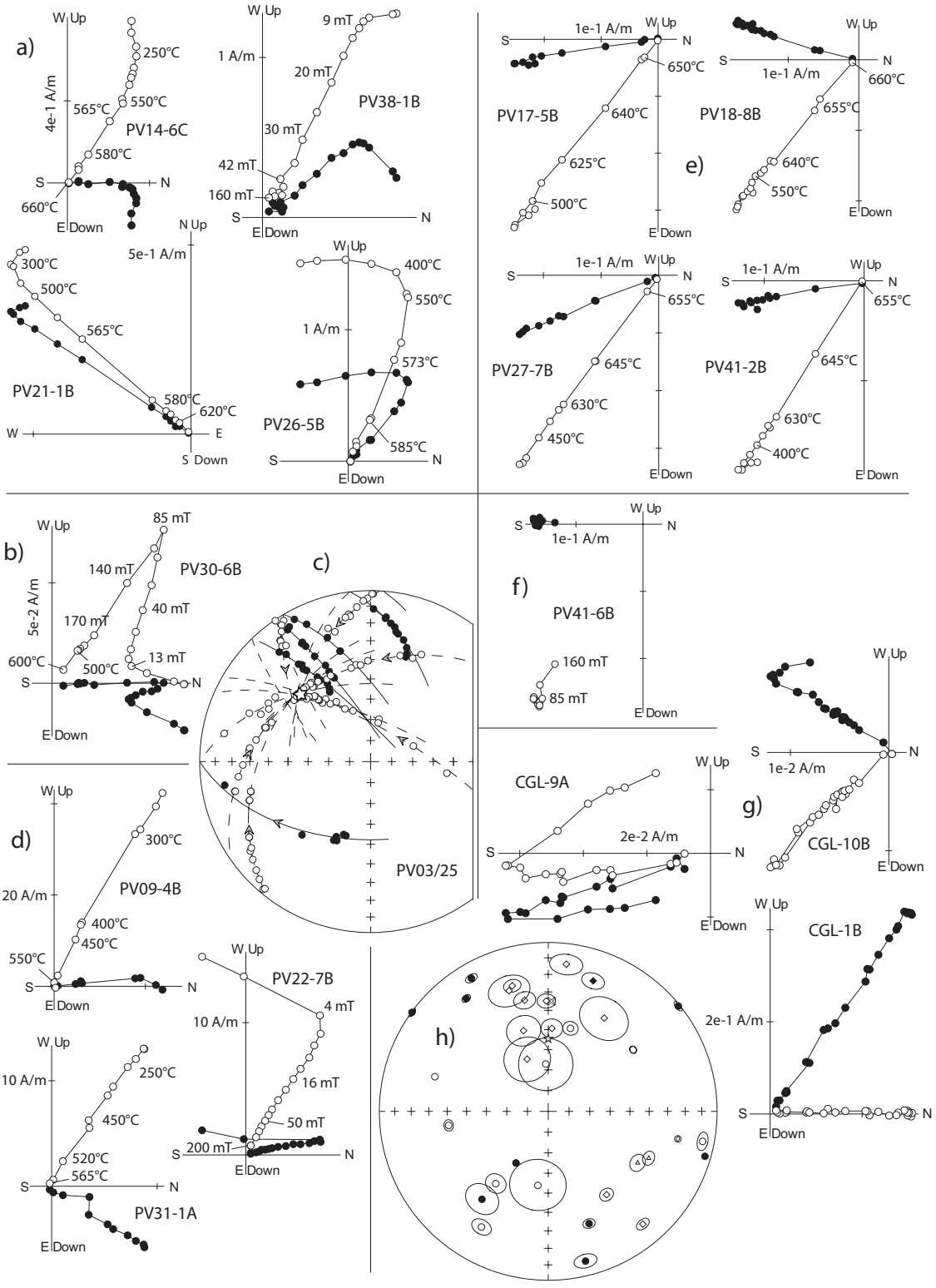
a)
W Up
4e-1 A/m
250°C
565°C
550°C
PV14-6C
580°C
S
N
660°C
E Down
W Up
9 mT
1 A/m
20 mT
PV38-1B
30 mT
42 mT
160 mT
S
N
E Down
N Up
5e-1 A/m
300°C
500°C
565°C
PV21-1B
580°C
620°C
W
E
S Down
W Up
400°C
550°C
1 A/m
573°C
PV26-5B
585°C
S
N
E Down
1e-1 A/m
W Up
S
N
650°C
PV17-5B
640°C
625°C
500°C
E Down
e)
W Up
S
N
1e-1 A/m
660°C
PV18-8B
655°C
640°C
550°C
E Down
1e-1 A/m
W Up
S
N
655°C
PV27-7B
645°C
630°C
450°C
E Down
1e-1 A/m
W Up
S
N
655°C
PV41-2B
645°C
630°C
400°C
E Down
b)
W Up
85 mT
5e-2 A/m
140 mT
PV30-6B
40 mT
170 mT
600°C
500°C
13 mT
S
N
E Down
c)
PV03/25
W Up
S
N
1e-1 A/m
f)
PV41-6B
160 mT
85 mT
E Down
d)
W Up
300°C
20 A/m
PV09-4B
400°C
450°C
550°C
S
N
E Down
W Up
PV22-7B
4 mT
10 A/m
16 mT
50 mT
200 mT
S
N
E Down
W Up
10 A/m
250°C
450°C
520°C
565°C
S
N
PV31-1A
E Down
h)
W Up
CGL-9A
2e-2 A/m
S
N
E Down
W Up
S
N
1e-2 A/m
g)
CGL-10B
E Down
W Up
CGL-1B
2e-1 A/m
S
N
E Down

these samples. The total remanence of site PV09 is likewise eliminated by ∼560 °C, but a discrete decay at ∼350 °C is likely due to the unblocking of a distinct magnetic phase. There is typically a subtle change in the magnetization direction after removal of this intermediate temperature phase, but its site-level mean direction is not statistically indistinguishable (95% conf.) from that of the more stable phase (component A). The demagnetization trajectory of site PV08 is characterized by great circles, again due to lightning-induced partial-remagnetization. As with the ignimbrites, we designate the A-component the ChRM of the basalts (Table 3.2).

Volcaniclastic rock samples are also dominated by univectorial decay during demagnetization (Fig. 3.6e). A change in the demagnetization trajectory is common in the initial, low-temperature steps, and is associated with a minor, randomly oriented overprint. The remanence of these samples remains highly stable during demagnetization; through the course of thermal treatment most remanence is lost in a narrow interval between ∼630 and 660 °C and the laboratory unblocking temperature spectra are sharp-shouldered. AF demagnetization is ineffective (Fig. 3.6f). There is no indication of discrete decay between ∼500 and 580 °C, as observed in the volcanic rock samples.

Demagnetization of the clast samples from the basal conglomerate commonly reveals a low-temperature component of magnetization, oriented sub-parallel to the PDD or PDF, that yields to a randomly oriented component at higher temperatures (Figs. 3.6g,h). The high temperature component decays univectorially to the origin. In some samples, unblocking of this high temperature component is confined to the intervals of ∼500-580 °C and/or ∼630-670 °C; in others the unblocking temperatures are more distributed. A test for randomness (Watson, 1956) confirms that the directions of this high temperature component are statistically random at the site

level (R: 3.98 < R0: 7.17 for P = 0.05, N = 20), suggesting that the clasts preserve a primary depositional remanent magnetization (DRM) (Table 3.2; Fig. 3.6h). The directions of the low-temperature component are not statistically random (R: 8.52 > R0: 5.52 for P = 0.05, N = 12), and probably represent a partial viscous overprint of the PDD/PDF.

Of the 42 sites collected and demagnetized, 36 have been retained for further analysis (14% rejected) (Table 3.2). Five of the six rejected sites were hosted in unwelded tuffs. Three of these sites (PV12, 13, 37) yielded samples that readily altered during thermal demagnetization and were highly-resistant to AF demagnetization. Site-level magnetization directions from the other 2 sites (PV15, 19) were highly scattered (k < 3). Site PV32 was rejected due to a low sample-count and sub-parallel great circle demagnetization trajectories. Of the samples from the retained sites, ∼8% have been discarded due to alteration, erratic behavior, or anomalous magnetization directions.

3.6.2 Upper Choiyoi Gr.

The demagnetization behavior of volcanic rock samples of the Upper Choiyoi Gr. is characteristically simple (Fig. 3.7). Results from samples of ignimbrites, tuffs, and volcanic breccias are discussed collectively due to their similarities. Typically, a weak, low-stability component of magnetization is removed during the initial demagnetization steps, revealing a high-stability component that decays univectorially to the origin. Laboratory unblocking temperature spectra show that the high-stability component usually unblocks within the intervals of ∼500-580 °C and/or ∼630-670 °C (Fig. 3.7). We interpret these discrete unblocking temperature intervals to reflect the presence of two distinct magnetic phases. Where co-existing, the directions of magnetization associated with these phases are typically statistically indistinct (95%

conf.) at the site level, if not within the individual samples (Fig. 3.7a). In the six sites where these directions are statistically distinct, only one pair of directions differs by more than 7° (two antipodal pairs are first inverted into a common polarity for comparison) (Fig. 3.7d). The occurrence of antipodal high-stability components is rare (restricted to sites RA10 and RA13; Fig. 3.7e) and is speculatively attributed to self-reversal. The remaining sites exhibit demagnetization behavior that suggests they possess one magnetic phase exclusively (Figs. 3.7b,c). In sites where the high-temperature directions from co-existing magnetic phases have indistinguishable (95% conf.) means, we average the directions at the sample level and assign this composite direction the ChRM (Table 3.3). Where the mean directions of the co-existing phases are distinct, we treat both means as independent values, and weight them the same as other site means. Some pairs of sites have been collected from the same cooling unit and exhibit indistinct (95% conf.) site means; these have been averaged at the sample level to prevent a weighting bias (Table 3.3).

Four sites (8%) have been rejected. Site CT03 is characterized by high NRM intensities and great-circle demagnetization trajectories that lack a common intersection point. We assume this site has been completely overprinted by lightning. Site CT04 yields an anomalous site mean direction and is suspected to be part of a slumped block; an absence of reliable structural indicators prevent its restoration. Demagnetization of site SL01 is defined by sub-parallel great circles that prevent a determination of the ChRM direction. Site SL05 yielded highly scattered directions ($k = 3.1$). From the retained sites, 7% of the samples were discarded due to erratic behavior, alteration, or anomalous magnetization directions.

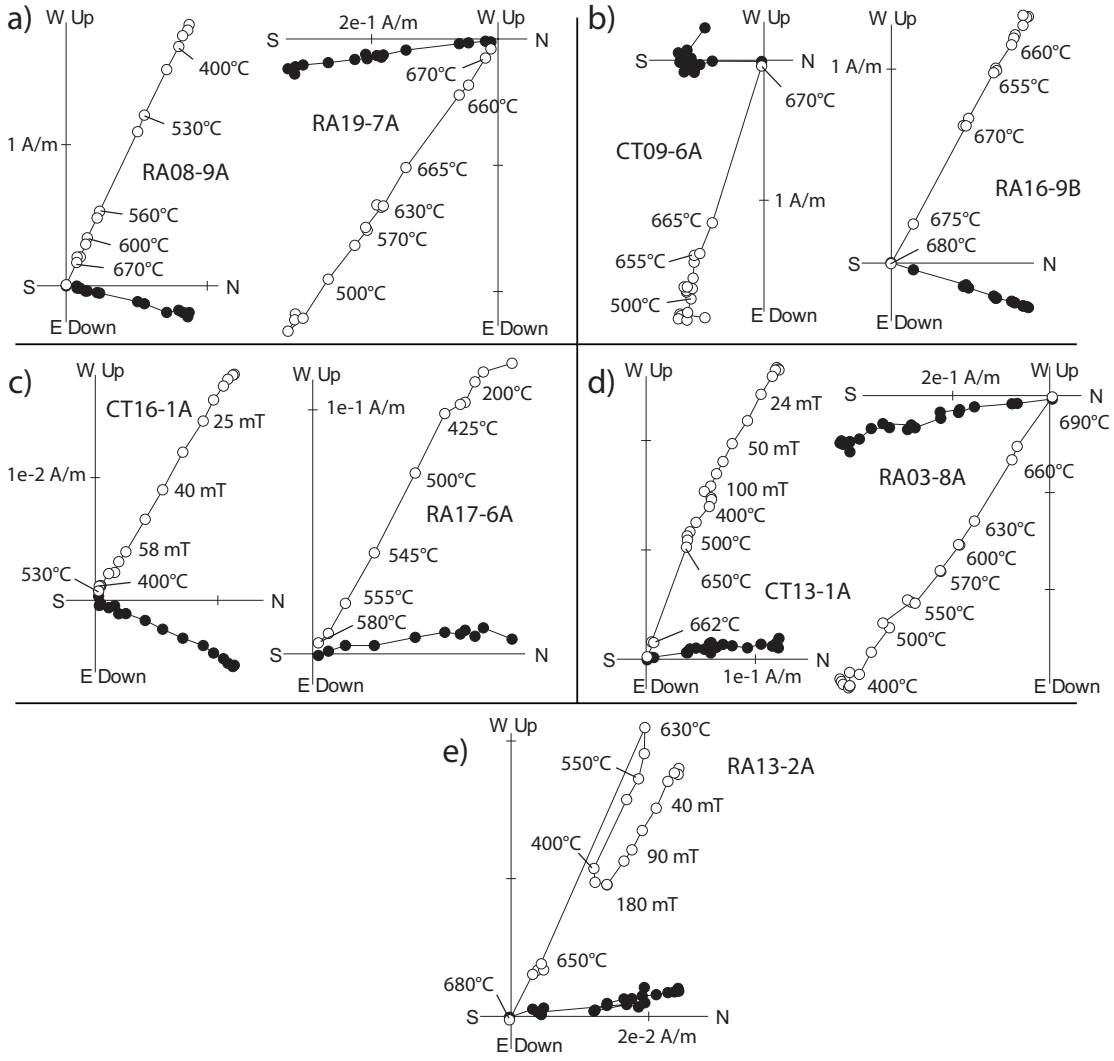

Figure 3.7: Characteristsic demagnetization behavior of samples from the Upper Choiyoi Gr. All directions are presented in geographic coordinates. The solid (open) symbols are projections onto the horizontal (vertical) plane. The illustrations are grouped according to the interpreted remanence carrier(s), as determined from demagnetization behavior and rock-magnetic experiments: (a) Two remanence carriers (magnetite and hematite), with parallel magnetization directions. (b) Remanence carried by hematite only. (c) Remanence carrier by magnetite only. (d) Two remanence carriers (magnetite and hematite) with statistically distinct (95% conf.) magnetization directions. (e) Example of rare, antipodal high-temperature components of magnetization, speculatively attributed to self-reversal.

3.7 Magnetic Mineralogy

3.7.1 Puesto Viejo Gr.

Thermomagnetic cycling (κ vs. T) of ignimbrite samples reveals a Curie temperature at ∼570 °C (Fig. 3.8a), indicative of magnetite. Hysteresis experiments show these samples to be dominated by a low-coercivity phase, corroborating the presence of magnetite, but also reveal the presence of a second, subsidiary phase with a distinctly harder coercivity (Figs. 3.8h,i). The absence of a second critical point in the thermomagnetic experiments suggests that this high-coercivity phase has a low intrinsic magnetic susceptibility. These characteristics are consistent with hematite, as is the observation of a stable remanence that survives thermal demagnetization at 600 °C (Fig. 3.6a). Low temperature remanence experiments reveal a change in the rate of remanence loss during warming through the interval of ∼110–120 K (Fig. 3.8d), which is diagnostic of the Verwey transition of magnetite (Muxworthy and McClelland, 2000). The natural remanent magnetization (NRM) of an undemagnetized sample is observed to decay across this transition (Fig. 3.8e), demonstrating that magnetite carries at least part of the NRM. In some cases, the Verwey transition is suppressed and remanence is observed to decay monotonically during warming from 20 K. This behavior can reflect the presence of partially-oxidized magnetite, the unblocking of superparamagnetic (SP) grains, or the re-organization of domains in multi-domain (MD) magnetite (Dormann et al., 1997; Moskowitz et al., 1998; Bowles et al., 2009). In the low-temperature cycling of an IRM imparted at room-temperature, a broad Morin transition can be observed between ∼260 and 160 K, corroborating the presence of hematite (Özdemir et al., 2008). FORC diagrams from ignimbrite samples exhibit the hallmarks of pseudo-single domain (PSD) magnetite: self-closing inner contours and outer contours which diverge toward Hc = 0 (Roberts

Figure 3.8: Rock magnetic experiments on Puesto Viejo Gr. samples. The lithology of the sample is denoted by the letter after the sample name: I = ignimbrite, B = basalt, S = volcaniclastic rock. (a–c) Thermomagnetic analysis (κ vs. T). The gray line in these panels shows the first derivative of the heating curve. Interpreted magnetic critical points are labeled: C (Curie) and N (Néel) temperatures. (d–g) Low-temperature remanence experiments. FC = field cooled, ZFC = zero field cooled. RT = isothermal remanent magnetization imparted at room-temperature, NRM = natural remanent magnetization. The gray line in these panels shows the first derivative of the FC curve. Interpreted magnetic transitions are labeled: V (Verwey) and M (Morin). (h) Hysteresis loops of characteristic samples after correction for paramagnetism. The inset shows the low-field behavior of sample PV09-3C. (i) Back-field curves for samples from (h). (j–k) Characteristic first-order reversal curves (FORC) for ignimbrite and basalt samples. A smoothing factor of 3 was applied to the FORC diagrams.

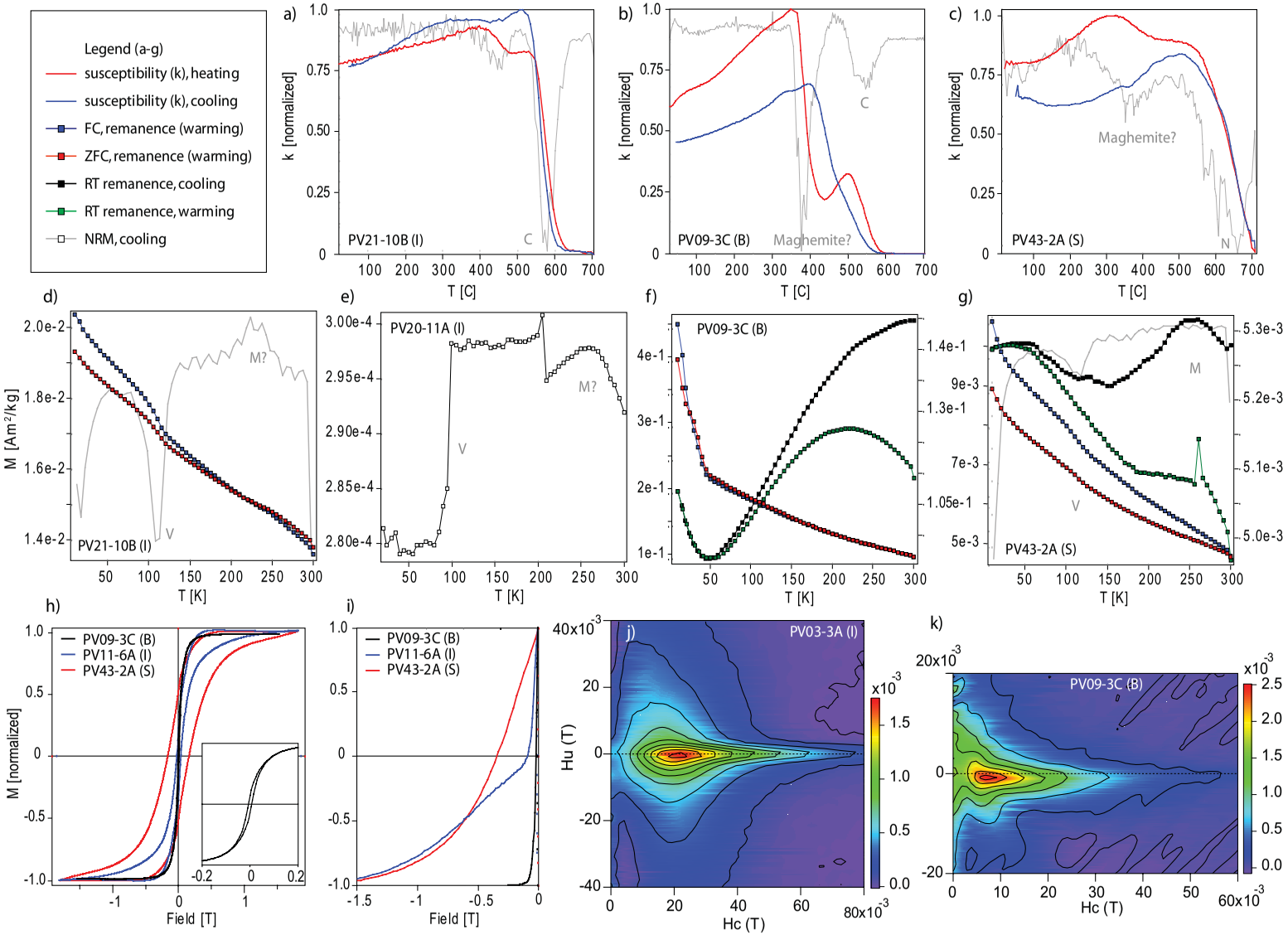
Legend (a-g)
susceptibility (k), heating
susceptibility (k), cooling
FC, remanence (warming)
ZFC, remanence (warming)
RT remanence, cooling
RT remanence, warming
NRM, cooling
a)
k [normalized]
T [C]
PV21-10B (I)
C
b)
PV09-3C (B)
Maghemite?
C
c)
PV43-2A (S)
Maghemite?
N
d)
M [Am²/kg]
T [K]
PV21-10B (I)
M?
V
e)
PV20-11A (I)
M?
V
f)
PV09-3C (B)
g)
PV43-2A (S)
M
V
h)
PV09-3C (B)
PV11-6A (I)
PV43-2A (S)
M [normalized]
Field [T]
i)
PV09-3C (B)
PV11-6A (I)
PV43-2A (S)
Field [T]
j)
PV03-3A (I)
Hu (T)
Hc (T)
k)
PV09-3C (B)
Hc (T)

et al., 2000; Carvallo et al., 2006) (Fig. 3.8j).

Thermomagnetic curves of basalt samples exhibit a Curie point at ∼550 °C (Fig. 3.8b), which we interpret as the Curie temperature of low-Ti titanomagnetite. A sample from site PV09 reveals a critical point at ∼375 °C (Fig. 3.8b), in agreement with the discrete unblocking at ∼350 °C observed during thermal demagnetization. The magnetic phase associated with this change is evidently metastable, as the heating curve is not reversible. Hysteresis loops and back-field curves do not show evidence of a second phase (Figs. 3.8h,i), so the intermediate and high-temperature phases may share a common, low coercivity. The thermal instability and low coercivity of the intermediate temperature phase are consistent with maghemite, which could have developed by secondary, low-temperature oxidation of primary titanomagnetite. Low temperature remanence experiments on a sample from site PV09 show monotonic remanence loss above ∼50 K and a suppressed Verwey transition (Fig. 3.8f); these can be expressions of partially-oxidized magnetite (Bowles et al., 2009). Low temperature cycling of an IRM imparted at room-temperature reveals a broad loss of remanence during cooling that could similarly reflect the presence of maghemite. FORC diagrams exhibit indications of both PSD and MD magnetite (Fig. 3.8k).

Volcaniclastic rock samples exhibit a Néel temperature at ∼660 °C during thermomagnetic cycling (Fig. 3.8c), indicating the presence of hematite. The minor change in susceptibility at ∼350 °C in sample PV43-2, which is not reflected in the laboratory unblocking temperature spectra, may be the expression of a minor population of magnetite or maghemite; this phase is destroyed by heating in air. Hysteresis loops and back-field curves reveal the presence of a single, high-coercivity phase, consistent with hematite (Figs. 3.8h,i). Low temperature remanence experiments yield a discernable Verwey transition (Fig. 3.8g), establishing the presence of magnetite in

these rocks. The Morin transition is not evident in these experiments, perhaps because the capacity of hematite to acquire a low-temperature remanence is negligible, relative to magnetite. A broad Morin transition can instead be seen between ∼260 and 150 K in the low-temperature cycling of an IRM imparted at room-temperature. The suppression of the Morin transition below ∼262 K has been observed to relate to grain size, cation substitution, and the density of lattice defects, implying that the hematite in these samples is either fine grained ($\lesssim 0.1$ μm) or non-stoichiometric (Ericsson et al., 1986; Özdemir et al., 2008; Jacob and Abdul Khadar, 2010). The observation of nanoparticle-like behavior—monotonic decay of low-temperature IRMs during warming and progressive blocking of room-temperature IRMs with decreasing temperature—in many of the volcaniclastic rock samples may be due to a population of SP grains (Dormann et al., 1997).

3.7.2 Upper Choiyoi Gr.

Thermomagnetic curves of ignimbrite samples reveal Curie temperatures of ∼560-580 °C and Néel temperatures of ∼645–660 °C (Figs. 3.9a,b), which are consistent with the presence of magnetite and hematite, respectively. As deduced from the demagnetization results, some samples appear to possess both phases, whereas others reveal the presence of either phase in isolation. Hysteresis experiments corroborate the presence of at least two distinct phases: low- and high-coercivity fractions, compatible with our magnetite and hematite assignments (Figs. 3.9g,h). "Goose-necked" and "wasp-waisted" hysteresis loops result from the mixing of these low- and high-coercivity components in various proportions (Tauxe et al., 1996). A widespread occurrence of magnetite in these samples is confirmed by the common observation of the Verwey transition in low-temperature remanence experiments (Figs. 3.9c,e). It is evident that magnetite acts as a carrier of the NRM by the discrete low-temperature

demagnetization of the NRM between ∼100 and 120 K in an undemagnetized sample (Fig. 3.9d). The Morin transition is also apparent in many samples as a broad interval of remanence loss between ∼260 and 140 K during low-temperature cycling of a room-temperature IRM (Fig. 3.9f). FORC diagrams exhibit a range of coercive behavior, but PSD- and MD-like results are the most common (Figs. 3.9i,j).

3.8 Magnetic Fabrics

3.8.1 Anisotropy of magnetic susceptibility

Magnetic anisotropy is the orientation-dependence of any magnetic property, and the quantification of this dependence is widely used as a tool for petrofabric analysis. Results of magnetic anisotropy measurements are routinely presented as ellipsoids, which are representative of a best-fitting second-rank tensor. The principal axes (K_{max}, K_{int}, K_{min}) of an ellipsoid are parallel to the eigenvectors of the matrix, and scaled according to the associated eigenvalues. Because measured magnetic properties are integrative, anisotropy will be a composite function of all the combined mineralogic sources. In felsic volcanic rocks, the anisotropy of low-field magnetic susceptibility (AMS) is typically controlled by accessory (titano)magnetite, which has a susceptibility that is 2 to 3 orders of magnitude greater than that of hematite and most paramagnetic minerals, and ∼6 orders of magnitude greater than diamagnetic materials (Rochette et al., 1992). Given the predominance of magnetite in the Puesto Viejo Gr. and Upper Choiyoi Gr. volcanic rocks, we assume this mineral controls their AMS. Hematite is assumed to contribute significantly to the AMS of the Puesto Viejo Gr. volcaniclastic rocks and to select Upper Choiyoi Gr. volcanic rocks where it dominates the NRM. Although crystallographic, strain, and grain-interaction effects all contribute to the low-field magnetic susceptibility of magnetite, it is the summation of weak shape-effects that commonly dominate the measured anisotropy (Hrouda,

Figure 3.9: Rock magnetic experiments on Upper Choiyoi Gr. samples. (a–b) Thermomagnetic analysis (κ vs. T). The gray line in these panels shows the first derivative of the heating curve. Interpreted magnetic critical points are labeled: C (Curie) and N (Néel) temperatures. (c–f) Low-temperature remanence experiments. FC = field cooled, ZFC = zero field cooled. RT = isothermal remanent magnetization imparted at room-temperature, NRM = natural remanent magnetization. The gray line in panels (c) and (e) shows the first derivative of the FC curve. The gray line in panel (f) shows the first derivative of the RT cooling curve. Interpreted magnetic transitions are labeled: V (Verwey) and M (Morin). (g) Hysteresis loops of characteristic samples after correction for paramagnetism. (h) Back-field curves for samples from (g). (i–j) Characteristic first-order reversal curves (FORC). A smoothing factor of 3 was applied to the FORC diagrams.

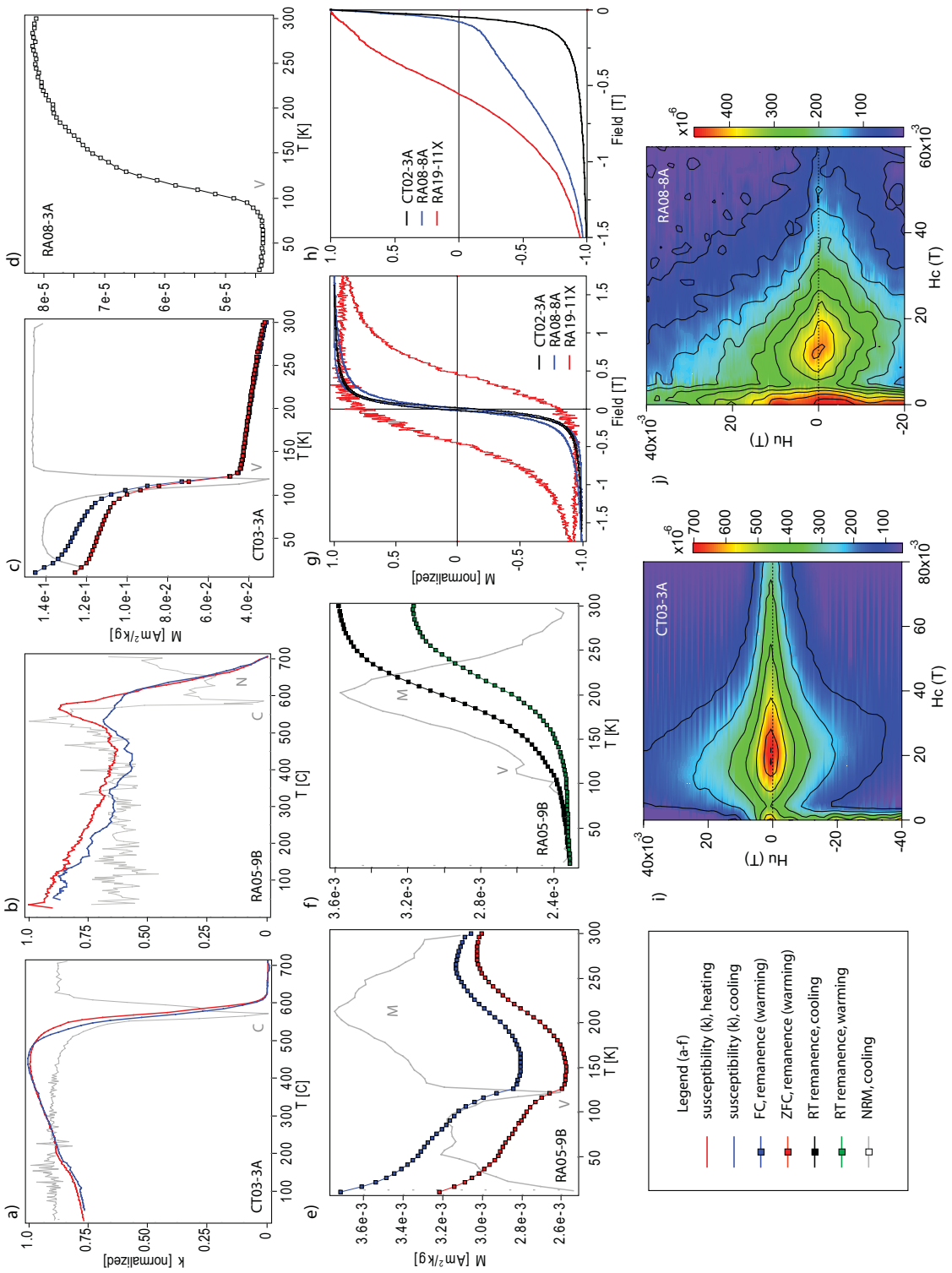
a)
CT03-3A
k [normalized]
T [C]
C
b)
RA05-9B
T [C]
N
C
c)
CT03-3A
M [Am²/kg]
T [K]
V
d)
RA08-3A
T [K]
V
e)
RA05-9B
M [Am²/kg]
T [K]
M
V
f)
RA05-9B
T [K]
M
V
g)
CT02-3A
RA08-8A
RA19-11X
M [normalized]
Field [T]
h)
CT02-3A
RA08-8A
RA19-11X
Field [T]
i)
CT03-3A
Hu (T)
Hc (T)
x10⁻⁶
j)
RA08-8A
Hu (T)
Hc (T)
x10⁻⁶
Legend (a-f)
susceptibility (k), heating
susceptibility (k), cooling
FC, remanence (warming)
ZFC, remanence (warming)
RT remanence, cooling
RT remanence, warming
NRM, cooling

1982; Grégoire et al., 1998). Inequant grains can become aligned during the emplacement of a rock body (via volcanic/fluvial flow) or by nucleation along preferred orientations in a pre-existing matrix, thus allowing the accessory magnetite to act as a proxy for bulk-rock petrofabric (Le Pennec et al., 1998; Pioli et al., 2008).

Magnetic fabric studies conducted on ignimbrites have classically been used to study flow directions and emplacement mechanisms, but here we employ AMS as a tool to interpret our structural field-observations. Ignimbrite AMS is generally characterized by a well-defined, sub-horizontal magnetic foliation (plane common to K_{max} and K_{int}), perhaps imbricated so that the foliation plane dips "upcurrent" (Ellwood, 1982; Incoronato et al., 1983; Baer, et al., 1997; Palmer and MacDonald, 1999). Within the foliation plane, particle long-axes may be aligned parallel or perpendicular to the transport direction, according to the flow regime (Khan, 1962; Tarling and Hrouda, 1993; Cagnoli and Tarling, 1997; Ort et al., 2003). We postulate that structurally perturbed ignimbrites can potentially be discriminated from units emplaced on a pre-existing slope through a comparison of AMS characteristics and field-observations. For example, an ignimbrite that was emplaced on a horizontal surface and subsequently tilted would not necessarily yield a magnetic lineation or imbrication with any correlation to the (younger) structural attitude. Indeed, the lineation and/or imbrication may be suppressed if local flow was not organized by a sloping surface. Conversely, in an ignimbrite emplaced on a pre-existing slope, K_{max} and K_{int} may correspond with the strike and dip directions of the slope, and an imbrication may leave the magnetic foliation shallower or steeper than the field-observed dip, depending on the relationship between flow direction and slope. Obviously, these expectations are qualitative in nature and may be rendered invalid by complexities in mineralogy or flow emplacement, or by later deformation. For this

reason, we treat the AMS results as an interpretive tool, rather than a structural dataset. In the following, we present two applications of this method to the current study; a discussion of the remaining data (Table 3.4) can be found in Appendix B.

In Cuesta de los Terneros, a thick sequence of Puesto Viejo Gr. sedimentary and volcanic rocks constitute a narrow WNW-ESE oriented plateau. Along the eastern margin of this plateau, the beds are tilted 22° W. This structural attitude is reflected in the highly-consistent AMS of ignimbrite samples from this sequence (Table 3.4): a well-defined magnetic foliation is parallel to the bedding plane (Fig. 3.10a). No statistically distinct (95% conf.) magnetic lineation is observed. These characteristics suggest that the structural attitude of this sequence is secondary.

In the Atuel River Canyon, a sequence of Upper Choiyoi Gr. volcanic rocks dips 13° SE. AMS data from samples of these volcanic rocks (Table 3.4) show a well-defined, sub-horizontal magnetic foliation and a subsidiary, but statistically significant (95% conf.) magnetic lineation (Fig. 3.10b). Although dipping to the southeast, the magnetic foliation plane is shallower than the field-estimated bedding attitude, possibly due to grain imbrication. The magnetic lineation is parallel to the strike of the bedding plane. This combination of characteristics is consistent with well-organized pyroclastic flow, directed parallel to the dip direction of the beds. We therefore interpret the structural attitude of this sequence to be primary (i.e. the dip pre-dates the volcanic rocks).

3.8.2 Other magnetic fabrics

As aforementioned, we have assumed that the low-field AMS is controlled largely by accessory magnetite (with an important contribution from hematite in select sites) and that the resulting magnetic fabrics are broadly representative of the bulk petrofabric of the rock. To validate these assumptions, we conducted additional magnetic

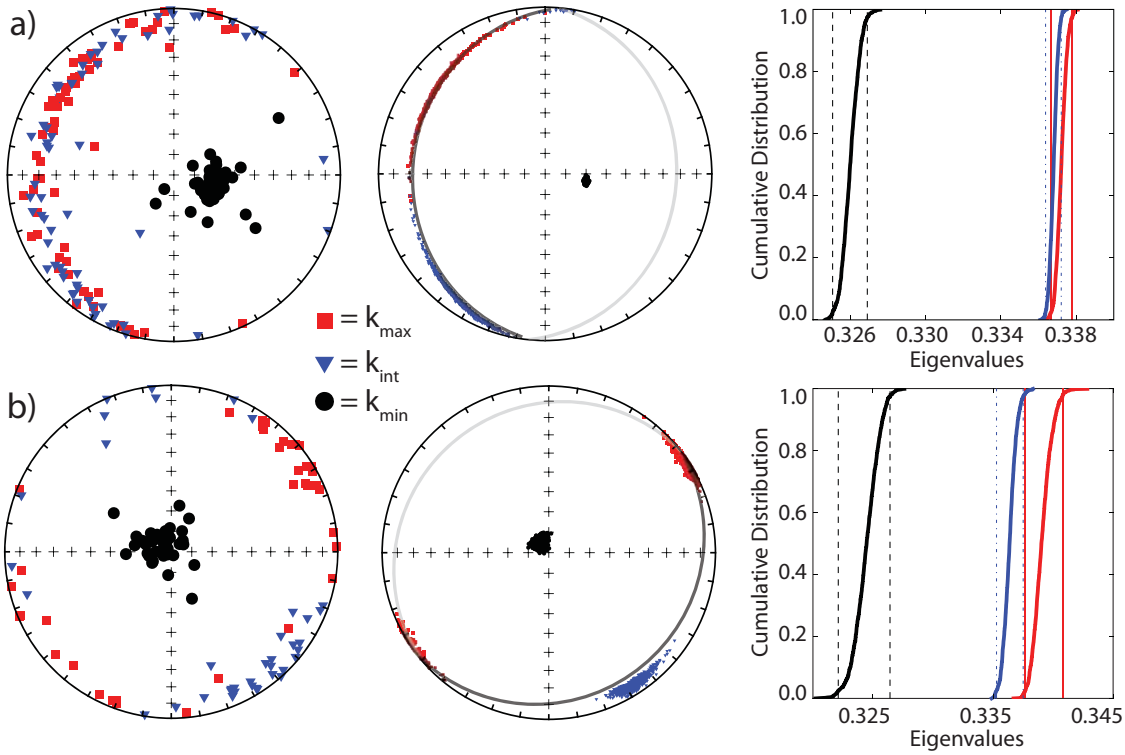

Figure 3.10: Example anisotropy of magnetic susceptibility (AMS) results. From sites PV03, 20–26 (a) and sites RA13–19 (b). Results are presented in geographic coordinates. All symbols are projections onto the lower hemisphere. The left panels show the raw sample-level data. The center panels show 1000 bootstrapped eigenvectors (Constable and Tauxe, 1990) of the raw data. The gray lines depict the bedding attitude of the sites, as estimated from field-observations; the darker (lighter) line is a projection onto the lower (upper) hemisphere. The right panels show the relative eigenvalues (as cumulative distribution functions) associated with the eigenvectors: red = maximum (τ_{max}), blue = intermediate (τ_{int}), black = minimum (τ_{min}). The vertical dashed lines are the 95% confidence bounds on the eigenvalue estimates.

anisotropy analyses on a select set of samples (Table 3.5). The anisotropy of anhysteric remanence (AARM), thermal remanence (ATRM), and high-field susceptibility (HF-AMS) target more specific mineral constituents, allowing a comparison of magnetic sub-fabrics and a means of determining the degree of alignment among different minerals. The AARM, ATRM, and HF-AMS results (discussed in appendix C) are in general agreement with the AMS data and reinforce the supposition that the AMS is controlled by magnetite, but is broadly representative of other mineral subfabrics.

3.9 Directional Analysis

3.9.1 Puesto Viejo Gr.

Tilt-corrections are applied to the Puesto Viejo Gr. ChRMs according to both raw field observations (hereafter "raw corrections") and AMS interpretations (hereafter "AMS corrections"). Results of the bootstrap foldtest (Tauxe and Watson, 1994) suggest that the ChRMs were acquired prior to tilting, as directional co-axiality peaks at 99% untilting (95% conf. bounds: 72–125%) for the raw corrections (Fig. 3.11a). The AMS corrections similarly result in peak co-axiality at 112% untilting (95% conf. bounds: 89–135%). Because the foldtest is designed to detect relative improvements in directional clustering, a comparison of the optimal untilting values from the raw and AMS corrections can be misleading. For example, the resultant vector length of the ChRMs, R (calculated after the directions are converted to a common polarity), is slightly higher at 100% untilting when the AMS corrections are used, even though the raw corrections reach peak co-axiality at 99% untilting (Fig. 3.11a). The decreased width of the 95% confidence bounds on the optimal untilting value of the AMS corrections also suggests they offer an improvement over the raw corrections.

In either case, after tilt-corrections are applied the ChRMs from the volcanic and

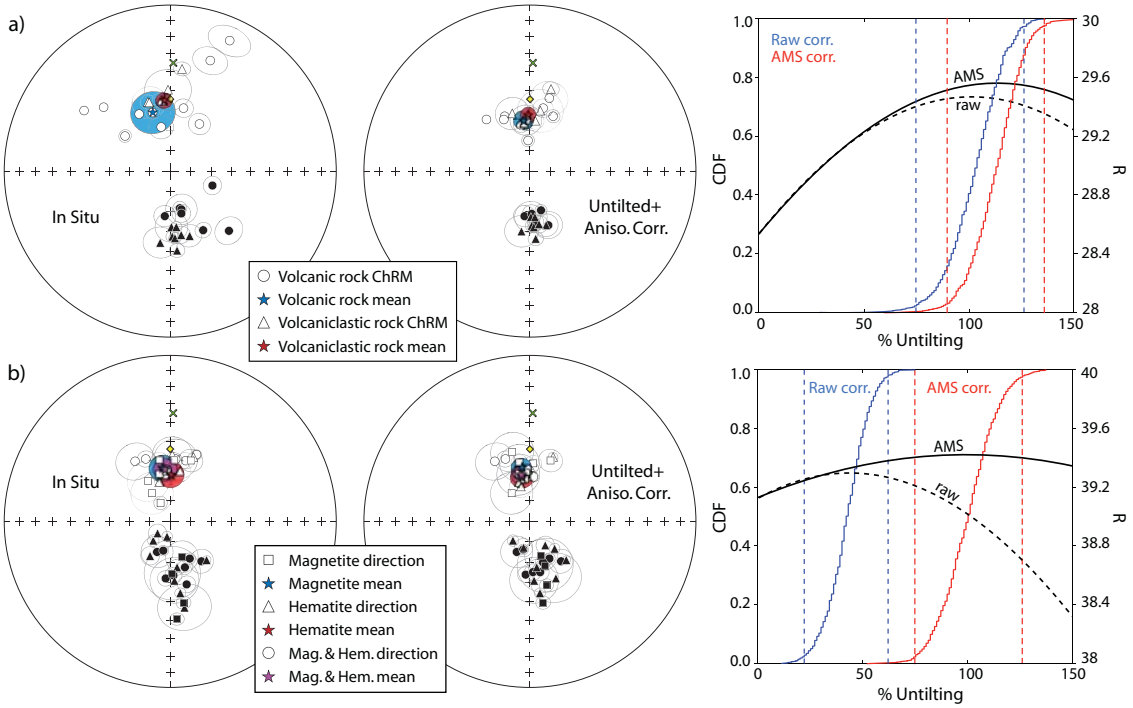

Figure 3.11: San Rafael Block site-mean paleomagnetic directions and fold-test results. From the Puesto Viejo Gr. (a) and the Upper Choiyoi Gr. (b). The left panels show the in situ site mean ChRM directions and group means with their associated α_{95} (projected cone of 95% conf.) The solid (open) symbols are projections onto the lower (upper) hemisphere. The green "x" (yellow diamond) denotes the direction of the present day field (present day dipole). The center panels show the site mean ChRM directions and group means after 100% untilting (using the AMS-interpreted corrections) and correction for magnetic anisotropy. The right panels show the results of the bootstrap foldtest, using the raw tilt-corrections (blue cumulative distribution function and dashed black curve) and the AMS-interpreted tilt-corrections (red cumulative distribution function and solid black curve). The cumulative distribution functions reveal the location of optimal untilting (maximum magnetization direction co-axiality), with 95% conf. bounds (dashed vertical lines). The black curves show the change in total resultant vector length (R) of the magnetization direction population as a function of unfolding.

volcaniclastic rock subsets remain statistically distinct (95% conf.), implying that they do not belong to a common distribution. Re-applying the foldtest to these individual ChRM subsets, the volcanic rock directions again yield a positive result: optimal untilting at 102% (95% conf. bounds: 70–134%, raw corrections) or 118% (95% conf. bounds: 94–142%, AMS corrections), but the test of the volcaniclastic rock ChRMs yields an inconclusive result: optimal untilting at 64% (95% conf. bounds: 31–97%, raw corrections) or 48% (95% conf. bounds: 8–89%, AMS corrections). Using either set of tilt-corrections, both the volcanic and volcaniclastic rock ChRM subsets independently pass the bootstrap reversal test, indicating that their normal and reverse components have a common origin, and that additional magnetizations have been effectively removed. After tilt-correcting locally faulted sites in the Valle Grande area, additional volcanic rock site-mean directions from neighboring sites are found to be statistically indistinct (95% conf.), and are merged to prevent a weighting bias (Table 3.2).

In addition to the application already discussed, magnetic anisotropy measurements can be used to correct for bias in a magnetization direction due to sedimentary flattening (pertinent to DRMs) or magnetic refraction (where a thermal remanent magnetization (TRM) is deflected from the ambient magnetic field direction due to shape effects). To test for such bias, ATRM measurements were made on select samples from sites with the highest degree of AMS (Table 3.5; appendix C). The results indicate that a minor bias is present in the volcanic rock samples with a relatively high degree of AMS ($P \geq 1.02$), but that the majority of the volcanic rock ChRMs have a negligible error ($\leq 1°$). For the select sites that we measured ATRM (those that had the highest degree of AMS), we corrected the site mean directions with the inverse ATRM tensor (Table 3.2).

ATRM measurements on select volcaniclastic rock samples reveal a more substantial shallow inclination bias of ∼5.5°. However, correction of the volcaniclastic rock directions is not straightforward because the ChRM is likely a DRM, and the intrinsic particle anisotropy (α) is not known. Moreover, the larger collection of AMS measurements cannot be used to determine the prevalence of any shallow inclination bias because the AMS is likely controlled by trace amounts of magnetite, whereas the ChRM is carried by hematite. Some assumptions are therefore necessary. If we assume that the ChRM is a DRM (discussed below) and all the volcaniclastic rocks have experienced the same degree of sedimentary flattening, we may apply a blanket correction following the relationship of King (1955): $\tan(\mathrm{I}_o) = f\ \tan(\mathrm{I}_f)$, where f is the "flattening" coefficient, and I_o and I_f are the observed and true field inclinations, respectively. The value of f can be calculated from the ATRM data if we further assume that $\alpha = \infty$, in which case the remanence (ATRM) ellipsoid is identical to the DRM ellipsoid (Jackson et al., 1991). Following this assumption, the ATRM results indicate that the volcaniclastic rocks have been flattened by $f = 0.8$. In reality, α is likely to be finite, so this is a minimum estimate of shallowing (the true value of f is likely lower). A more accurate value of f may be calculated if we assume that the difference in the mean ChRM directions of the volcanic and volcaniclastic rocks is due to inclination shallowing of the latter. The mean inclinations of these datasets can be brought into agreement by applying an inclination correction of $f = 0.71$ to the volcaniclastic rock ChRMs. For reference, f values from hematite-bearing sedimentary rocks have been observed to range from 0.40 to 0.83 (Bilardello and Kodama, 2010). Unfortunately, we do not have a sufficient number of sites from the volcaniclastic rocks to independently estimate the true inclination bias (as per the technique of Tauxe et al., 2008), so the validity of the $f = 0.71$ correction is

dependent on the assumption that the mean ChRM direction of the volcanic rocks is well-determined and that it shares a common true direction with the mean ChRM of the volcaniclastic rocks.

After anisotropy correction, the paleomagnetic pole derived from the raw tilt-corrected volcanic rock ChRMs is: 77.8° S, 322.4° E, A_{95}: 7.8°; if the AMS-interpreted tilt-corrections are used, the pole is: 76.7° S, 312.4° E, A_{95}: 7.3° (Table 3.2). For reference, the pole position previously determined from Puesto Viejo Gr. volcanic rocks by Valencio et al. (1975) was: 76° S, 236° E, A_{95}: 18°. The paleomagnetic pole derived from the $f = 0.8$ corrected volcaniclastic rock ChRMs is: 81.2° S, 301.0° E, A_{95}: 4.8° (100% untilted, AMS tilt-corrections). Using the larger anisotropy correction ($f = 0.71$) the paleomagnetic pole is: 77.9° S, 297.8° E, A_{95}: 4.6° (100% untilted, AMS tilt-corrections) (Table 3.2). If the volcaniclastic rock ChRMs are not corrected for anisotropy, the tilt-corrected paleopole is sub-parallel to the rotation axis (using either set of tilt-corrections).

3.9.2 Upper Choiyoi Gr.

The bootstrap foldtest of the Upper Choiyoi Gr. ChRMs is inconclusive if the raw tilt-corrections are used: optimal untilting occurs at 42% (95% confidence bounds: 22–62%), but positive if the AMS tilt-corrections are used: optimal untilting at 101% (95% confidence bounds: 75–126%) (Fig. 3.11b). The ChRMs pass the bootstrap reversal test after applying either set of tilt-corrections. A select set of ATRM measurements on samples with the highest degree of AMS (Table 3.5) again indicate that a directional bias is present in the most anisotropic samples. Unfortunately, ATRM measurements were not made on all Upper Choiyoi Gr. sites that may be affected by such a bias (sites with P (of AMS) ≥ 1.02), but the larger collection of AMS results may be utilized because they convey the bulk anisotropy of the remanence carrying

mineral in these rocks (magnetite). The FORC diagrams indicate that single-domain (SD) magnetite is not dominant in the Upper Choiyoi Gr. volcanic rocks, and the AARM measurements confirm that SD grains do not noticeably contribute to the AMS (Appendix C). Given this, we adopt the theoretical relationship $P_{TRM} \approx P_{AMS}^2$, which Cogné (1987) has shown to be a reasonable approximation where the AMS is controlled by MD magnetite. Because the majority of the Upper Choiyoi Gr. AMS ellipsoids are oblate with a sub-vertical K_{min}, we further simplify the anisotropy corrections by assuming that P (of AMS) describes a pure, horizontal foliation. ChRMs carried solely by hematite are not corrected, because its anisotropy is unknown. The resulting corrections are small; 10 sites are corrected by this method, and the average change in inclination is 1.8° (Table 3.3).

The mean directions from the different remanence carriers are statistically indistinguishable (95% conf.) after anisotropy- and tilt-correction. The combined results yield the paleomagnetic pole: 73.7° S, 315.6° E, A_{95}: 4.1° (AMS tilt-corrections). If the raw tilt-corrections are used the pole is: 81.0° S, 340.2° E, A_{95}: 4.4°.

3.10 Discussion

3.10.1 Interpretation of geochronology results

Our new Upper Choiyoi Gr. SHRIMP U-Pb zircon date of 263.0 ±2.4 Ma (sample "PV01d") is in agreement with the SHRIMP U-Pb zircon date determined for the Agua de los Burros Fm. (264.8 ±2.3 Ma) by Rocha-Campos et al. (2010). The comparable ^{40}Ar-^{39}Ar date of 260.7 ±2.1 Ma from sample RA03d implies that the U-Pb zircon dates are close to the true eruptive age of the volcanic rocks.

Unexpectedly, the SHRIMP U-Pb zircon dates from the Puesto Viejo Gr. yield mid-to-Late Permian age estimates that resemble those of the Upper Choiyoi Gr. (260.8 ±3.2 Ma and 269.0 ±3.2 Ma). These dates contradict the Early to Middle

Triassic age assigned to the Puesto Viejo Gr. on the basis of the paleontological record. However, the presence of angular unconformities and locally thick sequences of clastic sedimentary rocks between the Upper Choiyoi Gr. and Puesto Viejo Gr. volcanic rocks supports the notion that these eruptive episodes are separated by a significant interval of time. We therefore postulate that the dated zircons from the Puesto Viejo Gr. ignimbrites are xenocrysts from the underlying Permian rocks, assimilated during magma ascent and eruption. In support of this hypothesis, microscopic examination of Puesto Viejo Gr. volcanic rocks has revealed an association between zircons and lithic fragments, some of which appear to have undergone weathering (Fig. 3.12). All zircons are zoned in an oscillatory fashion, and overgrown rims, as might occur during high grade metamorphism or during long residence time within a large magma chamber, were not observed. We speculate that the Puesto Viejo magma chamber was insufficiently volumetric to generate new zircon grains or overgrowths (Watson, 1996).

The ^{40}Ar-^{39}Ar plateau dates from the Puesto Viejo Gr. volcanic rocks range from 235.4 ±2.3 Ma to 239.3 ±3.2 Ma, in agreement with the recalculated K-Ar dates of Valencio et al. (1975). We interpret these results to reflect the cooling ages of the volcanic rocks, corroborating a Middle Triassic age for Puesto Viejo Gr. volcanism. Late Permian and Early Triassic ^{40}Ar-^{39}Ar plateau dates from the Puesto Viejo Gr. volcaniclastic samples (248.6 ±2.3 Ma and 254.7 ±5.0 Ma) represent a minimum age for the Upper Choiyoi Gr. volcanic rocks, and a maximum age estimate for the overlying Puesto Viejo Gr. volcanic rocks. If the volcaniclastic rocks are constituted primarily by re-worked pyroclastic material from contemporaneous Puesto Viejo volcanism, these ages could be close to the true age of the volcaniclastic rocks.

The ^{40}Ar-^{39}Ar plateau date of 239.5 ±7.0 Ma from Upper Choiyoi Gr. sample CCH

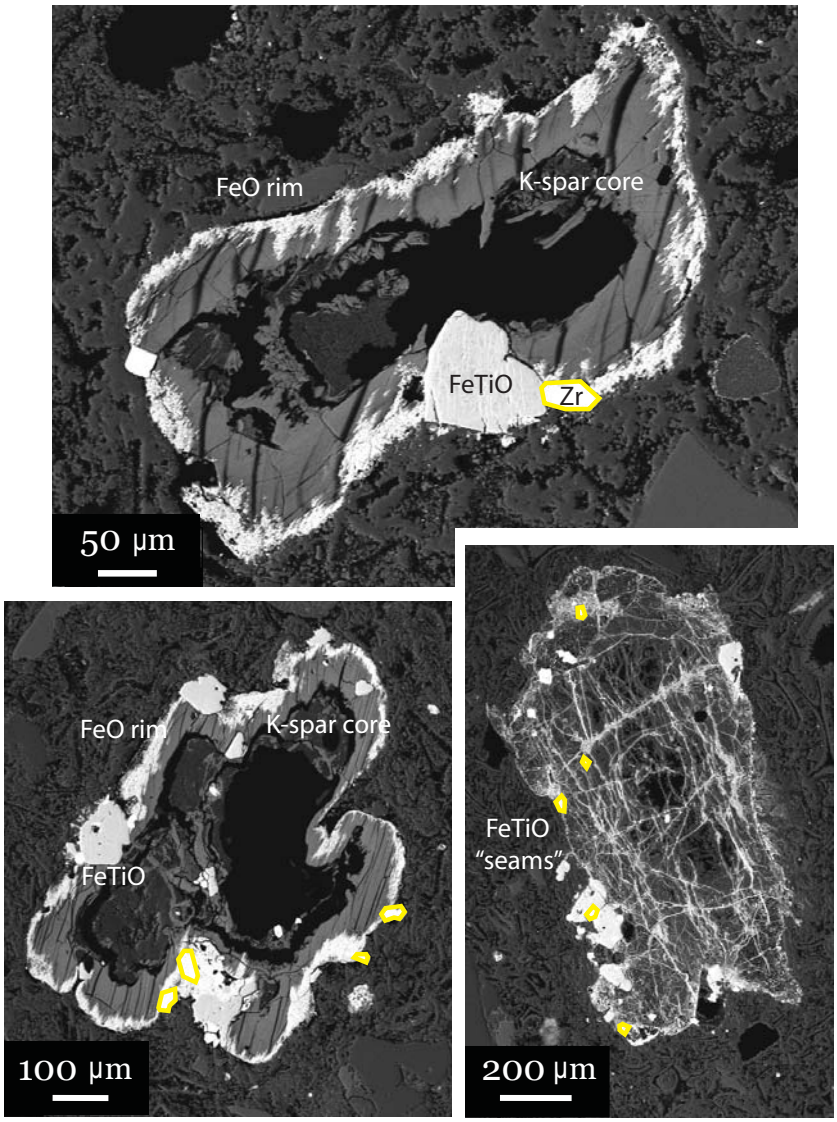

Figure 3.12: SEM photomicrographs of Puesto Viejo Gr. samples, showing an association between zircons and lithic fragments. FeO = unidentified iron-oxide phase, FeTiO = unidentified iron-titanium oxide phase, K-spar = potassium feldspar, Zr = zircon (also highlighted in yellow).

is attributed to thermal resetting during Middle Triassic volcanism/deformation, as it is proximal to Puesto Viejo Gr. volcanic rocks and a major post-SROP normal fault. Sample "PV01d-2" was collected from the Upper Choiyoi Gr., approximately 10 km to the southeast of sample CCH, along the same major normal fault. It has yielded an ^{40}Ar-^{39}Ar plateau date of 255.7 ±2.2 Ma that may represent a cooling age from late Upper Choiyoi volcanism (i.e. Cerro Carrizalito Fm.), or partial thermal resetting of an older age during Triassic volcanism/deformation.

The Late Triassic and Early Cretaceous whole-rock ^{40}Ar-^{39}Ar dates from Puesto Viejo Gr. ignimbrites are confounding, as no record of post-Middle Triassic volcanism has been documented in this region. However, we note that the date-spectra of these results are discordant (weighted-mean dates), indicating that the isotopic system of these samples has likely been disturbed. Notably, the ^{40}Ar-^{36}Ar ratio determined from sample PV30d is 235.7 ±25.9, which is statistically distinct (95% conf.) from the known atmospheric value of ∼298. Thus, we regard these whole-rock dates as unrepresentative of the emplacement age of these rocks.

With regard to these new results, we assign the sampled Upper Choiyoi Gr. (Agua de los Burros Fm.) a best-estimated age of ∼264 Ma (Capitanian). The volcanic rocks of the Puesto Viejo Gr. yield consistent Middle Triassic ^{40}Ar-^{39}Ar plateau dates with an average of ∼238 Ma, but the mean age of the group may be older, as reflected by the maximum ages of the volcaniclastic rocks and the identification of Early Triassic fossils. We therefore assign the Puesto Viejo Gr. an Early–Middle Triassic (Olenekian-Anisian) age of ∼245 Ma.

3.10.2 Interpretation of paleomagnetic results

The positive foldtest of the Puesto Viejo Gr. volcanic rocks implies that their magnetization acquisition was very early, if not primary, because the Puesto Viejo

Gr. was deformed by post-SROP regional tension that acted concurrently with Late Permian–Triassic volcanism. Post-Triassic deformation is not recognized in the SRB. A primary magnetization is further substantiated by the preservation of random directions in the clasts of the basal conglomerate of the Puesto Viejo Gr., which indicates that no pervasive regional remagnetizations are manifest. The broad sample-level agreement in the magnetization direction of the magnetite and hematite components suggests their magnetization acquisition was near-synchronous, precluding the possibility that either developed as a later product of diagenesis/alteration. The positive reversal test indicates that magnetization acquisition among the Puesto Viejo Gr. sites must have been sufficiently distributed in time so as to sample both field polarities and average secular variation. The antipodal nature of the ChRM directions implies that they have been sufficiently separated from secondary overprints. We conclude that the ChRM of the Puesto Viejo Gr. volcanic rocks is representative of the Early–Middle Triassic magnetic field, and we assign the associated paleopole the best-estimated age of 245 Ma.

The nature and age of the Puesto Viejo Gr. volcaniclastic rock ChRM is more difficult to interpret. The inconclusive foldtest is inconsequential because the structural restorations are very minor. The reversal test is positive for both the uncorrected and the 100% untilted datasets. The absence of a prominent secondary magnetization in the basal conglomerate or proximal volcanic rocks suggests that a widespread chemical remagnetization (CRM) is unlikely, but the volcaniclastic rock ChRMs (without anisotropy correction) are close to the PDD, both before and after tilt-correction. If the pre-Middle Triassic ^{40}Ar-^{39}Ar dates from the volcaniclastic rock samples have escaped thermal resetting, the rocks would also have escaped thermal remagnetization, and the ChRM could be a primary DRM. We interpret the ChRM of the Puesto

Viejo Gr. volcaniclastic rocks to be an early/primary DRM, but unrepresentative of the Early–Middle Triassic magnetic field due to a shallow inclination bias. However, it is important to reiterate that we cannot exclude the alternative possibility that the ChRM is a secondary CRM, in which case an inclination shallowing correction would not be applicable and the magnetization direction could be representative of a post-Middle Triassic magnetic field. In either case, this result is not useful for APWP construction.

The positive foldtest of the Upper Choiyoi Gr. ChRM immediately precludes a post-Triassic remagnetization, as regional deformation ceased in the SRB prior to the end of the Triassic. The age of the ChRM can be further constrained by the AMS interpretations of the structural attitudes, which imply that the oldest Upper Choiyoi Gr. rocks have experienced greater deformation (see Appendix B). This contention agrees with independent structural observations that indicate that the SROP waned during emplacement of the Agua de los Burros Fm., implying that the oldest rocks were subjected to greater compression (Kleiman and Japas, 2009). Therefore, acquisition of the Upper Choiyoi Gr. ChRM must have been very early, or primary, because deformation was partly contemporaneous with volcanism. An early/primary magnetization acquisition is again corroborated by a broad agreement in the magnetization direction of the magnetite and hematite components, and a positive reversal test implies that the ChRM is effectively purified of secondary magnetizations.

We interpret the ChRM to be representative of the Late Permian magnetic field and assign the paleomagnetic pole the best-estimated age of 264 Ma, but again note the possible inclusion of some site-level data from younger Permian rocks (i.e. the Cerro Carizzalito Fm., $\sim$252 Ma). We also note that the dual polarity of these results respects the presently known boundaries of the Kiaman Reversed Superchron

(∼318-265 Ma; Opdyke et al., 2000; Gradstein et al., 2004).

3.11 Implications

Since the late 1950s, it has been repeatedly demonstrated that the APWPs of Laurussia and Gondwana are disparate if a conventional "A-type" Pangea reconstruction is assumed (Irving, 2004). For example, using the (A-type) reconstruction parameters and global paleomagnetic data from the recent compilation of Torsvik et al. (2008), the mean 250 Ma paleopoles from Laurussia and Gondwana are separated by 20° (Fig. 3.13a). Our new Late Permian and Early–Middle Triassic volcanic rock-based paleopoles fall between these APWPs, close to the "global" APWP that is generated by merging the Laurussian and Gondwanan datasets (Fig. 3.13b). Specifically, the A_{95} of the Upper Choiyoi Gr. paleopole does not overlap with the APWP of Gondwana, but does overlap with the 265 Ma mean pole of the global APWP. The A_{95} of the Puesto Viejo Gr. volcanic rock-based paleopole is larger and overlaps the 245 Ma mean poles of both the Gondwanan and global APWPs, but the paleopole is closer to the latter. The position of these new volcanic-based paleopoles implies that the incongruity between the independent Laurussian and Gondwanan APWPs is due, at least in part, to bias in the paleomagnetic data from Gondwana. Such a bias could be due to inclination shallowing in sedimentary rocks, erroneous age assignments, unrecognized remagnetizations, and/or incompletely removed viscous overprints.

Inclination shallowing is especially notable because its effects are equatorially anti-symmetric. Because Pangea straddles the equator in the late Paleozoic–early Mesozoic, a shallow inclination bias will drive the apparent paleolatitudes of both Laurussia and Gondwana toward the equator, resulting in an artificial separation of

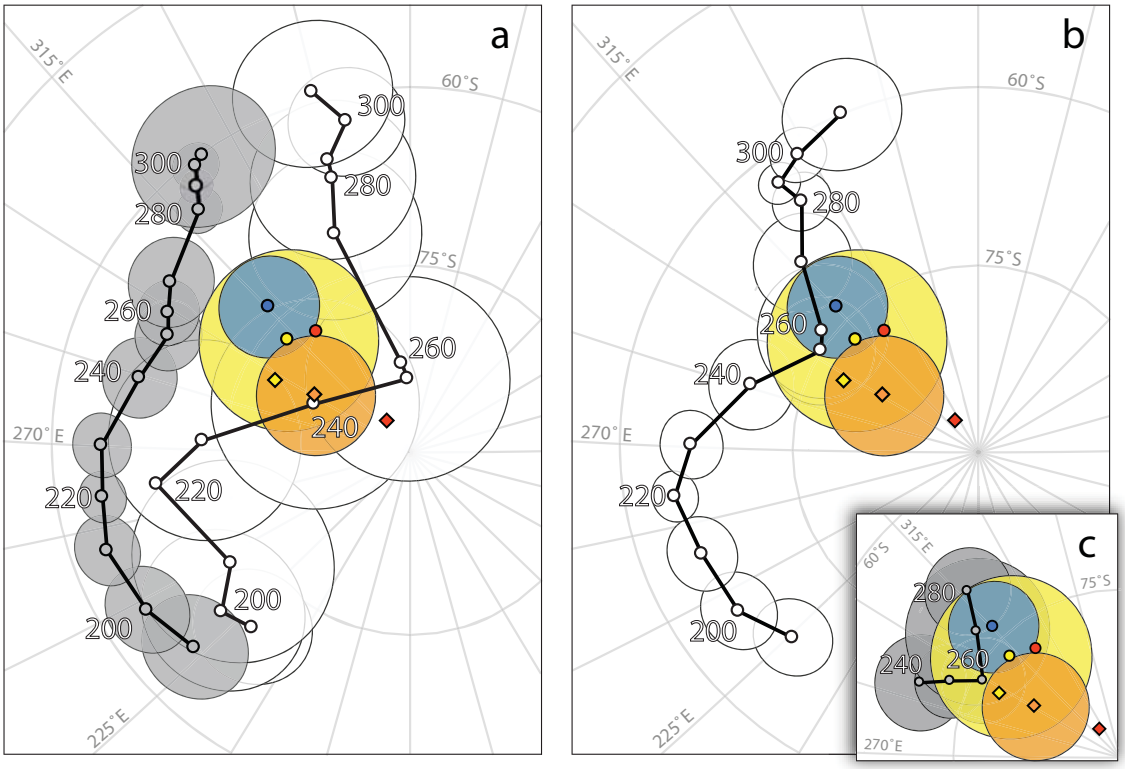

Figure 3.13: Comparison of new data and reference apparent polar wander paths (APWPs). (a) Comparison of the new Puesto Viejo Gr. and Upper Choiyoi Gr. paleomagnetic poles with the APWPs of Laurussia (gray) and Gondwana (white) from Torsvik et al. (2008). The APWPs and paleomagnetic poles are shown in Colorado (South American) Plate coordinates (Torsvik et al., 2008). The ages of the APWP mean poles are listed (in Ma). $A_{95} > 10°$ from the APWP of Gondwana have been removed for clarity. The blue circle is the Upper Choiyoi Gr. paleomagnetic pole (AMS tilt-corrected and anisotropy corrected). The yellow (red) circle is the anisotropy corrected Puesto Viejo Gr. volcanic rock paleomagnetic pole after AMS (raw) tilt-correction. The red diamond shows the Puesto Viejo Gr. volcaniclastic rock paleomagnetic pole after AMS tilt-correction. The orange (yellow) diamond shows the same volcaniclastic rock pole after applying an anisotropy correction of $f = 0.8$ ($f = 0.71$). Select A_{95} are shown. (b) Same as in panel (a), but comparing the new paleomagnetic poles against the "global" APWP of Torsvik et al. (2008), in Colorado Plate coordinates. (c) Comparison of the new paleomagnetic poles with an inclination-corrected ($f = 0.54$) APWP for Laurentia (Domeier et al., 2011a), rotated into Colorado Plate coordinates according to Torsvik et al. (2008).

the APWPs when the continents are correctly restored. The paleomagnetic results from the Puesto Viejo Gr. volcaniclastic rocks offer an example of such effects. If the volcaniclastic rock ChRMs are not corrected for inclination shallowing, the resulting paleopole has a very high latitude, far from the global APWP (Fig. 3.13). The A_{95} of this paleopole overlaps the 245 Ma mean pole of the Gondwanan APWP. With the application of increasing inclination corrections (decreasing f), the latitude of the paleopole decreases and it moves toward the global APWP. Using the minimum (ATRM-determined) f-correction ($f = 0.8$), the paleopole remains close to the APWP of Gondwana, but using $f = 0.71$, the paleopole is in better accord with the global APWP. From this example, it is clear how systemic inclination shallowing, if unrecognized or under-corrected, could artificially shift the entire APWP of Gondwana away from the APWP of Laurussia. Such a systemic bias is plausible because the effects of inclination shallowing can be impossible to recognize in the absence of anisotropy measurements, robust directional analysis, or complementary igneous-based paleomagnetic results.

Although a thorough analysis of Pangea reconstructions is beyond the limitations of the present study, the proximity of our new Late Permian and Early–Middle Triassic paleopoles to the global APWP of Torsvik et al. (2008) implies that an A-type Pangea configuration may be viable for this time. This finding concurs with several other recent studies from both Gondwana (Brandt et al., 2009; Domeier et al., 2011b) and Laurussia (Meijers et al., 2010; Dominguez et al., 2011; Yuan et al., 2011; Domeier et al., 2011a), which collectively show the APWPs of Gondwana and Laurussia (in an A-type reconstruction) to be converging through the progressive introduction of new, high-fidelity paleomagnetic data, and the retroactive correction of older results (Fig. 3.13c). The obvious implication common to these studies is

that alternative Pangea reconstructions and/or non-dipole paleomagnetic fields do not need to be invoked in order to accommodate the late Paleozoic–early Mesozoic paleomagnetic data from Laurussia and Gondwana, because the APWP discrepancy may simply be a manifestation of systemic bias in previous paleomagnetic results.

3.12 Conclusions

SHRIMP U-Pb and ^{40}Ar-^{39}Ar isotopic dating has confirmed earlier age assignments of Late Permian (∼264 Ma) for the Upper Choiyoi Gr. and Early–Middle Triassic (∼245 Ma) for the Puesto Viejo Gr. Zircons from the Puesto Viejo Gr. volcanic rocks are associated with lithic fragments and are interpreted to be assimilates derived from Permian rocks during ascent and eruption of Puesto Viejo magma; their mid-to-Late Permian SHRIMP U-Pb dates do not reflect the age of Puesto Viejo Gr. volcanism.

Field stability tests demonstrate that the ChRMs of the Upper Choiyoi Gr. and Puesto Viejo Gr. volcanic rocks are essentially primary. Field stability tests applied to the Puesto Viejo Gr. volcaniclastic rocks were inconclusive, but the ChRM is interpreted to be a primary DRM. Magnetic fabrics were used to discriminate between primary and secondary bedding attitudes, which ultimately improved the co-axiality of the tilt-corrected Upper Choiyoi Gr. and Puesto Viejo Gr. ChRMs. Magnetic anisotropy measurements were further utilized to correct for bias in the magnetization directions due to magnetic refraction (in the volcanic rocks) and inclination shallowing (in the volcaniclastic rocks). Rock magnetic experiments have been used to characterize the magnetic carriers, which are identified as (titano)magnetite and hematite.

The paleomagnetic poles derived from the Upper Choiyoi Gr. and Puesto Viejo Gr.

volcanic rocks fall between the APWPs of Laurussia and Gondwana, near the global APWP of Torsvik et al. (2008). This implies that the Late Permian–Middle Triassic APWP of Gondwana is biased by low-fidelity data and that its long-recognized separation from the APWP of Laurussia may be an artifact of such data. The paleomagnetic data derived from the Puesto Viejo Gr. volcaniclastic rocks serve as an illustration of this argument, in exhibiting relatively shallow inclinations that we interpret to be a consequence of sedimentary flattening of a primary DRM. A correction for the inferred shallow inclination bias results in a shift of the associated paleopole toward the global APWP of Torsvik et al. (2008). These new paleomagnetic results indicate that an A-type Pangea reconstruction may be viable during the Late Permian–Middle Triassic, and that alternative paleogeographic reconstructions and/or non-dipole paleomagnetic fields are not necessary to accommodate global paleomagnetic data at this time.

3.13 Acknowledgements

Jordan Kirshner, M. E. Woroszylo, Sonia Rousse, and Silvia Lagorio assisted in sample collection. Silvia Japas is thanked for discussions about the geology of the field area. Mike Jackson and the staff at the IRM are thanked for their help with the rock magnetic experiments, and discussions about the results. Use of the following freeware is acknowledged: Paleomac, PmagPy, Gmap, and FORCinel. Financial support for this research was provided by the Norwegian Geological Survey (NGU) and the U.S. National Science Foundation, Division of Earth Sciences (Tectonics Program), and NSF's Office of International Science and Engineering (Americas Program), grant EAR-0634807, and is gratefully acknowledged. Additional funding was provided by PIP CONICET 11220080102828, UBACYT X220, and an IRM

visiting fellowship. E. Tohver acknowledges funding from the Australian Research Council (LP0991834) and use of the UWA-Curtin joint facilities for imaging (Centre for Microscopy, Characterization and Analysis) and U-Pb SHRIMP II facility at the John de Laeter Centre for Geochronology.

Table 3.1: Summary of new ^{40}Ar-^{39}Ar geochronology data from the San Rafael Block.

Sample	Type	J-value	Steps (T/OP)	^{39}Ar(%)	Spec.	2σ	Iso.	2σ	MSWD	^{40}Ar/^{36}Ar	2σ
Upper Choiyoi Gr.											
PV01d-2	P (K-sp)	0.005892	1 to 12 (441 - 1276°C)	99.6	255.677 (PA)	2.2	255.84	2.2	1.8	295.0	18.2
CCH	I (WR)	0.001619	1 to 4 (2.0 - 3.5 W)	78.3	239.497 (WMA)	7.0	240.66	13.8	19.2	283.1	208.4
RA03d	I (Bio)	0.005967	8 to 16 (786 - 1154°C)	62.3	260.677 (PA)	2.1	258.08	4.2	0.4	404.5	147.2
Puesto Viejo Gr.											
PV04d	I (K-sp)	0.001710	2 to 7 (2.5 - 5.4 W)	95.8	235.351 (PA)	2.3	235.78	3.2	1.2	252.9	177.4
PV06d	I (WR)	0.001636	1 to 3 (2.0 to 3.0 W)	90.2	203.326 (WMA)	13.1					
PV30d	I (WR)	0.001618	2 to 6 (2.5 - 4.5 W)	89.6	138.915 (WMA)	4.3	144.70	3.2	2.1	235.7	25.9
PV09d	B (Amp)	0.001630	2 to 4 (3.0 - 4.0 W)	69.9	238.648 (PA)	2.8	233.57	11.2	0.3	357.2	127.3
PV09d	B (K-sp)	0.001626	1 to 4 (2.0 - 3.5 W)	51.2	239.329 (PA)	3.2	239.55	3.1	0.4	259.5	77.0
PV40d	V (Bio)	0.001625	3 to 5 (3.0 - 4.0 W)	68.0	254.689 (PA)	5.0	255.10	5.0	0.0	274.5	99.5
PV40d	V (K-sp)	0.001630	2 to 11 (2.5 - 8.2 W)	96.3	248.573 (PA)	2.3	250.59	3.7	0.8	−260.89∗	251.1
PV02d	I (K-sp)	0.005899	7 to 13 (896 - 1276°C)	91.8	239.163 (PA)	2.0	240.54	2.8	0.6	200.9	120.2

Type = rock: volcanic (P)orphyry, (I)gnimbrite, (B)asalt, (V)olcaniclastic rock / separates: K-sp (K-feldspar), (Bio)tite, (Amp)ibole, WR (Whole rock)
Steps = heating steps used in spectrum date. Extraction by oven in °C or extraction by CO_2 laser in (W)atts
Spec. = spectrum date (PA: plateau, WM: weighted mean). Iso. = inverse isochron date
2σ errors on dates include uncertainties in J-value, age of the flux monitors, and decay constants
∗ ^{40}Ar/^{36}Ar value is meaningless due to very tight clustering.

Table 3.2: Puesto Viejo Gr. site-mean paleomagnetic data

Site	Type	N/n/v	Dg	Ig	Ds	Is	α_{95}	k	Strike	Dip	AMS	Slat	Slon	$Plat_1$	$Plon_1$	A_{95}	$Plat_2$	$Plon_2$	A_{95}
Cuesta de los Terneros																			
PV38	I	9/9/9	330.3	−58.2	325.2	−43.7	1.7	926.4	42	15	P	34° 43.689’	68° 28.723’	58.7	209.0	2.1	66.0	182.8	2.5
PV39	I	10/10/10	332.4	−57.6	326.9	−43.3	2.9	285.1	42	15	P	34° 43.795’	68° 28.706’	60.0	210.9	3.6	67.6	184.4	4.3
PV22	B	7/7/7	343.2	−59.8	22.9	−60.6	3.3	338.0	185	22	S	34° 42.499’	68° 34.453’	70.8	49.2	5.0	70.8	49.2	5.0
PV20	I	9/8/2	305.2	−36.1	318.6	−53.9	3.8	252.2	185	22	S	34° 42.505’	68° 34.447’	56.2	189.8	5.3	56.2	189.8	5.3
PV21	I	10/10/10	304.9	−37.1	318.8	−54.9	1.9	631.1	185	22	S	34° 42.540’	68° 34.400’	56.5	188.1	2.7	56.5	188.1	2.7
PV24	I	12/11/3	315.2	−44.3	337.0	−58.5	3.3	223.1	185	22	S	34° 42.467’	68° 34.298’	71.1	180.9	4.9	71.1	180.9	4.9
PV23	I	7/7/7	313.7	−43.3	334.3	−58.1	3.8	254.8	185	22	S	34° 42.484’	68° 34.265’	69.1	182.7	5.6	69.1	182.7	5.6
PV25	I	5/5/2	311.7	−43.2	331.8	−58.6	2.7	1081.5	185	22	S	34° 42.541’	68° 34.220’	67.1	181.5	4.0	67.1	181.5	4.0
PV03	I	17/12/6	314.4	−42.9	334.9	−57.5	3.9	234.4	185	22	S	34° 42.541’	68° 34.220’	69.6	184.5	5.7	69.6	184.5	5.7
PV26	I	7/7/5	307.8	−61.8	356.5	−75.0	3.1	395.8	185	22	S	34° 42.395’	68° 34.158’	62.8	115.0	5.7	62.8	115.0	5.7
PV04	I	8/8/7	135.5	48.2	161.2	61.8	6.8	67.7	185	22	S	34° 42.542’	68° 34.161’	−73.2	346.2	10.5	−73.2	346.2	10.5
Cong.	low-T	21/12/12	7.8	−42.1	1.0	−28.0	29.3	3.2	165	15	–	34° 42.317’	68° 33.988’			$R = 8.52$			
Cong.	high-T	21/20/20	157.8	−69.1	186.7	−85.4	71.7	1.2	165	15	–	34° 42.317’	68° 33.988’			$R = 3.98$			
Atuel River area																			
PV37	*T*	*5/0/0*	–	–	–	–	–	–	210	10	*S*	*34° 49.693’*	*68° 27.944’*	–	–	–	–	–	–
PV36	S	8/8/6	342.0	−53.9	353.6	−60.7	3.6	251.3	210	10	S	34° 49.693’	68° 27.944’	81.5	145.8	5.5	81.5	145.8	5.5
PV35	S	7/7/7	352.6	−54.8	6.1	−59.9	4.2	208.9	210	10	S	34° 49.713’	68° 27.926’	82.3	74.4	6.3	82.3	74.4	6.3
PV34	S	7/7/7	6.6	−38.0	14.4	−41.3	3.8	253.0	210	10	S	34° 49.713’	68° 27.926’	73.3	343.8	4.6	73.3	343.8	4.6

PV07	I	7/7/7	150.9	56.5	173.6	64.8	3.9	242.5	195	15	S	34° 49.698’	68° 27.873’	−77.2	311.6	6.3	−77.2	311.6	6.3
PV06	I	12/10/10	153.0	55.5	175.1	63.4	3.5	187.2	195	15	S	34° 49.698’	68° 27.873’	−79.2	310.4	5.5	−79.2	310.4	5.5
PV33	S	6/4/4	358.4	−49.4	9.8	−53.8	10.8	110.8	210	10	S	34° 49.729’	68° 27.905’	81.9	20.9	15.1	81.9	20.9	15.1
PV32	*S*	*6/5/0*	60.8	11.6	58.6	16.6	–	–	210	10	*S*	*34° 49.729’*	*68° 27.905’*	–	–	–	–	–	–
PV16	S	10/10/5	178.8	62.5	178.8	62.5	7.8	40.9	224	<5	P	34° 49.534’	68° 27.433’	−80.9	297.0	12.2	−80.9	297.0	12.2
PV17	S	10/10/8	175.1	50.3	175.1	50.3	3.6	184.6	224	<5	P	34° 49.534’	68° 27.433’	−84.4	62.7	4.8	−84.4	62.7	4.8
PV18	S	9/7/7	188.0	54.1	188.0	54.1	8.0	57.7	224	<5	P	34° 49.534’	68° 27.433’	−83.4	202.1	11.2	−83.4	202.1	11.2
PV19	*T*	*10/8/8*	322.5	−72.7	322.5	−72.7	67.8	1.6	224	<5	*P*	*34° 49.534’*	*68° 27.433’*	–	–	–	–	–	–
PV15	*T*	*7/6/6*	311.7	−55.4	311.7	−55.4	50.7	2.7	224	<5	*P*	*34° 49.534’*	*68° 27.433’*	–	–	–	–	–	–
Valle Grande area																			
PV10	I	8/8/8	165.6	71.2	171.4	66.7	3.4	261.2	105	≤5	P	34° 53.486’	68° 32.285’	−74.3	312.6	5.6	−66.9	312.4	5.9
PV28	I	9/9/9	108.9	68.1	177.6	69.0	4.5	132.7	145	25	S	34° 53.662’	68° 31.854’	−72.3	296.3	7.6	−72.3	296.3	7.6
PV29	I	9/8/8	163.7	70.4	176.3	68.7	7.6	53.6	150	≤5	P	34° 53.629’	68° 31.751’	−72.6	299.1	12.9	−67.3	316.4	13.1
PV30	I	10/8/8	165.3	68.5	164.4	63.5	4.5	155.9	70	≤5	P	34° 53.629’	68° 31.751’	−74.3	336.2	7.1	−70.1	318.9	7.6
PV27	S	10/10/10	163.3	56.5	171.7	54.7	5.7	64.3	150	6	P	34° 53.552’	68° 31.693’	−83.2	16.2	8.1	−76.3	7.4	8.2
PV08	B	7/7/1	186.9	67.7	178.6	64.3	5.3	172.3	45	≤5	P	34° 53.269’	68° 32.930’	−78.7	296.4	8.5	−73.5	275.9	8.9
PV31	B	9/9/9	31.8	−62.7	348.9	−66.6	5.3	96.6	0	20	S	34° 53.184’	68° 33.073’	73.6	137.9	8.7	73.6	137.9	8.7
PV09	B	10/10/10	348.4	−67.9	342.7	−63.6	5.9	68.0	45	≤5	P	34° 53.113’	68° 33.044’	73.3	158.2	9.3	71.9	135.5	9.9
PV40	S	9/9/9	173.8	62.3	178.0	55.8	2.7	354.1	107	7	P	34° 53.326’	68° 31.911’	−87.8	339.1	3.9	−80.1	318.4	4.2
PV41	S	7/7/7	178.2	57.6	181.1	50.9	3.0	417.4	107	7	P	34° 53.301’	68° 31.897’	−86.6	127.4	4.1	−86.4	314.3	4.4
PV42	S	8/7/7	176.0	56.7	179.1	50.1	2.9	438.8	107	7	P	34° 53.326’	68° 31.911’	−85.9	100.6	3.9	−86.0	343.9	4.2

PV43	S	7/7/7	170.3	58.0	174.4	51.6	4.4	193.3	107	7	P	34° 53.326’	68° 31.911’	−84.6	49.4	6.0	−81.4	352.7	6.5
PV44	S	7/5/5	343.0	−54.4	347.6	−48.4	8.1	90.9	107	7	P	34° 53.240’	68° 31.892’	78.2	225.7	10.6	76.1	196.4	11.4
Old Puesto area																			
PV14	I	10/9/9	11.9	−58.2	11.9	−58.2	4.7	119.1	0	0	S	34° 53.735’	68° 25.604’	79.7	47.8	6.9	79.7	47.8	6.9
PV13	*T*	*5/0/0*	–	–	–	–	–	–	310	40	*S*	*34° 53.832’*	*68° 25.708’*	–	–	–	–	–	–
PV12	*T*	*5/0/0*	–	–	–	–	–	–	310	40	*S*	*34° 53.860’*	*68° 25.723’*	–	–	–	–	–	–
PV11	I	11/9/6	24.5	−14.7	14.9	−52.5	8.7	53.3	310	40	S	34° 53.857’	68° 25.741’	77.5	17.5	12.0	77.5	17.5	12.0
PV02	I	13/11/10	19.9	−29.9	355.5	−64.8	7.6	52.6	310	40	S	34° 53.870’	68° 25.761’	77.7	126.2	12.2	77.7	126.2	12.2

Merged sites																	
PV38-39	19/19/19	331.4	−57.9	326.1	−43.5	1.6	434.9	42	15	P	59.4	210.0	2.0	66.8	183.6	2.4
PV20-21	19/18/12	305.1	−36.7	318.8	−54.5	1.6	458.7	185	22	S	56.4	188.8	2.3	56.4	188.8	2.3
PV03,23-25	41/35/18	313.8	−43.7	334.8	−58.4	1.5	309	185	22	S	69.4	181.7	2.2	69.4	181.7	2.2
PV06-07	19/17/17	150.9	56.5	173.6	64.8	3.9	242.5	195	15	S	−77.2	311.6	6.3	−77.2	311.6	6.3

Merged post-tilt		**Ds_1**	**Is_1**	α_{95}	**k_1**	**Ds_2**	**Is_2**	α_{95}	**k_2**							
PV10,28-29	26/25/25	175.1	69.9	3.0	93.9	–	–	–	–		−70.8	300.3	5.2	–	–	–
PV10,29-30	27/24/24	–	–	–	–	164.2	70.0	2.9	110.2		–	–	–	−68.0	316.7	5.0
PV09,31	19/19/19	345.4	−65.0	3.8	79.5	349.3	−66.9	3.8	83.5		73.7	149.2	6.1	73.4	136.4	6.3

Anisotropy corr.	**Type**	**Di**	**Ii**	**Dc**	**Ic**	α_{95}			**$Plat_1$**	**$Plon_1$**	**A_{95}**	**$Plat_2$**	**$Plon_2$**	**A_{95}**
PV38-39	ATRM	331.4	−57.9	333.2	−61.5	1.6			60.8	205.4	2.1	67.8	172.7	2.5
PV20-21	ATRM	318.8	−54.5	319.9	−56.6	1.6			57.7	185.2	2.3	57.7	185.2	2.3

PV03,23-25	ATRM	334.8	−58.4	335.3	−60.2	1.5				69.6	175.8	2.3	69.6	175.8	2.3
PV40	ATRM	173.8	62.3	174.5	67.6	2.7				−73.9	304.2	4.5	−82.8	294.5	4.1
PV41	ATRM	178.2	57.6	179.2	63.1	3.0				−80.3	294.8	4.7	−87.1	247.1	4.3
PV42	ATRM	176.0	56.7	176.7	62.3	2.9				−80.9	306.8	4.5	−88.7	277.9	4.1
PV43	ATRM	170.3	58.0	170.4	63.5	4.4				−77.5	324.3	7.0	−85.4	342.8	6.4
PV44	ATRM	343.0	−54.4	342.3	−59.9	8.1				74.9	173.3	12.2	80.1	200.4	11.3

Final results	**N**	**Ds$_1$**	**Is$_1$**	α_{95}	**k$_1$**	**Ds$_2$**	**Is$_2$**	α_{95}	**k$_2$**	**Plat$_1$**	**Plon$_1$**	**A$_{95}$**	**Plat$_2$**	**Plon$_2$**	**A$_{95}$**
Volcanic rocks	14	350.8	−63.0	5.6	51.8	353.1	−64.7	5.0	63.8	−77.8	322.4	7.8	−76.7	312.4	7.3
Volcaniclastic rocks	13	360.0	−53.6	3.8	118.4	358.2	−56.4	4.1	103.3	−89.7	95.2	4.4	−87.0	325.0	4.9
(f=0.8 corrected)	13	0.0	−59.4	3.5	144.2	358.3	−61.9	3.7	129.9	−84.3	292.2	4.3	−81.2	301.0	4.8
(f=0.71 corrected)	13	0.1	−62.3	3.2	168.2	358.4	−64.6	3.4	150.0	−80.9	291.8	4.2	−77.9	297.8	4.6

Type: rhyolitic (I)gnimbrite, (B)asalt, unwelded (T)uff, volcanicla(S)tic rock
N/n/v: (N)umber of specimens measured / (n)umber of specimens used in site-mean calculation / number of directions defined by (v)ectors
Dg(s)/Ig(s): declination/inclination in geographic (stratigraphic) coordinates
α_{95}: the radius of the 95% cone of confidence about the site mean direction. k: estimate of the Fisher (1953) precision parameter
Strike/Dip: Bedding orientation determined from field observations
AMS: Interpreted nature of bedding attitude (P = primary, S = secondary) from anisotropy of magnetic susceptibility data
Slat/Slon: site latitude/longitude. Plat$_{1(2)}$/Plon$_{1(2)}$: VGP latitude/longitude determined from raw tilt-correction (AMS interpreted corrections)
A$_{95}$: the radius of the 95% cone of confidence about the virtual geomagnetic pole
Merged sites were calculated by combining data at the sample level from multiple sites that were interpreted to represent a single cooling unit
In sites merged after tilt-correction, directions are calculated for the raw tilt-corrections (Ds$_1$/Is$_1$) and AMS tilt-corrections (Ds$_2$/Is$_2$)
Magnetization directions were corrected for anisotropy by applying the inverse ATRM tensor. Di(c)/Ii(c): initial (corrected)declination/inclination
Italicized sites were not included in the calculation of the final results

Table 3.3: Upper Choiyoi Gr. site-mean paleomagnetic data

Site	Type	Min	N/n/v	Dg	Ig	Ds	Is	α_{95}	k	Strike	Dip	AMS	Slat	Slon	$Plat_1$	$Plon_1$	A_{95}	$Plat_2$	$Plon_2$	A_{95}
Cuesta de los Terneros																				
CT03	*I*	*M*	*9/9/3*	281.0	−6.1	283.0	−5.4	22.7	5.7	100	20	*P*	*34° 40.128'*	*68° 32.701'*	-	-	-	-	-	-
CT04	*I*	*B*	*5/5/5*	25.4	−30.3	25.4	−30.3	11.4	46.2	?	?		*34° 40.178'*	*68° 32.741'*	-	-	-	-	-	-
CT02	BV	M	6/6/6	18.7	−58.2	15.8	−38.4	5.7	137.3	100	20	P	34° 40.114'	68° 32.725'	70.9	342.3	6.8	74.5	42.7	8.4
CT13[1]	I	M	6/6/6	352.0	−65.1	7.0	−52.9	3.7	325.3	126	15	P	34° 42.608'	68° 34.082'	84.1	11.4	5.1	76.2	134.8	6.0
CT13[2]	I	H	6/6/6	344.4	−69.9	5.1	−58.4	2.3	886.9	126	15	P	34° 42.608'	68° 34.082'	84.0	70.4	3.4	68.0	136.5	4.0
CT06	I	B	7/6/6	176.6	63.4	181.0	48.7	4.1	218.1	100	15	P	34° 42.333'	68° 33.987'	−84.9	120.8	5.4	−79.4	304.7	6.5
CT05	I	B	9/9/9	184.6	61.8	178.3	46.4	3.9	178.9	75	16	P	34° 42.317'	68° 33.988'	−82.9	99.2	5.0	−81.0	269.5	6.0
CT12	I	B	6/6/6	203.4	73.7	178.9	53.5	7.8	74.6	70	23	P	34° 42.317'	68° 33.988'	−88.9	57.6	10.9	−60.7	267.2	14.0
CT09	I	H	6/6/6	171.5	67.2	185.1	51.0	4.0	278.2	115	18	P	34° 42.229'	68° 33.894'	−84.7	167.7	5.4	−73.5	311.0	6.6
CT07	I	B	9/9/9	162.3	66.3	174.8	51.0	3.6	209.2	105	17	P	34° 42.223'	68° 33.849'	−84.7	55.1	4.9	−70.8	329.1	5.9
CT16	T	B	7/7/7	14.3	−59.0	357.5	−67.7	4.1	217.1	320	12	S	34° 39.590'	68° 33.000'	73.9	117.1	6.9	73.9	117.1	6.9
CT17	T	B	6/5/3	5.0	−59.1	346.0	−66.2	10.3	64.6	320	12	S	34° 39.590'	68° 33.000'	72.6	144.0	16.9	72.6	144.0	16.9
CT15	T	H	5/4/1	9.9	−64.8	345.4	−72.3	5.5	299.9	320	12	S	34° 39.590'	68° 33.000'	65.2	130.2	9.7	65.2	130.2	9.7
CT18	I	M	7/6/4	331.4	−67.3	345.6	−54.4	10.1	51.2	100	15	S	34° 41.074'	68° 33.540'	78.2	196.2	14.2	78.2	196.2	14.2
CT10	I	M	8/5/5	327.1	−73.5	346.7	−60.7	10.3	56.5	100	15	P	34° 40.651'	68° 33.117'	77.4	163.4	15.7	57.3	142.3	18.5
CT14	I	M	8/8/8	332.3	−79.8	354.5	−66.1	3.3	280.6	100	15	S	34° 40.536'	68° 33.278'	75.6	126.3	5.4	75.6	126.3	5.4
Atuel River area																				
RA08	I	B	7/6/6	355.8	−65.5	3.8	−50.3	3.8	397.3	108	16	P	34° 47.756'	68° 27.250'	85.1	333.1	5.1	76.8	124.0	6.2

RA09	I	B	7/7/7	355.6	−63.4	3.2	−48.2	4.1	217.9	108	16	P	34° 47.798’	68° 27.246’	83.8	318.3	5.4	79.3	128.5	6.5
RA06	I	H	7/7/7	226.9	81.5	147.3	76.1	4.5	181.7	23	15	S	34° 51.240’	68° 30.460’	−54.9	316.1	8.3	−54.9	316.1	8.3
RA07	I	H	7/7/7	191.8	82.4	137.8	72.0	2.6	532.7	23	15	S	34° 51.240’	68° 30.460’	−54.1	330.3	4.6	−54.1	330.3	4.6
RA20	I	B	7/7/7	22.3	−53.8	6.0	−65.6	4.8	161.8	323	15	S	34° 50.018’	68° 28.175’	76.3	94.3	7.8	76.3	94.3	7.8
RA21	I	B	7/7/7	20.7	−55.1	2.8	−66.5	2.8	466.9	323	15	S	34° 49.902’	68° 28.066’	75.7	104.1	4.6	75.7	104.1	4.6
Valle Grande area																				
RA17	I	M	7/7/7	349.7	−59.1	342.6	−47.2	3.9	234.6	52	13	P	34° 53.067’	68° 34.411’	73.8	220.3	5.1	80.4	167.0	5.8
RA16	I	H	7/7/7	19.8	−56.1	6.7	−47.9	2.3	714.1	52	13	P	34° 53.067’	68° 34.411’	81.8	337.2	3.0	73.9	33.5	3.3
RA15	I	M	7/6/6	3.6	−59.8	352.8	−49.2	6.0	127.1	52	13	P	34° 52.970’	68° 34.379’	82.3	237.8	7.9	83.6	86.3	9.0
RA14	I	M	7/7/7	3.0	−59.8	352.3	−49.2	6.6	83.7	52	13	P	34° 52.970’	68° 34.379’	81.9	235.8	8.7	83.8	90.0	10.0
RA13[1]	VB	M	7/6/6	161.9	71.7	154.0	59.2	7.9	72.6	52	13	P	34° 52.970’	68° 34.379’	−68.8	359.9	11.8	−65.1	315.5	13.9
RA13[2]	VB	H	7/7/7	353.4	−66.6	343.1	−54.9	5.1	140.2	52	13	P	34° 52.970’	68° 34.379’	76.2	194.4	7.2	75.0	128.3	8.4
RA12	I	B	7/7/7	338.6	−56.8	334.6	−44.2	4.1	213.6	52	13	P	34° 52.970’	68° 34.379’	66.4	216.8	5.1	72.6	186.9	5.9
RA11	I	B	6/6/6	329.7	−55.5	327.9	−42.6	9.3	52.5	52	13	P	34° 52.970’	68° 34.379’	60.5	212.9	11.5	65.4	189.9	13.3
RA04[1]	I	M	8/8/8	347.0	−66.0	338.9	−53.8	3.8	209.5	52	13	P	34° 52.969’	68° 34.395’	72.7	197.1	5.3	73.5	143.1	6.2
RA04[2]	I	H	8/4/4	175.9	60.7	166.8	49.3	11.6	71.6	52	13	P	34° 52.969’	68° 34.395’	−77.9	40.6	15.4	−82.5	315.4	17.7
RA03[1]	I	M	9/9/9	170.7	48.9	165.3	37.2	3.4	229.8	52	13	P	34° 52.969’	68° 34.395’	−70.9	65.2	4.0	−80.7	51.7	4.5
RA03[2]	I	H	9/8/8	172.0	54.1	165.4	42.5	2.6	200.7	52	13	P	34° 52.969’	68° 34.395’	−73.7	56.7	3.2	−83.4	21.2	3.6
RA18	I	B	7/7/7	193.5	75.3	170.1	65.1	2.6	534.3	52	13	P	34° 52.989’	68° 34.756’	−75.7	319.6	4.2	−61.3	278.4	4.8
RA19	I	B	7/7/7	165.4	57.8	159.6	45.6	4.3	101.9	52	13	P	34° 52.989’	68° 34.756’	−70.9	40.0	5.5	−77.8	0.2	6.3
RA05	I	H	7/7/7	221.5	77.5	181.5	70.5	2.8	457.3	52	13	P	34° 53.052’	68° 34.804’	−70.2	288.8	4.8	−50.5	266.4	5.2

RA01	I	H	8/6/5	1.8	−57.1	349.8	−60.6	9.4	54.0	330	8	S	34° 54.173’	68° 37.003’	79.6	158.3	14.3	79.6	158.3	14.3
RA02[1]	I	M	7/5/5	177.7	64.3	160.9	67.0	13.5	33.1	330	8	S	34° 54.435’	68° 37.088’	−69.7	329.0	22.4	−69.7	329.0	22.4
RA02[2]	I	H	7/7/7	210.4	70.4	193.6	76.8	4.5	183.0	330	8	S	34° 54.435’	68° 37.088’	−59.0	280.2	8.4	−59.0	280.2	8.4
RA10[1]	I	M	7/7/7	176.1	40.7	165.5	54.9	3.3	341.2	295	17	S	34° 54.613’	68° 37.142’	−78.1	14.9	4.7	−78.1	14.9	4.7
RA10[2]	I	H	7/5/5	170.6	46.3	155.5	59.1	12.3	39.5	295	17	S	34° 54.613’	68° 37.142’	−70.0	359.8	18.4	−70.0	359.8	18.4
Rio Seco los Leones																				
SL01	*I*	*M*	*6/6/0*	297.3	16.6	293.7	−2.6	-	-	149	20	*P*	*35° 12.142’*	*68° 19.560’*	-	-	-	-	-	-
SL03	I	H	7/7/7	136.7	63.9	173.2	58.8	2.1	473.5	141	20	P	35 12.083’	68° 19.613’	−83.1	341.1	3.1	−55.9	350.5	3.3
SL02	I	B	6/5/5	142.0	65.1	189.6	76.2	5.9	182.0	198	19	P	35 12.011’	68° 19.572’	−60.7	283.0	10.9	−59.4	347.0	9.5
SL04	I	B	7/7/7	152.3	69.4	193.2	67.1	2.8	806.7	165	16	P	35 12.492’	68° 18.954’	−72.5	262.4	4.6	−63.6	330.6	4.8
SL05	*VB*	*H*	*7/7/4*	207.6	36.7	212.7	24.4	41.0	3.1	155	15	*P*	*35° 12.484’*	*68° 18.865’*	-	-	-	-	-	-
Averaged site means																				
RA08-09			14/13/13	355.6	−64.3	3.4	−49.1	2.6	281.5	108	16	P			84.4	322.8	3.4	78.3	126.7	4.2
RA20-21			14/14/14	21.5	−54.4	4.5	−66.0	2.5	253.6	323	15	S			76.1	99.1	4.1	76.1	99.1	4.1
RA14-15			14/13/13	3.3	−59.8	352.5	−49.2	4.0	108.1	52	13	P			82.1	236.7	5.3	83.7	88.1	6.0

Anisotropy corrected	**Type**	**Di**	**Ii**	**Dc**	**Ic**	α_{95}			**Plat$_1$**	**Plon$_1$**	**A$_{95}$**	**Plat$_2$**	**Plon$_2$**	**A$_{95}$**
CT13	AMS	352.0	−65.1	352.0	−68.8	3.7			82.4	41.5	5.3	71.6	127.1	6.3
CT06	AMS	176.6	63.4	176.6	65.0	4.1			−86.2	126.9	5.5	−77.4	302.2	6.6
CT05	AMS	184.6	61.8	184.6	63.7	3.9			−84.3	92.7	5.1	−78.8	274.5	6.2
CT07	AMS	162.3	66.3	162.3	68.9	3.6			−86.6	31.7	5.0	−68.3	321.6	6.1

RA20-21		AMS	4.5	−66.0	4.5	−68.1	2.5		73.3	101.7	4.2	73.3	101.7	4.2
RA17		AMS	349.7	−59.1	349.7	−60.4	3.9		74.1	216.4	5.1	79.6	159.7	5.9
RA14-15		AMS	3.3	−59.8	3.3	−61.3	4.0		82.5	226.7	5.4	82.1	93.5	6.2
RA13		AMS	161.9	71.7	161.9	72.4	7.9		−68.6	357.8	11.9	−64.2	313.9	14.0
RA18		AMS	193.5	75.3	193.5	75.9	2.6		−74.9	319.4	4.2	−60.4	279.2	4.8
RA19		ATRM	165.4	57.8	168.6	64.5	4.3		−73.7	22.3	5.9	−75.7	324.9	6.9
RA10		AMS	165.5	54.9	165.5	57.3	3.3		−78.0	2.7	4.8	−78.0	2.7	4.8

Final results	**N**	**Ds$_1$**	**Is$_1$**	α_{95}	**k$_1$**	**Ds$_2$**	**Is$_2$**	α_{95}	**k$_2$**	**Plat$_1$**	**Plon$_1$**	**A$_{95}$**	**Plat$_2$**	**Plon$_2$**	**A$_{95}$**
B	14	352.4	−58.2	6.3	40.2	349.0	−66.9	4.2	89.1	−82.3	334.5	7.8	−73.0	315.0	6.5
H	14	350.9	−61.4	6.5	38.8	349.5	−67.9	5.6	52.2	−78.1	326.3	8.5	−71.3	312.2	8.6
M	12	349.9	−54.8	6.5	45.8	351.0	−63.3	5.0	77.0	−81.3	8.6	7.3	−77.0	321.8	6.8
All	40	351.1	−58.3	3.6	41.4	349.8	−66.2	2.7	69.6	−81.0	340.2	4.4	-73.7	315.6	4.1

Type: I = dacitic to rhyolitic (I)gnimbrite, (BV) Basal vitrophyre, unwelded (T)uff, (VB) Volcanic breccia
Min (interpreted mineralogic carrier): (M)agnetite, (H)ematite, (B) Coexisting and colinear magnetite and hematite components
N/n/v: (N)umber of specimens measured / (n)umber of specimens used in site-mean calculation / number of directions defined by (v)ectors
Dg(s)/Ig(s): declination/inclination in geographic (stratigraphic) coordinates
α_{95}: the radius of the 95% cone of confidence about the site mean direction. k: estimate of the Fisher (1953) precision parameter
Strike/Dip: Bedding orientation determined from field observations
AMS: Interpreted nature of bedding attitude (P = primary, S = secondary) from anisotropy of magnetic susceptibility data
Slat/Slon: site latitude/longitude. Plat$_{1(2)}$/Plon$_{1(2)}$: VGP latitude/longitude determined from raw tilt-correction (AMS interpreted corrections)
A$_{95}$: the radius of the 95% cone of confidence about the virtual geomagnetic pole
Merged sites were calculated by combining data at the sample level from multiple sites that were interpreted to represent a single cooling unit
Magnetization dirs. were corrected for anisotropy by applying the inverse ATRM tensor, or by assuming $P_{TRM} \approx P^2_{AMS}$ (see text) and tan(Ii) = tan(Ic) / P_{TRM}
Di(c)/Ii(c): initial (corrected) declination/inclination
Italicized sites were not included in the calculation of the final results

Table 3.4: San Rafael Block anisotropy of magnetic susceptibility (AMS) data

Puesto Viejo Gr.										
Site	**N**	**Km**	**L**	**F**	**P**	**T**	**K_1 D**	**K_1 I**	**K_3 D**	**K_3 I**
Cuesta de los Terneros										
PV38	6	$4.12e^{-03}$	1.002	1.019	1.022	0.780	327.7	0.8	224.3	86.4
PV39	6	$2.92e^{-03}$	1.002	1.014	1.016	0.770	29.5	4.5	232.0	85.1
PV22	5	$7.35e^{-02}$	1.004	1.007	1.011	0.267	168.2	8.7	52.9	70.2
PV20	12	$6.21e^{-03}$	1.001	1.040	1.040	0.952	203.4	7.4	94.2	68.5
PV21	13	$1.66e^{-03}$	1.005	1.050	1.056	0.804	304.1	19.1	100.6	69.3
PV24	10	$3.53e^{-03}$	1.002	1.019	1.021	0.823	260.1	15.5	115.3	71.3
PV03	18	$7.52e^{-03}$	1.001	1.044	1.044	0.965	297.2	18.3	94.7	70.3
PV26	13	$6.33e^{-04}$	1.001	1.009	1.010	0.717	355.7	12.8	122.4	69.2
Atuel River area										
PV37	5	$9.06e^{-05}$	1.002	1.007	1.008	0.615	206.3	15.5	54.7	72.5
PV36	7	$8.77e^{-05}$	1.006	1.013	1.020	0.335	130.8	2.8	228.5	70.0
PV34	6	$2.84e^{-05}$	1.010	1.028	1.037	0.477	314.8	15.4	95.6	70.4
PV33	5	$5.65e^{-05}$	1.005	1.012	1.017	0.404	339.5	11.3	130.0	77.1
PV32	5	$2.08e^{-05}$	1.017	1.002	1.019	−0.804	332.8	10.4	198.0	75.4
PV16	5	$1.67e^{-04}$	1.001	1.009	1.010	0.745	83.2	5.6	324.1	78.6
PV17	7	$1.76e^{-04}$	1.002	1.006	1.008	0.547	264.1	8.2	128.3	78.7
PV18	5	$1.78e^{-04}$	1.001	1.006	1.008	0.613	329.1	6.8	113.4	81.6
PV15	11	$1.89e^{-04}$	1.000	1.002	1.002	0.669	100.7	10.5	256.3	78.4
Valle Grande area										
PV28	18	$5.96e^{-05}$	1.002	1.000	1.002	−0.776	148.2	26.9	13.8	54.1
PV31	5	$3.50e^{-02}$	1.006	1.020	1.026	0.550	86.6	22.5	291.3	65.5
PV09	9	$2.80e^{-02}$	1.011	1.008	1.019	−0.181	132.7	3.3	248.1	82.3
PV40	6	$1.55e^{-04}$	1.006	1.007	1.013	0.131	183.1	12.6	352.7	77.2
PV41	5	$1.83e^{-04}$	1.005	1.011	1.016	0.355	187.2	2.2	290.9	80.8
PV42	5	$1.66e^{-04}$	1.003	1.010	1.013	0.513	193.0	4.9	337.0	83.9
PV44	5	$1.87e^{-04}$	1.004	1.022	1.025	0.716	186.4	6.6	339.6	82.6
Old Puesto area										
PV14	7	$9.32e^{-04}$	1.001	1.013	1.015	0.836	137.4	4.3	333.2	85.5
PV11	9	$9.44e^{-05}$	1.001	1.007	1.008	0.708	38.3	48.4	215.8	41.6
PV02	9	$6.44e^{-04}$	1.001	1.003	1.004	0.535	23.4	36.3	220.9	52.4
Averaged Results										
PV38-39	12	$3.52e^{-03}$	1.001	1.017	1.018	0.887	351.6	2.3	227.9	85.8
PV03,20-26	66	$3.70e^{-03}$	1.001	1.033	1.034	0.931	304.3	18.6	99.9	69.7
PV32-37	28	$5.58e^{-05}$	1.008	1.011	1.019	0.193	326.2	9.0	120.9	80.1
PV15-18	28	$1.80e^{-04}$	1.001	1.005	1.006	0.774	271.3	0.7	129.8	89.1
PV40-44	21	$1.72e^{-04}$	1.004	1.013	1.017	0.518	186.2	6.5	332.6	82.2
PV02,11	18	$3.30e^{-04}$	1.001	1.005	1.006	0.664	31.1	44.4	217.5	45.5

Upper Choiyoi Gr.										
Site	**N**	**Km**	**L**	**F**	**P**	**T**	**K_1 D**	**K_1 I**	**K_3 D**	**K_3 I**
Cuesta de los Terneros										
CT03	7	$2.78e^{-04}$	1.019	1.021	1.040	0.040	185.3	18.3	345.2	70.6
CT04	5	$2.47e^{-03}$	1.005	1.004	1.001	−0.092	46.6	47.2	185.5	34.9
CT02	6	$8.27e^{-03}$	1.004	1.005	1.092	0.024	118.7	18.6	258.3	66.2
CT13	5	$8.28e^{-05}$	1.009	1.083	1.093	0.791	212.5	9.0	53.2	80.4
CT06	5	$9.65e^{-05}$	1.006	1.030	1.036	0.678	209.9	2.4	79.9	86.2
CT05	5	$1.21e^{-04}$	1.004	1.037	1.041	0.785	59.9	3.8	280.6	85.0
CT12	6	$2.04e^{-05}$	1.004	1.002	1.006	−0.286	235.0	14.3	347.5	56.3
CT09	5	$6.22e^{-05}$	1.004	1.081	1.086	0.890	206.5	7.4	0.4	81.8
CT07	9	$1.29e^{-04}$	1.004	1.062	1.067	0.862	163.3	3.8	26.2	84.9
CT17	7	$3.80e^{-05}$	1.001	1.001	1.002	0.196	50.7	6.2	299.8	73.1

CT18	7	$8.01e^{-05}$	1.004	1.005	1.009	0.106	273.7	13.2	172.2	40.3
CT14	8	$1.40e^{-04}$	1.006	1.002	1.008	−0.529	298.7	6.7	195.1	63.4
Atuel River area										
RA08	6	$1.31e^{-04}$	1.002	1.011	1.013	0.631	94.7	3.4	317.9	85.3
RA09	6	$2.25e^{-04}$	1.003	1.017	1.021	0.674	253.9	5.2	94.7	84.4
RA06	5	$2.81e^{-05}$	1.006	1.004	1.008	0.077	37.4	4.3	291.3	75.0
RA07	6	$5.56e^{-05}$	1.002	1.005	1.007	0.488	162.3	9.5	296.4	76.5
RA20	7	$4.25e^{-05}$	1.009	1.043	1.053	0.634	40.9	12.7	245.8	76.0
Valle Grande area										
RA17	5	$1.65e^{-04}$	1.005	1.022	1.027	0.655	271.9	1.2	41.7	88.1
RA16	7	$2.30e^{-05}$	1.007	1.036	1.043	0.679	206.9	5.9	16.1	84.0
RA14	6	$4.77e^{-05}$	1.003	1.028	1.032	0.790	64.0	8.7	285.0	78.6
RA13	5	$4.97e^{-05}$	1.002	1.019	1.021	0.789	50.5	2.0	305.8	82.1
RA12	7	$3.73e^{-05}$	1.001	1.001	1.001	−0.459	231.3	48.9	137.1	3.6
RA11	6	$3.64e^{-05}$	1.001	1.001	1.001	0.362	185.6	8.7	282.1	36.5
RA18	6	$3.32e^{-05}$	1.006	1.016	1.023	0.425	38.2	8.2	274.9	75.3
RA19	8	$7.03e^{-05}$	1.025	1.080	1.108	0.508	65.7	1.1	328.6	81.3
RA10	6	$1.16e^{-04}$	1.008	1.038	1.046	0.656	29.6	14.1	192.4	75.3
Rio Seco los Leones										
SL01	5	$2.97e^{-05}$	1.001	1.001	1.001	0.046	158.8	4.7	67.4	16.7
SL03	7	$1.84e^{-05}$	1.001	1.032	1.039	0.646	215.5	26.7	46.9	62.9
SL02	5	$8.74e^{-05}$	1.001	1.003	1.004	0.439	333.7	4.6	79.5	73.4
SL04	6	$3.31e^{-05}$	1.001	1.002	1.004	0.398	274.0	0.5	181.2	79.6
Averaged Results										
RA08-09	12	$1.78e^{-04}$	1.003	1.014	1.017	0.680	261.6	2.3	61.1	87.6
RA06-07	11	$4.08e^{-05}$	1.002	1.005	1.007	0.551	200.0	0.8	293.3	75.9
RA13-19	37	$6.17e^{-05}$	1.008	1.037	1.045	0.654	58.7	1.2	319.1	83.0

N: number of specimens. Km: average bulk volume susceptibility in SI units.

L (lineation): τ_{max}/τ_{int}. F (foliation): τ_{int}/τ_{min}

P (degree of anisotropy): τ_{max}/τ_{min}. T (shape factor; Jelinek, 1981): $2(\ln(\tau_{int}/\tau_{min})/\ln(\tau_{max}/\tau_{min}))$-1

$K_{1(3)}$ D/I: declination/inclination of site mean $K_{max(min)}$

Averaged results are combined sample-level data from adjacent sites with the same structural orientation and highly similar AMS

Table 3.5: Supplementary magnetic anisotropy results

					AARM					
Site	**N**	**Mrm**	**L**	**F**	**P**	**T**	**K_1 Dec**	**K_1 Inc**	**K_3 Dec**	**K_3 Inc**
PV38-39	13	$1.87e^{00}$	1.01	1.172	1.183	0.884	33.5	1.2	280.9	86.8
PV22	5	$2.63e^{00}$	1.002	1.014	1.016	0.695	13.8	26.5	209.9	62.6
PV20-24	17	$1.65e^{00}$	1.013	1.099	1.113	0.767	279.2	17.4	85.6	72.1
PV28	8	$1.51e^{-02}$	1.008	1.006	1.014	-0.103	211.4	46	32.1	44
RA19	8	$5.31e^{-01}$	1.079	1.171	1.264	0.35	64.2	4.4	310.4	79.1
					ATRM					
Site	**N**	**Mrm**	**L**	**F**	**P**	**T**	**K_1 Dec**	**K_1 Inc**	**K_3 Dec**	**K_3 Inc**
PV38-39	7	$1.89e^{00}$	1.061	1.077	1.142	0.116	134.3	10.4	299.2	79.2
PV20-24	14	$2.43e^{00}$	1.034	1.095	1.132	0.462	224.8	7.1	118.6	65.8
PV40-44	9	$1.82e^{-01}$	1.058	1.153	1.22	0.432	179.4	9.6	334.5	79.4
RA19	7	$2.70e^{00}$	1.112	1.206	1.341	0.276	134.3	2.8	343.1	86.8
					HF-AMS					
Site	**N**	**Km**	**L**	**F**	**P**	**T**	**K_1 Dec**	**K_1 Inc**	**K_3 Dec**	**K_3 Inc**
PV38-39	7	$1.05e^{-08}$	1.02	1.065	1.086	0.515	129.5	79	35.2	0.8
PV20-24	14	$4.73e^{-09}$	1.295	1.151	1.49	-0.296	47.7	73.7	142.7	1.5
PV03	4	$6.91e^{-10}$	-	-	-	-	233.5	24.6	136.4	15.1
PV28	7	$7.46e^{-09}$	1.089	1.038	1.131	-0.391	9.8	58.3	277	1.7
RA19	7	$2.22e^{-08}$	1.083	1.067	1.156	-0.102	114.8	59.3	16.5	4.9

AARM: anisotropy of anhysteretic remanent magnetization, ATRM: anisotropy of thermal remanent magnetization, HF-AMS: anisotropy of high-field magnetic susceptibility.
N: number of specimens. Mrm: average sample remanence in A/m. Km: average bulk high-field magnetic susceptibility in m^3/kg. L (lineation): τ_{max}/τ_{int}. F (foliation): τ_{int}/τ_{min}. P (degree of anisotropy): τ_{max}/τ_{min}. T (shape factor; Jelinek, 1981): $2(\ln(\tau_{int}/\tau_{min})/\ln(\tau_{max}/\tau_{min}))$-1. K_1 Dec/Inc: declination/inclination of site mean K_{max}. K_3 Dec/Inc: declination/inclination of site mean K_{min}.

References

Artabe, A. E., Morel, E. M., & Ganuza, D. G. (2007) Las floras triásicas de la Argentina. *Ameghiniana*, Publicación Especial, 11, 75-86.

Baer, E. M., Fisher, R. V., Fuller, M., & Valentine, G. (1997) Turbulent transport and deposition of the Ito pyroclastic flow: determinations using anisotropy of magnetic susceptibility. *Journal of Geophysical Research*, 102, 22,565-22,586.

Bilardello, D., & Kodama, K. P. (2010) Rock magnetic evidence for inclination shallowing in the Early Carboniferous Deer Lake Group red beds of western Newfoundland. *Geophysical Journal International*, 181, 275-289.

Bonaparte, J. F. (1982) Faunal replacement in the Triassic of South America. *Journal of Vertebrate Paleontology*, 2, 362-371.

Bowles, J., Jackson, M., Chen, A., & Solheid, P. (2009) Interpretation of low-temperature data part 1: superparamagnetism and paramagnetism. *IRM Quarterly*, 19.

Brandt, D., Ernesto, M., Rocha-Campos, A. C., & dos Santos, P. R. (2009) Paleomagnetism of the Santa Fé Group, central Brazil: Implications for the late Paleozoic apparent polar Wander path for South America. *Journal of Geophysical Research*, 114.

Briden, J. C., Smith, A. G., & Sallomy, J. T. (1971) The geomagnetic field in Permo-Triassic time. *Geophysical Journal of the Royal Astronomical Society*, 23, 101-117.

Cagnoli, B., & Tarling, D. H. (1997) The reliability of anisotropy of magnetic susceptibility (AMS) data as flow direction indicators in friable base surge and ignimbrite deposits: Italian examples. *Journal of Volcanology and Geothermal Research*, 75, 309-320.

Carvallo, C., Muxworthy, A. R., & Dunlop, D. J. (2006) First order reversal curve (FORC) diagrams of magnetic mixtures: micromagnetic models and measurements. *Physics of the Earth and Planetary Interiors*, 154, 308-322.

Cogné, J. P., (1987) TRM deviations in anisotropic assemblages of multidomain magnetite. *Geophysical Journal of the Royal Astronomical Society*, 91, 1013-1023.

Cogné, J. P. (2003) PaleoMac; a Macintosh^{TM} application for treating paleomagnetic data and making plate reconstructions. *Geochemistry, Geophysics, Geosystems*, 4.

Constable, C., & Tauxe, L. (1990) The bootstrap for magnetic susceptibility tensors. *Journal of Geophysical Research*, 95, 8383-8395.

Cortés, J. M., & Kleiman, L. E. (1999) La orogenia Sanrafaélica en los Andes de Mendoza, *XIV Congreso Geológico Argentino Actas*, 1, 31.

Creer, K. M., Embleton, B. J. J., & Valencio, D. A. (1970) Triassic and Permo-Triassic palaeomagnetic data for South America. *Earth and Planetary Science Letters*, 8, 173-178.

Creer, K. M., Mitchell, J. G., & Valencio, D. A. (1971) Evidence for a normal geomagnetic field polarity event at 263 ±5 m.y. B.P. within the late Paleozoic reversed interval. *Nature*, 233, 87-89.

De Fauw, S. L. (1993) The Pangean dicynodont Rechnisaurus from the Triassic of Argentina, in: Lucas S. G., and Morales, M. (Eds.), The nonmarine Triassic. *New Mexico Museum of Natural History and Science Bulletin*, 3, 101-105.

Domeier, M., Van der Voo, R., & Denny, F. B. (2011a) Widespread inclination shallowing in Permian and Triassic paleomagnetic data from Laurentia? Support from a shallow intrusive record and virtual geomagnetic pole distributions. *Tectonophysics*, 511, 38-52.

Domeier, M., Van der Voo, R., Tohver, E., Tomezzoli, R. N., Vizan, H., Torsvik, T. H., & Kirshner, J. (2011b) New Late Permian paleomagnetic data from Argentina refine the apparent polar wander path of Gondwana. *Geochemistry, Geophysics, Geosystems*, 12.

Dominguez, A. R., Van der Voo, R., Torsvik, T. H., Hendriks, B. W. H., Abrajevitch, A., Domeier, M., Larsen, B. T., & Rousse, S. (2011) The ∼270 Ma palaeolatitude of Baltica and its significance for Pangea models. *Geophysical Journal International*, 186, 529-550.

Domnanovich, N., & Marsicano, C. (2009) Los dicinodontes (Amniota: Terápsia) de Argentina: síntesis sobre el conocimiento actual del grupo. *Ameghiniana*, Resúmenes 46.

Dormann, J., Fiorani, D., & Tronc, E. (1997) Magnetic relaxation in fine particle systems, In: Prigogine, I., Rice, S., (Eds.) *Advances in Chemical Physics*, 98, 283-494.

Ellwood, B. B. (1982) Estimates of flow direction for calc-alkaline welded tuffs and paleomagnetic data reliability from anisotropy of magnetic susceptibility measurements: central San Juan Mountains, Southwest Colorado. *Earth and Planetary Science Letters*, 59, 303-314.

Ericsson, T., Krisnhamurthy, A., & Srivastava, B. K. (1986) Morin-transition in Ti-substituted hematite: A Mössbauer study. *Physica Scripta*, 33, 88.

Ezcurra, M. D., Lecuona, A., & Martinelli, A. G. (2010) A new basal archosauriform diapsid from the lower Triassic of Argentina. *Journal of Vertebrate Paleontology*, 30, 1433-1450.

Fisher, R. A. (1953) Dispersion on a sphere. *Proceedings of the Royal Society of London Series*, A, 217, 295-305.

González Díaz, E. P. (1972) Descripción geológica de la Hoja 27d, San Rafael. Provincia de Mendoza. *Boletín del Servicio Minero Nacional* 132, 1-127.

Gradstein, F. M., Ogg, J. G., & Smith, A. G. (2004) A geologic time scale 2004. Cambridge University Press, Cambridge, 610 pp.

Grégoire, V., Darrozes, J., Gaillot, P., Ndélec, A., & Launeau, P. (1998) Magnetite grain shape fabric and distribution anisotropy vs rock magnetic fabric: A three-dimensional case study. *Journal of Structural Geology*, 20, 937-944.

Halls, H. C. (1978) The use of converging remagnetization circles in palaeomagnetism. *Physics of the Earth and Planetary Interiors*, 16, 1-11.

Hrouda, F. (1982) Magnetic anisotropy of rocks and its application in geology and geophysics. *Geophysical Surveys*, 5, 37-82.

Incoronato, A., Addison, F. T., Tarling, D. H., Nardi, G., & Pescatore, T. (1983) Magnetic fabric investigations of pyroclastic deposits from phlegrean fields, Southern Italy. *Nature*, 306, 461-463.

Irving, E. (1977) Drift of the major continental blocks since the Devonian. *Nature*, 270, 304-309.

Irving, E. (2004) The case for Pangea B, and the intra-Pangean megashear. Timescales of the paleomagnetic field, *American Geophysical Union - Geophysical Monograph*, 145, 13-27.

Jackson, M. (1991) Anisotropy of magnetic remanence: a brief review of mineralogical sources, physical origins, and geological applications, and comparison with susceptibility anisotropy. *Pure and Applied Geophysics*, 136, 1-28.

Jacob, J., & Abdul Khadar, M. (2010) VSM and mössbauer study of nanostructured hematite. *Journal of Magnetism and Magnetic Materials*, 322, 614-621.

Japas, M. S., Salvarredi, J., & Kleiman, L. E. (2005) Self-similar behaviour of Triassic rifting in San Rafael, Mendoza, Argentina. *Gondwana XII Abstracts*, Mendoza, Argentina, 210.

Jelinek, K. (1981) Characterization of the magnetic fabric of rocks. *Tectonophysics*, 79, 63-67.

Khan, M. A. (1962) The anisotropy of magnetic susceptibility of some igneous and metamorphic rocks. *Journal of Geophysical Research*, 67, 2873-2885.

King, R. (1955) The remanent magnetism of artificially deposited sediments. *Geophysical Journal International*, 7, 115-134.

Kirschvink, J. L. (1980) The least-squares line and plane and the analysis of palaeomagnetic data. *Geophysical Journal of the Royal Astronomical Society*, 62, 699-718.

Kleiman, L. E. (2002) Magmatism and tectonic evolution of the Choiyoi and Puesto Viejo volcanics (Late Paleozoic–Early Mesozoic) at 34-35°S Latitude, San Rafael, Mendoza, Argentina. *XV Congreso Geológico Argentino, Actas II*, 15-16.

Kleiman, L. E., & Japas, M. S. (2005) The upper Choyoi volcanism, San Rafael, Mendoza, Argentina: a transitional sequence emplaced under changing geodynamic conditions. *Gondwana XII Abstracts*, Mendoza, Argentina, 211.

Kleiman, L. E., & Japas, M. S. (2009) The Choiyoi volcanic province at 34°S-36° S (San Rafael, Mendoza, Argentina): implications for the late Palaeozoic evolution of the southwestern margin of Gondwana. *Tectonophysics*, 473, 283-299.

Kleiman, L. E., & Salvarredi, J. A. (1999) Triassic bimodal volcanism in the San Rafael Massif, Mendoza: The Puesto Viejo Formation. *XIV Congreso Geológico Argentino, Actas I*, 101.

Kleiman, L. E., & Salvarredi, J. A. (2001) Petrology, geochemistry and tectonic implications of Triassic volcanism (Puesto Viejo Formation), San Rafael Massif, Mendoza. *Revista de la Asociación Geológica Argentina*, 56, 559-570.

Le Pennec, J., Chen, Y., Diot, H., Froger, J., & Gourgaud, A. (1998) Interpretation of anisotropy of magnetic susceptibility fabric of ignimbrites in terms of kinematic and sedimentological mechanisms: An Anatolian case-study. *Earth and Planetary Science Letters*, 157, 105-127.

Lee, J., Marti, K., Severinghaus, J. P., Kawamura, K., Yoo, H., Lee, J., et al. (2006) A redetermination of the isotopic abundances of atmospheric Ar. *Geochimica Et Cosmochimica Acta*, 70, 4507-4512.

Linares, E. (2007) Catálogo de edades radimétricas de la República Argentina. Años 1957-2005. *Asociación Geológica Argentina, Serie F*, Publicaciones en CD, 2.

Lucas, S. G. (1998) Global Triassic tetrapod biostratigraphy and biochronology. *Palaeogeography, Palaeoclimatology, Palaeoecology*, 143, 347-384.

Ludwig, K. R. (2003) User's manual for Isoplot/Ex, version 3.0: A geochronological toolkit for Microsoft Excel. *Special Publication 4*, Berkeley Geochronology Center,

Berkeley, CA, USA.

Martinelli, A. G. (2010) On the postcanine dentition of Pascualgnathus polanskii Bonaparte (Cynodontia, Traversodontidae) from the Middle Triassic of Argentina. *Geobios*, 43, 629-638.

Martinelli, A. G., de la Fuente, & M., Abdala, F. (2009) Diademodon tetragonus Seeley, 1894 (Therapsida: Cynodontia) in the Triassic of South America and its biostratigraphic implications. *Journal of Vertebrate Paleontology*, 29, 852-862.

McDougall, I., & Harrison, T. M. (1999) Geochronology and thermochronology by the $^{40}Ar/^{39}Ar$ method. Oxford University Press, New York, NY.

McFadden, P. L., & McElhinny, M. W. (1988) The combined analysis of remagnetization circles and direct observations in palaeomagnetism. *Earth and Planetary Science Letters*, 87, 161-172.

Meijers, M. J. M., Hamers, M. F., van Hinsbergen, D. J. J., van der Meer, D. G., Kitchka, A., Langereis, C. G., & Stephenson, R. A. (2010) New late Paleozoic paleopoles from the Donbas Foldbelt (Ukraine): Implications for the Pangea A vs. B controversy. *Earth and Planetary Science Letters*, 297, 18-33.

Melchor, R. N. (2000) Stratigraphic and biostratigraphic consequences of a new $^{40}Ar/^{39}Ar$ date for the base of the Cochico Group (Permian), eastern Permian basin, San Rafael, Mendoza, Argentina. *Ameghiniana*, 37, 271-282.

Morel, P., & Irving, E. (1981) Paleomagnetism and the evolution of Pangea. *Journal of Geophysical Research*, 86, 1858-1872.

Moskowitz, B. M., Jackson, M., & Kissel, C. (1998) Low-temperature magnetic behavior of titanomagnetites. *Earth and Planetary Science Letters*, 157, 141-149.

Muttoni, G., Gaetani, M., Kent, D. V., Sciunnach, D., Angiolini, L., Berra, F., et al. (2009) Opening of the neo-tethys ocean and the Pangea B to Pangea A transformation during the Permian. *GeoArabia*, 14, 17-48.

Muttoni, G., Kent, D. V., Garzanti, E., Brack, P., Abrahamsen, N., & Gaetani, M. (2003) Early Permian Pangea "B" to late Permian Pangea "A". *Earth and Planetary Science Letters*, 215, 379-394.

Muxworthy, A. R., & McClelland, E. (2000) Review of the low-temperature magnetic properties of magnetite from a rock magnetic perspective. *Geophysical Journal International*, 140, 101-114.

Opdyke, N. D., Roberts, J., Claoue-Long, J., Irving, E., & Jones, P. J. (2000) Base of the Kiaman: its definition and global stratigraphic significance. *Geological Society*

of America Bulletin, 112, 1315-1341.

Ort, M. H., Orsi, G., Pappalardo, L., & Fisher, R. V. (2003) Anisotropy of magnetic susceptibility studies of depositional processes in the Campanian Ignimbrite, Italy. *Bulletin of Volcanology*, 65, 55-72.

Ottone, E. G., & Garcia, G. B. (1991) A lower Triassic miospore assemblage from the Puesto Viejo Formation, Argentina. *Review of Palaeobotany and Palynology*, 68, 217-232.

Özdemir, Ö., Dunlop, D. J., & Berquó, T. S. (2008) Morin transition in hematite: size dependence and thermal hysteresis. *Geochemistry, Geophysics, Geosystems*, 9, Q10Z01.

Palmer, H. C., & MacDonald, W. D. (1999) Anisotropy of magnetic susceptibility in relation to source vents of ignimbrites: empirical observations. *Tectonophysics*, 307, 207-218.

Pioli, L., Lanza, R., Ort, M., & Rosi, M. (2008) Magnetic fabric, welding texture and strain fabric in the Nuraxi Tuff, Tardinia, Italy. *Bulletin of Volcanology*, 70, 1123-1137.

Roberts, A. P., Pike, C. R., & Verosub, K. L. (2000) First-order reversal curve diagrams: a new tool for characterizing the magnetic properties of natural samples. *Journal of Geophysical Research*, 105, 28,461-28,475.

Rocha-Campos, A. C., Basei, M. A., Nutman, A. P., Kleiman, L. E., Varela, R., Llambias, E., et al. (2011) 30 million years of Permian volcanism recorded in the Choiyoi igneous province (W. Argentina) and their source for younger ash fall deposits in the Paraná Basin: SHRIMP UPb zircon geochronology evidence. *Gondwana Research*, 19, 509-523.

Rochette, P., Jackson, M., & Aubourg, C. (1992) Rock magnetism and the interpretation of anisotropy of magnetic susceptibility. *Reviews of Geophysics*, 30, 209-226.

Rochette, P., & Vandamme, D. (2001) Pangea B: an artifact of incorrect paleomagnetic assumptions? *Annali Di Geofisica*, (1993), 44, 649-658.

Renne, P. R., Mundil, R., Balco, G., Min, K., & Ludwig, K. R. (2010) Joint determination of ^{40}K decay constants and ^{40}Ar*/^{40}K for the Fish Canyon sanidine standard, and improved accuracy for ^{40}Ar/^{39}Ar geochronology. *Geochimica Et Cosmochimica Acta*, 74, 5349-5367.

Rex, D. C. & Guise, P. G. (1995) Evaluation of argon standards with special emphasis on time scale measurements, In: Odin, G. S. (ed.) Phanerozoic Time Scale, *Bulletin*

Liaison of Information IUGS Subcommission on Geochronology, 13, 21-23.

Sepúlveda, E., Carpio, F., Regairaz, M., Zárate, M., & Zanettini, J. C. (2007) Hoja Geológica 3569 - II, San Rafael, Provincia de Mendoza. Instituto de Geología y Recursos Minerales, *Servicio Geológico Minero Argentino Bulletin*, 321, 59 pp..

Smith, A. G., & Livermore, R. A. (1991) Pangea in Permian to Jurassic time. *Tectonophysics*, 187, 135-179.

Spalletti, L. A., Merodio, J. C., Matheos, S. D., & Iñiguez Rodriguez, A. M. (1996) Petrology and geochemistry of Triassic silicoclastic sediments from the Sierra Pintada, Mendoza Province. *Revista de la Asociación Geológica Argentina*, 51, 51-60.

Stipanicic, P. N., González Díaz, E. F., & Zavattieri, A. M. (2007) Grupo Puesto Viejo nom. transl por Formación Puesto Viejo González Díaz, 19641967: nuevas interpretaciones paleontológicas, estratigráficas y cronológicas. *Ameghiniana*, 44, 759-761.

Tarling, D. H., & Hrouda, F. (1993) The magnetic anisotropy of rocks. Chapman & Hall, London, United Kingdom.

Tauxe, L., & Watson, G. S. (1994) The fold test: an eigen analysis approach. *Earth and Planetary Science Letters*, 122, 331-341.

Tauxe, L., Kodama, K. P., & Kent, D. V. (2008) Testing corrections for paleomagnetic inclination error in sedimentary rocks: a comparative approach. *Physics of the Earth and Planetary Interiors*, 169, 152-165.

Tauxe, L., Mullender, T. A. T., & Pick, T. (1996) Potbellies, wasp-waists, and superparamagnetism in magnetic hysteresis. *Journal of Geophysical Research*, 101, 571-583.

Tauxe, L., Kodama, K. P., & Kent, D. V. (2008) Testing corrections for paleomagnetic inclination error in sedimentary rocks: a comparative approach. *Physics of the Earth and Planetary Interiors*, 169, 152-165.

Terrizzano, C. M., Tomezzoli, R. N., Kleiman, L., & Salvarredi, J. (2005) Resultados paleomagnéticos preliminares sobre rocas de la Quebrada del Pimiento, Bloque de San Rafael, Provincia de Mendoza, Argentina. *XVI Congreso Geológico Argentino*, 5, 383-390.

Tomezzoli, R. N., Kleiman, L., Salvarredi, J., Terrizzano, C., & Cristallini, O. (2005) Relaciones estratigráicas de volcanitas del Choiyoi Inferior sobre la base de estudios paleomagnéticos, Bloque de San Rafael, Mendoza, Argentina. *XVI Congreso Geológico Argentino*, 1, 227-232.

Torcq, F., Besse, J., Vaslet, D., Marcoux, J., Ricou, L. E., Halawani, M., et al. (1997) Paleomagnetic results from Saudi Arabia and the Permo-Triassic Pangea configuration. *Earth and Planetary Science Letters*, 148, 553-567.

Torsvik, T. H., & Van der Voo, R. (2002) Refining Gondwana and Pangea palaeogeography: estimates of Phanerozoic non-dipole (octupole) fields. *Geophysical Journal International*, 151, 771-794.

Torsvik, T. H., Muller, R. D., Van der Voo, R., Steinberger, B., & Gaina, C. (2008) Global plate motion frames: toward a unified model. *Reviews of Geophysics*, 46, 1-44.

Valencio, D. A., & Mitchell, J. (1972) Edad potasio-argon y paleomagnetismo de rocas igneas de las Formaciones Quebrada del Pimiento y Las Cabras, provincia de Mendoza, Republica Argentina. *Asociación Geológica Argentina Revista*, 27, 170-178.

Valencio, D. A., Mendia, J. E., & Vilas, J. F. (1975) Palaeomagnetism and K-Ar ages of Triassic igneous rocks from the Ischigualasto-Ischichuca Basin and Puesto Viejo Formation, Argentina. *Earth and Planetary Science Letters*, 26, 319-330.

Van der Voo, R., & Torsvik, T. H. (2001) Evidence for late Paleozoic and Mesozoic non-dipole fields provides an explanation for the Pangea reconstruction problems. *Earth and Planetary Science Letters*, 187, 71-81.

Van der Voo, R., & Torsvik, T. H. (2004) The quality of the European Permo-Triassic paleopoles and its impact on Pangea reconstructions. Timescales of the paleomagnetic field, *American Geophysical Union - Geophysical Monograph*, 145, 29-42.

Vilas, J. F., & Valencio, D. A. (1982) Implicancias geodinámicas de los resultados paleomagneticos de formaciones asignadas al Paleozoico tardío-Mesozoico temprano del Centro-Oeste Argentino. *V Congreso Latinoamericano de Geología*, 3, 743-758.

Watson, B. E. (1996) Dissolution, growth and survival of zircons during crustal fusion: kinetic principles, geological models and implications for isotopic inheritance. *Geological Society of America Special Papers*, 315, 43-56.

Watson, G. S. (1956) A test for randomness of directions. *Monthly Notices of the Royal Astronomical Society*, Geophysical Supplement 7, 160-161.

Yuan, K., Van der Voo, R., Bazhenov, M. L., Bakhmutov, V., Alekhin, V., & Hendriks, B. W. H. (2011) Permian and Triassic palaeolatitudes of the Ukrainian shield with implications for Pangea reconstructions. *Geophysical Journal International*, 184, 595-610.

Zavattieri, A. M. & Batten, D. J. (1996) Miospores from Argentinian Triassic deposits and their potential for intercontinental correlation, In: Jansonius, J. & Mc.Gregor, D. C. (Eds.), Palynology: principles and applications. *American Association of Stratigraphic Palynologists Foundation*, 2, 767-778.

Zijderveld, J. D. A. (1967) A.C. demagnetization of rocks: analysis of results. In: D. W. Collinson, K. M. Creer and S. K. Runcorn, (Eds.), *Methods in Paleomagnetism*, Elsevier, Amsterdam. 254 pp.

CHAPTER IV

Widespread inclination shallowing in Permian and Triassic paleomagnetic data from Laurentia: Support from new paleomagnetic data from Middle Permian shallow intrusions in southern Illinois (USA) and virtual geomagnetic pole distributions

4.1 Abstract

Recent paleomagnetic work has highlighted a common and shallow inclination bias in continental redbeds. The Permian and Triassic paleomagnetic records from Laurentia are almost entirely derived from such sedimentary rocks, so a pervasive inclination error will expectedly bias the apparent polar wander path of Laurentia in a significant way. The long-standing discrepancy between the apparent polar wander paths of Laurentia and Gondwana in Permian and Triassic time may be a consequence of such a widespread data-pathology. Here we present new Middle Permian paleomagnetic data from igneous rocks and a contact metamorphosed limestone from cratonic Laurentia. The exclusively reversed Middle Permian magnetization is hosted by low-Ti titanomagnetite and pyrrhotite and yields a paleomagnetic pole at 56.3° S, 302.9° E (A_{95} = 3.8°, N = 6). This pole, which is unaffected by inclina-

Citation:
Domeier, M., Van der Voo, R., & Denny, F. B. (2011). Widespread inclination shallowing in Permian and Triassic paleomagnetic data from Laurentia: Support from new paleomagnetic data from Middle Permian shallow intrusions in southern Illinois (USA) and virtual geomagnetic pole distributions. *Tectonophysics*, 511, 38-52, doi:10.1016/j.tecto.2011.08.016.

tion shallowing, suggests that a shallow inclination bias may indeed be present in the Laurentian records. To further consider this hypothesis, we conduct a virtual geomagnetic pole distribution analysis, comparing theoretical expectations of a statistical field model (TK03.GAD) against published data-sets. This exercise provides independent evidence that the Laurentian paleomagnetic data is widely biased, likely because of sedimentary inclination shallowing. We estimate the magnitude of this error from our model results and present and discuss several alternative corrections.

4.2 Introduction

It is now well-established that depositional remanent magnetizations (DRMs) of sedimentary rocks are prone to a shallow inclination bias due to the settling and compaction of magnetized particles in the gravitational field, which may overcome the vertical torque applied to the particles by the geomagnetic field. When uncorrected, this shallow inclination bias will result in computation of a "far-sided" paleomagnetic pole, or one that is shifted (from the true location) away from the sampling site. The paleogeographic corollary is a low-latitude bias. It has been hypothesized that this bias may be a major contributing factor to the long-standing discrepancy between the Permian–Triassic segments of the apparent polar wander paths (APWPs) of Laurussia and Gondwana, when the landmasses are reconstructed in a conventional way (Rochette and VanDamme, 2001; Domeier et al., 2009). Recent paleomagnetic results from Gondwana, derived from volcanic rocks and sedimentary rocks corrected for inclination shallowing, have improved the agreement between these APWPs, thereby supporting this hypothesis (Brandt et al., 2009; Domeier et al., 2011).

Here we consider the possibility that such a shallow inclination bias may also be widely present in the Permian and Triassic paleomagnetic records from Laurentia (as

a proxy for Laurussia). After updating the compilation of paleomagnetic results from Torsvik et al. (2008), according to the 2009 geologic timescale (Walker and Geissman, 2009), the Permian-Middle Triassic (300–235 Ma) data-set from Laurentia includes only two poles derived from igneous rocks (of 37 records) (Table 4.2). The remaining 35 poles are derived from continental redbeds, which may be particularly susceptible to inclination shallowing (Kent and Tauxe, 2005; Bilardello and Kodama, 2010; Kent and Irving, 2010). To check for the presence (and magnitude) of a shallow inclination bias in these Laurentian sedimentary rock-based paleomagnetic records, we compare published data against theoretical virtual geomagnetic pole (VGP) distributions. Additionally, we present new Middle Permian paleomagnetic results from a suite of shallow intrusive rocks—impervious to sedimentary inclination shallowing—from the Illinois Basin, and thus from cratonic Laurentia. Comparison of this paleomagnetic result with data derived from coeval redbeds offers an independent means to test for a shallow inclination bias in the latter.

4.3 Background Geology for the Paleomagnetic Study

Our paleomagnetic study was conducted on a series of intrusive rocks that invade Devonian and Carboniferous sedimentary rocks in the south end of the Illinois Basin, in southern Illinois and western Kentucky (Fig. 4.1a). The sampling area lies at the junction of the Reelfoot Rift, the Rough Creek Graben, and the Cottage Grove Fault System, and is recognized as one of the most pervasively faulted regions in the mid-continent (Denny et al., 2008). This focused structural activity is likely due to a prominent weakness in the Precambrian basement that developed during a failed episode of rifting in the late Proterozoic-Early Cambrian, which may have nucleated on an even older lower crustal discontinuity (Trace and Amos, 1984; Ko-

lata and Nelson, 1997). In the late Paleozoic, a phase of N-NW compression inverted the extensional structures of the Reelfoot Rift and Rough Creek Graben, and resulted in right-lateral strike-slip displacement on the Cottage Grove Fault (Kolata and Nelson, 1997). Magmatism was broadly contemporaneous with this phase of regional shortening, and is represented by dikes that invade NW-trending tensional fractures, thin sills, diatreme-like breccias generated by the explosive release of magmatic volatiles, and the uplift of Hicks Dome and the Tolu Arch, which were elevated by intrusions in the lower crust (Fig. 4.1b; Bradbury and Baxter, 1992; Potter et al., 1995; Luczaj, 1998; Fifarek et al., 2001; Denny et al., 2008). Surface exposures, aeromagnetic surveys, and drilling/mining observations have demonstrated that this NW-SE oriented corridor of intrusions is more than 100 km long, stretching from the Tabb Fault System in Kentucky to the Cottage Grove Fault System and the Omaha Dome in Illinois (McGinnis and Bradbury, 1964; Sparlin and Lewis, 1994; Hildenbrand and Ravat, 1997; Padgett et al., 2002; Silverman et al., 2003). Although the dikes are recognized across this corridor, perhaps exploiting the structural grain of the Precambrian basement, the breccias are largely restricted to the vicinity of Hicks Dome, and most occur on the dome flanks (Denny et al., 2008).

Owing to extensive surface weathering and low-temperature alteration, compositional classification of the igneous rocks has proven difficult; the alkaline, ultramafic dikes have been variously described as lamprophyres, mica peridotites, and monticellites or alnöites (Currier, 1944; Koenig, 1956; Baxter and Desborough, 1965; Sparlin and Lewis, 1994; Denny et al., 2002; Denny et al., 2008). The dikes are fine-grained to porphyritic and commonly consist of phlogopite, pyroxene, and olivine (pseudomorphed by serpentine), with accessory apatite, titanomagnetite, garnet, perovskite, titanite, and chromite (Baxter and Desborough, 1965; Fifarek et al., 2001; Denny et

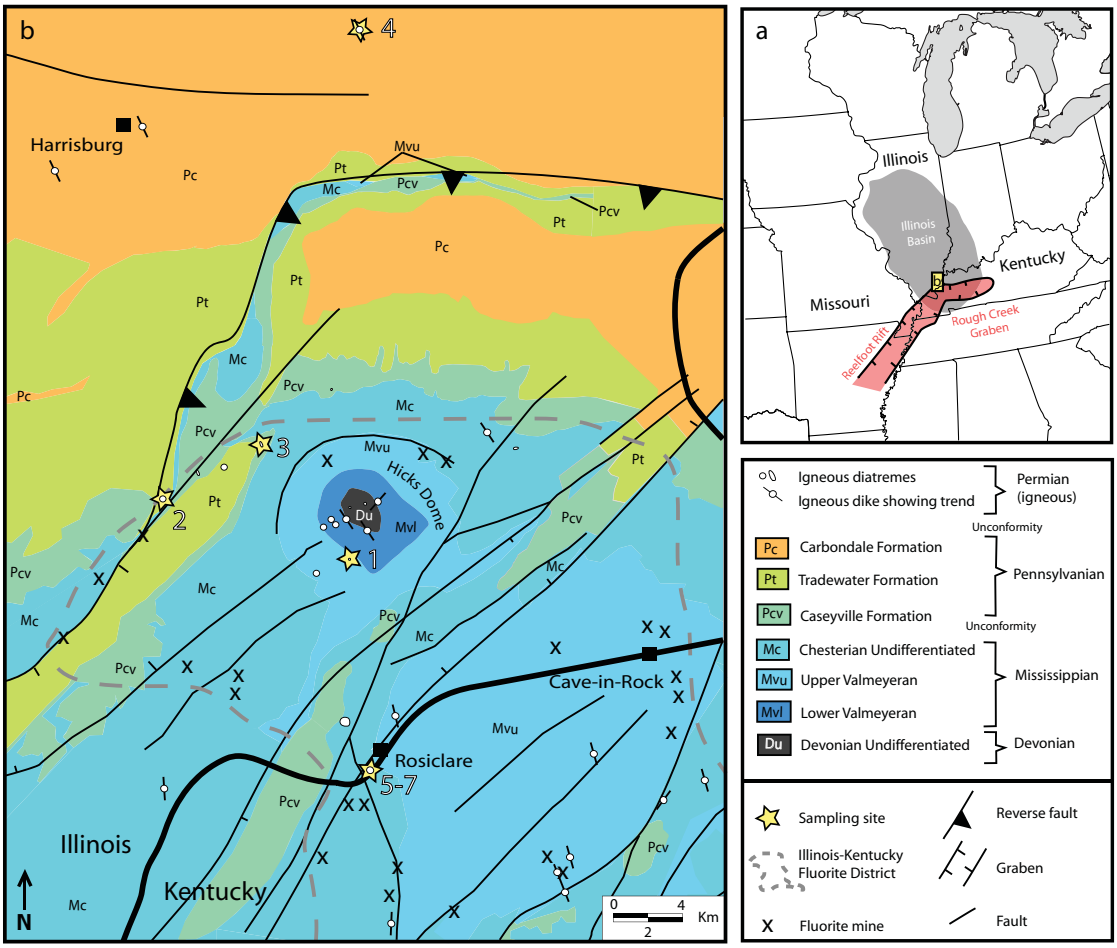

Figure 4.1: Geologic map of the southern Illinois sampling area. (a) Regional map showing the location of panel b (highlighted box). (b) Geologic map of Hicks Dome and the Illinois-Kentucky Fluorite District. Paleomagnetic sampling sites are labeled with stars and numbered: 1 = Grants Intrusive, 2 = Chamberlain Diatreme, 3 = Hart Creek Diatreme, 4 = Willow Lake Dike, 5 = Downeys Bluff Sill, 6 = Downeys Bluff Limestone (baked), 7 = Downeys Bluff Limestone (unbaked). Simplified from Denny et al. (2008).

al., 2002). Secondary carbonate and chlorite are abundant as replacement phases, in addition to serpentine. The poorly exposed and pipe-like breccia bodies at Hicks Dome have been subdivided into "shatter", "vent", and "carbonatitic" varieties, according to their intrusive morphology and the texture of matrix and clasts (Bradbury and Baxter, 1992). Shatter breccias are simply fragmented bodies of the host rock, with an absence of far-traveled or exotic clasts. Vent breccias have xenoliths from underlying sedimentary units, indicating substantial vertical clast-transport. Carbonatitic breccias contain igneous material, in addition to sedimentary clasts, and have a matrix of carbonate. Formation of the latter two breccia varieties is attributed to the explosive expansion of supercritical CO_2-charged fluids as they vaporized during ascent through crustal fractures, after being expelled from alkaline ultramafic magmas at depth (Bradbury and Baxter, 1992; Luczaj, 1998; Denny et al., 2008). The relatively high TiO_2 content and the trace element profile (elevated Zr, Sr, Zn, and REE) of the carbonatitic breccias (Bradbury and Baxter,1992; Fifarek et al., 2001) is supportive of an alkaline igneous affinity (Erickson and Blade, 1963; Heinrich, 1966).

The age of magmatism has been established as Middle Permian (∼270 Ma) on the basis of Rb-Sr, K-Ar, and ^{40}Ar-^{39}Ar geochronology. The following K-Ar and ^{40}Ar-^{39}Ar age estimates have been recalculated with the decay constants of Renne et al. (2010). Rb-Sr results have been recalculated with the decay constants of Steiger and Jaeger (1977). Zartman et al. (1967) presented biotite K-Ar dates of 255 ±13 and 272 ±13 Ma for a "mica-peridotite" dike and sill, respectively. Rb-Sr dating of the same dike and sill yielded dates of 289 ±27 Ma and 269 ±23 Ma. Grants Intrusive, a carbonatitic breccia near Hicks Dome, has yielded K-Ar dates of 261 ±13 Ma (on biotite) and 284 ±13 Ma (on hornblende). Reynolds et al. (1997) re-dated the

Grants Intrusive by the ^{40}Ar-^{39}Ar method and presented plateau age estimates of 274.5 ±0.7 Ma (on amphibole) and 275.1 ±0.7 Ma (on phlogopite). An intrusive breccia in Kentucky produced an average biotite K-Ar date of 276 ±14 Ma and a Rb-Sr date of 266 ±22 Ma (Zartman et al., 1967). Fifarek et al. (2001) presented phologopite ^{40}Ar-^{39}Ar isochron age estimates of 271.0 ±0.3 and 267.8 ±1.3 from dikes and 269.4 ±0.4 Ma from an intrusive breccia. The range of mean age determinations, after averaging the results from each intrusion, is 267.8–273.6 Ma. The average mean age of the dikes and intrusive breccias is 270.3 and 271.9 Ma, respectively, suggesting that their emplacement was essentially synchronous.

Subsequent to the late Paleozoic phase of N-NW shortening the regional stress-field again inverted, returning to a tensional regime with extension directed ∼NW-SE (Trace and Amos, 1984; Kolata and Nelson, 1997). This regime produced NE-trending, high-angle normal faults, some of which were re-activated Paleozoic structures, that cross-cut and displace the NW-trending dikes and the Tolu Arch. Due to a regional depositional hiatus extending from the Early Permian to the Late Cretaceous, the timing of this extensional episode is poorly resolved (post-Early Permian to pre-Late Cretaceous); however, it has been speculatively attributed to stresses generated by the Late Triassic–Early Jurassic breakup of Pangea (Kolata and Nelson, 1997; Denny et al., 2008). A concentrated fluorite mineralization event is spatially associated with the intrusions and normal faults at the junction of the Reelfoot Rift and the Rough Creek Graben, an area which is also known as the Illinois-Kentucky Fluorite District (Fig. 4.1b). Fluorite and other ore deposits occur in veins following the NE-trending faults and fractures, and as conformant replacement bodies in Paleozoic limestone (Baxter and Desborough, 1965). The age of the ore bodies and their relationship to the intrusions is debated, but geochemical observations have

suggested a genetic connection, as the close spatial association would imply. Specifically, gradients in fluid inclusion temperature and magmatic volatiles (Taylor et al., 1992; Plumlee et al., 1995), and trace and metallic element concentrations (Burruss et al., 1992; Goldhaber et al., 1992) in ore bodies around Hicks Dome suggest that the underlying intrusions acted as thermal and elemental sources for the mineralizing fluids. Attempts to define the age of mineralization have yielded dates of Early Permian (277.0 ±15.6 Ma by $^{147}Sm/^{144}Nd$, Chesley et al., 1994), Early Jurassic (∼200 Ma by $^{87}Sr/^{86}Sr$, Ruiz et al., 1988), Late Jurassic (∼150 Ma by paleomagnetism, Symons, 1994) and Early Cretaceous (∼138 Ma by fission track by Harder, 1987, *in* Symons, 1994). If mineralization occurred after the Middle Permian, the temperature of ore precipitation must have been lower than the closure temperature of biotite (≈ 300 °C, Hodges, 1991); otherwise the K-Ar and ^{40}Ar-^{39}Ar ages of the intrusions should have been reset at that time. Fluid inclusion homogenization temperatures in the Fluorite District range from 68 to 227 °C in hydrothermal quartz, and 116 to 153 °C in fluorite (Richardson and Pinckney, 1984; Spry et al., 1990).

Although there is evidence of more recent movement on some faults in the region—offset Quaternary deposits and recent earthquakes in the neighboring New Madrid Seismic Zone—many faults in the Fluorite District have remained inactive since pre-Late Cretaceous time (Kolata and Nelson, 1997; Denny et al., 2008).

4.4 Sampling and Laboratory Methods

Paleomagnetic samples were selectively collected from the freshest available outcrops: a carbonatitic breccia (Grants Intrusive), two vent breccias (Chamberlain Diatreme and Hart Creek Diatreme), an ultramafic dike exposed in an underground coal mine (Willow Lake Dike), and an ultramafic sill (Downeys Bluff Sill, "sill" dated

by Zartman et al., 1967), as well as samples of the Downeys Bluff Limestone baked by the sill and others distant from it (Fig. 4.1b). The paleomagnetism of Grants Intrusive and Downeys Bluff Sill/Limestone has been previously studied by Reynolds et al. (1997).

Core samples were collected from the breccias, sill, and limestone with a gasoline powered drill; the orientation of the samples was determined with magnetic and solar compasses. Block samples were collected from the underground dike, from which core specimens were drilled in the laboratory. Sample orientation readings with the magnetic compass were compared with sighted estimates away from the dike, which suggest that local declination anomalies are small ($\leq 3°$). Paleomagnetic samples were stored and processed in a magnetically shielded room with a rest field of ≤ 200 nT. Measurements of remanent magnetization were made with a three-axis 2G cryogenic magnetometer. Sister specimens from long cores were subjected to alternating field (AF) and thermal demagnetization techniques in order to determine the most effective demagnetization approach for each site. AF demagnetization was carried out according to a static 3-position procedure. Thermal demagnetization was conducted in air; samples were cooled in a magnetically shielded chamber with a typical DC field of ≤ 5 nT. Demagnetization data were analyzed with orthogonal vector diagrams and stereographic projections (Zijderveld, 1967; Cogné, 2003). Principal component analysis was used to quantitatively define magnetization vectors (Kirschvink, 1980). Fisher (1953) statistics were used to compute site mean directions from purely vectorial populations; where remagnetization circles defined some samples, the statistical approach of McFadden and McElhinny (1988) was applied.

Hysteresis measurements, conducted on a vibrating sample magnetometer, and a low-temperature remanence experiment, conducted on a magnetic properties mea-

surement system, were performed at the Institute for Rock Magnetism, University of Minnesota.

4.5 Paleomagnetic Results

Both AF and thermal demagnetization of the intrusive breccias revealed the presence of two components of magnetization: a north-directed component angled steeply downward (Component A), and a component inclined horizontally to shallowly upward and directed to the south-southeast (Component B) (Figs. 2a–c). Component A is the less-stable component, and is most readily removed by AF treatment; it is typically eliminated by ∼20 mT or ∼400 °C. In samples from Grants Intrusive, component B decays to the origin between 400 and 560 °C, or by ∼80 mT. Two (of 16) samples from this site behaved erratically at high temperature and were excluded from further analysis. Samples from the Chamberlain Diatreme became unstable above 400 °C, yielding erratic directions due to thermal alteration, so component B is only defined by AF demagnetization; it is observed to decay by ∼60 mT. In samples from the Hart Creek Diatreme, component A is removed more rapidly during the initial demagnetization steps, and holds a greater proportion of the total remanence, relative to the corresponding component from the other intrusive breccias. Component B is largely unblocked between 450 and 560 °C, but in some samples a remanence remains above 600 °C, and the segment defining component B does not trend to the origin (Fig. 2c). In these samples, a higher laboratory unblocking temperature component (C) can be defined, and it is sub-parallel to component A. This C-component is also observed to persist above 200 mT in some samples that were AF-demagnetized. In two (of 10) samples, only components A and C were identified.

Samples from the Willow Lake Dike and Downeys Bluff Sill yield two components

Figure 4.2: Characteristic demagnetization behavior of Illinois intrusive rock samples. In the orthogonal vector diagrams, the solid (open) symbols are projections onto the horizontal (vertical) plane. All results are presented in geographic coordinates. (a) Grants Intrusive, (b) Chamberlain Diatreme, (c) Hart Creek Diatreme, (d) Willow Lake Dike, (e) Downeys Bluff Sill, (f) Downeys Bluff Limestone (baked contact), (g) Downeys Bluff Limestone (unbaked).

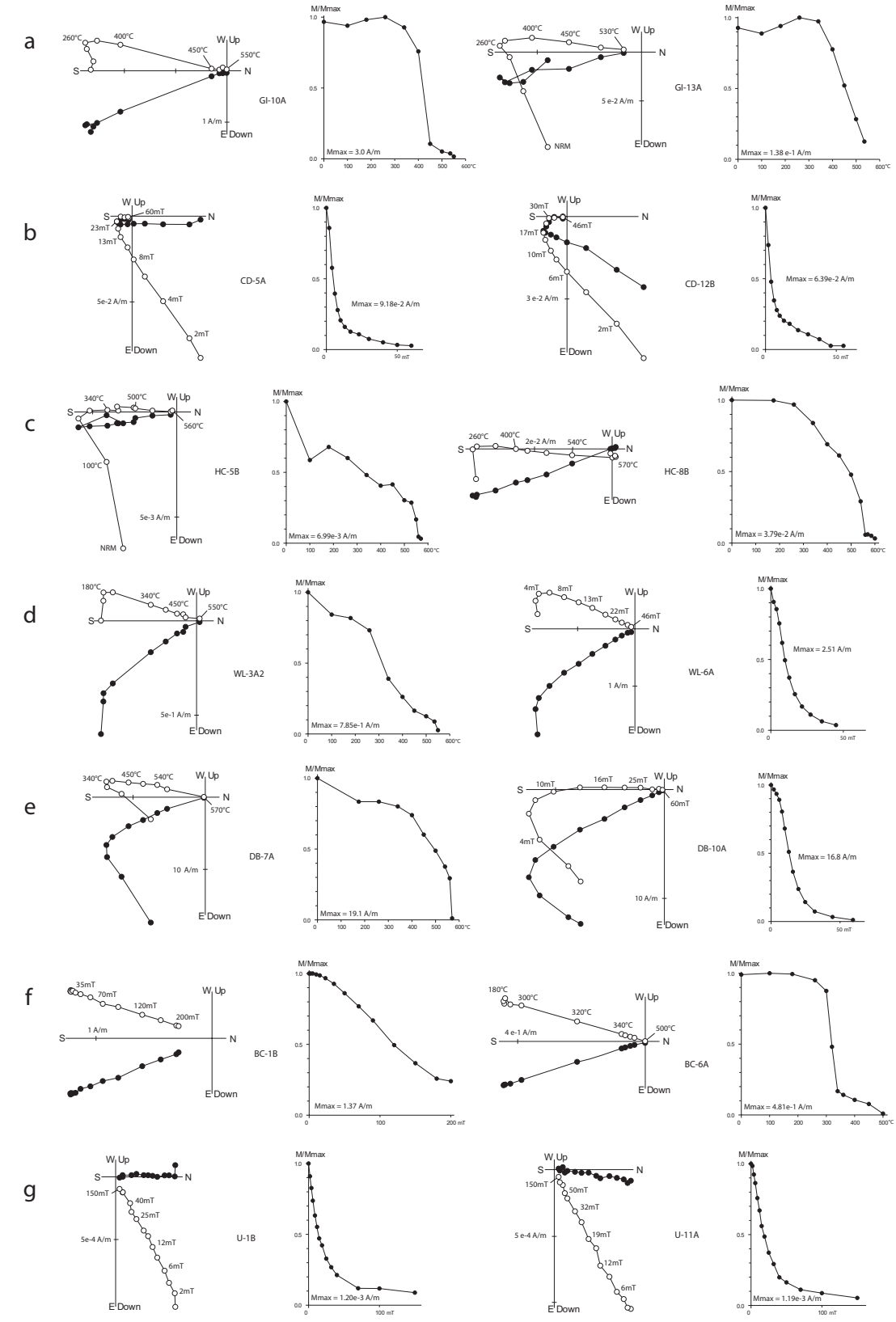
a
260°C
400°C
450°C
550°C
W, Up
S
N
1 A/m
E Down
Gl-10A
M/Mmax
Mmax = 3.0 A/m
400°C
450°C
530°C
260°C
5 e-2 A/m
NRM
Gl-13A
Mmax = 1.38 e-1 A/m
b
60mT
23mT
13mT
8mT
5e-2 A/m
4mT
2mT
CD-5A
Mmax = 9.18e-2 A/m
30mT
17mT
46mT
10mT
6mT
3 e-2 A/m
CD-12B
Mmax = 6.39e-2 A/m
c
340°C
500°C
560°C
100°C
5e-3 A/m
NRM
HC-5B
Mmax = 6.99e-3 A/m
260°C
400°C
2e-2 A/m
540°C
570°C
HC-8B
Mmax = 3.79e-2 A/m
d
180°C
340°C
450°C
550°C
5e-1 A/m
WL-3A2
Mmax = 7.85e-1 A/m
4mT
8mT
13mT
22mT
46mT
1 A/m
WL-6A
Mmax = 2.51 A/m
e
340°C
450°C
540°C
570°C
10 A/m
DB-7A
Mmax = 19.1 A/m
10mT
16mT
25mT
60mT
4mT
10 A/m
DB-10A
Mmax = 16.8 A/m
f
35mT
70mT
120mT
200mT
1 A/m
BC-1B
Mmax = 1.37 A/m
180°C
300°C
320°C
340°C
500°C
4 e-1 A/m
BC-6A
Mmax = 4.81e-1 A/m
g
150mT
40mT
25mT
12mT
6mT
2mT
5e-4 A/m
U-1B
Mmax = 1.20e-3 A/m
150mT
50mT
32mT
19mT
12mT
6mT
5 e-4 A/m
U-11A
Mmax = 1.19e-3 A/m

of magnetization that are highly-similar to those identified in the intrusive breccias, and we assign them the same labels (components A and B) (Figs. 4.2d,e). In the Willow Lake Dike, component A can represent up to 50% of the natural remanent magnetization (NRM) and is removed by ∼20 mT or ∼300 °C, after which component B decays univectorially to the origin. Unblocking of component B is often distributed between 300 and 560 °C during thermal demagnetization and is complete by 50 mT during AF demagnetization. Demagnetization of Downeys Bluff Sill samples is complete by 60 mT or 570 °C, and cleaning of the lower stability component (A) is complete by ∼10 mT or ∼300 °C. Unblocking of the B-component is typically distributed between 300 and 570 °C, but, in a few samples, unblocking at an intermediate temperature (250–450 °C) appears to be distinct from higher temperature decay (500–570 °C), suggesting the presence of a distinct phase. Directional differences between the intermediate and high-temperature vector segments are less than 5°. AF demagnetization spectra do not reveal any correlative distinction in coercivity during removal of the B-component.

Samples of the Downeys Bluff Limestone taken from the baked contact zone adjacent to the ∼0.2–0.5 m sill typically preserve only one component of magnetization, sub-parallel to the B-component identified in the sill (Fig. 4.2f). Unblocking of this magnetization occurs primarily between 260 and 330 °C, but a minor fraction of the remanence can persist to 550 °C. AF demagnetization is only partly effective; ∼30% of the remanence remains after application of a 200 mT peak field. Component A is apparent in a few samples, but it represents a very minor fraction of the NRM and is removed during the initial demagnetization steps. By contrast, unbaked samples of the Downeys Bluff Limestone preserve only the A-component, which decays univectorially to the origin (Fig. 4.2g). The remanence of the unbaked samples is distinctly

less stable, as ∼90% of the NRM is removed by application of 100 mT or 300 °C.

Considering its relative stability and directional consistency, we assign the B-component the characteristic remanent magnetization (ChRM) of these rocks. We have calculated site mean directions of this ChRM from 6 of the 7 sites sampled (the unbaked Downeys Bluff Limestone does not exhibit component B) (Fig. 4.3; Table 4.1). Within these 6 sites, 87% of the samples (n = 68/78) were retained for the ChRM site mean calculations. 13% of the samples were rejected due to thermal alteration, erratic behavior, or anomalous directions. The combined site-means give the following paleomagnetic pole: 54.1° S, 300.7° E, A_{95} = 4.8°, N = 6. If tilt-corrections are applied, the pole (hereafter "IL") is located at 56.3° S, 302.9° E (A_{95} = 3.8°). Our results are in excellent agreement with the earlier findings of Reynolds et al. (1997); site mean directions common to both studies (from Grants Intrusive and Downeys Bluff Sill/Limestone) differ by ≤ 2.2°.

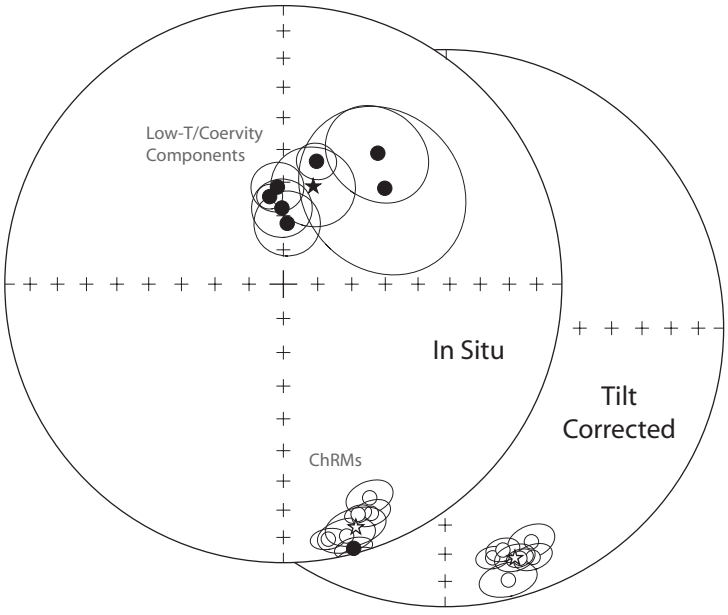

Figure 4.3: Site-mean paleomagnetic directions from Illinois intrusive rocks. Solid (open) symbols are projections onto the lower (upper) hemisphere. The stars represent the mean of the site means.

4.6 Magnetic Mineralogy

Hysteresis measurements reveal that the Chamberlain Diatreme, Grants Intrusive, Downeys Bluff Sill, and the Willow Lake Dike are dominated by a low-coercivity magnetic phase (Figs. 4.4a,b). In conjunction with the thermal demagnetization observations (wherein the ChRM was typically removed by 560–570 °C), and known mineralogy of these igneous bodies, we interpret the ChRM of these rocks to be carried by low-Ti titanomagnetite. Reynolds et al. (1997) reported evidence of low-Ti titanomagnetite in Grants Intrusive and Downeys Bluff Sill from thermomagnetic analysis. There are no strong indications of a second magnetic component in the hysteresis behavior of samples of these rocks, suggesting that the low-temperature/coercivity A-component is held by a less-stable sub-population of titanomagnetite, perhaps distinct in composition or size. Specimens from the contact metamorphosed Downeys Bluff Limestone show both low- and high-coercivity components in variable proportions, indicating that some magnetic phases may be heterogeneously distributed relative to the chip-size used in the experiments. The low-coercivity phase is again consistent with low-Ti titanomagnetite, according to the thermal demagnetization observations. The high-coercivity phase may be the principal ChRM carrier, observed to unblock between 260 and 330 °C. Reynolds et al. (1997) interpreted this phase as pyrrhotite, which has a high-coercivity and a Curie point of ∼325 °C (Rochette et al., 1990). The hysteresis behavior of a specimen from the Hart Creek Diatreme is controlled by a high-coercivity phase; demagnetization of a sister-specimen (from the same sample) shows the NRM of this sample is dominated by the C-component. The persistence of the C-component above 600 °C and its association with the observed high-coercivity behavior suggests it may be carried by hematite.

The lower temperature components (A and B) are again attributed to titanomagnetite, although the low-coercivity phase in the measured specimen—evident by the "goose-necked" shape of the loop (Tauxe et al., 1996)—is minor.

Low-temperature remanence data from a specimen of the baked Downeys Bluff Limestone support the interpretation that its remanence is carried by pyrrhotite. The specimen was imparted with an isothermal remanent magnetization at room-temperature and cycled down to 10 K and back, during which time regular measurements of remanence were made. Notable changes in remanence occurred at ∼120 K and ∼32 K, which correspond to known magnetic transition temperatures in magnetite and pyrrhotite, respectively (Fig. 4.4c).

4.7 VGP Distribution Analysis

It is commonly assumed that the distribution of VGPs is approximately circularly symmetric at all latitudes (but with increasing scatter pole-ward, due to the relative intensity of non-dipole fields) (Tauxe and Kent, 2004; Harrison, 2009). Due to the non-linear relationship between VGPs and magnetic field directions, the corollary of this latitude-independent circular symmetry of VGPs is the expectation of non-circular and latitude-dependent distributions of directions (except at high-latitudes) (Creer et al., 1959; Tanaka, 1999). Tauxe and Kent (2004) used a statistical model of the field to define this theoretical distribution of directions as a function of latitude and insightfully proposed that it could be used to identify departures from the expected distribution of a set of directions generated by a geocentric axial dipole (GAD) at any given latitude. In practice, this is achieved by comparing the observed "elongation" of a directional data-set with the expected elongation from the theoretical function at a specific latitude defined by the mean inclination of the data-set.

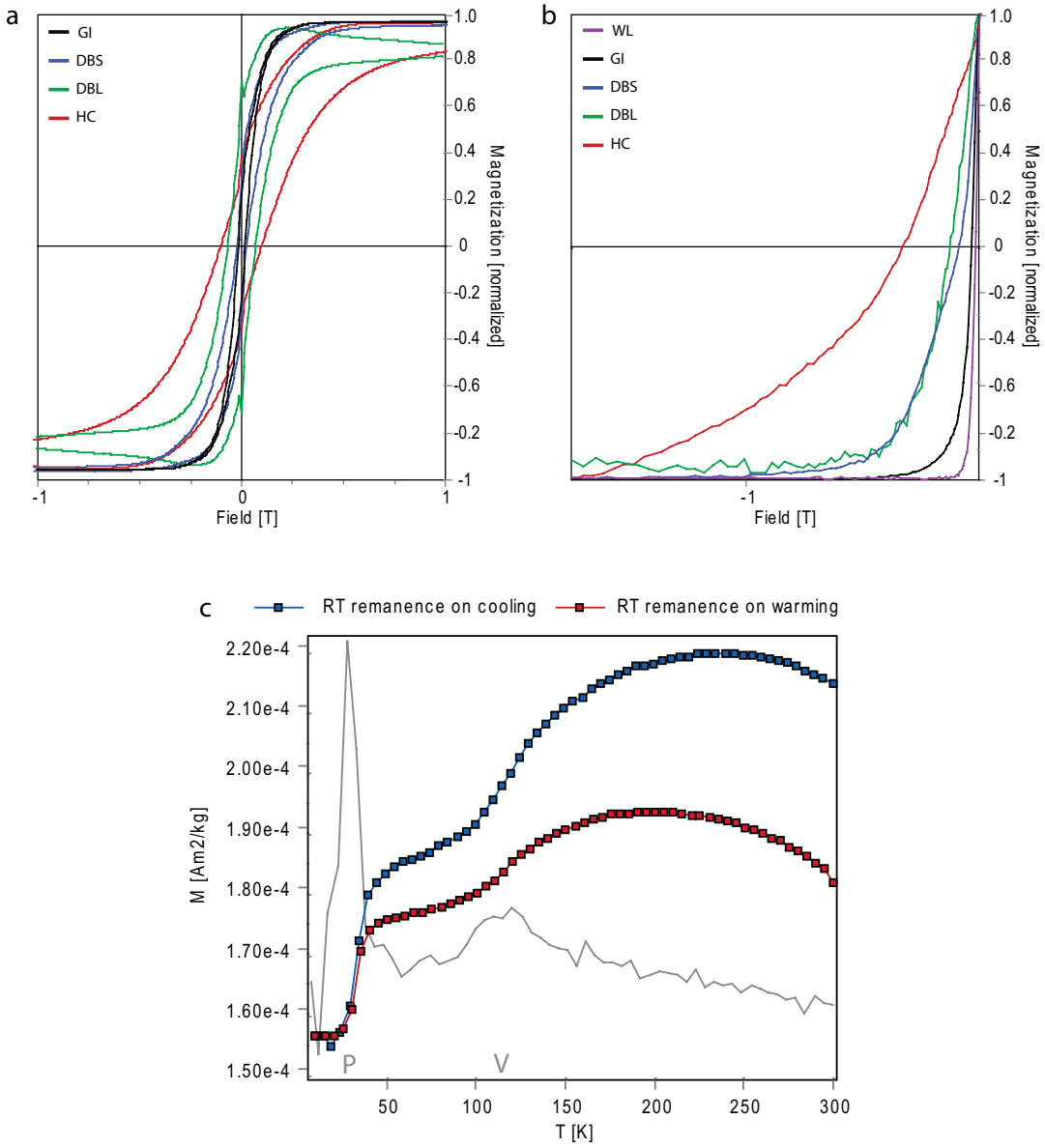

Figure 4.4: Rock magnetic experiments on Illinois intrusive rocks. Hysteresis loops, after paramagnetic correction (a), and back field curves (b) of representative samples. Loops were driven to 1.5 T, but the figure is truncated to highlight the low-coercivity behavior expressed by most samples. WL = Willow Lake Dike, GI = Grants Intrusive, DBS = Downeys Bluff Sill, DBL = Downeys Bluff Limestone (baked zone), HC = Hart Creek Diatreme. Results from the Chamberlain Diatreme are not depicted, but are similar to those of Grants Intrusive. Note the "goose-necked" behavior of the HC loop, which may be due to the mixing of magnetite (low-coercivity) and hematite (high-coercivity) signals (Tauxe et al., 1996). (c) Low-temperature cycling experiment on a specimen from the baked zone of Downeys Bluff Limestone. Blue and red curves show the change in remanence during cooling and warming, respectively. The gray curve is the first-derivative of the cooling curve; interpreted transitions are labeled: P (pyrrhotite) and V (Verwey).

Elongation is defined by Tauxe (1998) as the ratio of the intermediate and minimum eigenvalues (τ_2/τ_3) of the orientation matrix of the magnetization directions. This so-called "elongation-inclination" (E/I) technique has led to an increasing recognition of inclination shallowing in sedimentary rocks (Kent and Tauxe, 2005; Yan et al., 2005; Krijgsman and Tauxe, 2006) and to discussions regarding the structure of the geomagnetic field through time (Tauxe, 2005; Tauxe and Kodama, 2009).

The principal drawback of the E/I technique is that a large amount of data ($\geq$ 100–150 site-level directions) are required to conduct a meaningful analysis, because the method assumes that the data-set fully captures the directional variance due to secular variation (Tauxe et al., 2008). Small data-sets, therefore, may exhibit apparent elongations reflecting an under-sampling of the short-term field variance, rather than a true departure from GAD expectations. Unfortunately, paleomagnetic studies with > 100 independent site mean directions are currently rare; there are none within the paleomagnetic records we are considering here (Table 4.2). Thus, none of the individual studies present a sufficiently large data-set for a rigorous directional distribution analysis. Yet, collectively, these studies constitute an ample data-set that likely represents a full characterization of secular variation. Because several of these studies were conducted on the same formations (e.g. Moenkopi Fm., Chugwater Fm., Cutler Fm.), and many more are derived from lithologically similar continental redbeds, we postulate that it is reasonable, although admittedly not ideal, to combine and collectively analyze these data-sets for common/widespread departures from GAD expectations, as they may be similarly biased. The latitude-dependence of the expected distribution for magnetization directions prevents us from combining data-sets with distinct mean inclinations, thereby significantly limiting our analysis. For this reason, we instead elect to analyze VGP distributions, which have a latitude-

independent (consistently circular) expected distribution. As aforementioned, there is an increasing element of VGP scatter with increasing latitude, but we argue that this effect is negligible given that the data come from a narrow range of low-latitude sites.

Because we are specifically interested in testing the hypothesis that the Laurentian data-sets have been systemically biased by inclination shallowing, we employ the statistical field model TK03 (Tauxe and Kent, 2004) to simulate the effect of shallowing on VGP distributions expected from an ideal GAD field. As such, we assign the non-dipole terms in the statistical model a mean of 0 (i.e. TK03.GAD). Shallowing of the ideal synthetic directions follows the relationship determined by King (1955): $\tan(I_o) = f \tan(I_f)$, where f is the "flattening" coefficient, and I_o and I_f are the observed and true field inclinations, respectively. Laboratory re-deposition experiments, E/I analyses, and anisotropy measurements of hematite-bearing rocks have found a mean f of $\sim$0.55, and values as low as $f = 0.4$ ($f = 1$ results in no shallowing ($I_o = I_f$)) (Tauxe and Kent, 1984; Kent and Tauxe, 2005; Bilardello and Kodama, 2010). At 5° intervals between latitudes 0° and 85° we have: (1) drawn 300 directions from TK03.GAD with a mean declination of 0° (no reversals), (2) shallowed the directions by f, (3) transformed the directions to VGPs, and (4) calculated the mean VGP latitude, elongation of the data-set, and the direction of the elongation. This process was repeated 1000 times at each 5° interval to determine the variance in the calculated parameters. The complete experiment was run under three different shallowing conditions: $f = 1$, 0.55, and 0.4; the results are presented in Figure 4.5.

To compare the Laurentian paleomagnetic records with the model results, we rotated selected data-sets into the same reference frame according to the following

Figure 4.5: Results of variable inclination shallowing on statistical field model-generated VGP distributions and their apparent pole latitudes. (a) Elongation of VGP distribution vs. sampling site latitude, according to various shallowing factors: $f = 1.0$ (purple), 0.55 (blue), 0.4 (red). Elongation is defined as the ratio of the intermediate and minimum eigenvalues (τ_2/τ_3) of the orientation matrix of the VGPs; a circular distribution has an elongation of 1 (dashed line). The shallowing factor (f) relates an observed inclination (Io) to the true inclination (If), according to: $\tan(\mathrm{I}_o) = f\ \tan(\mathrm{I}_f)$; $f = 1.0$ results in no shallowing. The solid curves are mean results, bounded by the colored areas which enclose 95% of the individual estimates. The results were determined by generating 300 directions from statistical field model TK03.GAD at each 5° interval of latitude, shallowing them by *f*, and measuring the elongation of the resulting VGP distribution. The mean estimates and 95% envelopes were determined after 1,000 iterations of this process. (b) Apparent pole latitude vs. sampling site latitude, after application of the various shallowing factors from (a). The solid curves are mean results, bounded by the colored areas which enclose 95% of the individual estimates. The results were determined by the same process in (a), but rather measuring the latitude of the resulting mean VGP in each individual iteration. Estimates and 95% envelope were determined after the process was repeated 1,000 times. (c) Example VGP distributions from TK03.GAD according to changes in sampling site latitude and *f*. Open (closed) symbols are projections onto the upper (lower) hemisphere. Note the increasing elongation and changing center of mass of the distributions as a function of *f*.

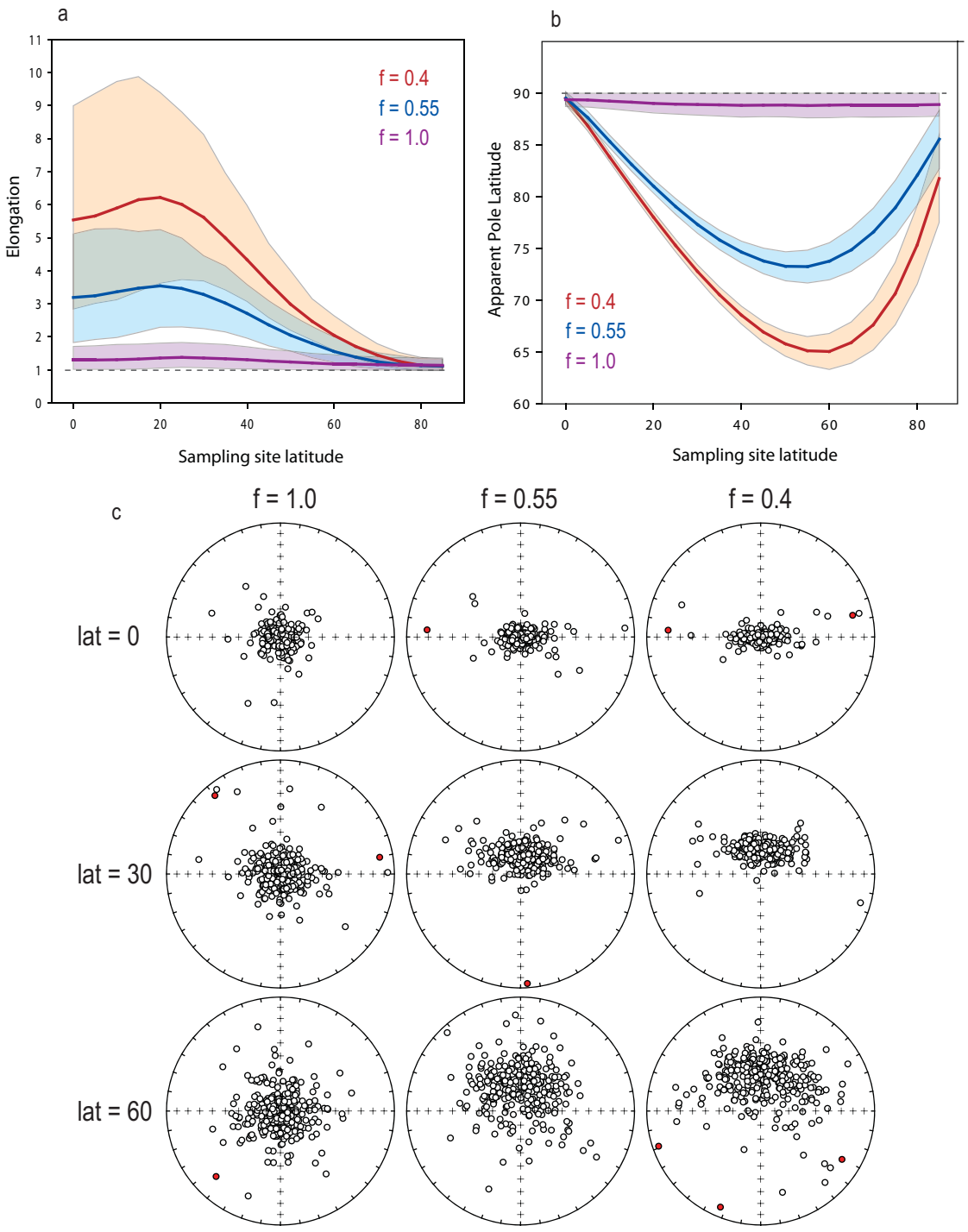
a
Elongation
Sampling site latitude
f = 0.4
f = 0.55
f = 1.0
b
Apparent Pole Latitude
Sampling site latitude
f = 0.4
f = 0.55
f = 1.0
c
f = 1.0
f = 0.55
f = 0.4
lat = 0
lat = 30
lat = 60

steps: (1) a mean direction (principal eigenvector) is calculated from the orientation matrix (Tauxe, 1998) of the published site-level mean directions, (2) the mean directions are rotated to a declination of 0° (reversed polarity magnetization directions are first inverted) around a vertical axis, (3) the directions are transformed to VGPs according to the dipole formula, (4) the sampling sites (and thus the VGPs) are rotated to a longitude of 0° around a vertical axis, (5) a mean VGP is calculated from each VGP-set (again using principal component analysis), (6) each VGP set is rotated around a horizontal axis (trending E-W) until the mean VGP is vertical. The results of this exercise are shown in Figure 4.6a. Also depicted in Figure 4.6 are the elongations and their declinations for each record. We stress that the small number of site-level VGPs in each of these individual records ($N \leq 36$) means that these elongation values are not likely representative of the "true" elongation that would be derived from a data-set that fully captured the directional variance of a time-averaged field. Again, it is for this reason that we combine and collectively analyze these individual records, according to the argument that the lithologically similar redbeds may have been similarly affected by inclination shallowing. To minimize the bias introduced by the centering process, we exclude data-sets with < 8 listed site-level directions, which reduces our compilation to 14 records with a total of 285 site means.

The magnitude and direction of the elongation of the combined data-set was calculated (Fig. 4.7b); confidence bounds on the estimate of the elongation were determined via 1000 re-calculations of elongation from randomly sampled sub-sets of the original data (i.e. bootstrap). A fundamental assumption in this analysis is that all VGPs belong to the same general population, meaning that the presence of secondary magnetizations or incompletely removed overprints may significantly bias

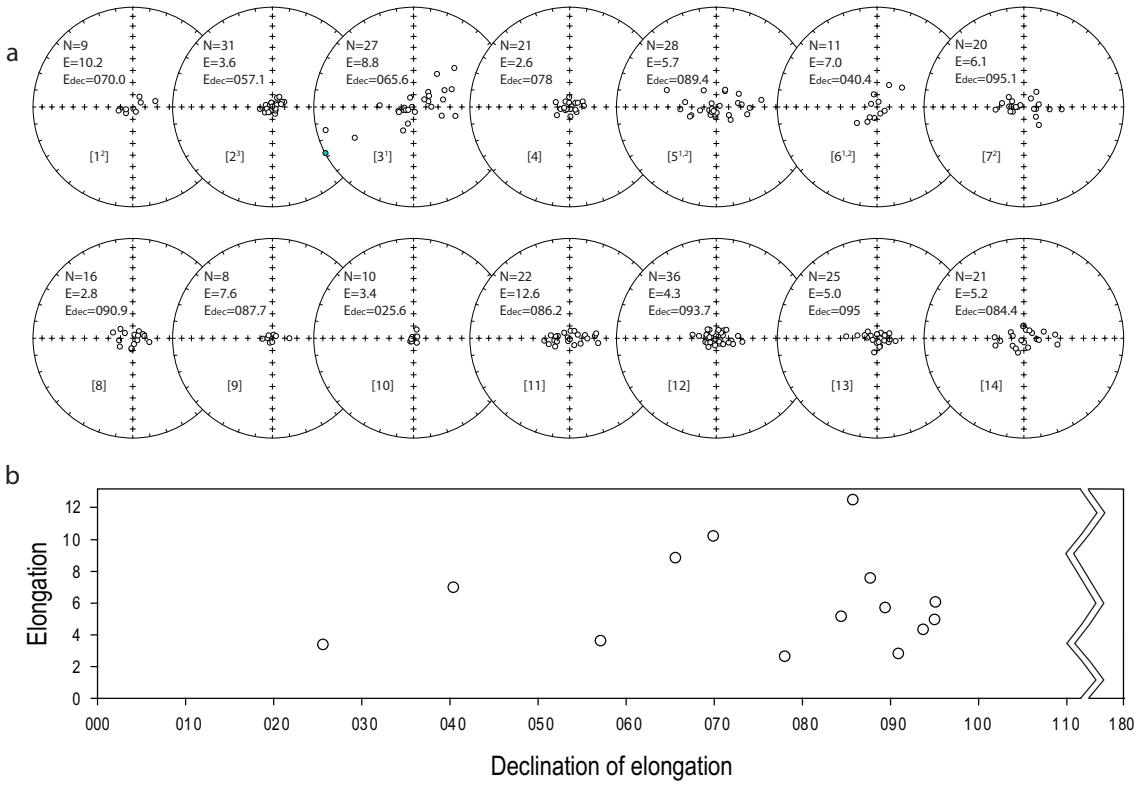

Figure 4.6: VGP distributions of selected Laurentian paleomagnetic records (N $\geq$ 8; Table 4.2). (a) VGP distributions after centering according to the procedure described in the text. All symbols are projections onto the upper hemisphere. N = number of site-level VGPs, E = elongation, Edec = declination of elongation, [#] = reference number of record; 1: Wolfcampian units, Peterson and Nairn (1971), 2: Cutler Fm., Gose and Helsley (1972), 3: Lykins and Fountain Fms., McMahon and Strangway (1968), 4: Pictou redbeds, Symons (1990), 5: Lower Maroon Fm., McMahon and Strangway (1968), 6: Upper Maroon Fm., McMahon and Strangway (1968), 7: Dewey Lake Fm., Molina-Garza et al. (2000), 8: Dewey Lake Fm., Molina-Garza et al. (1989), 9: Chugwater Fm., Herrero-Bervera and Helsley (1983), 10: Chugwater Fm., Shive et al. (1984), 11: Moenkopi Fm., Steiner and Lucas (1992), 12: Moenkopi Fm., Molina-Garza et al. (1991), 13: Moenkopi Fm., Molina-Garza et al. (1996), 14: Lower Fundy Group, Symons et al. (1989). [1] Results not adequately demagnetized (see text for explanation). [2] Results not included in the compilation of Torsvik et al. (2008). [3] ChRM explicitly interpreted as CRM by original authors (Gose and Helsley, 1972). (b) Elongation of VGP distributions vs. declination of elongation for studies in (a). Specific elongation estimates are likely unreliable due to the small size of the data-sets (N $\leq$ 36).

the elongation calculation. For this reason, we repeated the analysis after excluding three records from the study of McMahon and Strangway (1968), where AF demagnetization was used sparingly, and no samples were subjected to thermal or chemical demagnetization (Fig. 4.7c). Thermal and/or chemical demagnetization is necessary to ensure that a magnetization held principally by hematite is purified of secondary overprints.

To ensure that we are able to recognize an "unshallowed" VGP distribution, we conduct this analysis on a sequence of published paleomagnetic results from volcanic rocks from Yemen (i.e. from similarly low latitudes), as volcanic rocks are not affected by the inclination shallowing process (Fig. 4.7d; data from Riisager et al., 2005). Finally, to consider the possible bias introduced by small data-sets and/or the centering process, we: (1) collect a series of small data-sets (N = 20), randomly sampled from a larger population (N = 500) generated by TK03.GAD, and (2) calculate the elongation of combined groups of these data-sets (15 sets of N = 20) after centering them individually according to the procedure described above. We compare the elongation determined from several iterations of this experiment against the "true" elongation of the original population (Fig. 4.7e); the experiment was run both with $f = 1$ and $f = 0.4$.

4.8 Discussion

4.8.1 Interpretation of Paleomagnetic Results

We interpret the ChRM of the intrusive rocks and contact metamorphosed limestone to be a primary, Middle Permian (∼270 Ma) magnetization. The exclusively reversed polarity of this remanence is consistent with magnetization acquisition during the Kiaman Reversed Superchron, which extended from ∼318–265 Ma (Opdyke et al., 2000; Gradstein et al., 2004). The Middle Permian K-Ar and ^{40}Ar-^{39}Ar age

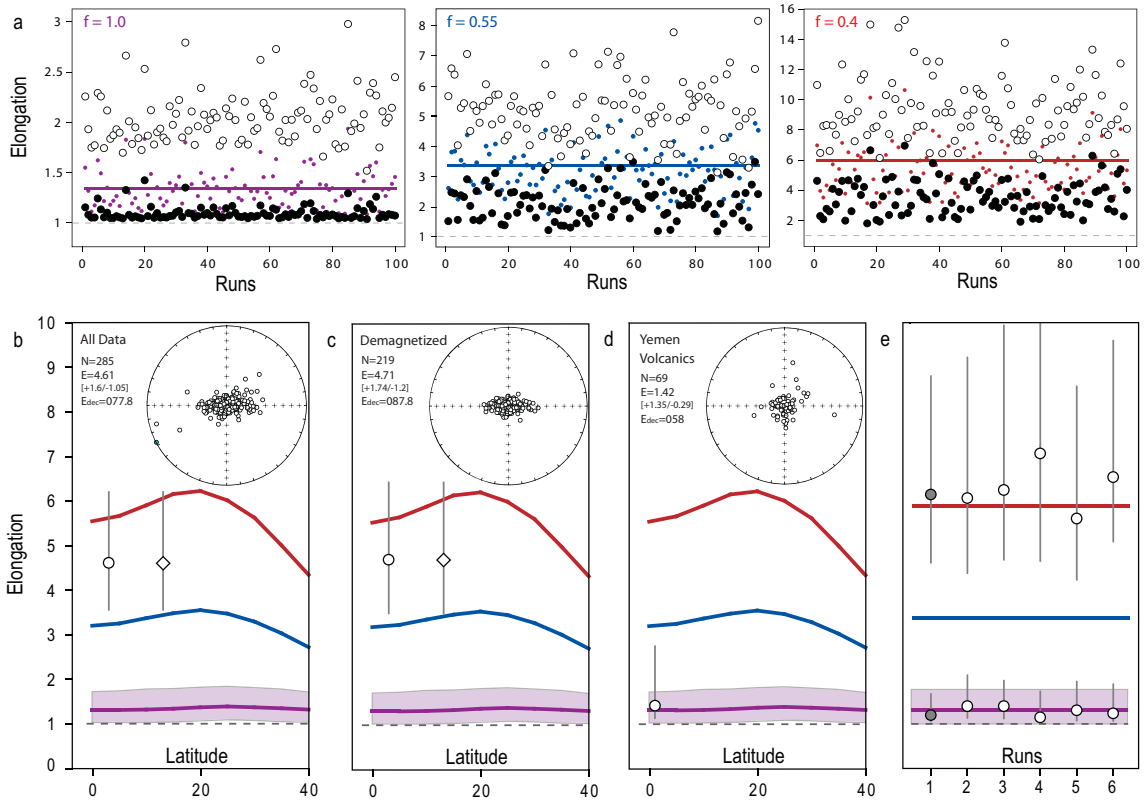

Figure 4.7: Results of VGP distribution analysis. (a) Example elongation estimates from 100 randomly generated data-sets (N = 300) at a latitude of 10°, under shallowing conditions of f = 1.0, 0.55, and 0.4 (note, the vertical scales are different). Small colored symbols are the mean elongation estimates, the larger solid (open) symbols are the minimum (maximum) elongation estimates from the 95% bootstrap confidence limits. The solid horizontal line is the mean elongation estimate determined from 1,000 iterations (Fig. 4.5a); the dashed line represents a distribution with circular symmetry (elongation=1.0). 95% of the individual estimates overlap with the mean estimate (within error). (b–d) Elongation estimates of published VGP records. Circles (diamonds) depict mean elongation estimates vs. sampling site latitude determined from the uncorrected (max. corrected) mean inclination. The vertical gray lines show the 95% bootstrap confidence limits on the mean elongation estimates. The solid curves in each panel are taken from Figure 4.5a (purple: f = 1.0, blue: f = 0.55, red: f = 0.4). The inset stereonets show the VGP distributions. N = number of VGPs, E = mean elongation (95% confidence bounds are in brackets), Edec = declination of elongation. (b) All data from Figure 4.6a. (c) Data from (b) after removal of poorly demagnetized records (i.e. the records from McMahon and Strangway (1968); denoted by [1] in Figure 4.6a). (d) Results from Oligocene volcanic rocks from Yemen; data from Riisager et al. (2005). e) Test for bias introduced by small data-sets and/or the centering process described in the text. The gray circles are elongation estimates determined from a data-set with N = 500, generated by TK03.GAD at a latitude of 10° and a mean declination of 0°. The open circles are elongation estimates determined from a collection of small (N = 20), randomly sampled subsets of the initial data which are individually rotated according to the centering process before being grouped together (into 15 sets of N = 20 for a grouped collection of N = 300) and collectively analyzed. The experiment was conducted using both f = 1.0 and f = 0.4. The consistency of the elongation estimates suggests that no significant bias is introduced by combining small data-sets or centering the VGP distributions.

determinations on the Grants Intrusive and Downeys Bluff Sill discount the possibility of a significant (> 300 °C) thermal event after ∼270 Ma, which rules out a secondary magnetization of thermal origin. A secondary chemical remanent magnetization (CRM) is similarly unlikely due to the identification of titanomagnetite as the principal remanence carrier. Reynolds et al. (1997) observed magnetite-ilmenite intergrowths and TiO_2-rich high-temperature alteration products—both indicative of an igneous origin—in Grants Intrusive and Downeys Bluff Sill. Furthermore, we note that the position of the paleomagnetic pole resembles other Middle Permian poles from Laurentia, but not younger ones (Kent and Irving, 2010). We interpret the low-temperature/coercivity component (A) to be an overprint of recent origin. The paleomagnetic pole determined from this component (79.7° N, 349.7° E, $A_95 = 18.4°$; in situ coordinates) resembles that of the present day field. The C-component observed in the Hart Creek Diatreme and interpreted to reside in hematite, is also interpreted as a recent overprint, perhaps developed by surface oxidation of primary titanomagnetite.

We observe a minor reduction in the estimated α_{95} of the mean paleomagnetic direction after tilt-correction (applied to data from the Chamberlain Diatreme and Grants Intrusive), but note that this is not statistically significant at the 95% confidence level, and does not constitute a positive tilt-test. Furthermore, the nature and timing of the tilting is not well-established. Host strata for the Willow Lake Dike and the Downeys Bluff Sill exhibit no significant structural dip ($< 5°$). Strata near the Hart Creek Diatreme exposure exhibit a minor dip to the NW, but the cross-bedded nature of this poorly exposed sandstone precludes any confident structural restoration. Exposures of strata near Grants Intrusive and the Chamberlain Diatreme exhibit clear bedding contacts with a significant dip. The Chamberlain

Diatreme occurs along the Herod Fault Zone, a NE-trending structure which was likely active after emplacement of the Diatreme, and may be responsible for this locally observed dip. Grants Intrusive is exposed on the southwest flank of Hicks Dome, which is assumed to have developed contemporaneously with the regional magmatism; thus, the structure may pre- or post-date the intrusion. We prefer the tilt-corrected result, due to the minor improvement in site-mean clustering.

4.8.2 Interpretation of VGP Distribution Analysis

It is evident from the example VGP distributions (Fig. 4.5c) that the shallowing of magnetic field directions results in an elongation of the VGP distribution along meridians perpendicular to those containing the sampling site. In the model, the site longitude was set to 0°, so the flattening of directions has expectedly resulted in an elongation of the VGP distribution along the 90°–270° meridians. Because all of the Laurentian data-sets have been rotated into the same reference frame (sampling site longitude = 0°), the incidence of inclination shallowing in these records should be reflected in an elongation of the VGP distribution in the same sense. Figure 4.6 illustrates a clear 90° (= 270°) preference in the elongation direction of these data-sets, in support of the hypothesis that inclination shallowing has affected the paleomagnetic records from these redbeds. The grouped results in Figures 4.7b,c similarly exhibit a clear 90°–270° elongation of the VGP distribution. In both grouped analyses, the calculated value of elongation is statistically distinct (95% conf.) from a circular distribution (elongation = 1), indicating that significant shallowing of the inclinations has occurred. This conclusion is reinforced by the analysis of the Yemeni volcanic rocks, which yield a very low VGP elongation, in agreement with the expectation that unshallowed directions (from a GAD) should produce a circularly symmetric VGP distribution (Fig. 4.7d). Our exercises in sub-sampling and centering synthetic

data have resulted in elongation estimates that are reasonably close to (and statistically indistinguishable from) the elongations derived from the original data and the model expectations, thereby implying that our sample sizes and centering procedure are not introducing any systematic bias (Fig. 4.7e).

Beck et al. (2003) conducted a similar VGP distribution analysis of Triassic and Jurassic redbeds from the Colorado Plateau, but concluded that the observed elongations were due to a protracted magnetization acquisition. Cederquist et al. (1997), examining the elongation of Carboniferous–Early Jurassic magnetization directions from Laurentia, also concluded that the observed elongate distribution was due to the inclusion of apparent polar wander in the data as a consequence of protracted magnetization acquisition. This alternative interpretation is predicated on the assumption that the ChRM of these redbeds is dominantly chemical in nature, and was acquired over a prolonged period by the slow growth of authigenic (pigmentary) hematite in the form of a grain-coating/cement. However, a review of the original studies shows that the contribution of pigmentary hematite to the ChRM is often minor (if existent), relative to the contribution by specular hematite, of detrital origin. Such a depositional remanent magnetization (DRM) is supported by the lateral continuity of polarity intervals across hundreds of kilometers and across lithologic boundaries (Purucker et al., 1980; Steiner et al., 1993), sequential changes in magnetization through thin sedimentary units (Shive et al., 1984), positive intraformational conglomerate and soft-sediment fold tests (Elston and Purucker, 1979; Symons et al., 1989; Symons, 1990, Magnus and Opdyke, 1991; Molina-Garza et al., 1991), co-linear magnetization directions with detrital magnetite (Steiner, 1988), characteristic specularite demagnetization behavior (Collinson, 1974; Gose and Helsley, 1972), and by petrographic observations (Elston and Purucker, 1979). More broadly, recent work

on Carboniferous and Late Triassic–Early Jurassic redbeds from North America has demonstrated a common shallow inclination bias, implying that the ChRM of these redbeds is predominantly a DRM (Kent and Tauxe, 2005; Bilardello and Kodama, 2010; Kent and Irving, 2010). Following our review of the original studies, we have labeled the records that present evidence consistent with a DRM as the ChRM (Table 4.2). We have also labeled the results that the primary authors explicitly associated with a CRM, although we stress that these determinations are not conclusive. If most of the paleomagnetic records are derived from DRMs, as we argue the evidence suggests, then the agreement between VGP distribution elongation and Laurentian APW, as observed by Cederquist et al. (1997) and Beck et al. (2003), is merely coincidental. Indeed, the late Paleozoic–early Mesozoic APWP of Laurentia is roughly orthogonal to its central meridian, so that most sampling sites with a shallow inclination bias could be expected to yield a VGP distribution with an elongation apparently coincident with the APWP. We consider most of the redbed paleomagnetic records to be depositional in nature, and interpret the elongate VGP distributions to be a consequence of inclination shallowing.

4.9 Magnitude of shallow inclination bias

The obvious reduction in VGP scatter in the "demagnetized" data-set (Fig. 4.7c), relative to the starting data-set (Fig. 4.7b), is an indication of the presence of unremoved magnetization overprints in the data of McMahon and Strangway (1968). As such, we regard the demagnetized data as more representative of the primary records, although the change in the elongation estimate between them is negligible. The elongation determined from the demagnetized data is 4.71; the bootstrap confidence limits extend from 3.51 to 6.45. Numerical exercises conducted on the

VGP-sets generated by TK03.GAD have demonstrated that the 95% bootstrap confidence limits on the estimated elongation of any given data-set have a 95% probability of overlapping with the "true" mean VGP elongation (from Fig. 4.5a), provided that the data-set is sufficiently large (N $\geq$ 100–150) (Fig. 4.7a). This is an expected outcome where both the "true" mean VGP elongation is well-determined and the individual sample-sets fully characterize the short-term directional variance in the field (model). Because our combined Laurentian data-set is sufficiently large, we may exclude all theoretical shallowing factors (f) that do not produce mean VGP distribution elongations that overlap with the bootstrap confidence bounds on the elongation estimate from the Laurentian data. If we use the uncorrected mean inclination of the data-set to calculate the sampling site latitude, our elongation estimate (with error) suggests that shallowing by a factor of $f = 0.52$ to $f = 0.37$ has occurred (circle, Fig. 4.7c). However, this approach is not strictly correct, as the theoretical curves are estimates of VGP distribution elongation for various f values at the true sampling site latitude (i.e., determined from the corrected mean inclination, which is typically unknown). Instead, a recursive correction-calculation process can be employed, wherein the maximum and minimum allowable inclination corrections can be determined according to those f values that would still lie within the confidence bounds of the elongation estimate after the inclination correction is performed. The highest sampling site latitude allowed by the data (by the maximum inclination correction consistent with the elongation estimate) is depicted by a diamond in Figures 4.7b,c. The shallow nature of the theoretical curves at low-latitudes and the low-mean inclination (5.3°) of the grouped data-sets precludes any dramatic shift in the range of potential f values; applying the recursive inclination corrections changes the potential range to: $f = 0.54$ to $f = 0.39$, with a mean of $f = 0.46$. For refer-

ence, Bilardello and Kodama (2010) compiled published f values determined from hematite-bearing sedimentary rocks. They range from $f = 0.83$ to $f = 0.4$, with a mean value of $f = 0.59$. More specifically, Kent and Tauxe (2005) determined eight f values from Late Triassic redbeds from North America, which ranged from $f = 0.66$ to $f = 0.4$, with a mean value of $f = 0.56$.

4.9.1 Implications for APWP of Laurentia

Although the IL pole resembles other Middle Permian poles from Laurentia, it does exhibit a significantly higher paleolatitude, as evident by its position relative to the Middle Permian segment of the Laurentian APWP of Torsvik et al. (2008) (Fig. 4.8a). Due to the prevalence of paleomagnetic records from continental redbeds in the compilation by Torsvik et al. (2008), we argue that this discrepancy is due to a widespread shallow inclination bias in the poles derived from sedimentary rocks. Our VGP distribution analysis supports this argument, in that the compiled data exhibit an elongation that is statistically distinct (95% conf.) from the expectations of a VGP distribution generated by a GAD. Our conservative estimate of elongation suggests that an average shallow inclination bias equivalent to shallowing by $f = 0.54$ is present in the paleomagnetic records of these continental redbeds.

To consider the effect that an inclination correction will have on the Laurentian APWP, we have first updated the 300–235 Ma compilation of Torsvik et al. (2008), according to the 2009 geologic timescale (Table 4.2). Of the five igneous results that were reported in the original compilation, only one result (#37) remains after updating the ages; and this result is derived from a single intrusion (i.e. single cooling-unit), highlighting the importance of the new IL result. We have also added an Early Triassic result from a diatreme in British Columbia (#36), but this result is also based on a single cooling unit. In Figure 4.8b we plot the updated APWP

after correcting the inclination of all redbed records with an f value of 0.54. There is an obvious improvement in the agreement between the IL result and the Middle Permian segment of the APWP after these corrections. In Figure 4.8c we correct the redbed records according to $f = 0.46$, which corresponds to the mean estimated shallowing factor determined from our VGP distribution analysis. This correction does not appreciably improve the agreement between the IL pole and the APWP relative to the more conservative correction of $f = 0.54$. We note the increasing A_{95} of the mean poles with increasing inclination correction (decreasing f), and attribute this to our simplistic "average" correction. Although we have argued that the redbeds are all likely affected by a shallow inclination bias, it is unlikely that they all share a bias of exactly the same magnitude. We contend that our analysis is a valuable demonstration of the widespread presence of too-shallow inclinations in these records, and that our correction offers a better approximation of the true Laurentian APWP, but future detailed work will be necessary to more precisely correct the individual results. Due to the correlation between mean pole A_{95} and f, and the lack of significant improvement between the corrections of $f = 0.54$ and $f = 0.46$, we prefer the conservative correction.

Regardless of the improvement between the IL pole and the Laurentian APWP, the shift in the APWP after inclination correction brings it into better agreement with the APWP of Gondwana. After updating the ages of the poles used in the Laurentian compilation, the APWP also exhibits a curvature in the latest Paleozoic, as previously observed in Gondwana's APWP (Domeier et al., 2011). The discrepancy remaining between the APWPs in Figure 4.8b may be ascribed to a similar shallow inclination bias—among other data-pathologies—in the paleomagnetic records from Gondwana. In Figure 4.8d we compare the $f = 0.54$ inclination corrected APWP of

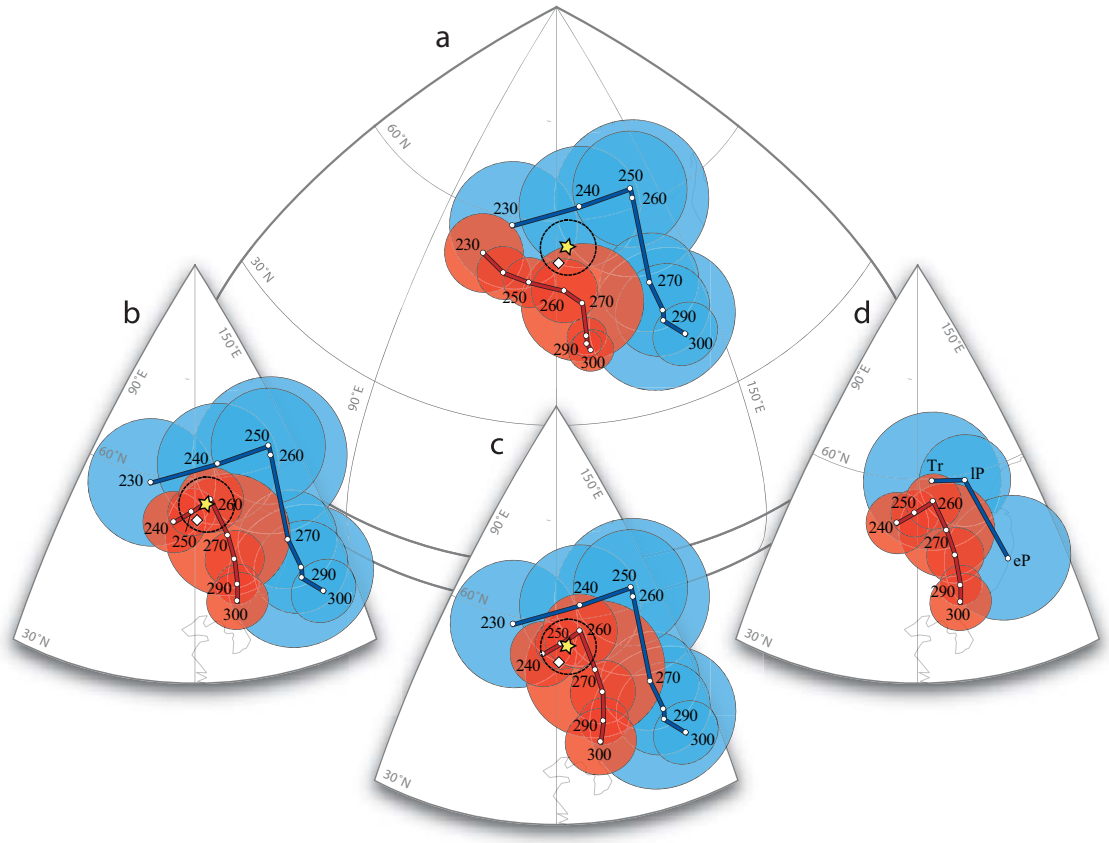

Figure 4.8: Inclination shallowing corrections of the Laurentian apparent polar wander path (APWP). (a) APWPs of Laurentia (red) and Gondwana (blue) plotted in North American coordinates according to the paleomagnetic compilation and Pangea reconstruction parameters of Torsvik et al. (2008). The star (diamond) depicts the tilt-corrected (in situ) IL paleopole, the dashed line is the A_{95} of this result. Note the large discrepancy between the Middle Permian to Early Triassic mean poles of the APWPs and the location of the IL result relative to them. (b) As in (a), but after updating the ages of the Laurentian paleomagnetic data and applying an inclination correction using $f = 0.54$ (conservative estimate from Fig. 4.7c). Note the improvement between the Middle Permian segment of the APWP and the IL result. (c) As in (b), but after application of an inclination correction using $f = 0.46$ (mean estimate from Fig. 4.7c). (d) Laurentian APWP from (b) (corrected by $f = 0.54$) compared with an APWP constructed from a filtered paleomagnetic data-set from South America (Domeier et al., 2011), rotated into North American coordinates according to the reconstruction parameters of Torsvik et al. (2008). eP = Early Permian, lP = Late Permian, Tr = Triassic.

Laurentia with a filtered Permian–Triassic paleomagnetic data-set from South America (Domeier et al., 2011). Although this filtered data-set is not explicitly corrected for inclination shallowing, it includes relatively more poles based on data from igneous rocks than the larger Torsvik et al. (2008) compilation, and the included records have been subjected to more stringent selection criteria. The separation between the Late Permian pole from the filtered South American data-set and the Late Permian poles of the inclination corrected APWP of Laurentia in Figure 4.8d is greatly reduced, relative to Figure 4.8a, supporting the contention that the long-standing discrepancy between the APWPs of Laurussia and Gondwana may simply be a manifestation of systemic bias.

4.10 Conclusions

Our investigation of shallow intrusive rocks and a contact metamorphosed limestone in southern Illinois (cratonic Laurentia) yields a new Middle Permian (∼270 Ma) paleomagnetic pole with a paleolatitude that is distinctly higher than that of the Middle Permian segment of the reference APWP of Laurentia. We argue that this discrepancy is due to a widespread, shallow inclination bias in the Laurentian paleomagnetic data, following the observation that the reference APWP is dominated by data derived from continental redbeds. A comparison between theoretical VGP distributions and published VGP-sets from the Laurentian redbeds reveals the latter to have a distribution that is incompatible with the expectations of TK03.GAD. The commonly elongate VGP distributions of the redbed paleomagnetic records are instead consistent with a pervasive shallow inclination bias, suggesting that a "flattening" on the order of $f = 0.54$ to $f = 0.39$ (mean of $f = 0.46$) has affected the inclinations. Using the conservative estimate of shallowing ($f = 0.54$), we correct

the inclinations of the redbed paleomagnetic records and demonstrate that the modified Laurentian APWP agrees more closely with both our new igneous rock-based paleomagnetic pole and the APWP of Gondwana. We contend that such a shallow inclination bias is also likely to be widespread in the sedimentary rock-based paleomagnetic records from Gondwana, and that this data-pathology may be the principal cause of the long-standing disparity between the APWPs. Finally, we note that the approach adopted here is simplistic in its assumption that all the redbeds have experienced the same degree of shallowing; future detailed work on individual units will be necessary to refine our corrections.

4.11 Acknowledgements

Local landowners and Peabody Energy are thanked for site access. Kunal Singh and Joseph Mulvaney-Norris helped with sample collection. Use of the following freeware is acknowledged: PmagPy, Paleomac, and Gmap. The valuable comments from the journal's reviewer, J. W. Geissman, helped improve the manuscript. Financial support for this research was provided by the U.S. National Science Foundation, Division of Earth Sciences (Tectonics Program), and NSF's Office of International Science and Engineering (Americas Program), grant EAR-0634807, and is gratefully acknowledged. Experiments at the IRM were financially supported by a visiting fellowship.

Table 4.1: Site-mean paleomagnetic data from Illinois intrusive rocks

Site	**N/n/v**	**Dg**	**Ig**	**Ds**	**Is**	**k**	α_{95}	**Slat (°N)**	**Slon (°W)**	**Plon**	**Plat**	$\mathbf{A_{95}}$
ChRM Directions												
GI	16/14/9	170.0	−7.8	168.3	−16.9	95.8	4.0	37° 30.49’	88° 22.59’	294.8	−59.3	4.1
WL	9/8/8	158.0	−18.4	158.0	−18.4	90.9	5.8	37° 49.10’	88° 20.80’	312.3	−55.4	6.1
HC	10/8/6	165.9	−7.5	165.9	−7.5	77.1	6.5	37° 33.92’	88° 26.44’	295.8	−53.8	6.5
CD	16/14/4	165.1	2.1	165.4	−18.8	100.5	4.1	37° 32.76’	88° 28.54’	300.5	−59.2	4.3
DB sill	14/13/7	159.0	−12.9	159.0	−12.9	87.4	4.6	37° 24.82’	88° 20.85’	308.6	−53.7	4.6
DB-baked	13/11/11	162.0	−14.2	162.0	−14.2	212.2	3.2	37° 24.82’	88° 20.85’	304.6	−55.7	3.2
Mean	**6**	163.4	−9.8	163.1	−14.8	193.4	4.8	Uncorrected:		300.7	−54.1	4.8
								Tilt Corrected:		302.9	−56.3	3.8
Low Temperature/Coercivity Components												
GI	16/11/11	3.6	72.2	327.2	81.2	23.7	9.6	37° 30.49’	88° 22.59’	277.4	70.1	16.9
WL	9/7/7	46.6	48.5	46.6	48.5	7.0	24.5	37° 49.10’	88° 20.80’	359.6	50.8	32.2
HC	10/7/7	358.9	67.7	358.9	67.7	49.1	8.7	37° 33.92’	88° 26.44’	268.5	76.9	14.5
CD	16/14/14	15.1	52.3	42.6	66.3	52.2	5.6	37° 32.76’	88° 28.54’	17.9	76.8	7.6
DB sill	14/12/12	35.8	41.6	35.8	41.6	9.2	14.5	37° 24.82’	88° 20.85’	52.8	47.9	17.7
DB-baked	13/7/7	356.5	61.4	356.5	61.4	66.5	7.5	37° 24.82’	88° 20.85’	245.3	84.2	11.5
DB-unbaked	12/12/12	351.1	64.0	351.1	64.0	141.8	3.7	37° 24.82’	88° 20.85’	235.9	79.4	5.8
Mean	**7**	17.0	59.9	19.9	63.9	26.2	12.0	**Uncorrected:**		349.7	79.7	18.4
								Tilt Corrected:		325.0	76.5	22.5

N/n/v = number of samples measured/number of samples used in site mean calculation/number of results defined by a vector (n-v=number of results defined by great-circles).
Dg/Ig = declination/inclination in geographic coordinates. Ds/Is = declination/inclination in tilt-corrected coordinates.
k = estimate of the precision parameter of Fisher (1953). α_{95} = half-angle (radius) of the cone of 95% confidence about the site mean direction.
Slat/Slon = latitude/longitude of sampling site. Plat/Plon = latitude and longitude of the site-level VGP.
A_{95} = half-angle (radius) of the cone of 95% confidence about the site-level VGP.

Table 4.2: Permian–Middle Triassic Laurentian paleopoles

#	Rock Unit	Plat	Plon	$Plat_{0.54}$	$Plon_{0.54}$	$Plat_{0.46}$	$Plon_{0.46}$	A_{95}	Age	Notes	Reference
	Sedimentary Records										
1	Upper Red Peak Fm.	−49.0	285.0	−53.5	288.5	−55.2	290.0	5.0	235	D	1134
2	Lower Fundy Group, Nova Scotia[1]	−45.0	277.0	−46.3	276.6	−46.8	276.4	7.2	235	D	2266
3	Moenkopi Fm., Anton Chico Mem.[1]	−45.0	301.0	−45.6	301.6	−45.9	301.8	4.9	243	D	2979
4	Moenkopi Fm., Anton Chico Mem.[1]	−40.0	307.0	−39.5	306.4	−39.4	306.2	5.3	243	D	2632
5	Moenkopi Fm.	−56.0	285.0	−60.3	289.7	−61.8	291.8	4.5	243	D	2808
6	Moenkopi Fm.[1]	−56.0	289.0	−60.0	293.6	−61.4	295.5	3.4	243	D	2489
7	Chugwater Fm.[1]	−45.0	295.0	−49.8	299.5	−51.5	301.4	4.0	245	D	1266
8	Chugwater Fm.[1]	−47.0	294.0	−52.3	299.1	−54.2	301.3	3.3	245	D	1271
9	Moenkopi Fm.	−53.0	291.0	−58.5	297.2	−60.4	300.0	3.1	245	?	159
10	Moenkopi Fm. (Gray Mtn.)	−55.0	286.0	−59.5	291.3	−61.2	293.6	5.0	245	D	1221
11	Lower Red Peak Fm.	−46.0	301.0	−51.7	307.6	−53.7	310.3	7.0	245	D	1134
12	Moenkopi Fm. (drill core)	−55.0	289.0	−61.3	296.5	−63.4	300.0	2.5	247	?	160
13	Moenkopi Fm.	−56.0	279.0	−61.7	283.8	−63.7	286.1	4.9	247	C	571
14	Dewey Lake Fm. (Texas)[1]	−51.0	306.0	−54.5	310.7	−55.8	312.7	5.0	252	D	2303
15	Dewey Lake Fm. (New Mex.)[1,2]	−55.0	298.0	−58.2	302.1	−59.3	303.9	6.0	252	D	M
16	Bernal Fm.	−50.0	300.0	−52.5	303.2	−53.4	304.5	8.0	255	D	2489
17	Ochoan redbeds	−55.0	299.0	−59.5	305.3	−61.1	308.1	15.0	255	?	688
18	Upper Maroon Fm.[1]	−58.0	292.0	−66.2	304.2	−68.8	310.4	12.8	256	?	504
19	Guadalupian redbeds	−51.0	305.0	−54.7	310.2	−56.0	312.4	5.0	265	?	688
20	Toroweap Fm.	−52.0	305.0	−56.1	311.2	−57.5	313.7	10.0	273	?	688
21	Leonardian subset	−52.0	299.0	−55.0	302.6	−56.0	304.1	5.0	275	?	688
22	Artinskian Pictou redbeds[1]	−42.0	306.0	−41.0	305.9	−40.6	305.8	3.6	280	?	2281
23	Fountain and Lykins Fms.[1]	−45.0	306.0	−49.4	311.2	−50.9	313.4	13.1	285	?	504
24	Abo Fm.	−47.0	305.0	−49.3	308.1	−50.2	309.3	2.1	286	D	1311
25	Cutler Fm.[1]	−41.0	302.0	−42.5	303.6	−43.1	304.3	2.0	287	C	671
26	Cutler Fm.	−40.0	308.0	−43.0	311.7	−44.1	313.2	12.3	287	?	675

. . . Table 4.2 continued

#	Rock Unit	Plat	Plon	$Plat_{0.54}$	$Plon_{0.54}$	$Plat_{0.46}$	$Plon_{0.46}$	A_{95}	Age	Notes	Reference
27	Cutler Fm. (Lison Valley)	−41.0	308.0	−44.0	311.7	−45.1	313.2	7.1	287	C	1341
28	Upper Casper Fm.	−51.0	303.0	−58.3	313.1	−60.6	317.7	1.5	289	C	1455
29	Elephant Canyon Fm	−42.0	302.0	−44.1	304.3	−44.8	305.2	5.0	289	C	671
30	Ingelside Fm.	−43.0	308.0	−47.2	312.9	−48.7	314.8	2.0	292	C	1142
31	Minturn and Maroon Fms.	−40.0	301.0	−40.5	301.4	−40.6	301.5	2.8	298	?	1685
32	Dunkard Fm.	−44.0	303.0	−41.0	301.7	−39.8	301.2	3.9	300	?	302
33	Laborcita Fm.	−42.0	312.0	−43.2	313.5	−43.6	314.1	2.1	300	D	1311
34	Prince Edward Is. redbeds	−42.0	313.0	−41.7	312.9	−41.6	312.9	6.0	300	?	336
35	Prince Edward Is. redbeds	−41.0	306.0	−39.2	305.8	−38.5	305.7	5.8	300	?	276
	Igneous Records										
36	Cross Diatreme, British Columbia[2]	−49.0	295.0	-	-	-	-	6.0	245	-	W
37	Basic Sill, Prince Edward Is.	−52.0	293.0	-	-	-	-	5.0	252	-	431
38	Southern Illinois Intrusives ("IL")[2]	−56.3	302.9	-	-	-	-	3.8	270	-	This study

$Plat/Plon_{(0.54/0.46)}$: paleopole latitude/longitude (after inclination correction of f=0.54/0.46)

A_{95}: radius of cone of 95% confidence about the paleopole

Notes: D = ChRM interpreted to be a DRM

C = Original authors explicitly interpret ChRM to be a CRM

? = insufficient evidence to draw a conclusion about the nature of the ChRM

Reference = global paleomagnetic database reference lookup number or:

M = Molina-Garza et al. (2000), W = Wynne et al. (1992)

[1]Result included in the VGP distribution analysis

[2]Result not listed in Torsvik et al. (2008)

References

Baxter, J. W., & Desborough, G. A. (1965) Areal geology of the Illinois Fluorspar District: part 2, Karbers Ridge and Rosiclare quadrangles. *Illinois State Geological Survey Circular*, 40 pp.

Beck, M. E., Burmester, R. F., & Housen, B. A. (2003) The red bed controversy revisited: shape analysis of Colorado Plateau units suggests long magnetization times. *Tectonophysics*, 362, 335-344.

Bilardello, D., & Kodama, K. P. (2010) Rock magnetic evidence for inclination shallowing in the Early Carboniferous Deer Lake Group red beds of western Newfoundland. *Geophysical Journal International*, 181, 275-289.

Bradbury, J. C., & Baxter, J. W. (1992) Intrusive breccias at Hicks Dome, Hardin County, Illinois. *Illinois State Geological Survey Circular* 550, 23 pp.

Brandt, D., Ernesto, M., Rocha-Campos, A. C., & dos Santos, P. R. (2009) Paleomagnetism of the Santa Fé Group, central Brazil: implications for the late Paleozoic apparent polar wander path for South America. *Journal of Geophysical Research*, 114. doi:10.1029/2008JB005735.

Burruss, R. C., Richardson, C. K., Grossman, J. N., Lichte, F. E., & Goldhaber, M. B. (1992) Regional and microscale zonation of rare earth elements in fluorite of the Illinois-Kentucky Fluorspar District. *U.S. Geological Survey Open-File Report* 92-1, 6 pp.

Cederquist, D. P., Mac Niocaill, C., & Van der Voo, R. (1997) Application of Bingham statistics to a paleopole data set: towards a better definition of APWP trends? *Earth and Planetary Science Letters*, 146, 97-106.

Chesley, J. T., Halliday, A. N., Kyser, T. K., & Spry, P. G. (1994) Direct dating of Mississippi Valley-Type mineralization: use of Sm-Nd in fluorite. *Economic Geology*, 89, 1192-1199.

Cogné, J. P. (2003) PaleoMac; a Macintosh^{TM} application for treating paleomagnetic data and making plate reconstructions. *Geochemistry, Geophysics, Geosystems*, 4. doi:10.1029/2001GC000227.

Collinson, D. W. (1974) The role of pigment and specularite in the remanent magnetism of red sandstones. *Geophysical Journal of the Royal Astronomical Society*, 38, 253-264.

Creer, K. M., Irving, E., & Nairn, A. E. M. (1959) Palaeomagnetism of the Great Whin Sill. Geophysical *Journal of the Royal Astronomical Society*, 2, 306-323.

Currier, L. W. (1944) Geological and geophysical survey of fluorspar areas in Hardin County, Illinois. *U.S. Geological Survey Bulletin*, 59, 128 pp.

Denny, F. B., Fifarek, R. H., Guillemette, R. N., & Padgett, P. L. (2002) Petrographic and microprobe analysis of the Cottage Grove Dike (Saline County, Illinois). *Geological Society of America Program with Abstracts*, 34, 92-93.

Denny, F. B., Goldstein, A., Devera, J. A., Williams, D. A., Lasemi, Z., & Nelson, W. J. (2008) The Illinois-Kentucky Fluorite District, Hicks Dome, and Garden of the Gods in southeastern Illinois and northwestern Kentucky. *GSA Field Guide*, 12, 11-24.

Domeier, M., Van der Voo, R., Tomezzoli, R. N., Torsvik, T. H., Vizan, H., Dominguez, A., & Kirshner, J. (2009) Alternative Pangea Reconstructions: A Matter of Flawed Data? Implications of a new Early Triassic paleopole from Argentina. *American Geophysical Union Abstracts*, GP11A-05.

Domeier, M., Van der Voo, R., Tohver, E., Tomezzoli, R. N., Vizan, H., Torsvik, T. H., & Kirshner, J. (2011) New Late Permian paleomagnetic data from Argentina: Refinement of the apparent polar wander path of Gondwana. *Geochemistry, Geophysics, Geosystems*, 12. doi:10.1029/2011GC003616.

Elston, D. P., & Purucker, M. E. (1979) Detrital magnetization in red beds of the Moenkopi Formation (Triassic), Gray Mountain, Arizona. *Journal of Geophysical Research*, 84, 1653-1665.

Erickson, R. L., & Blade, L. V. (1963) Geochemistry and petrology of the alkalic igneous complex at Magnet Cove, Arkansas. *U.S. Geological Survey Professional Paper* 425, 95 pp.

Fifarek, R. H., Denny, F. B., Snee, L. W., & Miggins, D. P. (2001) Permian igneous activity in southeastern Illinois and western Kentucky: implications for tectonism and economic resources. *Geological Society of America Abstracts*, 33, 420.

Fisher, R. (1953) Dispersion on a sphere. *Proceedings of the Royal Society of London.* Series A. 217, 295-305.

Goldhaber, M. B., Folger, H. W., Taylor, C. D., Mosier, E. L., Gent, C. A., Hackley, K. C., et al. (1992) Paducah CUSMAP subsurface geochemical studies: mineral resources of the Illinois Basin in the context of basin evolution. *U.S. Geological Survey Open-File Report* 92-1, 14-16.

Gose, W. A., & Helsley, C. E. (1972) Paleomagnetic and rock-magnetic studies of the Permian Cutler and Elephant Canyon Formations in Utah. *Journal of Geophysical Research*, 77, 1534-1548.

Gradstein, F. M., Ogg, J. G., & Smith, A. G. (2004) A geologic time scale 2004. Cambridge University Press, Cambridge, 610 pp.

Harrison, C. G. A. (2009) Latitudinal signature of earth's magnetic field variation over the last 5 million years. *Geochemistry, Geophysics, Geosystems*, 10, Q02012. doi:10.1029/2008GC002298.

Heinrich, E. W. (1966) The geology of carbonatites. Rand McNally, Chicago, 555 p.

Herrero-Bervera, E., & Helsley, C. E. (1983) Paleomagnetism of polarity transition in the Lower(?) Triassic Chugwater Formation, Wyoming. *Journal of Geophysical Research*, 88, 3506-3522.

Hildenbrand, T. G., & Ravat, D. (1997) Geophysical setting of the Wabash Valley fault system: investigations of the Illinois Basin earthquake region. *Seismological Research Letters*, 68, 567-585.

Hodges, K. V. (1991) Pressure-temperature-time paths. *Annual Review of Earth and Planetary Sciences*, 19, 207-236.

Kent, D. V., & Irving, E. (2010) Influence of inclination error in sedimentary rocks on the Triassic and Jurassic apparent pole wander path for North America and implications for Cordilleran tectonics. *Journal of Geophysical Research*, 115, B10103.

Kent, D. V., & Tauxe, L. (2005) Corrected Late Triassic latitudes for continents adjacent to the North Atlantic. *Science*, 307, 240-244.

King, R. (1955) The remanent magnetism of artificially deposited sediments. *Geophysical Journal of the Royal Astronomical Society*, 7, 115-134.

Kirschvink, J. L. (1980) The least-squares line and plane and the analysis of palaeomagnetic data. *Geophysical Journal of the Royal Astronomical Society*, 62, 699-718.

Koenig, J. B. (1956) The petrography of certain igneous dikes of Kentucky. *Kentucky Geological Survey Bulletin*, 21, 57 pp.

Kolata, D. R., & Nelson, W. J. (1997) Role of the Reelfoot Rift/Rough creek graben in the evolution of the Illinois Basin: middle Proterozoic to Cambrian rifting, central North America. *Geological Society of America Special Paper*, 312, 287-298.

Krijgsman, W., & Tauxe, L. (2006) E/I corrected paleolatitudes for the sedimentary rocks of the Baja British Columbia hypothesis. *Earth and Planetary Science Letters*, 242, 205-216.

Luczaj, J. (1998) Argument supporting explosive igneous activity for the origin of "cryptoexplosion" structures in the midcontinent, United States. *Geology*, 26, 295-298.

Magnus, G., & Opdyke, N. D. (1991) A paleomagnetic investigation of the Minturn Formation, Colorado: a study in establishing the timing of remanence acquisition. *Tectonophysics*, 187, 181-189.

McFadden, P. L., & McElhinny, M. W. (1988) The combined analysis of remagnetization circles and direct observations in palaeomagnetism. *Earth and Planetary Science Letters*, 87, 161-172.

McGinnis, L. D., & Bradbury, J. C. (1964) Aeromagnetic study of the Hardin County area, Illinois. *Illinois State Geological Survey Circular*, 12.

McMahon, B. E., & Strangway, D. W. (1968) Investigation of Kiaman magnetic division in Colorado redbeds. *Geophysical Journal of the Royal Astronomical Society*, 15, 265-285.

Molina Garza, R. S., Geissman, J. W., & Lucas, S. G. (2000) Palaeomagnetism and magnetostratigraphy of uppermost Permian strata, southeast New Mexico, USA: correlation of the Permian-Triassic boundary in non-marine environments. *Geophysical Journal International*, 141, 778-786.

Molina-Garza, R. S., Geissman, J. W., Lucas, S. G., & Van der Voo, R. (1996) Palaeomagnetism and magnetostratigraphy of Triassic strata in the Sangre de Cristo Mountains and Tucumcari Basin, New Mexico, USA. *Geophysical Journal International*, 124, 935-953.

Molina-Garza, R. S., Geissman, J. W., & Van der Voo, R. (1989) Paleomagnetism of the Dewey Lake Formation (Late Permian), northwest Texas: end of the Kiaman superchron in North America. *Journal of Geophysical Research*, 94, 17,881-17,888.

Molina-Garza, R. S., Geissman, J. W., Van der Voo, R., Lucas, S. G., & Hayden, S. N. (1991) Paleomagnetism of the Moenkopi and Chinle Formations in central New Mexico: implications for the North American apparent polar wander path and Triassic magnetostratigraphy. *Journal of Geophysical Research*, 96, 14,239-14,262.

Opdyke, N. D., Roberts, J., Claoue-Long, J., Irving, E., & Jones, P. J. (2000) Base of the Kiaman: its definition and global stratigraphic significance. *Geological Society of America Bulletin*, 112, 1315-1341.

Padgett, P. L., Pilcher, D., Ames, P. R., Staub, J. R., & Denny, F. B. (2002) Igneous intrusions associated with the Cottage Grove fault system in southern Illinois: their effects on mine planning. *Geological Society of America Abstracts*, 34, 103.

Peterson, D. N., & Nairn, A. E. M. (1971) Palaeomagnetism of Permian redbeds from the south-western United States. *Geophysical Journal of the Royal Astronomical Society*, 23, 191-205.

Plumlee, G. S., Goldhaber, M. B., & Rowan, E. L. (1995) The potential role of magmatic gases in the genesis of Illinois-Kentucky Fluorspar deposits: implications from chemical reaction path modeling. *Economic Geology*, 90, 999-1011.

Potter, C. J., Goldhaber, M. B., Heigold, P. C., & Drahovzal, J. A. (1995) Structure of the Reelfoot-Rough Creek Rift System, fluorspar area fault complex, and Hicks Dome, southern Illinois and western Kentucky: new constraints from regional seismic reflection data. *U.S. Geological Survey Open-File Report* 92-1, 49-51.

Purucker, M. E., Elston, D. P., & Shoemaker, E. M. (1980) Early acquisition of characteristic magnetization in red beds of the Moenkopi Formation (Triassic), Gray Mountain, Arizona. *Journal of Geophysical Research*, 85, 997-1012.

Renne, P. R., Mundil, R., Balco, G., Min, K., & Ludwig, K. R. (2010) Joint determination of ^{40}K decay constants and ^{40}Ar*/^{40}K for the Fish Canyon sanidine standard, and improved accuracy for ^{40}Ar/^{39}Ar geochronology. *Geochimica Et Cosmochimica Acta*, 74, 5349-5367.

Reynolds, R. L., Goldhaber, M. B., & Snee, L. W. (1997) Paleomagnetic and ^{40}Ar/^{39}Ar results from the Grant Intrusive breccia and comparison to the Permian Downeys Bluff Sill: evidence for Permian igneous activity at Hicks Dome, Southern Illinois Basin. *U.S. Geological Survey Bulletin*, 2094-G, 16 pp.

Richardson, C. K., & Pinckney, D. M. (1984) The chemical and thermal evolution of the fluids in the Cave-in-Rock Fluorspar District, Illinois: mineralogy, paragenesis, and fluid inclusions. *Economic Geology*, 79, 1833-1856.

Riisager, P., Knight, K. B., Baker, J. A., Ukstins-Peate, I., Al-Kadasi, M., Al-Subbary, A., & Renne, P. R. (2005) Paleomagnetism and ^{40}Ar/^{39}Ar geochronology of Yemeni Oligocene volcanics: implications for timing and duration of Afro-Arabian traps and geometry of the Oligocene paleomagnetic field. *Earth and Planetary Science Letters*, 237, 647-672.

Rochette, P., Fillion, G., Mittei, J., & Dekkers, M. J. (1990) Magnetic transition at 30-34 Kelvin in pyrrhotite: insight into a widespread occurrence of this mineral in rocks. *Earth and Planetary Science Letters*, 98, 319-328.

Rochette, P., & Vandamme, D. (2001) Pangea B: an artifact of incorrect paleomagnetic assumptions? *Annali Di Geofisica*, 44, 649-658.

Ruiz, J., Richardson, C. K., & Patchett, P. J. (1988) Strontium isotope geochemistry of fluorite, calcite, and barite of the Cave-in-Rock Fluorite District, Illinois. *Economic Geology*, 83, 203-210.

Shive, P. N., Steiner, M. B., & Huycke, D. T. (1984) Magnetostratigraphy, paleomagnetism, and remanence acquisition in the Triassic Chugwater Formation of Wyoming. *Journal of Geophysical Research*, 89, 1801-1815.

Silverman, M., Pugin, A., Larson, T., Finley, R. (2003) Aeromagnetic and surface seismic surveys for dike detection in Illinois coal seams, Saline County, Illinois. *Illinois State Geological Survey Technical Report*, ICCI Project 02-1/US-2.

Sparlin, M. A., & Lewis, R. D. (1994) Interpretation of the magnetic anomaly over the Omaha oil field, Gallatin County, Illinois. *Geophysics*, 59, 1092-1099.

Spry, P. G., Koellner, M. S., Richardson, C. K., & Jones, H. D. (1990) Thermochemical changes in the ore fluid during deposition at the Denton Mine, Cave-in-Rock Fluorspar District, Illinois. *Economic Geology*, 85, 172-181.

Steiger, R. H., & Jaeger, E. (1977) Subcommission on geochronology: convention on the use of decay constants in geo- and cosmochronology. *Earth and Planetary Science Letters*, 36, 359-362.

Steiner, M. B. (1988) Paleomagnetism of the Late Pennsylvanian and Permian; a test of the rotation of the Colorado Plateau. *Journal of Geophysical Research*, 93, 2201-2215.

Steiner, M. B., & Lucas, S. G. (1992) A Middle Triassic paleomagnetic pole for North America. *Geological Society of America Bulletin*, 104, 993-998.

Steiner, M. B., Morales, M., & Shoemaker, E. M. (1993) Magnetostratigraphic, biostratigraphic, and lithologic correlations in Triassic strata of the western United States. Applications of paleomagnetism to sedimentary geology. *Society of Economic Paleontologists and Mineralogists - Special Publication*, 49, 41-57.

Symons, D. T. A. (1990) Early Permian pole: evidence from the Pictou red beds, Prince Edward Island, Canada. *Geology* (Boulder), 18, 234-237.

Symons, D. T. A. (1994) Paleomagnetism and the Late Jurassic genesis of the Illinois-Kentucky Fluorspar deposits. *Economic Geology*, 89, 438-449.

Symons, D. T. A., Bormann, R. E., & Jans, R. P. (1989) Paleomagnetism of the Triassic red beds of the lower Fundy Group and Mesozoic tectonism of the Nova Scotia platform, Canada. *Tectonophysics*, 164, 13-24.

Tanaka, H. (1999) Circular asymmetry of the paleomagnetic directions observed at low latitude volcanic sites. *Earth, Planets and Space*, 51, 1279-1286.

Tauxe, L. (1998) Paleomagnetic principles and practice. *Modern Approaches in Geophysics*,17, Kluwer Academic Publishers, Dordrecht, Netherlands. 299 pp.

Tauxe, L. (2005) Inclination flattening and the geocentric axial dipole hypothesis. *Earth and Planetary Science Letters*, 233, 247-261.

Tauxe, L., & Kent, D. V. (1984) Properties of a detrital remanence carried by haematite from study of modern river deposits and laboratory redeposition experiments. *Geophysical Journal of the Royal Astronomical Society*, 76, 543-561.

Tauxe, L., & Kent, D. V. (2004) A simplified statistical model for the geomagnetic field and the detection of shallow bias in paleomagnetic inclinations: was the ancient magnetic field dipolar? Timescales of the paleomagnetic field. *American Geophysical Union - Geophysical Monograph*, 145, 101-115.

Tauxe, L., & Kodama, K. P. (2009) Paleosecular variation models for ancient times: clues from Keweenawan lava flows. *Physics of the Earth and Planetary Interiors*, 177, 31-45.

Tauxe, L., Kodama, K. P., & Kent, D. V. (2008) Testing corrections for paleomagnetic inclination error in sedimentary rocks: a comparative approach. *Physics of the Earth and Planetary Interiors*, 169, 152-165.

Tauxe, L., Mullender, T. A. T., & Pick, T. (1996) Potbellies, wasp-waists, and superparamagnetism in magnetic hysteresis. *Journal of Geophysical Research*, 101, 571-583.

Taylor, C. D., Rowan, E. L., Goldhaber, M. B., & Hayes, T. S. (1992) A relationship between Hicks Dome and temperature zonation in fluorite in the Illinois-Kentucky Fluorspar District - a fluid inclusion study. *U.S. Geological Survey Open-File Report* 92-1, 62-64.

Torsvik, T. H., Muller, R. D., Van der Voo, R., Steinberger, B., & Gaina, C. (2008) Global plate motion frames: toward a unified model. *Reviews of Geophysics*, 46, 1-44.

Trace, R. D., & Amos, D. H. (1984) Stratigraphy and structure of the western Kentucky Fluorspar District. *U.S. Geological Survey Professional Paper* 1151-D, 41 pp.

Walker, J. D., & Geissman, J. W. (compilers). (2009) Geologic time scale. *Geological Society of America*, doi: 10.1130/2009.

Wynne, P. J., Irving, E., Schulze, D. J., Hall, D. C., & Helmstaedt, H. H. (1992) Paleomagnetism and age of three Canadian Rocky Mountain diatremes. *Canadian Journal of Earth Sciences*, 29, 35-47.

Yan, M., Van der Voo, R., Tauxe, L., Fang X., & Parés, J. M. (2005) Shallow bias

in Neogene palaeomagnetic directions from the Guide Basin, NE Tibet caused by inclination error. *Geophysical Journal International*, 163, 944-948.

Zartman, R. E., Brock, M. R., Heyl, A. V., & Thomas, H. H. (1967) K-Ar and Rb-Sr ages of some alkalic intrusive rocks from central and eastern United States. *American Journal of Science*, 265, 848-870.

Zijderveld, J. D. A. (1967) A.C. demagnetization of rocks: analysis of results. In: D. W. Collinson, K. M. Creer and S. K. Runcorn, (Eds.), *Methods in Paleomagnetism*, Elsevier, Amsterdam. 254 pp.

CHAPTER V

Paleomagnetism and Pangea: the road to reconciliation

5.1 Abstract

Outside the realm of paleomagnetic studies, it has been a long held tenet that Pangea amalgamated into and disseminated from essentially the same paleogeography, the conventional Pangea reconstruction of Alfred Wegener. There is widespread geologic and geophysical support for this continental configuration during the Late Triassic–Early Jurassic, but global paleomagnetic data have been repeatedly shown to be incompatible with this reconstruction for pre-Late Triassic time. This discrepancy, which has endured from the late 1950s to the present day, has developed into a fundamental enigma of late Paleozoic–early Mesozoic paleomagnetism. The problem stems from a large disparity in the apparent polar wander paths (APWPs) of Laurussia and Gondwana when the landmasses are restored to the conventional fit. If the APWPs are forced to coincide while some semblance of this fit is maintained, a substantial crustal overlap (> 1,000 km) results between Laurussia and Gondwana. To resolve this problem, alternative Pangea reconstructions have been built to accommodate the paleomagnetic data, but these invariably require large-scale shearing between Laurussia and Gondwana to reach the conventional configuration,

Citation:
Domeier, M., Van der Voo, R., & Torsvik, T. H. (2012). Paleomagnetism and Pangea: the road to reconciliation. *Tectonophysics*, in press.

from which it is unanimously agreed that the Atlantic Ocean opened in the Jurassic. Evidence for a megashear between these landmasses is critically lacking. Another proposed solution invokes time-dependent non-dipole fields, but challenges the common assumption that the geomagnetic field has effectively been a geocentric axial dipole through the Phanerozoic. The remaining alternative is that the problem is a manifestation of artifacts/contamination in the paleomagnetic data. Here we review the historical development of this problem and conduct an up-to-date re-analysis. Using the most recent late Paleozoic–early Mesozoic paleomagnetic data, we examine the influence of data-quality, refined continental fits, and theoretical inclination shallowing corrections, and confirm that the paleomagnetic data can be reconciled with Pangea, without invoking alternative reconstructions or non-dipole fields.

5.2 Introduction

While a vast array of geological and geophysical data support the conventional paleogeographic model of Pangea for the Jurassic, it has been known since the earliest paleomagnetic investigations of Pangea that the late Paleozoic–early Mesozoic paleomagnetic data are incompatible with this reconstruction. Paleomagnetic analysis is the only quantitative method for determining paleolatitude prior to the Cretaceous, so this prominent model-data discrepancy is a fundamental problem that undermines the conclusions drawn from innumerous studies of pre-Jurassic tectonics. Here we review the development of this problem, which has endured for more than a half-century, and present a new analysis that enables us to reconcile the paleomagnetic data and the conventional paleogeographic model. We begin with a historical perspective, including the early recognition of the model-data discrepancy, and an account of some early paleomagnetic observations from Europe which curi-

ously foretell the broader course of this work. Our review continues with a summary of the various solutions that have been proposed to explain the discrepancy, and their counter-arguments. From there we consider what roles data-quality, reconstruction parameters, and sedimentary inclination shallowing play in this problem, and we end with a discussion of the implications these findings have on Pangea reconstructions.

5.3 Historical Development of Pangea and Early Problems

5.3.1 The Origins of Pangea A

The origin of Pangea, as a concept, has been attributed to the 16^{th} century geographer Abraham Ortelius, who perhaps first noted the congruency of the peri-Atlantic coasts of America, Europe, and Africa, in his 1596 Thesaurus Geographicus (Romm, 1994). Two and a half centuries later, Snider-Pellegrini (1858) drafted the first paleogeographic map of what would later be recognized as Pangea (Fig. 1.1), and, notably, remarked on some geologic relicts common to the peri-Atlantic continents. But, it wasn't until the early 20^{th} century that Pangea was introduced to mainstream science as a defensible paleogeographic model (Wegener, 1915; 1922), presented as the vanguard of the then-contentious hypothesis of continental drift; it took another half-century of impassioned, community-wide debate before Pangea, and its precondition of tectonic mobility, was broadly adopted (Hallam, 1973). Remarkably, the geographic framework of Wegener's Pangea (he called it "Urkontinent") has endured as the conventional late Paleozoic–early Mesozoic paleogeographic model, with minor modification, despite the gross continental distortion in his reconstruction (Fig. 5.1). This paleogeography, which is also known as Pangea "A", results from simple closure of the Atlantic so that Africa lies to the south of Europe and is juxtaposed with the eastern seaboard of North America, and South America lies to the south of North America. Yet, even before plate tectonics gained general acceptance, nascent

alternatives to this model were being formulated. Alexander du Toit, best-known as an early promulgator of Wegener's ideas of continental drift, treated Gondwana and Laurussia as independent, in contrast to the unified and internally rigid Pangea of Wegener (du Toit, 1937). Fundamentally, it is this challenge to the model of a single, largely static landmass that the following arguments adhere; and, invariably, the alternative reconstructions return to the general supercontinental boundaries of du Toit (Irving, 2004).

Figure 5.1: Late Paleozoic reconstruction of Pangea ("Urkontinent"), according to Wegener (1922); the classic "A-type" reconstruction. Note the prominent distortion of India, among more minor flaws.

5.3.2 Initial Paleomagnetic Tests

Carey (1958) improved upon the schematic reconstruction of Wegener (1922) through a semi-quantitative "orocline analysis", which involved the closing of ocean basins through continental rotations that straightened curved mountain belts. Interestingly, one of the most prominent features introduced in Carey's treatise, a hypothetical intra-continental shear zone called the Tethyan Shear System, anticipated a series of similar structures later invoked to reconcile global paleomagnetic data; we shall return to this shortly. While some aspects of Carey's synthesis are

now recognized as invalid, the resulting reconstruction was effectively identical to Wegener's, but, importantly, comparatively free of distortion (Fig. 5.2). For example, Carey (1958) verified the actuality of the South American–African continental margin congruence by means of movable spherical tracings on a globe, countering criticism that the fit was only apparent or an artifact of projection. Using the very few paleomagnetic data from North America and Europe available at the time (which, moreover, predated routine laboratory demagnetization and principal component analysis), Carey (1958) and Irving (1958) were able to show the first-order veracity of the reconstruction of the northern continents (Laurussia) for the late Paleozoic and early Mesozoic. With respect to the global reconstruction, however, Jaeger and Irving (1957) discovered a disparity in the position of the late Paleozoic–early Mesozoic paleopoles of Laurussia and Australia, and concluded that the reconstruction was in need of revision (Fig. 5.2). Similarly, Carey (1958) noted a wider scatter in the Carboniferous and Permian paleopoles (from both Laurussia and Gondwana), relative to those from the Triassic and Jurassic. He interpreted this to be an indication that the reconstruction was only appropriate for the latter periods, and that additional (late Paleozoic) strain would need to be reversed in order to reach the true paleogeography of the late Paleozoic. Although preliminary, these early observations represent the inception of the conundrum that has persisted to the present day: the paleomagnetic data appear irreconcilable with the conventional paleogeographic model of Pangea for late Paleozoic–early Mesozoic time.

5.3.3 The Tethys Twist

In the early 1960s, students of the University of Utrecht, under the supervision of R.W. Van Bemmelen, began conducting routine paleomagnetic investigations during their graduate studies. From the course of this work it was discovered that Per-

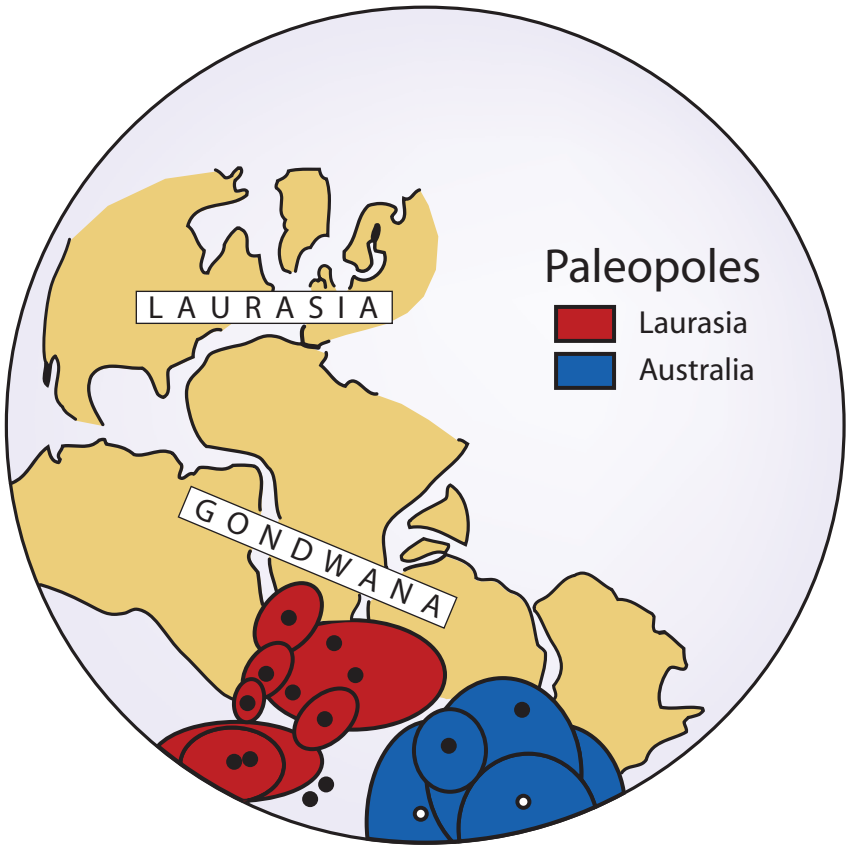

Figure 5.2: Semi-quantitative Pangea reconstruction of Carey (1958), generated in part by his "orocline analysis". Distortion was minimized through the use of spherical tracings, but Carey ultimately abandoned a completely distortion-free approach to achieve a good fit. Superposed are the late Paleozoic–early Mesozoic paleomagnetic data of Jaeger and Irving (1957), showing the already-then recognized disparity between data from Laurussia (Laurasia) and Gondwana (Australia). From Irving (2004).

mian rocks from Alpine Europe repeatedly yielded paleomagnetic poles that were incompatible with those derived from stable (interior) Europe (Dietzel, 1960; Van der Lingen, 1960; Van Hilten, 1962; 1964; De Boer, 1963; 1965; Guicherit, 1964; and references therein). Although it was initially considered plausible that these "anomalous" results were discordant due to insufficient averaging of secular variation, an internal consistency among them became apparent as the number of studies grew, and this seemed to imply a common tectonic origin for the anomalous poles. The Permian paleomagnetic directions from Alpine Europe were consistently steeper than those determined from rocks from the stable interior; the inclinations from Alpine Europe ranged from -20° (northeastern Spain) to -30° (northern Italy), vs. the expected range of -5° to +5° extrapolated from stable Europe (Fig. 5.3). The smallest theoretical displacement of Alpine Europe that could explain the observed anomalous inclinations was immediately recognized as untenable, as it would require the region to occupy the same space as northern Europe during the Permian. It was also regarded as implausible that Alpine Europe had drifted northward from the southern hemisphere, as the declinations were approximately south-directed, in agreement with the concomitant Kiaman Reversed Superchron (∼318–265 Ma). Drift from the southern-hemisphere would have been accompanied by a requisite ∼180° rotation, necessitating that the original (Permian) magnetizations were acquired in a normal polarity field, in violation of the Kiaman Reversed Superchron.

Instead, De Boer (1963; 1965) and Van Hilten (1964), recognizing the longitude indeterminacy of paleomagnetic data, argued that Alpine Europe was far-traveled, originating $>$ 4,500 km to the east of its present location (near present-day Pakistan), where the -20°/-30° paleoisoclines, extrapolated from stable Europe, intersected the Tethyan mobile belt (Fig. 5.4). Building on the conceptual idea of a Tethyan Shear

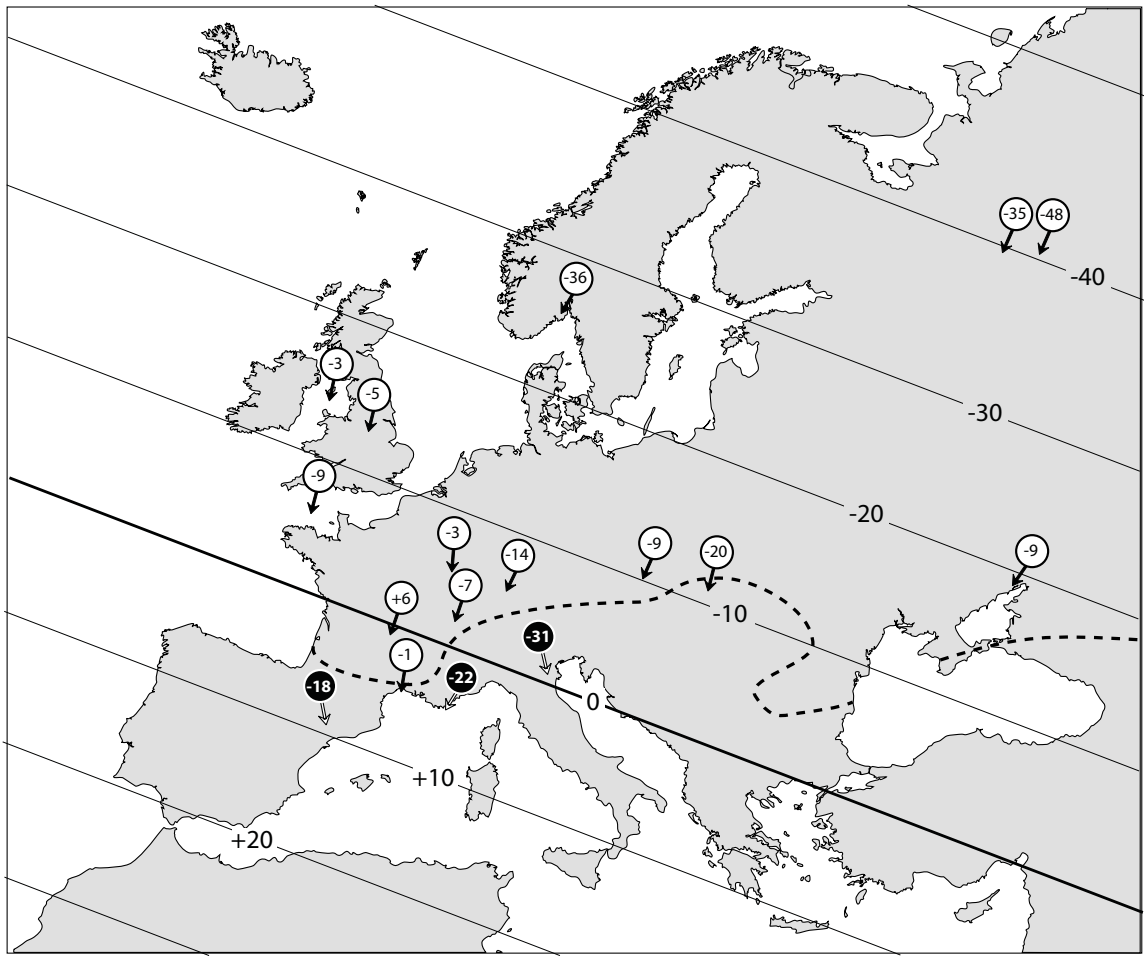

Figure 5.3: Permian isocline map redrawn after Van Hilten (1964) and De Boer (1965). The circles represent locations of paleomagnetic study: the values denote the mean inclination and the arrows portray the mean declination as measured in rocks from these locations. The dashed line separates Alpine Europe (filled circles) from stable interior Europe (open circles). The Permian isoclines were determined from the stable European results, which are in stark disagreement with the neighboring inclinations from Alpine Europe. Later work showed both populations of results to be in need of improvement (see text).

System (Carey, 1958) and the Indian Ocean "mega-undations" of Van Bemmelen (see Van Bemmelen, 1966), Van Hilten (1964) and De Boer (1965) postulated that Alpine Europe was transported > 4,500 km along a dextral megashear between Laurussia and Gondwana, which ran parallel to their Tethyan margins (see also Irving, 1967). It was suggested that Alpine Europe was an extension of Gondwana, and therefore moving in concert with it, until it was "smeared off" during Alpine orogenesis. Accordingly, the megashear was determined to be active from Permian to Eocene time through a comparison of Triassic and Cenozoic paleomagnetic data from Alpine Europe with that of stable Europe (De Boer, 1965); Van Hilten (1964) called this ∼200 Myr event the "Tethys Twist".

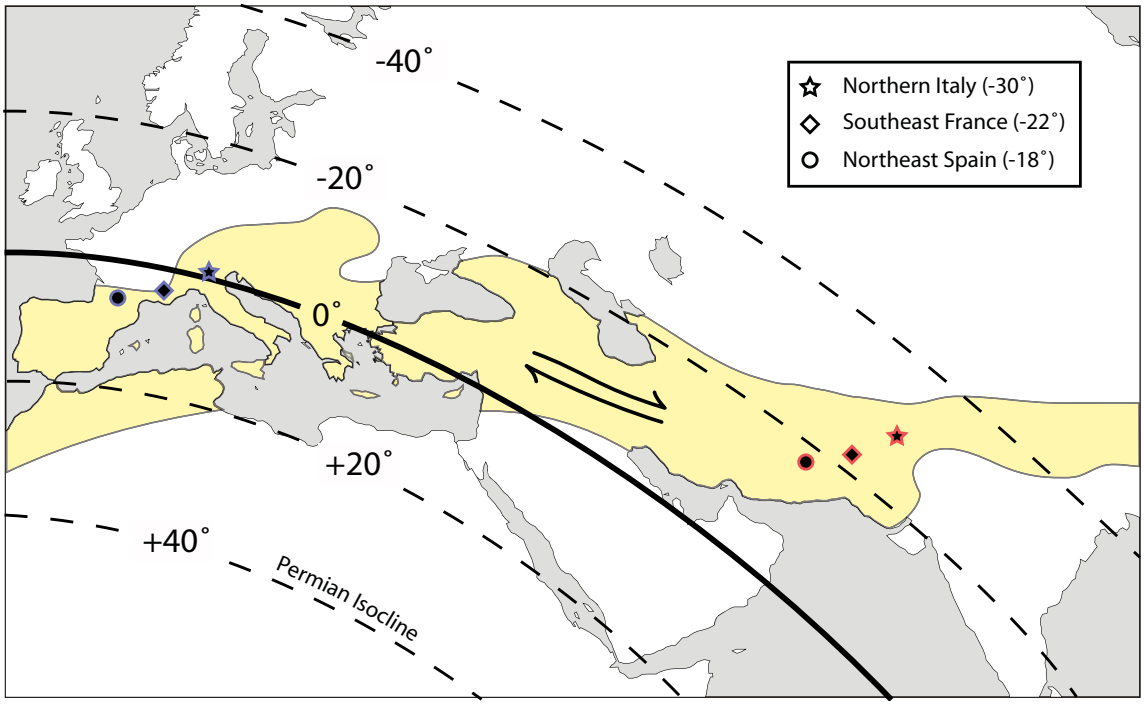

Figure 5.4: Extrapolation of Permian isoclines from Fig. 5.3 along the "Tethyan mobile belt" (yellow zone). Van Hilten (1964) and De Boer (1965) concluded that the anomalous inclinations observed in Alpine Europe (Fig. 5.3), here denoted as solid shapes with blue outlines, must have been transported along a dextral megashear from where the -20° Permian isocline meets the Tethyan mobile belt (solid shapes with red outlines). The arrows illustrate the inferred dextral sense of motion between Gondwana + Alpine Europe with respect to stable Eurasia. Redrafted from De Boer (1965) and Irving (2004).

Subsequent studies of late Mesozoic and Cenozoic tectonics have demonstrably shown the postulated timing of the Tethys Twist to be indefensible. More importantly, the underlying paleomagnetic argument was refuted by later paleomagnetic work, which demonstrated that the reported Permian reference magnetization directions (from stable Europe; Fig. 5.3) were too shallow, due to contamination by viscous overprints (Zijderveld, 1967). Similarly, successive paleomagnetic work in northern Italy demonstrated that the Permian inclinations from this region, as reported by Van Hilten (1964) and De Boer (1965), were too steep (Zijderveld et al., 1970). Using the more reliable stable European paleomagnetic results of Zijderveld (1967), Hospers and Van Andel (1969) showed that there was no longer a statistically significant difference between the inclinations measured from rocks in Alpine Europe vs. the expected inclinations extrapolated from reference directions from stable Europe. And so the Tethys Twist was refuted. Yet, it would be less than a decade before a renewed model of intra-continental dextral megashear would be proposed on the grounds of disparate paleomagnetic data between Laurussia and Gondwana.

5.4 Quantitative A-type Pangea Reconstructions

5.4.1 Pangea A-1

The first quantitative reconstruction of the Atlantic-bordering continents was produced by Bullard et al. (1965) by least-squares fitting of the 500 fathom bathymetric contours of the continental margins, performed by computer (Fig. 1.2). Modifications to the modern margins, including the omission of prominent Cenozoic features, such as the Niger Delta, and the rotation of the Iberian Peninsula to close the Bay of Biscay, were minimal. The result was a landmark achievement that illustrated the remarkable congruence of the Atlantic coastlines, free of relative distortion. Smith and Hallam (1970) applied this technique to the task of reconstructing Gondwana,

which allowed them to verify and refine the earlier work of du Toit (1937). Being similar in framework to the conceptual reconstruction of Pangea A (Wegener, 1922), the reconstruction built from the combined parameters of Bullard et al. (1965) and Smith and Hallam (1970) has become known as Pangea A-1 (Fig 5.5a). Although numerous modifications have been proposed for the peri-Atlantic fit of the A-1 reconstruction (Dietz and Holden, 1970; LePichon et al., 1977, etc.), they have generally been minor and the parameters of Bullard et al. (1965) have endured as the conventional reference. An important exception is the Euler rotation used to bring Laurussia and Gondwana together (thereby closing the Central Atlantic), which, as noted by Bullard et al. (1965), is the least well-constrained parameter, due to the non-unique fit of the Central Atlantic continental margins. This ill-defined reconstruction parameter exerts a strong control on the separation of North and South America (present-day Gulf of Mexico), which is relatively large in the A-1 reconstruction. By reducing this continental gap through a modification of the Euler rotation, West Gondwana can be more tightly fit against southern North America; we consider the paleomagnetic and geologic consequences of this adjustment next.

5.4.2 Pangea A-2

Van der Voo and French (1974) tested the Pangea A-1 fit of Bullard et al. (1965) with late Paleozoic and Mesozoic paleomagnetic data from North America, Europe, and West Gondwana. Although they concluded that the fit along the North Atlantic was satisfactory, according to good agreement among the paleomagnetic poles from North America and Europe, they reported a distinct and systematic difference between the late Paleozoic poles of West Gondwana and Laurussia. Yet, the late Paleozoic APWPs defined by these distinct pole populations shared a common trend, such that they could be brought into alignment (although with skewed ages) by a

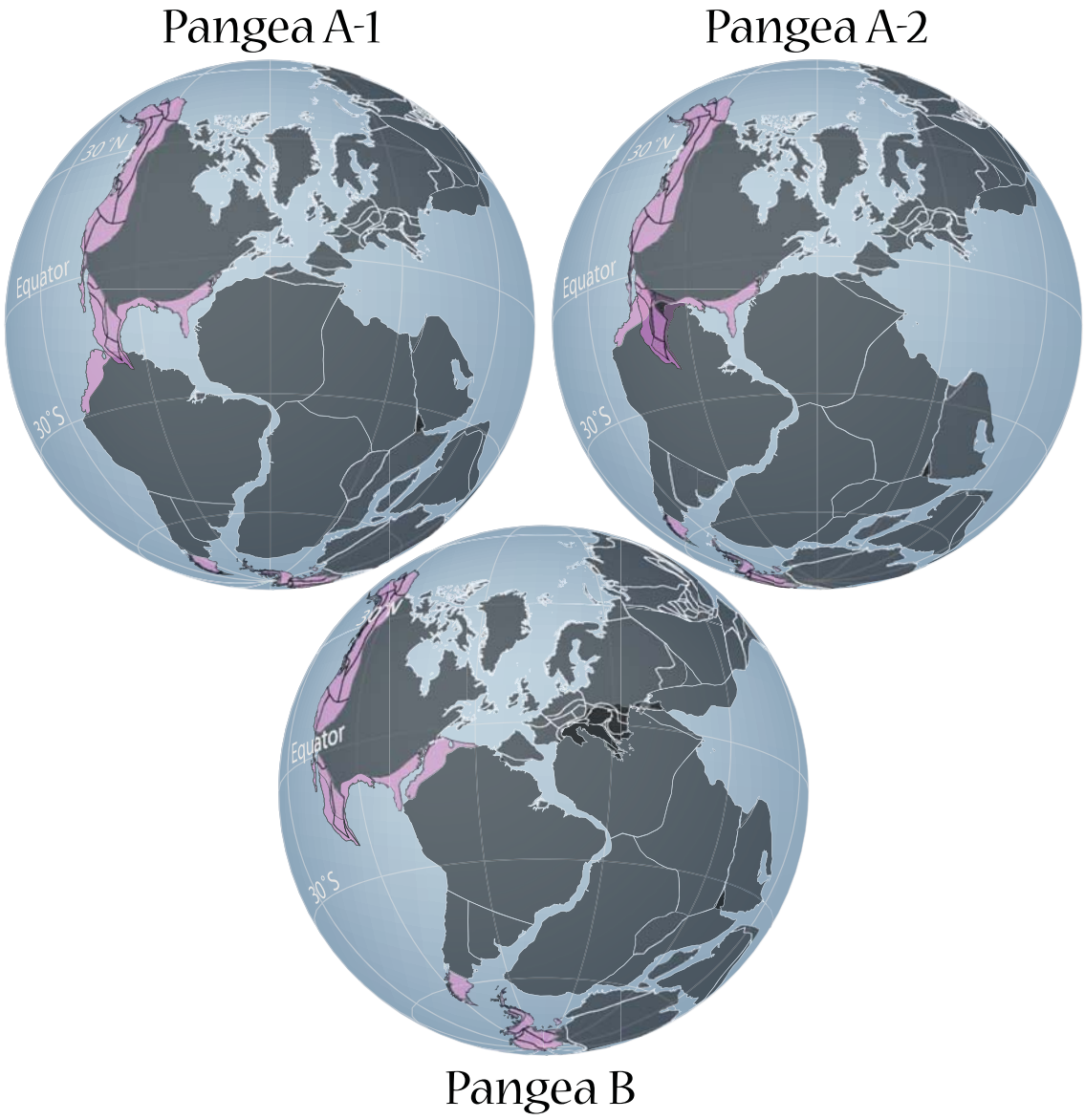

Figure 5.5: A comparison of proposed Pangea reconstructions. Pangea A-1 after Bullard et al. (1965). Pangea A-2 after Van der Voo and French (1974). Pangea B after Irving (1977) and Morel and Irving (1981). The (pink) highlighted regions are not correctly positioned, but we have kept them in their present-day configuration so as to be comparable with other published illustrations. Redrafted after Livermore et al. (1986).

single ∼20° clockwise rotation applied to Gondwana, about an Euler pole situated in the southern Sahara. This rotation effectively closes the Gulf of Mexico gap in the Pangea A-1 fit, bringing northern South America into a snug fit with southern North America (Fig. 5.5b). This modified A-type reconstruction, which was earlier proposed by LePichon and Fox (1971) and Walper and Rowett (1972) on geologic grounds, is called Pangea A-2. As discussed by Van der Voo et al. (1976), this model improves the alignment of late Paleozoic orogenic belts and provides a more reasonable paleogeographic setting for the Florida peninsula, but it also complicates any scheme describing the tectonic evolution of Central America and the Caribbean, as it eliminates the space for northern Mexico and its neighboring continental blocks (Yucatan, Cuba, etc.) in the Gulf of Mexico. Consequently, most subsequent Central Atlantic reconstructions (Klitgord and Schouten, 1986; Lottes and Rowley, 1990; Labails et al., 2010) have selected reconstruction parameters intermediate between the "loose" A-1 fit of Bullard et al. (1965) and the "tight" A-2 fit of Van der Voo and French (1974). Nonetheless, the A-1 and A-2 models remain useful as reference points; the term "Pangea A" will be used as a broad reference to these models in general.

5.5 Alternatives to A-type Reconstructions

5.5.1 Pangea B

By the late 1970s there was widespread agreement that the paleogeography of Early Jurassic time—just prior to the opening of the Central Atlantic—was essentially that of Pangea A. This was perhaps most convincingly demonstrated by detailed correlations of conjugate sea floor magnetic anomalies and marine fracture zones (see Klitgord and Schouten, 1986), but Early Jurassic paleomagnetic data were also shown to be in good agreement with Pangea A. However, the relevance of this

paleogeography in earlier Mesozoic and late Paleozoic time, from which no in situ seafloor survives, was disputed on paleomagnetic grounds by Irving (1977), Westphal (1977), Kanasewich et al. (1978), Morel and Irving (1981), and others later.

Irving (1977) conducted an analysis using Pangea A reference latitudes: arbitrarily selected reference localities on the margins of the peri-Atlantic continents that would have been juxtaposed in Pangea A. If these continents are restored to the paleolatitudes dictated by their independent paleomagnetic data for a particular time, the reference latitudes can be compared, and significant relative differences can be interpreted as a failure of the Pangea A reconstruction for that specific time. Irving found that the paleomagnetic data agreed with Pangea A for the Early Jurassic, but could not be rectified with the model in Permian or Triassic time (Fig. 5.6a). Specifically, he found significant disagreement ($\sim 10^{\circ}$) between the North American and European reference latitudes for the Triassic, and a significant and persistent difference in the North American and Gondwanan reference latitudes for pre-Jurassic time. The relative difference of the latter implied that, during the Permian and much of the Triassic, Gondwana must have been farther north, relative to North America, than its position specified by Pangea A. This was particularly problematic because, in Pangea A, northwestern Africa is fit snugly against the eastern seaboard of North America and is juxtaposed with southwestern Europe, and South America is positioned directly south of North America; significant northward displacement of Gondwana, relative to these northern continents, would therefore result in implausible cratonic overlap (Fig. 5.6b).

To resolve this problem, Irving (1977) returned to the conceptual ideas of Van Hilten (1964) and De Boer (1965). Again noting the longitude indeterminacy of paleomagnetic data, he shifted Gondwana east, relative to the northern continents,

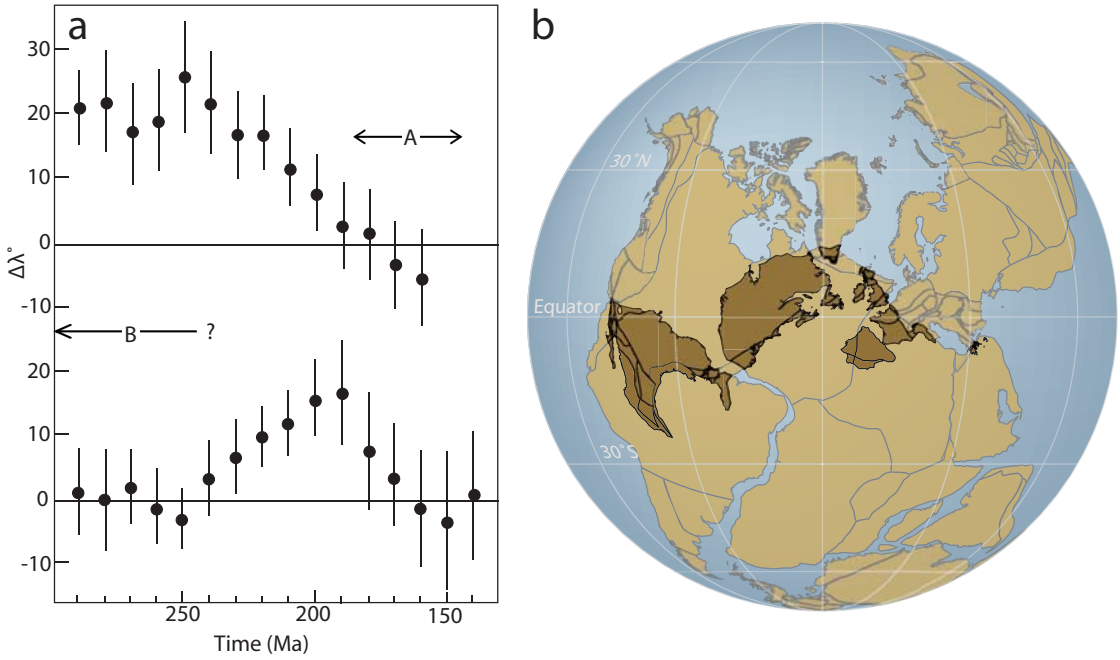

Figure 5.6: The rationale for Pangea B. (a) Latitude differences ($\Delta\lambda^\circ$) between Pangea A reference latitudes in North America and Gondwana (top panel) and North America and Europe (bottom panel) as a function of time. The interpreted duration of Pangea B and A are denoted. From Irving (1977). (b) Continental overlap that results if an A-type reconstruction is forced, using the 260 Ma paleomagnetic data of Morel and Irving (1981) to reconstruct Laurussia and Gondwana.

where it could occupy the more northerly position indicated by the paleomagnetic data, without resulting in continental overlap. The result is a paleogeography where Africa is beneath central Europe and South America is juxtaposed with the eastern seaboard of North America (Fig. 5.5c). Also, the western Tethys is replaced with northern Africa and southern North America is flanked by open ocean. Irving (1977) called this configuration Pangea "B" and he considered it relevant from the mid-Carboniferous to the end Permian/earliest Triassic, in accordance with the paleomagnetic data. However, the geological and geophysical data overwhelmingly indicate that the Atlantic opened from Pangea A, requiring Pangea B to transform to Pangea A during the Middle–Late Triassic. In a proposal evocative of the Tethys Twist, Irving (1977) hypothesized that this transformation occurred via a ∼3,500 km dextral megashear between Gondwana and Laurussia. He further speculated that the westward displacement of Gondwana caused North America to move northward, relative to Europe, thereby causing the difference he observed in their reference latitudes during the Triassic.

The initial proposal of Pangea B was shortly followed by the paleomagnetic studies of Kanasewich et al. (1978) and Morel and Irving (1981), which re-affirmed the general conclusions of Irving (1977), namely the necessity of Pangea B in the Carboniferous and Permian, by re-evaluating the agreement between late Paleozoic and Mesozoic paleomagnetic data from the major continents, when rotated into different Pangea reconstructions. These conclusions were later reiterated by Torcq et al. (1997) and, most recently, by Rapalini et al. (2006), but were based on limited datasets. Torcq et al. (1997) compared an updated (to 1996) Permo-Triassic paleomagnetic dataset from Laurussia against a comparatively dated dataset from Gondwana, which included only two post-1980 results. Notably, with the updated

dataset from Laurussia, they did not detect a significant difference between the Triassic paleopoles of North America and Europe, as observed by Irving (1977) and Morel and Irving (1981). The study of Rapalini et al. (2006) incorporated several additional post-1980 paleopoles from Gondwana, but exclusively from Argentina and Peru; paleomagnetic data from the other Gondwana blocks were not included in the analysis, which compared the South American Permo-Triassic data against the North American APWP of McElhinny and McFadden (2000).

Westphal (1977) also determined that the paleogeography of the Permian was essentially that of Pangea B, but arrived at this conclusion by different means. He performed a spherical harmonic analysis using Permian paleomagnetic data from Laurussia and Gondwana and found that he could best align the center of the apparent offset dipoles, calculated from the data of each landmass, by rotating them into a Pangea B geometry. Although novel, this analysis must be considered dubious. A reliable spherical harmonic analysis requires a robust dataset, ideally one with a global distribution of observations; the small amount of geographically restricted data utilized in this study is most certainly inadequate. Additionally, the apparent persistence of the offset dipole may imply that the Permian paleomagnetic data used do not constitute a time-averaged field, and therefore may not be comparable, or representative of the Permian. Finally, the physical interpretation of the generating field is non-unique; the effects of an offset dipole can be equally well expressed by a series of non-dipole fields. Given the latter observation, a persistent offset dipole, if a lasting geomagnetic characteristic, could be a manifestation of a long-term non-dipole element in the paleomagnetic field, which calls into question the fundamental assumption implicit in traditional paleomagnetic reconstructions. We will return to this last point in section 5.6.

5.5.2 The Intra-Pangean Megashear

Pangea B—being built to accommodate the paleomagnetic data—presents several serious geologic problems. Ross (1979) and Hallam (1983) showed paleobiogeographic, stratigraphic, and structural evidence to be in greater accord with Pangea A. The paleontologic argument includes the recognition of strong faunal affinities among Permian invertebrates in southern North America and northwestern South America, and similarities between late Paleozoic flora and fauna of northern Africa and western Europe–eastern North America, rather than central Asia. The stratigraphic argument similarly links comparable late Paleozoic sedimentary facies between southern North America and northwestern South America, and between northern Africa and western Europe–eastern North America. However, the most serious challenge to Pangea B is the structural argument against it, which cites an absence of evidence for the proposed ∼3,500 km dextral megashear in the Triassic. Although it must be emphasized that an absence of evidence is not equivalent to an evidence of absence, it does pose a critical question about the validity of the model. Given the magnitude of the supposed structure, and the irregular geometry of the plate boundary between Laurussia and Gondwana, it would be expected that the Pangea B to A transformation would leave abundant structural relics. Specifically, dextral motion upon the plate boundary would subject southwestern Europe to regional transpression, whereas the southern margin of North America would experience regional transtension, in addition to local expressions of transpression/transtension along bends in the trace of the shear zone, or en echelon structures (Hallam, 1983; Smith and Livermore, 1991; Weil et al., 2001). However, as discussed by Hallam (1983) and Smith and Livermore (1991), the mid-Permian to Middle Triassic was a tectonically stable interval; evidence for extension in southern North America or compression in south-

western Europe is minimal. Oft-referenced in discussions of the Pangean megashear, the conclusions of Arthaud and Matte (1977), namely that the Laurussia-Gondwana boundary may have acted as dextral shear zone, are only applicable to late Paleozoic time—too old to be pertinent to the Triassic transformation proposed by Irving (1977) and Morel and Irving (1981) (see also, Gates et al., 1986). Moreover, the displacements estimated on the principal faults are an order of magnitude smaller than required by the proposed transformation (Arthaud and Matte, 1977; Gates et al., 1986; Smith and Livermore, 1991). Finally, the adoption of Pangea B would require a fundamental re-consideration of conventional models of late Paleozoic orogenesis, as the Appalachian–Mauritanide–Variscan belt would have developed from a very different incipient framework than generally accepted. In Pangea B, the Ouachita-Marathon margin is open to the Panthalassa, the Appalachians are juxtaposed with the northern Andes, and the European Variscan margin is opposite western Africa (Fig. 5.5c).

5.5.3 A Revision in Timing

Beginning with Muttoni et al. (1996), several more recent paleomagnetic investigations have concluded that although the Carboniferous–Early Permian paleomagnetic data from Laurussia and Gondwana are suggestive of a Pangea B paleogeography, the Late Permian–Triassic paleomagnetic data can be reconciled with Pangea A (Muttoni et al., 2003; 2009, Rakotosolofo et al., 2006). The obvious implication borne from this conclusion is that the transformation from Pangea B to A must have been initiated and largely completed within the Permian period, contrary to the Triassic-age assigned to the event by earlier work (as discussed above).

The analysis of Muttoni et al. (1996) chiefly differs from the preceding studies by the use of Permian–Triassic paleopoles from the Southern Alps as proxy data

for West Gondwana, according to the argument that Adria has acted as an African promontory, already during the late Paleozoic. Torcq et al. (1997), for example, explicitly omitted the paleomagnetic data from Adria in their analysis, arguing that the coherence between Adria and stable Africa was not well-demonstrated (see also Dercourt et al., 1986; Vai, 2003). Nevertheless, Muttoni et al. (1996) showed that a mean paleopole compiled from Early Permian results from the Southern Alps was statistically indistinct from an Early Permian paleopole compiled from data from West Gondwana. This comparison, however, is predicated on the reliability of the latter dataset, which is comparatively old (pre-1980 results, except one pole from 1981) and of poor quality; indeed its low quality was the stated impetus for adopting the Adria data as a proxy. With an Early Permian to Early Jurassic APWP, built from the merged Southern Alps–West Gondwana datasets, and the North American APWP of Van der Voo (1993), Muttoni et al. (1996) concluded that Pangea A was untenable during the Early Permian; Pangea B was necessary. However, by Late Permian/Early Triassic time the Pangea A-2 model of Van der Voo and French (1974) was able to accommodate the data, and by the Late Triassic the A-1 model was permissible (Fig. 5.7). Thus, they advocated an "evolutionary model" of Pangea, one in which the supercontinent underwent progressive internal change.

Following this contribution—and aiming, in part, to address arguments subsequently raised against it—Muttoni et al. (2003) presented additional paleomagnetic data from the Southern Alps and re-affirmed their earlier conclusion that the paleomagnetic evidence support Pangea B during the Early Permian, but Pangea A during the Late Permian. To sidestep the argument that inclination shallowing in sediments (discussed in section 5.7) could have biased the findings of Muttoni et al. (1996), Muttoni et al. (2003) used only igneous-based paleomagnetic poles in their

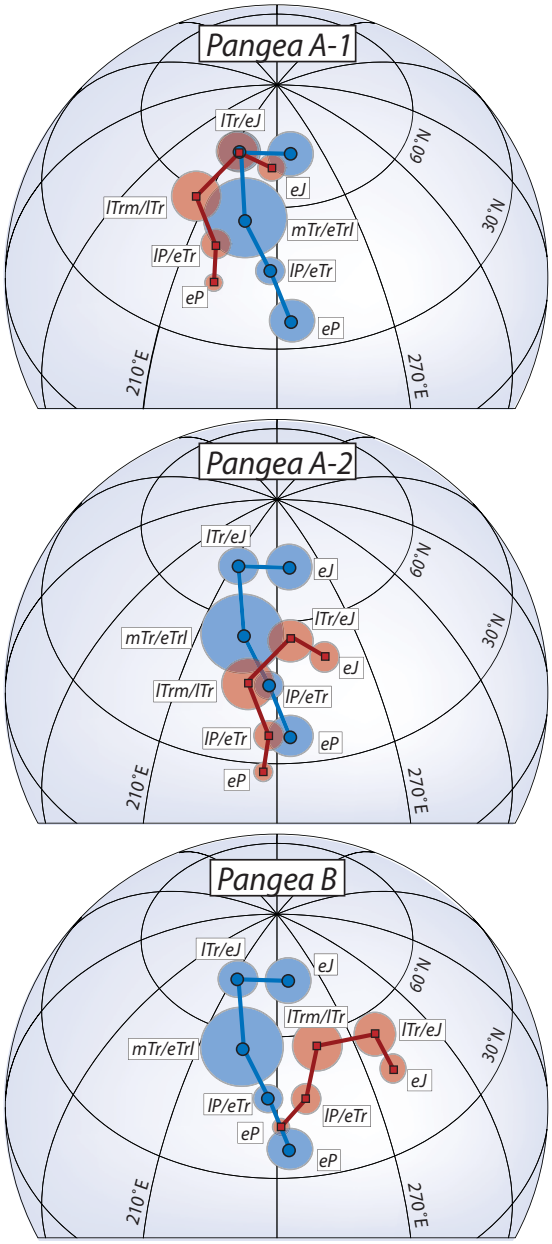

Figure 5.7: Late Paleozoic–early Mesozoic apparent polar wander paths (APWPs) of Muttoni et al. (1996) for Laurussia (red) and West Gondwana (blue), according to Pangea A-1, A-2, and B reconstructions. Muttoni et al. (1996) noted that the models appear to best-fit the data at different times and proposed an evolution of Pangea from B (Early Permian) to A-2 (Late Permian–Early Triassic) to A-1 (Late Triassic–Jurassic). Note that the Early Permian data are strongly discordant in a Pangea A-1 fit, and that the Pangea A-2 reconstruction better fits the trends of the paths, but fails to align mean poles of the same age.

analysis. They reiterated the assertion that Adria has moved in concert with stable Africa since the late Paleozoic, and showed an agreement between Early Permian volcanic-based paleopoles from the Southern Alps and Morocco. Again, however, the African poles used for comparison were comparatively old (pre-1980 results) and of questionable quality. The authors built a mean Early Permian paleopole for Gondwana by merging the Southern Alps and Moroccan datasets and, by comparing this with an igneous-based mean Early Permian paleopole from Europe, showed that if Pangea were reconstructed according to the longitude constraints of an A-type model, it would still result in ∼1,000 km of crustal overlap between West Gondwana and Laurussia. They further argued that this result was insensitive to zonal non-dipole fields (discussed in section 5.6), as the paleomagnetic inclinations analyzed were from a narrow band of low paleolatitudes from the same hemisphere.

Bachtadse et al. (2002) and Rakotosolofo et al. (2006) similarly calculated a mean Early Permian paleopole for Gondwana and, after comparing it with the mean Early Permian paleopole for Laurussia (Van der Voo, 1993), concluded that it supported a Pangea B paleogeography. Rakotosolofo et al. (2006) further claimed that unpublished Early Triassic paleomagnetic data from southern Peru were compatible with Pangea A-2, thereby corroborating a Permian-age for the Pangea B to A transformation, as proposed by Muttoni et al. (1996; 2003).

The broader tectonic and geodynamic implications of a Permian-age megashear were discussed by Muttoni et al. (2003; 2009). In particular, these authors drew an association between the timing of the Pangean transformation, the opening of the Neotethys Ocean, and lithospheric wrenching, basin development, and magmatism in central Europe and the Southern Alps during the Permian. The hypothetical plate circuit for Gondwana included a subduction zone to the south and west (Pantha-

lassa trench), a spreading center to the east (Neotethys ridge), and the Intra-Pangean dextral megashear to the north (Fig. 5.8). Although a Permian megashear is more temporally coincident with documented dextral activity in Europe (Arthaud and Matte, 1977; Schaltegger and Brack, 2007) than a Triassic transformation, the hypothetical motion required still grossly exceeds estimates of the true net displacement. Furthermore, many Gondwana–Laurussia boundary zones lack significant structural relicts indicative of dextral strike-slip motion that post-dates Carboniferous–Permian continental convergence. For example, the prevailing Permian paleostress field in northern Iberia is N-S compressive (NNE-SSW compressive in paleogeographic coordinates), reflecting final Variscan deformation due to the collision of Gondwana and Laurussia (Weil et al., 2001) (Fig. 5.9a). This paleostress field precludes significant, Permian-age, ENE-WSW oriented, dextral shear in the region, which would require WNW-ESE compressive stress (NW-SE compressive in paleogeographic coordinates) (Fig. 5.9b).

5.5.4 Pangea C

According to the longitude indeterminacy of paleomagnetism, Pangea B is perfectly acceptable with respect to the data of Irving (1977) and others, but it is also non-unique. Irving (1977) acknowledged this, noting that Gondwana could be placed to the west of North America, or farther to the east than its position in Pangea B, but he ultimately deemed these alternatives untenable, given the geologic difficulties already manifest in the "more conservative" Pangea B model, as discussed above. Despite this, Smith et al. (1981) argued that Pangea B did not fully conform to the paleomagnetic data, and presented an alternative paleogeographic model (Pangea "C") in which Gondwana is displaced farther east, relative to its position with respect to Laurussia in Pangea B. In this reconstruction, northern South America is

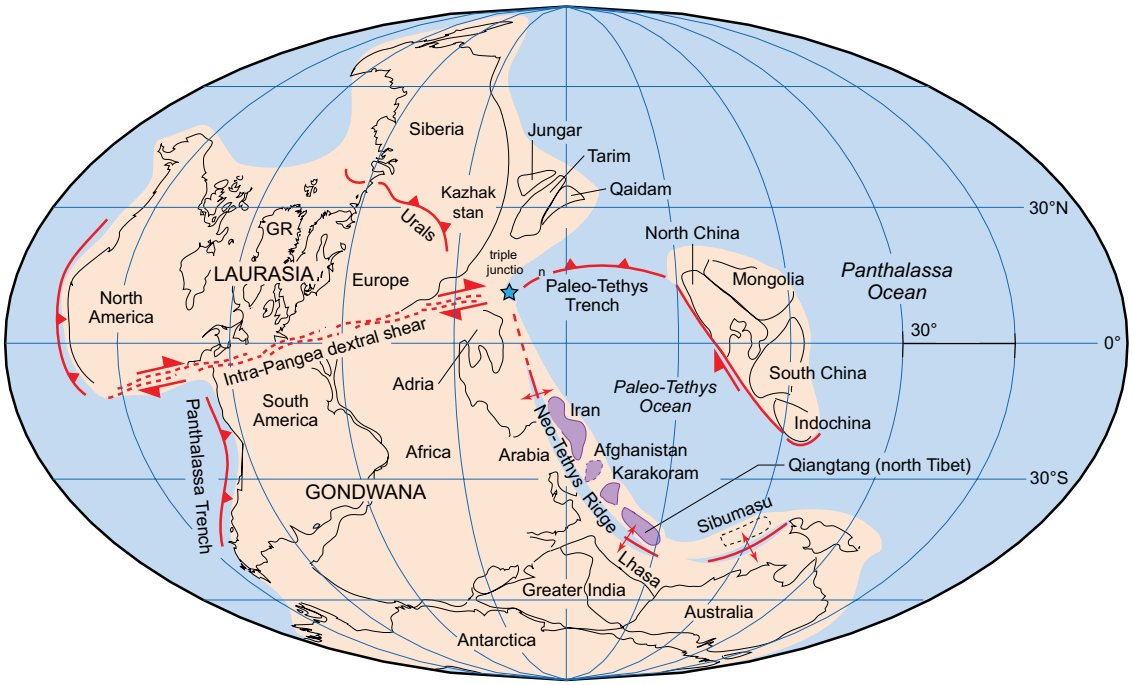

Figure 5.8: Early Permian Pangea B reconstruction of Muttoni et al. (2009) displaying theoretical plate kinematics.

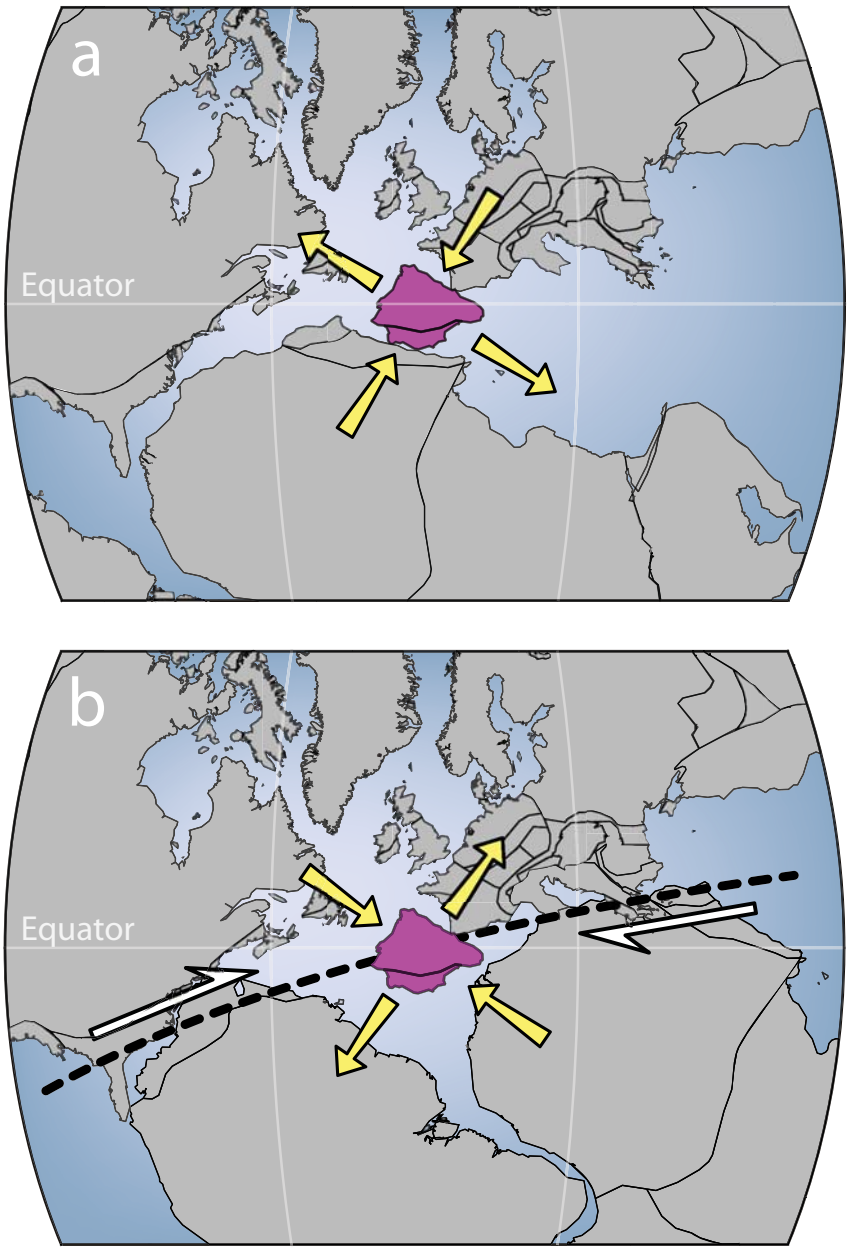

Figure 5.9: Observed vs. expected Early Permian paleostress field for northern Iberia. (a) Early Permian paleostress field as determined by Weil et al. (2001). (b) Paleostress field expected from the hypothetical Intra-Pangean megashear. Redrawn after Weil et al. (2001).

juxtaposed with southern Europe and Africa is situated beneath Asia; this affords further space for Gondwana to be nudged northward to conform to the paleomagnetic data, without resulting in overlap between continents. Pangea C faces the same problems as Pangea B, but exacerbated by the greater offset between Gondwana and Laurussia. For example, if Pangea C is assumed to transform to Pangea A within either the Permian or the Triassic (∼50 Myr), the requisite ∼6,000 km displacement must have occurred at the remarkable average rate of 12 cm/yr. Furthermore, no major continent borders eastern North America in Pangea C, obliging advocates of Pangea C to explain the Alleghenian Orogeny in lieu of continent-continent collision. A variety of similar paleogeographic permutations of Pangea are obviously permissible according to the longitude indeterminacy of paleomagnetism, but are ultimately subject to the same geologic problems.

5.6 Non-dipole Fields

5.6.1 A Long-Term Zonal Octupole?

In all of the paleomagnetic studies previously referenced, it is implicitly (or explicitly) assumed that the time-averaged paleomagnetic field can be approximated by a geocentric axial dipole (GAD). This is generally a necessary assumption, for without prior knowledge of the geomagnetic field structure, it is impossible to define a function relating inclination and latitude. By assuming that the paleomagnetic field was "always" a GAD, and that rocks can act as high-fidelity magnetic recorders on geologic timescales, changes in paleomagnetic direction can be interpreted as tectonic motion (or true polar wander). Thus, paleomagnetic plate reconstructions are made according to the assumption that the structure of the paleomagnetic field is perfectly well-known. Briden et al. (1971) turned this notion on its head. They took Pangea A-1 to be the true paleogeography of the Permo-Triassic and assumed that

the paleomagnetic discrepancy with this reconstruction was due to a geomagnetic departure from a GAD. Comparing the limited data available at the time against theoretical inclination vs. latitude curves, the authors concluded that the Permo-Triassic geomagnetic field was, to a first approximation, a GAD, but that significant axially-symmetric non-dipole contributions were evident. They observed that the theoretical field with the best visual fit to the data appeared to be a prevailing dipole with a subsidiary zonal octupole of the same sign. Interestingly, they also observed a systematic incongruity in the Permian and Triassic inclinations of Europe and North America (later observed by Irving (1977) and Morel and Irving (1981)), which they noted could not be explained by zonal magnetic fields.

Three decades later, amid revived debate about Pangea reconstructions, this concept was revisited by Van der Voo and Torsvik (2001) and Torsvik and Van der Voo (2002). Van der Voo and Torsvik (2001) analyzed 300 Ma to 40 Ma paleopoles from North America and Europe for evidence of zonal non-dipole fields by comparing predicted and observed paleolatitudes derived from the data. Importantly, the primary uncertainty in the reconstruction of Laurussia is orthogonal to the effects of zonal non-dipole fields, so artifacts from fitting errors were of no significant consequence to their analysis. Their slope-fitting analysis revealed a consistent departure from the expectations of a GAD field (wherein predicted = observed paleolatitudes; yielding a slope of 1) that could be indicative of a long-term octupole component, representing $\sim$10% of the total geomagnetic field. The authors demonstrated that by re-calculating paleolatitudes with a 10% octupole contribution in the late Carboniferous and a 20% contribution in the Late Permian-Early Triassic, Pangea A could be accommodated without significant continental overlap (Fig. 5.10). These conclusions were broadened by Torsvik and Van der Voo (2002), who conducted a similar

analysis on Paleozoic and Mesozoic paleomagnetic data from Gondwana. Assuming a Pangea A reconstruction, they built running mean APWP pairs for Laurussia and Gondwana using several different geomagnetic field structures (varying octupole contributions; Fig. 5.11) and measured the great circle difference between concomitant mean poles for each APWP pair (due to the paleogeographic position of Gondwana on the south geographic pole for much of the Paleozoic, they could not apply the linear regression analysis comparing predicted vs. observed paleolatitudes used by Van der Voo and Torsvik (2001)). They found it generally necessary to correct for an octupole contribution to achieve an optimal fit between the APWPs, but that the relative contribution of this optimal octupole component was time-varying. The relative contributions ranged from 20% to 0% and generally diminished with time; the largest values were required in the late Paleozoic–early Mesozoic, again confirming that Pangea A could not be reconciled with the uncorrected paleomagnetic data. The authors noted that the late Paleozoic–early Mesozoic paleomagnetic poles from Gondwana were dominantly sedimentary-based, whereas the younger paleomagnetic poles were mostly derived from volcanic rocks. The implication of this observation is that inclination shallowing could be partly responsible for the apparently stronger octupole in the late Paleozoic–early Mesozoic, as it can produce an equivalent magnetization bias in sediments. An igneous-only analysis suggested that inclination shallowing was not significant; but, notably, the data from Gondwana included few reliable igneous records. We will return to a discussion of inclination shallowing in section 5.7.

5.6.2 Return to the GAD hypothesis

Paleomagnetism is the only available tool to make quantitative paleogeographic reconstructions for pre-Cretaceous time. Yet, this indispensible utility is predicated

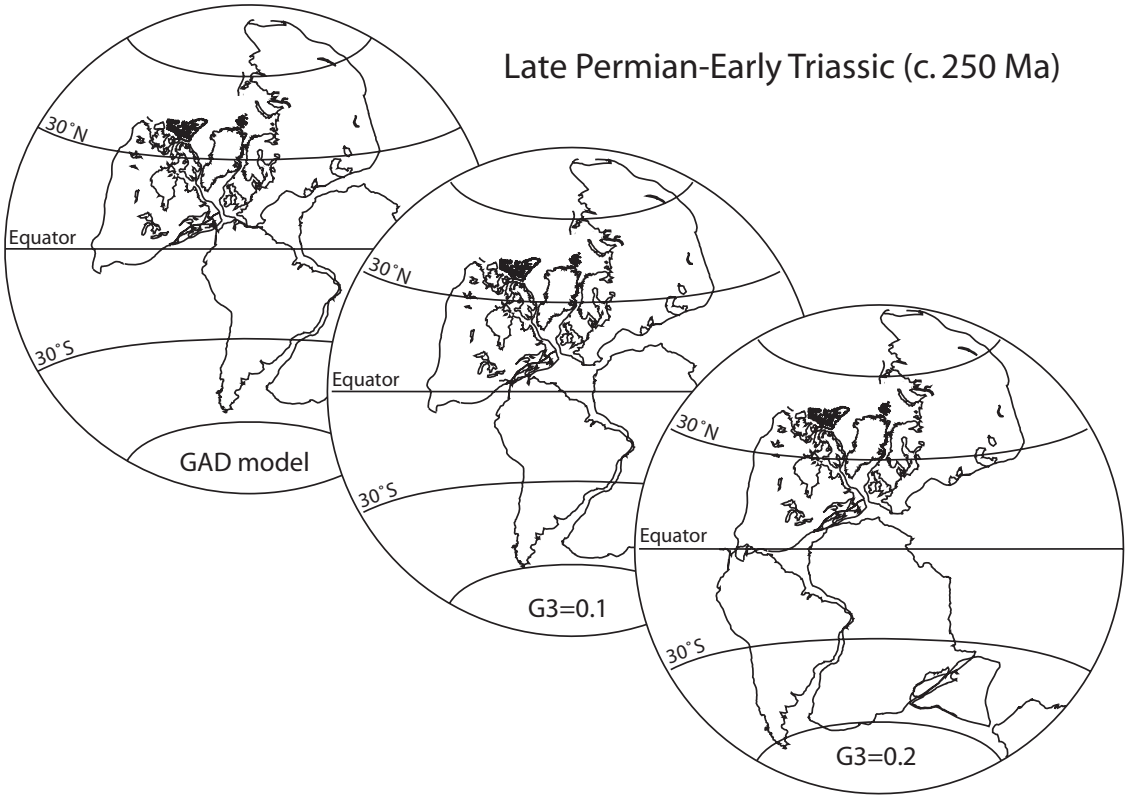

Figure 5.10: Permissible Pangea reconstructions (i.e. those that do not require significant continental overlap) at 250 Ma, according to paleomagnetic data from Van der Voo and Torsvik (2001), assuming different paleomagnetic field configurations. G3 = strength of zonal octupole field relative to an ideal dipole. Pangea A is permissible at 250 Ma if an octupole contribution of 20% is assumed. From Van der Voo and Torsvik (2001).

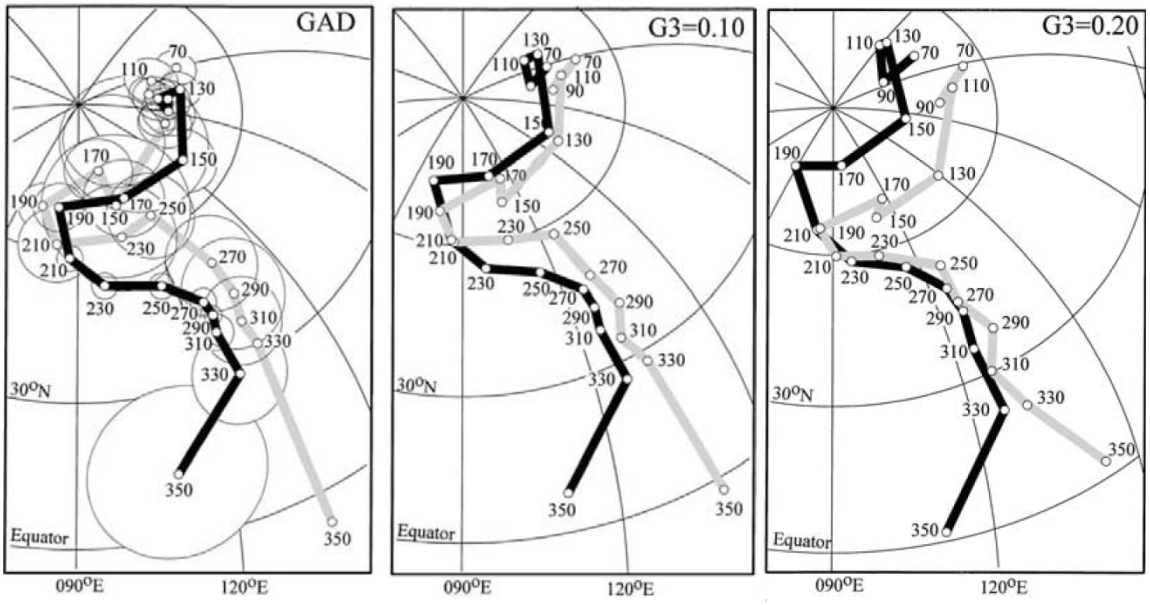

Figure 5.11: Late Paleozoic-Mesozoic apparent polar wander paths (APWPs) for Laurussia (black) and Gondwana (gray), constructed according to different assumed paleomagnetic field structures (i.e. including a varying octupole contribution). G3 = strength of zonal octupole field relative to an ideal dipole. The late Paleozoic–early Late Triassic interval exhibits a good-fit with an assumed G3 of 20%, but the fit of the later Mesozoic poles clearly worsens; suggesting that the G3 contribution (if any) may be time-variant. From Torsvik and Van der Voo (2002).

on the hypothesis of a static (on time-scales of ∼10–100 ka) paleomagnetic field structure, ideally (and near-invariably assumed to be) a GAD. As aforementioned, without prior knowledge of the field structure, inclination can not be used to solve for paleolatitude; and for pre-Pangean time this problem cannot be inverted (as per the approach of Briden et al. (1971)), as the gross paleogeography has only been established by paleomagnetic work underpinned by the GAD assumption. Thus, if the GAD hypothesis is abandoned, so, too, is our confidence in any pre-Pangean paleogeographic reconstruction derived from paleomagnetic results. It is prudent, therefore, to consider what persistent bias could manifest as an apparent octupole contribution; we will consider this in the next section (5.7). Here we will briefly review recent work that suggests the hypothesis of a GAD may be relevant since the late Mesoproterozoic.

Analyses of paleomagnetic data from the last 5 Myr—during which the contribution of tectonic plate motion is negligible—have demonstrated that the time-averaged field is approximately a GAD, with a subsidiary geocentric axial quadrupole representing ∼2–5% of the total field (McElhinny, 2004; Johnson et al., 2008; Valet and Herrero-Bervera, 2011). Contributions from a persistent zonal octupole are generally regarded as insignificant (McElhinny, 2004), but may represent up to 5% of the total field (Johnson and Constable 1997; Kelly and Gubbins, 1997; Johnson et al., 2008). Similarly, Courtillot and Besse (2004) detected no significant evidence of an octupole contribution in their analysis of global 0–200 Ma paleomagnetic data, which they searched for hemispheric inclination antisymmetry, relative to a synthetic global APWP. Bazhenov and Shatsillo (2010) devised an approach to investigate the structure of the paleomagnetic field from paleomagnetic data distributed across a large single plate and used this method to demonstrate that zonal non-dipole con-

tributions to the Late Permian paleomagnetic field were unlikely to exceed ∼10% of the total GAD. As previously discussed, Muttoni et al. (2003) also questioned the evidence of a significant zonal octupole field in the Early Permian and showed that paleomagnetic data from a narrow, low paleolatitude band in the same hemisphere exhibited the same discrepancy the octupole fields had been invoked to solve; such a distribution of sites should greatly minimize relative errors introduced by unrecognized octupole fields. Indeed, Van der Voo and Torsvik (2004) conducted a simpler test for evidence of an octupole bias in the Permo-Triassic paleomagnetic data of western Europe and concluded that the results were ambiguous; no evidence of an octupole was found in the 280 Ma or 250 Ma data, while the 290 Ma data were consistent with a subsidiary octupole.

Repeating the paleomagnetic inclination frequency analysis introduced by Evans (1976) with an updated dataset, Kent and Smethurst (1998) concluded that the Precambrian and Paleozoic paleomagnetic fields may have included strong zonal quadrupole and octupole components (estimated at 10% and 25%, respectively) that diminished with time. Such a non-dipole field decay was apparent in the analysis of Torsvik and Van der Voo (2002), where the octupole contribution needed to optimize the fit between the Laurussian and Gondwanan APWPs was observed to diminish with time. However, the assumption of a random paleogeographic sampling that underlies the analysis of Kent and Smethurst (1998) has been shown to be invalid by Meert et al. (2003) and McFadden (2004). Moreover, recent comparisons of Proterozoic paleomagnetic inclinations and climate-sensitive paleolatitude proxies (Evans, 2006) and normal and reversed paleomagnetic data from the 1.1 Ga Keweenawan basalts (Swanson-Hysell et al., 2009) exhibit no remarkable departures from GAD expectations.

5.7 Bias in the Paleomagnetic Record

As an alternative to challenging the conventional paleogeographic model or the uniformitarian GAD hypothesis, Rochette and Vandamme (2001) and Van der Voo and Torsvik (2004), among others, have explicitly suggested that the discrepancy between the late Paleozoic–early Mesozoic paleomagnetic data of Laurussia and Gondwana could simply be a manifestation of bias in the paleomagnetic data. We use the term bias rather than error to denote a systematic quality; random errors, which are invariably present in any paleomagnetic dataset, are eliminated through the tiered treatment and averaging of data. With respect to the gross paleogeography of the late Paleozoic–early Mesozoic, the most corruptive data bias is that which is equatorially anti-symmetric, as Pangea straddles the equator during this time. As discussed above, an unrecognized subsidiary zonal octupole field can impart an anti-symmetric bias to paleomagnetic data, but it is not the only phenomenon capable of such. Indeed, the inclination shallowing of sediments inherently leads to an anti-symmetric bias, and can produce near-identical results to those of an octupole field (Fig. 5.12). Less intuitively, systematic errors in age assignment or unrecognized overprints or remagnetizations can yield a similarly anti-symmetric bias, albeit under specific circumstances. In the following, we explore each of these potential sources of bias in more detail, with a specific focus on their possible contributions to the late Paleozoic–early Mesozoic paleomagnetic discrepancy.

5.7.1 Inclination Shallowing

Examples of sedimentary inclination shallowing have been well-documented in a variety of natural settings and rock-types (Zijderveld, 1975; Tauxe and Kent, 1984; Celaya and Clement, 1988; Arason and Levi, 1990; Garcés et al., 1996; Gilder et al.,

2003a; Kent and Tauxe, 2005; Tan et al., 2007; Bilardello and Kodama, 2010a,b,c; Iosifidi et al., 2010) and by numerous laboratory re-deposition experiments (King, 1955; Løvlie and Torsvik, 1984; Tauxe and Kent, 1984; Anson and Kodama, 1987; Deamer and Kodama, 1990; Levi and Banerjee, 1990; Sun and Kodama, 1992; van Vreumingen, 1993; Mitra and Tauxe, 2009). The bias appears to affect some sedimentary magnetic records which are defined by a depositional remanent magnetization (DRM) or a post-depositional remanent magnetization (pDRM). In the case of the former, the bias arises from the settling and compaction of inequant magnetized grains or sedimentary flocs in the gravitational field, which may overcome the vertical torque applied to the particles by the geomagnetic field. The shallow inclination bias of a pDRM is imparted by post-depositional compaction, wherein the long-axes of magnetic particles are preferentially rotated toward the horizontal plane, perhaps by riding passively on larger plate-like clays to which they are adsorbed. Interestingly, Rochette and Vandamme (2001) and Tan and Kodama (2002) have suggested that even a chemical remanent magnetization (CRM), potentially acquired millions of years after deposition, could "inherit" a shallow inclination bias by developing along the depositional/compacted fabric of the host rock, or by mimicking the fabric via alteration of pre-existing grains; an early acquired CRM could also be subject to active compaction-driven shallowing.

Due to the great diversity of sediment characteristics and depositional conditions, in addition to the assortment of specific mechanisms by which a magnetization may acquire a shallow inclination bias, the magnitude of the bias in sedimentary rocks is variable. Yet, the bias can be expressed by a very simple relationship between the local geomagnetic field inclination (I_f) and the acquired inclination (= the measured inclination, I_m), namely that of King (1955): $\tan(I_m) = f \tan(I_f)$, where f

is the shallowing coefficient, which can range from 0 (complete shallowing) to 1 (no shallowing) (Fig. 5.12). For a given value $0 < f < 1$, this relationship implies that the greatest inclination bias will occur at mid-latitudes, whereas no value $f > 0$ can modify the inclination at the equator or poles (where the inclination is horizontal and vertical, respectively). According to the compilation of Bilardello and Kodama (2010a), f values from magnetite-dominated sedimentary rocks have been found to range from 0.54 to 0.79, with a mean of 0.65, whereas hematite-dominated sedimentary rocks have yielded f values from 0.4 to 0.83, with a mean of 0.59. The minimum f values equate to maximum inclination errors of $\sim$17° (at $\lambda = |34|$) for magnetite and $\sim$25° (at $\lambda = |38|$) for hematite. In a normal (reverse) polarity field, inclination error is negative (positive) in the northern hemisphere and positive (negative) in the southern hemisphere, thus it is inherently anti-symmetric about the equator (Fig. 5.12). Obviously, then, paleomagnetic errors due to inclination shallowing can be exacerbated by comparing biased directions from the two hemispheres.

Inclination shallowing is particularly ruinous in that it is generally undetectable from routine paleomagnetic analysis. In studies conducted on one homogeneous formation, or on similar lithologic units, many, if not all, sample inclinations may be similarly biased, whereas magnetic declinations are not affected by inclination shallowing. Two independent methods have been developed to identify and correct for inclination shallowing, neither of which can generally be retroactively applied to published paleomagnetic datasets. The magnetic anisotropy method (Jackson et al., 1991) is built on the premise that an unbiased magnetic recorder must be effectively magnetically isotropic. A sedimentary rock affected by inclination shallowing, therefore, can be recognized by its departure from magnetic isotropy. The magnetic anisotropy of a rock is a function of both the magnetic anisotropy of the

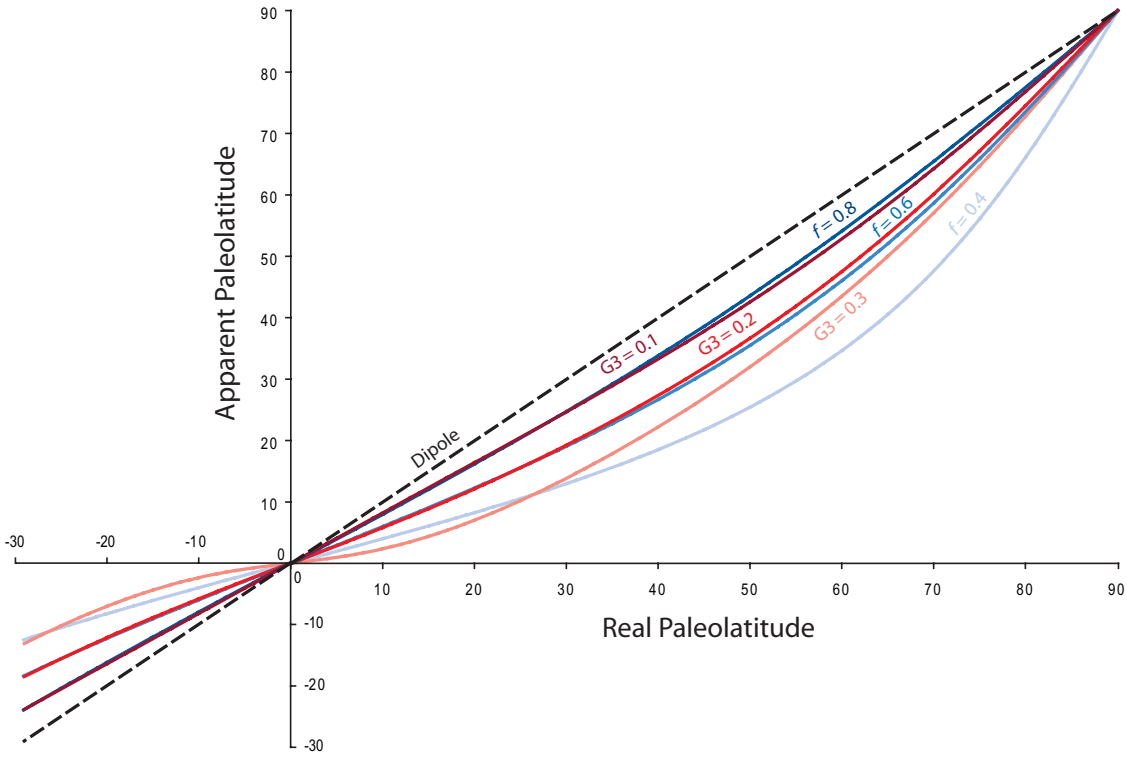

Figure 5.12: The effects of a zonal octupole field and inclination shallowing on paleomagnetic determinations of paleolatitude. The dashed black line indicates the reference paleolatitude expected from an ideal dipole (apparent paleolatitude = real paleolatitude). The warm-colored lines illustrate the effects of an increasing octupole contribution: G3 = strength of zonal octupole field relative to an ideal dipole. The cool-colored lines illustrate the effects of increasing inclination shallowing (f = shallowing coefficient, see text). The effects are highly similar (compare the G3 = 0.2 and f = 0.6 curves) and most pronounced at mid-latitudes.

individual particles and the degree of axial alignment among the particles. If both of these parameters are quantified, they can be used to correct the inclination of a sample. Unfortunately, when magnetic anisotropy is quantified in paleomagnetic studies, which is atypical, it is usually in the form of the anisotropy of magnetic susceptibility, which is an integrative measure of all the magnetic sources (including diamagnetic and paramagnetic contributions), and not exclusively a measure of the orientation of the remanence carrying particles. Moreover, determining the anisotropy of individual particles is an especially time-consuming and tricky operation that is rarely performed (although Bilardello et al. (2011) show that, for hematite, a mean particle anisotropy value of $\sim$1.38 may be reliably assumed because its anisotropy is controlled by magnetocrystalline forces). The alternative approach to eliminating inclination bias, the "elongation-inclination" (E/I) method (Tauxe and Kent, 2004), assumes that the distribution of directions in datasets that perfectly capture the full expression of secular variation will exhibit a latitude-dependence that is time-invariant. This latitude-dependence is due to the non-linear relationship between directions and virtual geomagnetic poles (VGPs): as VGP populations are commonly assumed to be circularly symmetric, the distribution of directions cannot be circular, except at very high-latitudes. The distribution of directions faithfully mapped from a circular distribution of VGPs will be elliptical, with the long axis oriented along the meridional (up-down) plane (Fig. 5.13a); the elongation of this elliptical distribution is latitude dependent, reaching a maximum at the equator. By contrast, a distribution of directions that have been subjected to inclination shallowing will be "squashed", so that the observed elongation is less than expected, or, alternatively, greater than expected but re-oriented so that the elongation is zonal (horizontal) (Fig. 5.13b). Thus, by comparing the distribution of measured directions with the

predictions of a statistical paleosecular variation model, inclination shallowing can be detected and reversed (Fig. 5.13c). Interestingly, this technique can also be used to detect contributions from octupole fields, which would exaggerate the meridional elongation of directional datasets. The impediment to this method is the requirement that secular variation be fully expressed in the directional dataset; Tauxe et al. (2008) demonstrate that $\gtrsim$ 100–150 independent site-means are necessary to conduct a meaningful E/I analysis. Such large paleomagnetic datasets are exceedingly rare, even among recently published studies. It is possible that the E/I technique can yield reliable shallowing estimates from smaller datasets ($\sim$100 samples), where sampling is stratigraphically homogenous and the sedimentation rate is not too high (Bilardello et al., 2011). However, it should be noted that such datasets do not allow for the elimination of sample-level random error, which reduces the effectiveness of the E/I technique.

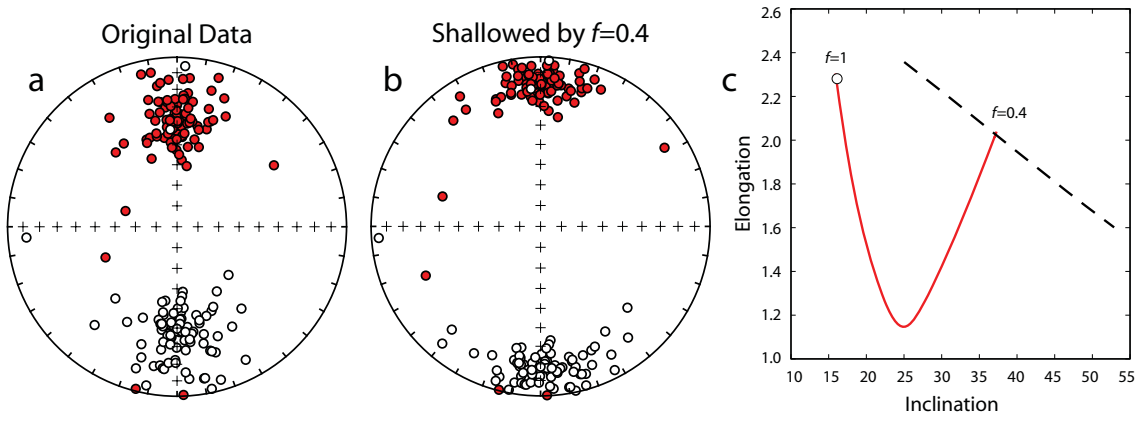

Figure 5.13: Illustration of the Elongation/Inclination (E/I) technique for identifying and correcting a shallow inclination bias in a sedimentary-based paleomagnetic record. (a) Data generated from paleosecular variation model TK03.GAD at $\lambda = 20°$. (b) Data from (a) after shallowing by $f = 0.4$; note that the direction of elongation in the distribution of data-points has changed from north-south (up-down) to east-west (horizontal) as a consequence of shallowing. (c) Finding the best match to the theoretical E/I curve of Tauxe and Kent (2004) (black dashed line) by assuming different f values and evaluating the change to the data (red line). The best fit, where the red and black lines intersect, is found to be $f = 0.4$.

Despite the difficulty in retroactively identifying inclination shallowing in published results, and the tedious laboratory (for the remanence anisotropy method) or laborious field (for the E/I method) work required to rigorously correct for it, headway has recently been made in the context of late Paleozoic–early Mesozoic paleomagnetism. Kodama (2009) applied the anisotropy of remanence method to the Late Pennsylvanian Glenshaw Formation in Pennsylvania and determined that the magnetite-dominated sequence of limestone and siltstone had a $\sim$10° shallow inclination bias. Bilardello and Kodama (2010b) similarly applied this method (although using a different measurement technique) to Late Mississippian–Early Pennsylvanian hematite-dominated redbeds in the Canadian Maritimes. They ascertained that the Shepody and Maringouin Formations had a shallow inclination bias of $\sim$10° and $\sim$4°, respectively. As discussed by Bilardello and Kodama (2010b,c), the corresponding corrected Carboniferous paleopoles place North America farther south, as the sampling areas were situated in the southern hemisphere at this time and inclination shallowing acts as a low-paleolatitude bias. This correction actually worsens the overlap between North and South America in a Carboniferous Pangea A reconstruction. However, it is likely that if the North American sedimentary-based Carboniferous paleopoles are biased by inclination shallowing, so, too, are the paleopoles from Gondwana. Furthermore, because West Gondwana was situated at mid-latitudes during the mid-to-late Carboniferous, a set of f values, comparable to those from the North American results, would result in a greater inclination error (Fig. 5.12). In considering the maximum possible effects of inclination error on the Carboniferous reconstruction of Pangea, Bilardello and Kodama (2010c) employed the minimum observed f values to correct the sedimentary-based results from Gondwana, and found that Pangea A could easily be accommodated.

The E/I method has been successfully applied to Late Triassic/Early Jurassic continental sedimentary sequences in North America and Greenland (Kent and Tauxe, 2005; Kent and Olsen, 2008). Kent and Tauxe (2005) examined the paleomagnetic records from the Dan River, Newark, and James Land basins and showed that they have average inclination errors of ∼4°, 10°, and 15°, respectively; these correspond to average paleolatitude errors of ∼2°, 6°, and 14°. Kent and Olsen (2008) similarly demonstrated that paleomagnetic inclinations from the Hartford basin have an average shallow inclination bias of ∼14° (∼8° error in paleolatitude). In both studies, the corrected inclinations were found to be in closer accord with the paleomagnetic data from proximal and concomitant igneous rocks, as well as with the paleolatitudes implied by regional paleoclimate data. Although these corrections pertain to magnetizations too young to be directly applicable to the paleogeographic problem of interest here, they importantly affirm the presence of a pervasive shallow inclination bias in typical clastic sedimentary rocks. The Late Carboniferous to Triassic (320–200 Ma) paleomagnetic record from North America, for example, is dominated by results derived from such rocks; in the compilation of Torsvik et al. (submitted) they constitute 60 of the 72 paleomagnetic poles from this interval.

The E/I method has also been applied to an Early Permian result from Brazil (Brandt et al., 2009) and to Carboniferous results from Ukraine (Meijers et al., 2010), which yielded paleolatitude corrections of ∼1–5°. However, the dataset of Meijers et al. (2010) does not meet the requisite ∼ 100 site/sample means necessary for a rigorous E/I analysis (they used <100 specimens), and the corrections may thus be unreliable.

Because paleomagnetic results derived from sedimentary sequences have not been routinely subjected to tests for a shallow inclination bias, the extent of the bias

in any given APWP is difficult to estimate. Kent and Irving (2010) side-stepped this problem in their construction of a Triassic through Paleogene APWP for North America by excluding all sedimentary-derived paleomagnetic poles that were not explicitly checked/corrected for inclination error. Correspondingly, the paleolatitudes that they determined for North America were higher than those calculated from other APWPs, especially those dominated by results derived from sedimentary rocks. Unfortunately, very few igneous-based paleomagnetic results exist for the Early and Middle Triassic, so Kent and Irving (2010) began their analysis at 230 Ma (they retained only one pre-Late Triassic paleomagnetic pole in their dataset). To correct for shallow inclination bias in the paleomagnetic records of earlier time, when igneous-based and inclination-corrected sedimentary poles are scarce, it is necessary to make some assumptions. Torsvik et al. (submitted) assumed an average shallowing coefficient of $f = 0.6$ for all clastic sedimentary sequences and showed an improved agreement in the APWPs of Laurussia and Gondwana through the late Paleozoic–early Mesozoic by correcting for it. In a preceding study, Rochette and Vandamme (2001) concluded that an average shallowing coefficient of $f = 0.5$ could reconcile the paleomagnetic poles from Laurussia and Gondwana in a Pangea A-type fit. To verify the veracity of these average shallowing estimates, in lieu of direct diagnostic tests, Domeier et al. (2011b) conducted a VGP distribution analysis on a set of Permian to Middle Triassic paleomagnetic poles from North America. Following the aforementioned assumption that unbiased VGPs should be circularly symmetric, and that the redbeds from which the poles were derived shared a common shallowing coefficient, they calculated a range of inclination corrections which would "unflatten" the observed (elongate) distribution of combined VGPs. The authors compared the variably-corrected North American APWP against a new Middle Per-

mian igneous-based paleomagnetic pole and found a good agreement with the use of shallowing coefficient $f = 0.54$, which falls between the assumed values of Rochette and Vandamme (2001) and Torsvik et al. (submitted).

5.7.2 Age Bias

Pangea consistently drifted northward (∼8 cm/yr) during the late Paleozoic–early Mesozoic (Steinberger and Torsvik, 2008; Torsvik et al., submitted; Fig. 5.14). It is obvious, therefore, that a paleomagnetic pole from this time interval with an erroneous age assignment can be expected to generate an error, in the sense that a predicted paleolatitude for the erroneous age will differ from what it should be. However, a globally uniform age bias would result only in absolute paleolatitude errors, where no relative differences would be detectable in the paleomagnetic poles of correctly restored continental blocks. Instead, paleomagnetic discrepancies will arise from regional age bias, such as that arising from systematic errors in intercontinental correlation. For example, the significant difference in the Triassic paleopole positions of North America and Europe (restored to Laurussia) observed by Irving (1977) and Morel and Irving (1981) has been recognized as an artifact of intercontinental correlation error (Livermore et al., 1986, Kent and Tauxe, 2005).

To explain the observed late Paleozoic–early Mesozoic paleomagnetic discrepancy between Laurussia and Gondwana in terms of an age bias, there must be a hemispheric disparity in the age estimate errors (i.e. a hemispheric bias). For example, the age estimates from Laurussia could be erroneously young, relative to the (approximately correct) age estimates from Gondwana. In other words, a comparison of (relatively) old paleomagnetic data from Laurussia and (relatively) young paleomagnetic data from Gondwana will result in a paleogeographic overlap of the landmasses, due to their common and progressive northward drift through late Paleozoic–early

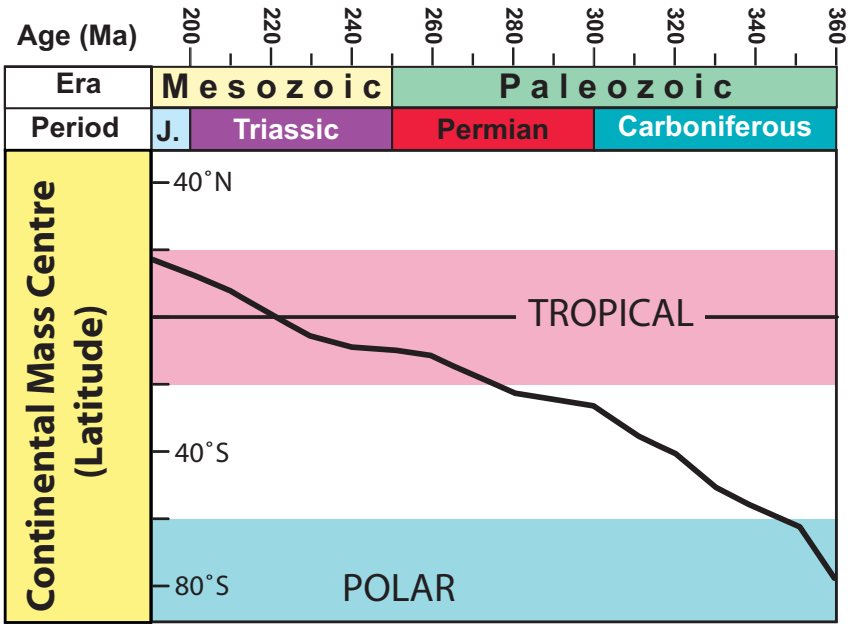

Figure 5.14: Paleolatitude of the center-of-mass of Pangea in late Paleozoic–early Mesozoic time, as determined by Torsvik et al. (submitted), showing a steady (∼8 cm/yr) northward drift. Center-of-mass is determined from the mean weighted latitude of all continents at any given time and is independent of longitude. Simplified from Torsvik et al. (submitted)

Mesozoic time. Rochette and Vandamme (2001) argued that the paleomagnetic discrepancy observed by Torcq et al. (1997) in their 244 Ma A-type reconstruction was due to a hemispheric age bias; the 244 Ma pole of Laurussia was weighted by Permian-age poles, whereas the 244 Ma pole of Gondwana was weighted by Late Triassic-age data (or even Cretaceous age data; see next section). This disparity would act to drive the apparent 244 Ma paleolatitudes of Laurussia and Gondwana toward one another, resulting in continental overlap if an A-type reconstruction is maintained. Rochette and Vandamme (2001) concluded that an A-type reconstruction was permissible in the Triassic, according to the results of Torcq et al. (1997), if the 244 Ma pole of Gondwana was compared with the 214 Ma pole of Laurussia (which may be more equivalent in true age).

More generally, Van der Voo and Torsvik (2004) revealed the presence of an age bias in the Permian paleomagnetic record of stable Europe, by comparing several mean 250 Ma and 280 Ma paleopoles, calculated from populations of data with varying age estimate reliability (Fig. 5.15). For both intervals, they found that the mean paleopoles derived from data with higher-quality age estimates yielded higher European paleolatitudes, indicating that the low-quality age estimates may be biased toward younger dates. Unfortunately, in applying their highest age quality filter, the pole-set of Van der Voo and Torsvik (2004) was reduced from six poles to one (83% rejected) at 250 Ma, and from 27 poles to three (89% rejected) at 280 Ma. These drastic reductions in pole quantity prevent such a filter from being routinely applied, especially to less ample or lower-quality paleomagnetic datasets, such as those from Gondwana. In this respect, an age bias can be one of the most challenging data-pathologies to deal with, as only meticulous attention to newly published or re-assessed age estimates and timescale revisions can resolve unrecognized and

enduring age disparities. Fortunately, the marked improvements in isotopic dating over the previous decades have allowed age estimates to be made (or revised) with increasing precision and reliability, so that recent paleopole compilations are much less corrupted by relative age errors than older datasets.

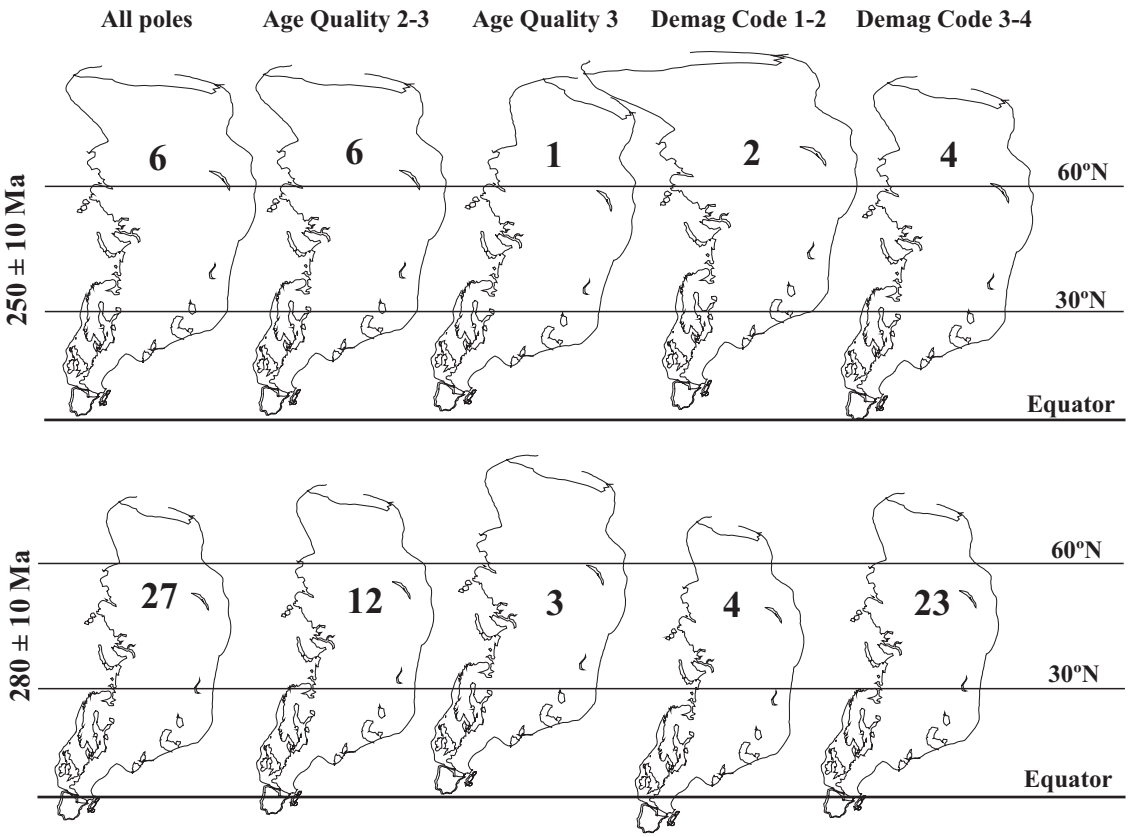

Figure 5.15: The paleogeographic position of Eurasia at 280 Ma and 250 Ma, according to different data selection criteria by Van der Voo and Torsvik (2004). The bold values denote the number of paleopoles used in each instance to calculate the paleolatitude. For both intervals, the selection of data with the most reliable ages (U-Pb or $^{40}Ar/^{39}Ar$ methods) results in a northward shift in the estimated paleolatitude. This can be explained by the assignment of erroneously young absolute ages by the outdated geochronologic methods. Selecting the most well-demagnetized data similarly results in a northward shift at 280 Ma, which can be explained by a present-day field magnetization contamination in the less well-demagnetized data.

5.7.3 Contaminated Magnetizations

Secondary magnetizations are well-known in the study of paleomagnetism, mostly as a nuisance in the form of a minor overprint, and often parallel to the present day field (PDF). In most cases, the magnetization of interest, the characteristic remanent magnetization (ChRM), must be separated from these secondary magnetizations by demagnetization techniques. If the secondary magnetization is not completely eliminated (or the ChRM completely isolated), the calculated ChRM direction will be corrupted by incorporation of the secondary component(s). Because secondary magnetizations, like a PDF overprint, can be consistently oriented and regionally/lithologically pervasive, an unrecognized or incompletely removed secondary magnetization has the potential to significantly bias a paleomagnetic result. If a consistently-oriented secondary magnetization contaminates an assemblage of ChRM directions of mixed polarity, the bias may cancel out, as the normal and reversed directions would be diametrically modified. Correspondingly, the contamination would then be detectable by the reversal test, which would reveal the normal and reverse mean directions to be non-antipodal. However, in an assemblage of ChRM directions of single polarity, such a bias would not cancel, and a reversal test would not be applicable. This is relevant to the discussion at hand, due to the presence of a long interval of reversed polarity from ∼318 to 265 Ma, the Kiaman Reversed Superchron.

Given the low paleolatitude of Laurussia during the late Paleozoic, a primary Kiaman magnetization contaminated with a normal-polarity PDF overprint will be biased downward, toward positive inclinations. The paleogeographic corollary of this bias is an apparent southward shift of Laurussia. Such a bias would affect Kiaman-age magnetizations from Gondwana in an identical manner, resulting in erroneously high

southerly paleolatitudes. The effect of a normal-polarity overprint superposed on a late Paleozoic–early Mesozoic magnetization of normal polarity would thus result in paleolatitude estimates for both Laurussia and Gondwana that were too northerly. Van der Voo and Torsvik (2004) tested the Permian paleomagnetic data of Europe for an overprint bias by comparing mean 250 Ma and 280 Ma paleopoles calculated from well-demagnetized vs. poorly demagnetized data, following the assumption that the poorly demagnetized data were more likely to be contaminated by PDF overprints (Fig. 5.15). For the earlier interval (280 Ma), which falls within the Kiaman, the European paleolatitude derived from the well-demagnetized data was 5° higher than the one derived from the poorly demagnetized results, which supports the contention of a PDF contaminant in the latter. For the younger, mixed polarity interval (250 Ma), the poorly demagnetized data yielded a paleolatitude estimate 3° higher than that derived from the well-demagnetized data, but this analysis was based on very few poles.

Finally, it is worth noting that a complete remagnetization, if unrecognized as such, can affect a paleomagnetic dataset in the same manner as an "old-age" bias (where the assigned age is older than the true age of the magnetization). Where field stability tests are not applicable, remagnetized units may be difficult to recognize, especially if the secondary magnetization is not conspicuously different in orientation from the expected direction. This is especially relevant to paleomagnetic data from redbeds, which may acquire their ChRM from a chemical process, millions of years after deposition. As an example of this potential bias, we return to the critical remarks of Rochette and Vandamme (2001) on the conclusions of Torcq et al. (1997). Torcq et al. (1997) used three Moroccan paleomagnetic poles with estimated ages of 238 Ma in the calculation of the 244 Ma mean paleomagnetic pole for Gondwana,

which was then used in support of an argument for Pangea B. However, Rochette and Vandamme (2001) noted that in the 50+ sites represented by these three Moroccan paleomagnetic poles, all site mean directions have yielded normal polarity (except one dubious result), and the poles are indistinct from mid-Cretaceous African results. The predominance of normal polarity could therefore be interpreted as an indication that the units were remagnetized during the Cretaceous Normal Superchron, which would imply that the 244 Ma mean paleopole of Gondwana, as calculated by Torcq et al. (1997), is biased by Cretaceous data.

5.8 Approaching Resolution

To succinctly summarize the previous sections: the paleomagnetic data from Laurussia and Gondwana have been repeatedly shown to be incompatible with a Pangea A-type paleogeography for the late Paleozoic, and by some accounts, for the Early to Middle Triassic as well. However, the magnitude and duration of this incongruence have been diminishing with continued study, a trend which suggests that it may simply be a long-lived data artifact. Indeed, it has been demonstrated that several subtle biases may cooperatively act to corrupt the paleomagnetic dataset in such a way as to drive the apparent paleogeographic positions of both Laurussia and Gondwana toward lower latitudes (i.e. toward the equator). This hypothesis is an important potential solution to this paleomagnetic problem, which otherwise requires either a fundamental restructuring of Pangea (unsupported geologically), or adoption of a non-uniformitarian non-dipole geomagnetic field during the late Paleozoic–early Mesozoic (implicitly calls into question all prior conclusions from pre-Mesozoic paleomagnetic work). In the following, we re-evaluate the above hypothesis by re-calculating and comparing the APWPs of the major peri-Atlantic continental blocks

in light of the most recent paleomagnetic data, newly refined continental fits, and theoretical inclination shallowing corrections. As we are here concerned with the first-order fit between Laurussia and Gondwana, we omit paleomagnetic data from East Gondwana (Antarctica, Australia, India-Pakistan, Madagascar), which would otherwise introduce additional uncertainty when reconstructed to West Gondwana (due to their less-than-perfectly known reconstruction parameters). However, we note that discrepancies between late Paleozoic–early Mesozoic paleomagnetic data from East Gondwana and West Gondwana/Laurussia remain an important unresolved problem that merits future investigation. One possibility that already appears to be rather evident is that the paleomagnetic results obtained from the detrital sedimentary formations of East Gondwana are very likely in need of inclination-corrections. With a complete absence of results from this interval from Antarctica, only Australian igneous rocks are—in principle—suitable for comparisons.

5.8.1 Data Quality

"Data quality" is difficult to evaluate, as it is a subjective measure, but the use of even a crude quality-criterion can be useful in illuminating the impact of any bias that may be present in the form of unreliable or corrupt data. As an example, we consider the difference in the APWPs of North America, Europe, and West Gondwana, as constructed from the updated paleomagnetic dataset of Torsvik et al. (submitted) (Table 5.1), relative to those constructed by Morel and Irving (1981), following the assumption that newer results are generally of higher quality due to improved laboratory techniques and analytical treatments. We have elected to use the dataset of Morel and Irving (1981) because many of the more recent studies which assert support for Pangea B have focused on a limited interval of time, such as the latest Permian–earliest Triassic (Torcq et al., 1997) or the Early Permian (Bachtadse

et al., 2002; Muttoni et al., 2003; Rakotosolofo et al., 2006), rather than considering the complete late Paleozoic–early Mesozoic time frame of interest here. Because the quantity and quality of the available paleomagnetic data are highly variable across this interval, it is important to consider all results in the context of their temporal neighbors; isolated comparisons can be seriously misleading, as expounded in our discussion of the potential sources of bias. Moreover, the conclusions of several of these more recent studies are predicated on the use of data collected prior to 1980 (as noted in section 5.5); this data was already included in the study of Morel and Irving (1981).

We constructed the APWPs using a 30-Myr moving window, as was originally done by Morel and Irving (1981), and all APWPs were rotated into African coordinates, according to Bullard et al. (1965) (Table 5.2; Fig. 5.16). Unfortunately, significant changes in the reference timescale prevent a direct comparison between specific mean poles of the "new" and "old" paths, but qualitative comparisons of their shapes and trends are nonetheless informative. In the newer APWPs of both North America and Europe there is a clear eastward shift in the Permian segments, relative to the older paths of Morel and Irving (1981), and the trend of the Late Permian–Early Triassic curvature is inverted (Figs. 5.16a,b). Conversely, the newer path for Gondwana is displaced west, and slightly north, relative to the older one. The Permian segments of the Gondwana paths are more congruous with one another, but the Triassic section of the newer path is more westward convex. These changes result in greater accord between the North America–Gondwana and Europe–Gondwana paths for the Permian–Early Triassic; a reduction in the great circle distance (GCD) between the paths is on the order of $\sim$5°-10° (Figs. 5.16d,e), and their trends are visibly more congruent. We again emphasize that these improvements are free of differences

in APWP construction or continental-reconstruction parameters; they are due solely to data selection, which in turn is reflective of the impact of data-quality.

To further consider the reliability of the Torsvik et al. (submitted) compilation, we have conducted a simple data-filtering exercise. We re-calculated the APWPs as before, having excluded all results with ≤ 29 samples and/or ≤ 3 sites and/or a global paleomagnetic database DEMAG code of ≤ 2 (Table 5.1). While these specific filter thresholds are admittedly arbitrary, smaller data-sets are less likely to average secular variation, and poorly demagnetized samples are less likely to be purged of secondary magnetizations, so the sample/site quantity and DEMAG code parameters are particularly well-suited for such a quality-filtering exercise. We elected not to apply any age-quality filters (as per Van der Voo and Torsvik, 2004), as the datasets of North America and Gondwana still contain too few high-quality age data for the filtered results to be useful. Moreover, age reliability was already considered in the pole selection by Torsvik et al. (submitted). Upon filtering, the APWPs of North America and Europe change rather little, both exhibiting a minor northeastward shift in the Late Carboniferous–Early Permian (Fig. 5.16c). The APWP of Gondwana becomes less-well defined with filtering, losing much of its sinuosity, but it does not exhibit any consistent shift in position. The GCDs between the North America–Gondwana and Europe–Gondwana APWPs reveal a small reduction with filtering, supporting the contention that the APWP separation is, at least in part, an artifact of data-quality. However, the GCD reductions are typically near-negligible, implying that the remaining separation is due to additional factors, and that the unfiltered dataset of Torsvik et al. (submitted) is relatively free of bias due to low-quality data.

Figure 5.16: The importance of data quality as illustrated by a comparative apparent polar wander path (APWP) analysis. Columns (a), (b), and (c) depict data from Morel and Irving (1981), Table 5.1, and a filtered version of Table 5.1, respectively. The details of the filter are described in the text. Rows (1), (2), and (3) exhibit the APWPs of North America, Europe, and West Gondwana, respectively. Each APWP is constructed from a 30-Myr moving window, as originally done by Morel and Irving (1981), and rotated into African coordinates according to Bullard et al. (1965). Mean poles with an A_{95} greater than 10° are transparent. Mean poles with a solid symbol are determined from less than 4 results. The dashed lines in columns (b) and (c) depict the trend of the APWP from the previous (direct left) panel for comparison. (d) Great circle distance (GCD) between North America and West Gondwana for columns (a), (b), and (c). (e) GCD between Europe and West Gondwana for columns (a), (b), and (c). The orange area highlights the improvement (decreased GCD) between results from columns (a) and (b), whereas the light gray shows intervals of increased GCD.

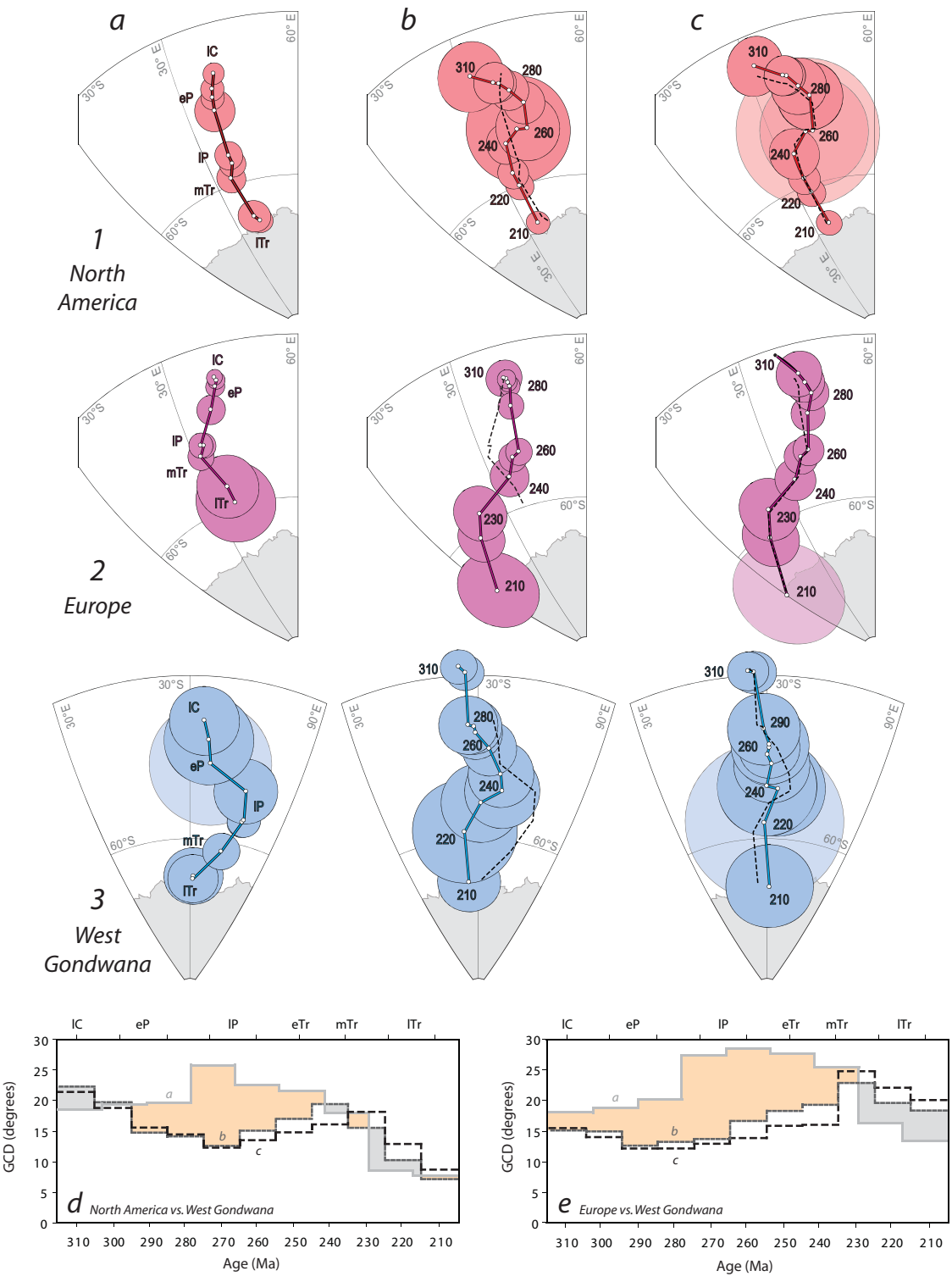
a
b
c
1
North America
2
Europe
3
West Gondwana
IC
eP
IP
mTr
lTr
310
280
260
240
230
220
210
290
30°S
60°S
30° E
60° E
90°E
d North America vs. West Gondwana
e Europe vs. West Gondwana
GCD (degrees)
Age (Ma)
eTr

5.8.2 Euler Rotations

In testing various Pangea reconstructions with paleomagnetic data, the most significant variables are the Euler parameters. Euler rotations exert a much greater control on the relative positions of the APWPs than data selection or the choice of APWP construction method, as is evident in the differences in relative APWP position according to Pangea A-1, A-2, and B. Yet, the sensitivity of APWPs to Euler parameter adjustments internal to these general frameworks is often overlooked. For example, most paleomagnetic tests of Pangea reconstructions focus only on the fit between Gondwana and Laurussia, implicitly assuming that the other required Euler parameters are comparatively unimportant. A direct comparison of paleomagnetic poles requires rotation to a common reference frame, so a comparison of data from Laurussia and West Gondwana invariably necessitates definition of at least three Euler parameters: Europe vs. North America, South America vs. Africa, and Laurussia vs. Gondwana. The first two parameters are independent of the Pangea A-1, A-2, and (most) B model distinctions, which are defined by the Laurussia vs. Gondwana fit. However, significant inaccuracies in either the Laurussia or the West Gondwana reconstruction could compromise any comparative analysis of the Pangea models. This is especially true for the Europe vs. North America parameter, as the paleomagnetic dataset from Europe is the largest and most reliable for the late Paleozoic–early Mesozoic. In addition to these first-order variables, important internal deformation/rotations have been recognized within some continents (Nürnberg and Müller, 1991; Torsvik et al. 2008, 2009, submitted), further compounding the uncertainty in relative APWP position that may be independent of the Laurussia–Gondwana fit.

To demonstrate the significance of these parameters, we have re-calculated the

APWPs of Laurussia and Gondwana using the unfiltered compilation of Torsvik et al. (submitted for publication) and a series of recently re-determined Euler parameters (Table 5.2), and compare them with the same APWPs constructed with the conventional Euler parameters of Bullard et al. (1965). Bullard et al. (1965) treated the continents as rigid plates, so reconstruction of the APWPs requires only the three rotations listed above (Fig. 5.17a). In reconstructing Laurussia according to more recent work, we adopt the Europe vs. North America parameter of Torsvik et al. (2006), which is supported by continental lithospheric extension estimates determined from gravity inversion and seismic refraction profiles (Alvey, 2009, and manuscript in preparation). For West Gondwana, we have elected to use the reconstruction parameters of Torsvik et al. (2009), which are based on a relocation of the South Atlantic continent-ocean boundaries (COBs) by analysis of a variety of geophysical data and geological information. Following the earlier work of Nürnberg and Müller (1991), Torsvik et al. (2009) divide South America into four domains (Amazonia, Parana, Colorado, and Patagonia) and Africa into five domains (NW Africa, NE Africa, Somalia, Lake Victoria Block, and southern Africa), which results in a much improved fit between the restored COBs. We initially keep the Laurussia vs. Gondwana parameter constant (retaining that of Bullard et al., 1965), so that any change in the GCD between the APWPs of Laurussia and Gondwana in our first comparative analysis must be due solely to the Europe vs. North America and/or South America vs. Africa parameters (Fig. 5.17b). Only minor differences are observed in the APWPs of Gondwana (as constructed according to Bullard et al. (1965) and Torsvik et al. (2009), respectively), but the APWPs of Laurussia are considerably different. The Laurussian path constructed according to Torsvik et al. (2006) exhibits a significant and consistent shift eastward, which is due entirely to

the difference in the rotation of Europe. In terms of GCD, the APWPs constructed according to the more recent parameters are an average of 7° closer than those constructed according to Bullard et al. (1965) (Fig. 5.17d); this improvement represents ∼46% of the initial difference between the paths.

Turning next to the fit between Laurussia and Gondwana, we compare the reconstruction parameter of Bullard et al. (1965) with the recently proposed parameter of Labails et al. (2010) (Table 5.2), which is based on a redefinition of the African COB by Sahabi et al. (2004). We also follow Labails et al. (2010) in applying a minor rotation to the Moroccan Meseta, relative to NW Africa, which improves the congruence of the North America-Africa fit. Because we retain an African coordinate frame, the minor changes to the APWP of Gondwana are due only to this rotation of the Moroccan Meseta (Fig. 5.17c). The modified rotation of Laurussia results in a northeast shift of its APWP, bringing it into closer proximity with the APWP of Gondwana. This improvement is reflected in the overall reduction of the GCD between these paths, excepting the intervals of 290 Ma and 260 Ma, in which the mean poles are now found to be primarily separated in a north-south direction (orthogonal to the initial separation). The mean 290 Ma and 260 Ma poles of Gondwana are both situated at what appear to be short periods of relatively fast and brief APW; it is likely that these are artifacts of under-sampling (or sampling with a poor temporal distribution: there are no Gondwana poles in the dataset between 300 and 290 Ma), and we do not consider these intervals of APWP mis-fit to be critical inadequacies of the Labails et al. (2010) fit. With the adoption of this fit, the GCD between mean poles is consistently less than 10°, and the average separation of 6° is close to the commonly assumed ∼5° minimum uncertainty threshold of paleomagnetism (Fig. 5.17d). Overall, the adoption of these new Euler parameters results in a ∼58%

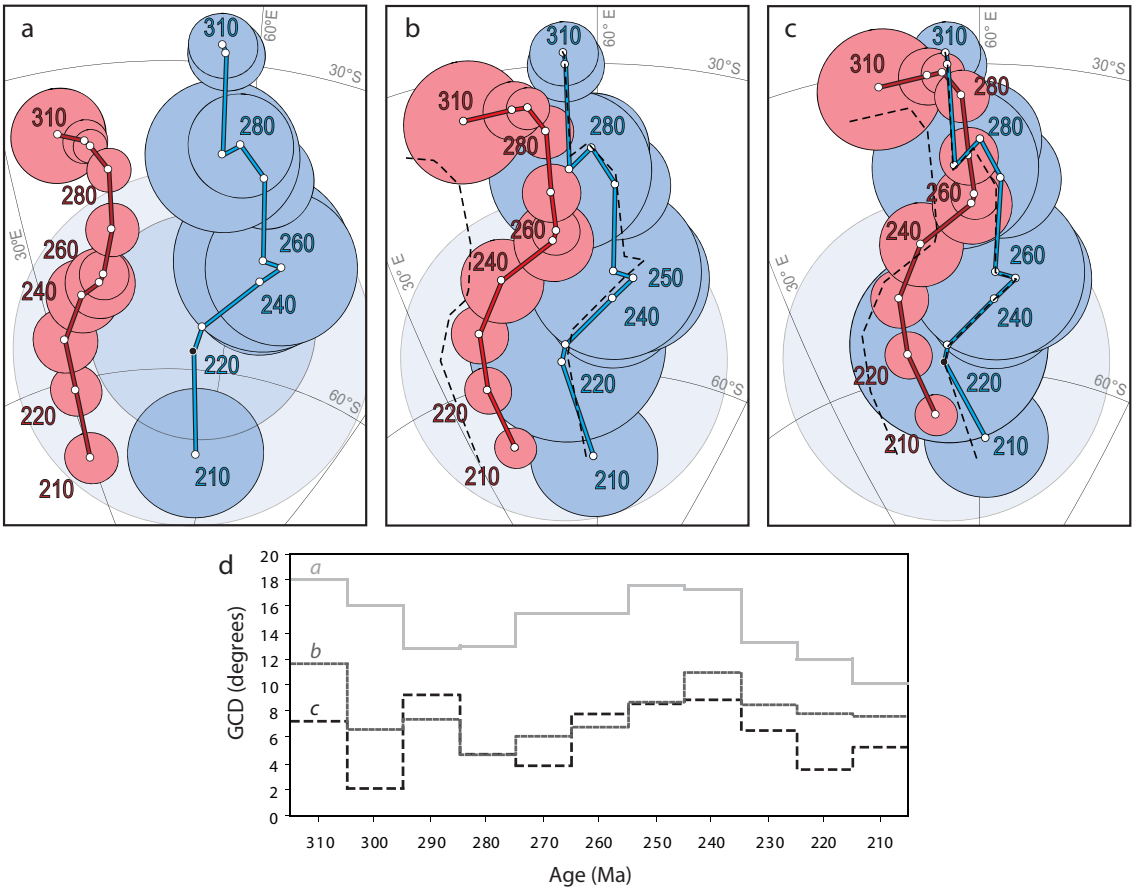

Figure 5.17: The significance and influence of Euler rotations as illustrated by a comparative apparent polar wander path (APWP) analysis. Panels (a)–(c) depict the APWPs of Laurussia (red) and Gondwana (blue) from the paleomagnetic data in Table 5.1 and using a moving window of 20-Myr. Mean poles with an A_{95} greater than 10° are transparent and poles with a solid symbol are determined from less than 4 results. (a) APWPs according to the Euler parameters of Bullard et al. (1965). (b) Same as panel a), but using the Laurussia reconstruction parameters of Torsvik et al. (2006) and the West Gondwana reconstruction parameters of Torsvik et al. (2009) (the Central Atlantic remains reconstructed according to Bullard et al. (1965)). (c) as in (b), except adopting the Central Atlantic reconstruction parameter and the Moroccan Meseta rotation of Labails et al. (2010). The dashed lines in panels (b) and (c) depict the trend of the APWP from the previous (direct left) panel for comparison. Euler parameters are listed in Table 5.2. (d) GCD between the APWPs of each panel.

reduction in the GCD between the APWPs of Laurussia and Gondwana, relative to our starting point with the parameters of Bullard et al. (1965), an improvement which is independent of data selection or other factors.

5.8.3 Inclination Shallowing Corrections

The previous exercises have all but demonstrated that the late Paleozoic–early Mesozoic paleomagnetic Pangea problem is an artifact arising from the inclusion of low-quality data and usage of coarse and/or inaccurate Euler parameters. However, after adopting the updated rotation schemes discussed above and using the most recent compilation of paleomagnetic data, a significant, albeit smaller, separation remains between the APWPs for the Late Permian–Middle Triassic (Fig. 5.17c). The paleomagnetic datasets of the interval 270-220 Ma contain a relatively high fraction of sedimentary-based results that have not been checked/corrected for inclination shallowing, suggesting that this bias may be prominent for these times (Fig. 5.18). In the dataset of Laurussia, 81% (21 of 25) of the constituent paleomagnetic poles for the 230–250 Ma window are derived from sedimentary sequences which have not been corrected for inclination shallowing, the highest proportion in the entire 210–310 Ma interval. In the dataset of Gondwana, 87% (8 of 9) of the constituent paleomagnetic poles for the 240–260 Ma window are derived from uncorrected sedimentary sequences, the highest proportion in its 210–310 Ma dataset.

To check these datasets for the presence of a shallow inclination bias, we have re-calculated the APWPs after removing all clastic sedimentary-based poles that are uncorrected for inclination shallowing (Figs. 5.19a, b). Accordingly, the 240–260 Ma segment of the Laurussian APWP shifts to the southeast with this treatment, implying that the unfiltered dataset is significantly biased by shallow inclinations in this interval. A less pronounced, but discernable eastward shift is also observed

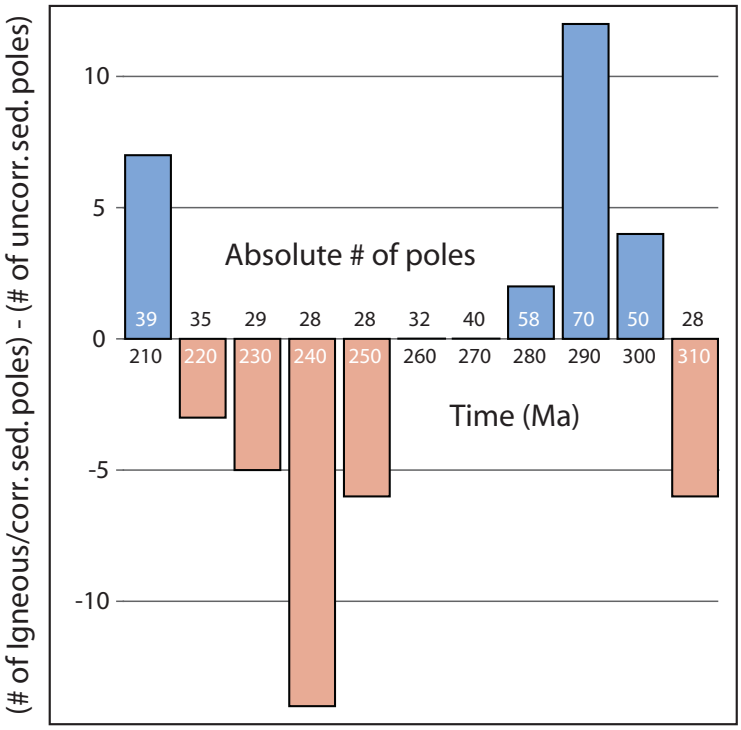

Figure 5.18: The quantity of "corrected" vs. "uncorrected" paleomagnetic data from 310 to 210 Ma. Difference calculated as: (1) the number of igneous-based/inclination-corrected sedimentary-based paleopoles minus (2) the number of uncorrected sedimentary-based paleopoles (as in Table 5.1), plotted against time. Time (in Ma) is listed below the central horizontal axis. Each 10-Myr bin includes data from a 20-Myr moving window (for direct comparison with the APWPs) centered on the time listed. The absolute number of poles in each bin is listed above the central horizontal axis.

for the 280–270 Ma interval, in which recent results from igneous rocks in Laurussia take on some prominence (Dominguez et al., 2011; Yuan et al., 2011). Interestingly, a northeastward shift is observed in the 300–290 Ma interval, due to the presence of part of Laurentia in the southern hemisphere at that time, and owing to the valuable inclination-corrected results obtained by Bilardello and Kodama (2010b). The filtered dataset of Gondwana is less illuminating, due to the severe reduction in the quantity of data; only the 210 Ma and 270 Ma mean poles are built from more than five results (including several new paleopoles from Argentina (Domeier et al., 2011a, 2012)), and the average pole quantity for the 20-Myr moving windows in the 310–210 Ma time-frame is 3.8. Consequently, the filtered APWP is erratic and unreliable for the interval of interest (260-230 Ma).

Following the observations from this filtering exercise, and the identification of a widespread shallow inclination bias in the Permian-Middle Triassic paleomagnetic data of North America by Domeier et al. (2011b), we apply an average shallow inclination correction ($f = 0.6$) to all sedimentary-based results that are prone to inclination shallowing, as also done by Torsvik et al. (submitted) (Fig. 5.19c). The application of this correction to the APWP of Laurussia appears to under-correct the most strongly biased intervals (230–250 Ma and 290–300 Ma), while coinciding reasonably well with the filtered mean poles of the remaining intervals (210–220 Ma and 260–280 Ma), suggesting that the correction is not excessive. The change evident in the APWP of Gondwana is more pronounced, partly due to the greater proportion of sedimentary-based results in its dataset, but also because Gondwana occupied higher latitudes than Laurussia during the late Paleozoic–early Mesozoic and the correction yields the greatest change at mid-latitudes. We are unfortunately unable to evaluate the pertinence of this correction to the Gondwana dataset, again

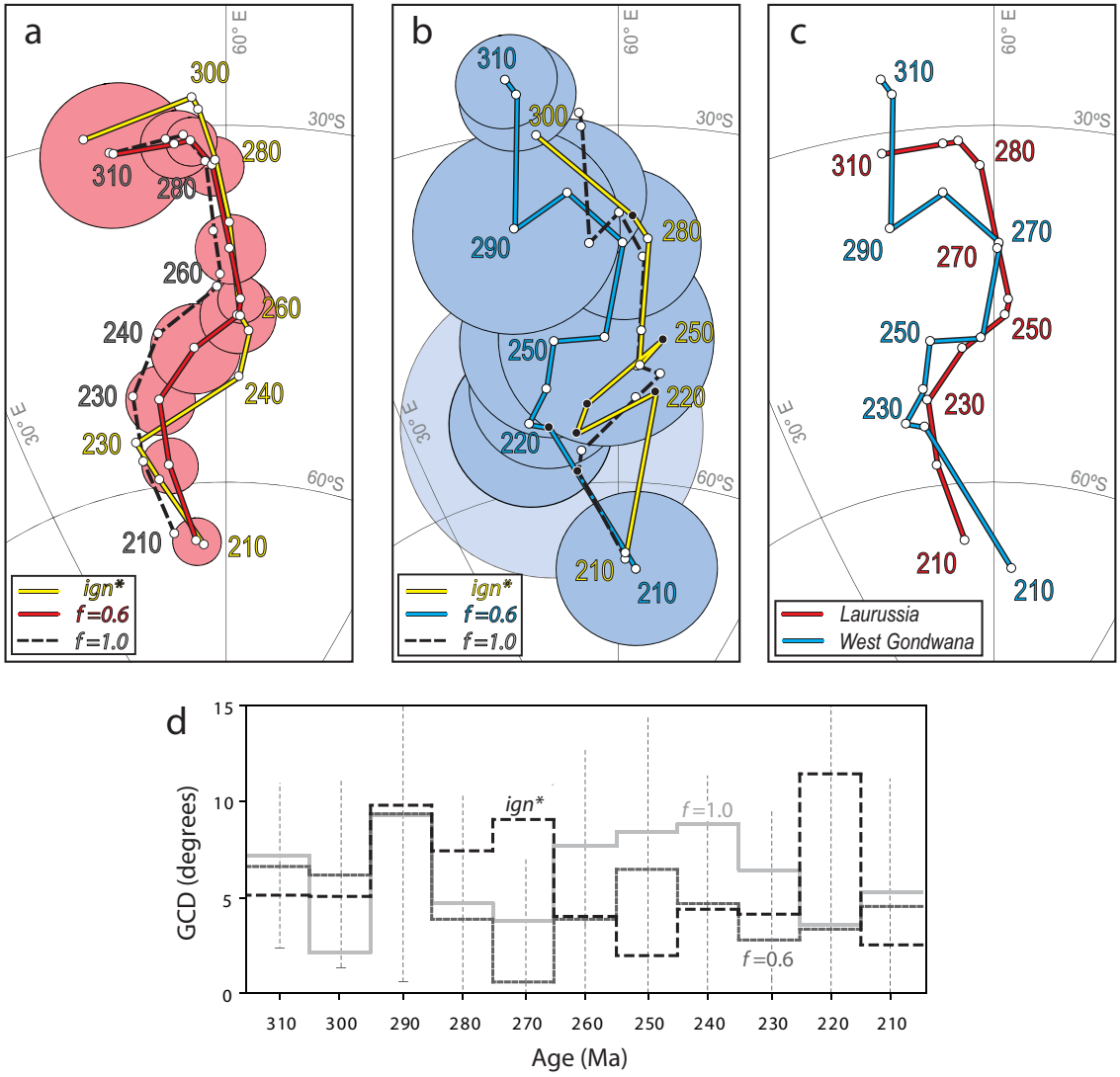

Figure 5.19: Tests and corrections for inclination shallowing in the apparent polar wander paths (APWPs) of (a) Laurussia and (b) Gondwana. In these panels, the APWPs are built from the data in Table 5.1 and constructed using a 20-Myr moving window and the rotation parameters used in Fig. 5.17c. The dashed black paths are calculated from the raw data ($f = 1$; i.e. no shallowing correction), the yellow paths are calculated from the same data after removing all poles derived from clastic sedimentary rocks (leaving results derived from igneous and carbonate rocks), and the solid colored paths are calculated after applying a blanket inclination correction (f=0.6) to all poles derived from clastic sedimentary rocks. Mean poles with an A_{95} greater than 10° are transparent and poles with a solid symbol are determined from less than 4 results. (c) The solid colored paths (inclination corrected) from panels (a) and (b) for direct comparison. (d) GCD between the APWPs for each treatment. The vertical dashed lines show the extent of the A_{95} error on the Gondwana mean pole estimates, relative to the GCD between poles of the inclination corrected paths. No statistically distinct separation is observed between 280 and 210 Ma.

due to the low-quality of the filtered APWP, but we see no reason to expect that the mechanics of shallowing should have a hemispheric distinction. With the application of this correction, the average GCD between the APWPs is reduced to 4.7°, and only for the 290–310 Ma interval is the separation larger than the uncertainty on the position of the mean Gondwana poles (Fig. 5.19d). Importantly, this separation is inverted relative to the original problem; the 290–300 Ma mean poles from Gondwana are west of the equivalent mean poles from Laurussia, a separation which does not introduce any unacceptable cratonic overlap, but rather requires a greater distance between the continents than expected by the Labails et al. (2010) fit.

It is worth noting that our use of an average inclination correction is not strictly correct. As aforementioned, f is a function of numerous variables (grain size, sedimentation rate, post-depositional history, timing of magnetization acquisition, size and composition of magnetic carrier, etc.) and will therefore be formation-specific (or even horizon-specific if such variables are prone to substantial intra-formational change). However, it will be some time before formation-specific f values are known for the bulk of the (currently uncorrected) sedimentary-based results. In the absence of these specific values, application of an average correction likely offers a more realistic estimate of the true trend of the APWPs, assuming the average correction is reasonably close to the "true" (and unknown) average value. In the compilation of Bilardello and Kodama (2010a), the average f value (from magnetite- and hematite-bearing rocks) is 0.61, with a standard deviation of 0.11, very close to the value of $f = 0.6$ assumed above. This assumed value is conservative with respect to the hematite-only average ($f = 0.59$), the values determined from re-deposition experiments (not included in the compilation of Bilardello and Kodama (2010a)), and the averaged value calculated from the VGP distribution analysis of Domeier et al.

(2011b). Moreover, the appropriateness of the applied average value is independently substantiated by the improved agreement between the sedimentary-based poles and the igneous-only results in the APWP of Laurentia, as described above.

To consider what variability could be anticipated in the position of the APWPs, given the so-far observed variation in f values, we conducted a numerical exercise. Each sedimentary-based paleomagnetic pole (without a known f) was corrected with a random value of f that was drawn from a normal distribution with a mean of 0.61 and a standard deviation of 0.11. 10-Myr mean poles were then recalculated with a 20-Myr moving window, as before (igneous-based poles and previously corrected sedimentary-based poles were still used in the calculation of mean poles); the procedure was repeated 1,000 times (Fig. 5.20). The resulting assemblages of re-estimated poles show various distributions, according to the number of sedimentary-based constituents and the geographic distribution of their sampling sites. Importantly, the re-estimated poles do not fall outside the A_{95} of the original means (which have a constant assumed value of $f = 0.6$). This reveals that the variation in formation-specific (and unknown) f values is comparatively unimportant, assuming that the average correction is close to the "true" average. This is because pole-specific corrections will only result in local and random mean pole adjustments, whereas a change in the average correction will result in a systematic shift of the entire APWP. Given the f values so-far determined, we contend that the average correction $f = 0.6$ is very reasonable, and offers a first-order estimate of the true APWP positions. Future adjustments to the average value and incorporation of pole-specific f values should be made to these initial estimates.

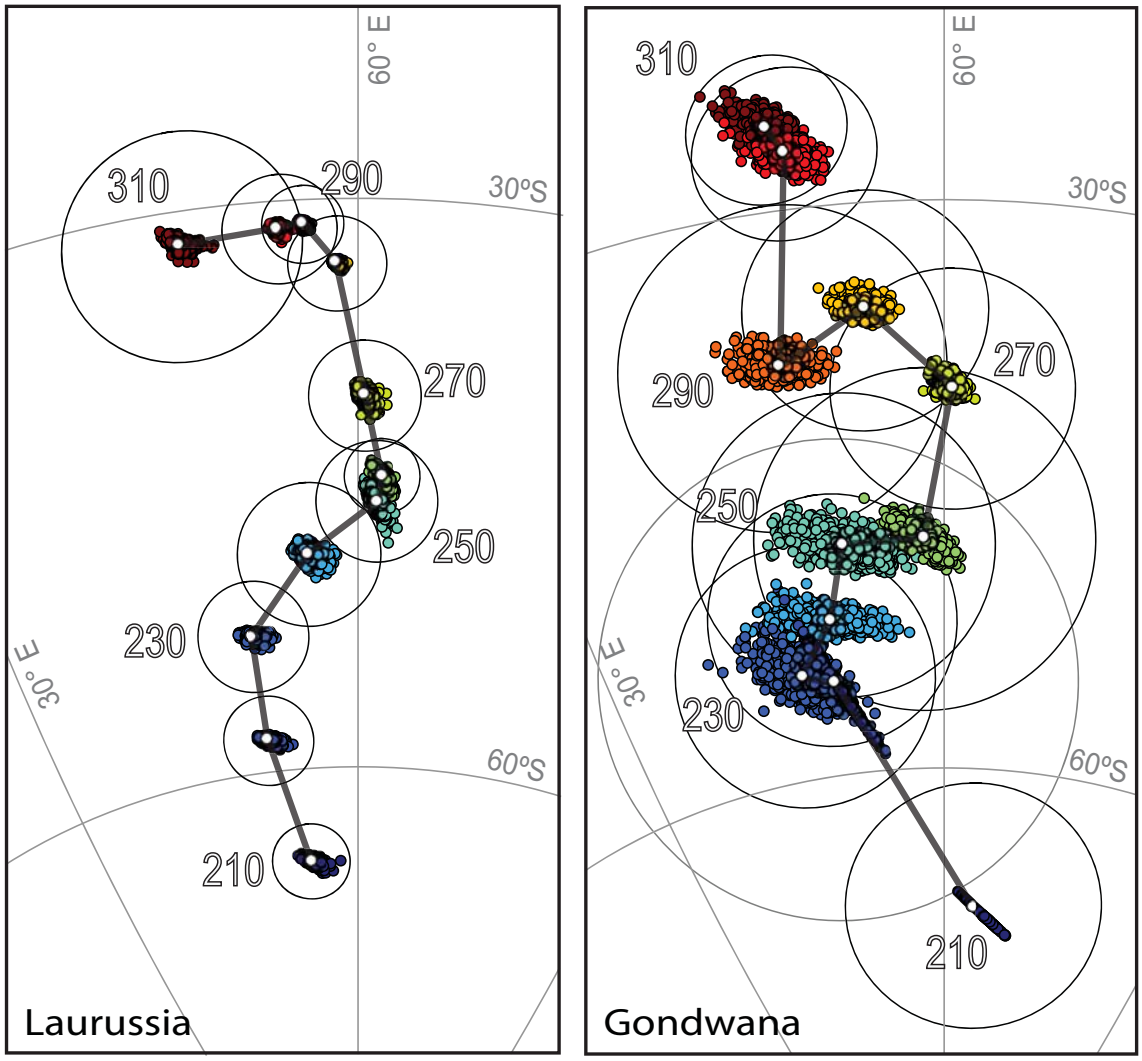

Figure 5.20: Numerical illustration of potential variation in mean pole positions, assuming the so-far observed variation in inclination shallowing coefficients (f), as compiled in Bilardello and Kodama (2010c). The left (right) panel shows re-estimations of the mean pole positions in the APWP of Laurussia (Gondwana). Each panel shows the mean poles re-estimated by: (1) assigning all uncorrected clastic sedimentary-based paleopoles a value of f drawn randomly from a normal distribution with a mean of 0.61 and a standard deviation of 0.11, and (2) re-calculating the mean poles by re-averaging the newly-corrected sedimentary-based poles with the igneous-based and previously corrected sedimentary-based poles. The process is repeated 1,000 times (i.e. each mean pole is re-estimated 1,000 times). The color scheme was applied to distinguish pole assemblages of different age. The white poles and their A_{95} depict the result using a constant value of $f = 0.6$ (i.e. the mean poles and A_{95} from Fig. 5.19c). The distribution of re-estimated poles is controlled by the relative number of constituent uncorrected sedimentary-based poles, and the geographic distribution of their sampling sites. Note that none of the re-estimated poles falls outside of the A_{95} on the $f = 0.6$ means.

5.9 Reconstructions

Having confirmed that the paleomagnetic data can be reconciled with an A-type Pangea reconstruction through the 310–210 Ma interval, we now adopt the complimentary approach to reconstructing Laurussia and Gondwana. We assume the Laurussia vs. Gondwana reconstruction parameter to be unknown, and instead reconstruct these landmasses independently according to their paleomagnetic records at each 10-Myr interval between 310 and 210 Ma. For the reconstruction parameters internal to Laurussia and Gondwana, we retain those used in section 5.8.2. As longitude is unconstrained by paleomagnetism, the east-west fitting of Laurussia to Gondwana is determined by visual inspection in all instances (Table 5.2). In each case, we attempt to rotate the landmasses into the closest permissible fit; permissible reconstructions are those that require no more than a few hundred kilometers of overlap of modern COBs. A minor overlap of modern COBs is expected in pre-drift reconstructions, as some extension occurs before continent break-up. For example, the pre-drift (max. closure) fit of Labails et al. (2010) results in ∼100 km of COB overlap between North America and NW Africa. Our delimitation of the Central Atlantic COBs follows that of Labails et al. (2010). Following this approach, we can broadly determine which reconstruction is in closest accord with the paleomagnetic data for a given interval in the late Paleozoic–early Mesozoic. We consider the results using both the raw and inclination-corrected ($f = 0.6$) datasets (Table 5.3). It is worth re-iterating here that our use of an average inclination correction is not strictly correct, and the veracity of the derived reconstructions is ultimately dependent on the validity of the assumed (average) correction.

If the raw datasets are used in the Late Carboniferous (310 Ma), reconstruction of

the landmasses according to an A-type geometry results in a large COB overlap (350–550 km) between Laurussia (specifically eastern North America and Iberia) and NW Africa. There is also a tight fit between the southern margin of North America and northern South America, so any small, relative sinistral translation applied to the landmasses (to reduce Central Atlantic COB overlap) will result in cratonic overlap between the Americas, unless Pangea B is adopted. By the latest Carboniferous (300 Ma), a clockwise rotation and northward drift of Laurussia, relative to Gondwana, yields a small paleo-Gulf, ∼200–300 km wide, and an excellent fit between Laurussia and NW Africa (∼100–250 km of COB overlap) in an A-type geometry. At this time, most of Laurussia has drifted into the northern hemisphere and northwestern Africa is a few degrees south of the equator. With the application of inclination correction (for 310–300 Ma), Gondwana is pulled south, away from Laurussia, resulting in a Central Atlantic COB separation of ∼200–600 km and a much larger paleo-Gulf between North and South America (∼300–900 km wide) (Fig. 5.21). The applied inclination shallowing correction may therefore be excessive in this interval.

Laurussia and Gondwana continued drifting northward during the Early Permian (290–270 Ma). If the raw data are used during this interval, and an A-type reconstruction is forced, the COB overlap between Laurussia and NW Africa is large (∼300–700 km; greatest at 290 Ma). The North–South America fit is loose at 290 Ma but becomes increasingly tight with decreasing age (tight at 270 Ma). Again, application of a small relative sinistral translation between Laurussia and Gondwana (to relieve some Central Atlantic COB overlap) is not possible due to consequent overlap of the Americas and northern Gondwana–southern Europe. With inclination correction, a tight to slightly loose fit (minor to no COB overlap) is achieved between Laurussia and NW Africa, and a wide paleo-Gulf is observed between North

Figure 5.21: Paleogeographic reconstruction for the Late Carboniferous (310 Ma) using the inclination corrected datasets of Laurussia and Gondwana (Table 5.3) to restore the landmasses independently. Euler rotations internal to Laurussia and Gondwana are those used in Fig. 5.17c. The optimal longitude fit between Laurussia and Gondwana was determined by visual inspection (Table 5.2), as paleomagnetic data offer no constraints on longitude, and was applied by rotating Laurussia along fixed latitude lines, relative to Gondwana. Arbitrary (undefined) longitudes are depicted at 30° intervals for reference. The darker brown areas depict (present-day) submerged continental crust which extends to the continent ocean boundary (COB). The boundaries of the central Atlantic COBs are taken from Labails et al. (2010). The layers are transparent so that crustal overlap is evident by darker shades of color. The Piedmont-Florida terrane has been placed in its present-day position to allow for a comparison between the Atlantic-bordering COBs. In this particular reconstruction (310 Ma), the central Atlantic COBs are separated by ∼200–400 km, indicating that the inclination correction ($f = 0.6$) may well have been excessive in this interval.

and South America (∼300–900 km) (Fig. 5.22).

In the Late Permian, Laurussia and Gondwana continue to drift north and rotate counter-clockwise. Laurussia resides entirely in the northern hemisphere and NW Africa extends to ∼10°N (Fig. 5.23). At 260 Ma, use of the raw data results in large Central Atlantic COB overlap (∼400–700 km) if an A-type geometry is assumed, and the fit between North and South America remains tight. The inclination corrected data yield an excellent Central Atlantic fit and a wide paleo-Gulf (Fig. 5.23). At the Permian–Triassic boundary (250 Ma), an A-type reconstruction does not appear permissible with the raw data; it would yield ∼500–800 km of COB overlap between Laurussia and NW Africa and minor cratonic overlap between North and South America. As before, relative sinistral translation between Laurussia and Gondwana results in additional overlap until a B-type geometry is reached. The $f = 0.6$ correction appears to over-compensate for any bias present in this interval, as it results in a ∼350 km separation of the Central Atlantic COBs and the paleo-Gulf exceeds 900 km in width.

In the Early to Middle Triassic, Laurussia and Gondwana continue to rotate counter-clockwise, but with minimal northward drift. If an A-type fit is forced with the raw data, the overlap of the Central Atlantic COBs peaks in this interval (∼600–1,000 km at 240 Ma), and significant cratonic overlap between southern North America and northern South America is again observed. The inclination corrected data yield a tight COB fit (no overlap) and a wide (∼500–800 km) paleo-Gulf (Fig. 5.24). In the early Late Triassic (230 Ma), the Central Atlantic COB overlap begins to lessen (∼300–700 km) with use of the raw data; by 220–210 Ma the overlap is further reduced (∼300–600 km). North and South America are tightly fitting to overlapping throughout the Late Triassic; at 230 Ma this overlap is large (∼300–400

Figure 5.22: Paleogeographic reconstruction for the Early Permian (280 Ma) using the inclination corrected datasets for Laurussia and Gondwana (Table 5.3). In this reconstruction, the Central Atlantic COBs are closer to each other, relative to Fig. 5.21, but still separated by ∼100–150 km, so the applied inclination correction may again have been somewhat excessive. The paleo-Gulf of Mexico is wide, very similar to the A-1 configuration of Bullard et al. (1965).

Figure 5.23: Paleogeographic reconstruction for the Late Permian (260 Ma) using the inclination corrected datasets for Laurussia and Gondwana (Table 5.3). A good fit is observed between the Central Atlantic COBs (minor overlap). A significant paleo-Gulf is still present, again in agreement with the A-1 model.

km). With inclination correction, the Central Atlantic fit becomes tight at 230 Ma (minor COB overlap), and the paleo-Gulf is moderately wide (∼400–700 km). For 220 Ma, the corrected data yields a good fit of the Central Atlantic COBs (0–200 km) and a wide paleo-Gulf (∼600 km). No appreciable change is observed with the application of inclination correction at 210 Ma. Both Laurussia and Gondwana continue to slowly rotate counter-clockwise through the Late Triassic, and again begin to drift northward.

In summary, an A-type Pangea reconstruction is permissible for the entire 310–210 Ma interval if the paleomagnetic data from Laurussia and Gondwana are corrected for inclination shallowing (by $f = 0.6$). The specific reconstruction achieved by restoration of Laurussia and Gondwana according to their independent paleomagnetic data is similar to the fit of Bullard et al. (1965), but with a slightly tighter central Atlantic closure, as in the assembly of Labails et al. (2010) (Table 5.2). Even if the paleomagnetic data are not corrected for inclination shallowing, an A-type reconstruction is arguably acceptable for the Late Carboniferous (310–300 Ma), the late Early to middle Permian (280–270 Ma), and the Late Triassic (220–210 Ma). It is only in the Early Permian (290 Ma) and the Late Permian–Middle Triassic (260–230 Ma) that a forced A-type reconstruction will result in untenable continental overlap (again, only in the case that the paleomagnetic data are not corrected for inclination shallowing). Rather than advocate a rapidly evolving paleogeography (alternating between Pangea B and A), we contend that this apparent failure of the A-type model in the Early Permian and Late Permian–Middle Triassic is a manifestation of a recurring data-artifact. Following our earlier arguments and the observation that the paleomagnetic data of the 250-230 Ma interval include an especially high relative number of results derived from clastic sedimentary rocks (Fig. 5.18), we favor the

Figure 5.24: Paleogeographic reconstruction for the Middle Triassic (240 Ma) using the inclination corrected datasets for Laurussia and Gondwana (Table 5.3). A loose fit is observed in the Central Atlantic, and a sizable paleo-Gulf is present between Laurentia and northern South America. Comparison with Fig. 5.21 reveals that Pangea has drifted north and rotated counter-clockwise since the Late Carboniferous.

interpretation that this data-artifact equals a shallow inclination bias.

5.10 Conclusions

A prominent discrepancy between late Paleozoic–early Mesozoic paleomagnetic data and the most commonly assumed paleogeographic model of Pangea has been recognized (and has persisted) for half a century. Three theoretical solutions have been proposed to resolve this problem: an alternative paleogeographic reconstruction (notably Pangea B), modification to the GAD hypothesis for (at least) late Paleozoic–early Mesozoic time, and eradication of, or correction for, systemic bias in the paleomagnetic data. The former two hypothetical solutions require substantial revision to widely used and well-supported models, whereas the latter solution implies that these models can be reconciled by the use of high-quality data. We have confirmed that the late Paleozoic–early Mesozoic paleomagnetic data from Laurussia and Gondwana can be reconciled with a conventional A-type Pangea reconstruction, using an updated paleomagnetic dataset, recently refined Euler parameters, and theoretical inclination shallowing corrections. Our review of previous work and our comparative analysis of APWPs with/without results derived from clastic sedimentary rocks details support for the presence of a significant shallow inclination bias in such rocks. The longitudinally best-fitting reconstruction of Laurussia and Gondwana, after independently restoring these landmasses to paleolatitudes determined by their respective paleomagnetic data, yields a central Atlantic fit similar to the conventional A-type reconstruction of Bullard et al. (1965). These findings indicate that Pangea can be reconciled with the paleomagnetic data without requiring serious paleogeographic re-structuring or non-dipole fields. We have generated a series of new reconstructions based on our preferred dataset, which may act as a first-order

reference to be updated as new data and formation-specific inclination shallowing corrections become available.

5.11 Acknowledgements

New geochronologic results have been invaluable to our new findings, and continue to improve the global paleomagnetic data-set; we acknowledge the recent and ongoing contributions of Eric Tohver and Bart Hendriks in this respect. We thank Dario Bilardello and an anonymous reviewer for their constructive comments. Financial support for this research was provided by the Norwegian Geological Survey (NGU), the Center for Advanced Study at the Norwegian Academy for Science and Letters, and the U.S. National Science Foundation, Division of Earth Sciences (Tectonics Program), and NSF's Office of International Science and Engineering (Americas Program), grant EAR-0634807, and is gratefully acknowledged. THT acknowledges funding from the European Research Council under the European Union's Seventh Framework Programme (FP7/2007-2013)/ERC Grant agreement number 267631.

Table 5.1: 325–195 Ma paleopoles from Laurussia and West Gondwana, compiled by Torsvik et al. (submitted)

Formation	Plat	Plon	α_{95}	Age	Notes	Reference
LAURUSSIA:						
NORTH AMERICA						
Newark volcanics I	−63.0	263.1	2.3	197		1702
Connecticut Valley volcanics	*−65.5*	*267.5*	*11.1*	*197*	X	477
Moenave Fm	−62.5	251.0	2.8	197	r,i	Donohoo-Hurley et al. (2010)
Hartford Newark basalts and volcanics	−68.0	268.5	4.0	197		2278
Watchung basalts	−63.6	268.7	6.2	197		1339
Hettangian Newark red beds	−55.6	274.6	6.0	198	*	2312
Piedmont dikes	−61.5	234.0	7.9	199		1809
North Mountain basalt	−66.4	252.0	10.7	200		1932
Hartford basin	−66.6	268.2	3.2	201	i	Kent and Olsen (2008)
Newark Martinsville core	−67.8	275.8	5.0	204	i	Kent and Tauxe (2005)
Chinle Group, Redonda Fm	−58.5	256.9	8.0	204	*	2979
Chinle Fm	−58.7	250.9	10.7	204	r,*	2800
Chinle Fm, Redonda Member	*−57.8*	*259.3*	*4.2*	*204*	X,*	152
Newark Martinsville core	−64.9	276.6	6.5	204	i	Tan et al. (2007)
Newark Weston core	−58.1	271.8	2.5	207	i	Tan et al. (2007)
Newark Westonville	−66.9	267.2	5.0	207	i	Kent and Tauxe (2005)
Passaic Fm, baked sediments	−65.5	255.1	4.7	211		2791
Passaic Fm	−55.6	274.6	5.6	211	*	2312
Chinle Fm	−56.6	255.9	3.4	211	r,*	2380
Newark Somerset core	−61.7	274.7	4.0	211	i	Kent and Tauxe (2005)
Newark Basin both polarities	−57.6	269.6	3.0	211	*	1339
Taylor Mountain batholith	−61.4	282.2	5.2	212		Symons et al. (2009)
Newark Rutgers core	−60.1	277.1	3.1	214	i	Kent and Tauxe (2005)
Manicouagan Stucture, Quebec	−60.1	271.8	7.0	215		434
Manicouagan Stucture, Quebec	*−59.0*	*267.6*	*10.0*	*215*	X	443
Popo Agie Fm, Chugwater	*−56.1*	*276.0*	*14.0*	*215*	X,*	1334
Ankareh Fm	−50.5	267.6	7.8	215	*	Weil et al. (2010)
Chinle Fm, Bull Canyon Member	−57.4	267.7	5.6	216	*	2380
Newark Titusville core	−59.9	279.4	3.2	217	i	Kent and Tauxe (2005)
Chinle, Sangre de Cristo	−52.9	282.0	5.1	218	r,*	2979
Dockum Group, Trujillo and Tecovas Fms	−56.4	276.8	7.7	218	*	2944
Shinarump Member, Chinle Fm	−59.6	277.5	5.0	220	r,*	2489
Newark Basin, Lower redbeds	−53.4	281.7	5.0	220	*	2331
Dan River-Danville Basin	−58.5	279.5	2.0	221	i	Kent and Tauxe (2005)
Newark Nursery core	−60.5	281.6	5.0	221	i	Kent and Tauxe (2005)
Abbott Pluton	*−48.3*	*272.3*	*3.9*	*221*	X	1831
Newark Princeton core	−54.1	285.2	4.0	227	i	Kent and Tauxe (2005)
Agamenticus Pluton	−48.4	278.5	3.2	228		1831
Upper Moenkopi drillcore	*−54.1*	*288.3*	*2.5*	*230*	r,X,*	160
Chugwater Fm	*−45.2*	*295.4*	*4.0*	*230*	X,*	1266
Upper Moenkopi Fm	*−52.5*	*290.7*	*3.1*	*230*	r,X,*	159
Moenkopi Fm (upper)	−56.5	283.2	4.5	230	r,*	2808
Chugwater Fm	−46.1	293.6	3.3	230	*	1271
Moenkopi Fm (Gray Mountain)	−54.6	284.5	5.0	234	r,*	1221
Moenkopi Fm, Anton Chico Member	−44.7	301.4	4.9	234	r,*	2979
Combined Moenkopi	−57.6	280.3	2.8	234	Com.,*	2489
Moenkopi Fm., CO	−55.6	285.8	4.9	234	r,*	571
Moenkopi Fm	*−41.1*	*305.6*	*5.3*	*234*	r,X,*	2632
Combined Red Peak	−47.3	294.0	5.8	230	Com.,*	1334
Lower Fundy Group	−44.3	271.6	7.2	246	*	Symons et al. (1989)
Dewey Lake Fm	−51.0	306.5	5.0	250	*	2303
Bernal Fm	*−49.9*	*298.1*	*8.0*	*255*	r,X,*	2489
Ochoan red beds	−54.8	299.3	15.0	258	*	688
Guadalupian red beds	−51.5	306.7	5.0	263	*	688
Illinois intrusives	−56.3	302.9	3.8	270		Domeier et al. (2011b)

. . . continued

Formation	Plat	Plon	α_{95}	Age	Notes	Reference
Downey Bluff sill	*−53.0*	*308.7*	*3.8*	*272*	X	Reynolds et al. (1997)
Hicks Dome breccia	*−54.8*	*292.1*	*8.6*	*272*	X	Reynolds et al. (1997)
Toroweap Fm	*−51.9*	*303.0*	*10.0*	*277*	r,X,*	688
Leonardian subset	−51.7	302.1	5.0	277	*	688
Artinskian Pictou red beds	−42.1	306.5	3.6	280	*	2281
Churchland pluton	*−33.5*	*306.3*	*16.3*	*282*		1264
Fountain and Lykins Fms	*−44.6*	*305.3*	*13.1*	*283*	r,X,*	504
Abo Fm	−46.8	304.0	2.1	285	r,*	1311
Piedmont Mafic intrusions	−38.9	300.8	10.2	289		1527
Upper Casper Fm	−50.5	303.0	1.5	291	*	1455
Elephant Canyon Fm	*−37.5*	*296.6*	*5.0*	*292*	r,X,*	671
Cutler Fm, Lisbon Valley	*−40.1*	*307.7*	*7.1*	*292*	r,X,*	1341
Ingelside Fm	−43.1	307.9	2.0	292	r,*	1142
Cutler Fm	*−41.6*	*300.4*	*2.0*	*292*	r,X,*	671
Minturn and Maroon Fms	−40.1	300.5	2.8	298	r,*	1685
Upper Maroon Fm	*−55.3*	*279.8*	*12.8*	*299*	r,X,*	504
Dunkard Fm	−44.1	301.5	3.9	300	*	302
Laborcita Fm	−42.1	312.1	2.1	301	*	1311
Wescogame Fm	−44.1	303.9	3.4	301	r,*	1311
Lower Casper Fm	−45.7	308.6	1.8	303	*	1455
Glenshaw Fm	−28.7	299.8	3.1	303	i	Kodama (2009)
Riversdale Group	−36.0	302.0	6.0	310	*	1110
Shepody Fm, Nova Scotia	−29.0	298.3	7.7	317	i	Bilardell and Kodama (2010)
Mauch Chunk	−22.6	294.4	8.3	320	i	Bilardell and Kodama (2010)
Maringouin Fm, Nova Scotia	−29.7	296.4	15.3	322	i	Bilardell and Kodama (2010)
GREENLAND						
Gipsdalen and Fleming Fjord Fms	−52.7	278.7	5.0	209	i	Kent and Tauxe (2005)
STABLE EUROPE						
Kerforne dyke, France	−61.0	259.0	7.5	198		2743
Hettangian-Sinemurian limestone	*−55.0*	*280.0*	*9.0*	*201*	X	3141
Paris Basin sediments	−51.0	285.0	3.0	201		3029
Andesites, Ukraine	−50.0	286.4	4.5	204		Yuan et al. (2011)
Rhaetian sediments, Germany, France	−50.0	292.0	8.0	208	*	3141
Merci mudstone, Somerset	−50.0	308.0	5.1	215	*	3311
Sunnhordland dike	*−50.0*	*305.0*	*4.6*	*221*	X	Walderhaug (1993)
Gipskeuper sediments	−49.0	311.0	6.0	226		3141
Taimyr Sills, Siberia	−47.1	301.6	2.9	228		Walderhaug et al. (2005)
Heming limestone, France	−54.0	321.0	3.0	234		2411
Musschelkalk carbonates, Poland	−53.0	303.0	12.0	234		3253
Bunter and Musschelkalk, Germany	−49.0	326.0	15.0	239	*	158
Upper Buntsandstein, France	−43.0	326.0	5.0	243	*	1028
Volpriehausen Fm, Germany	−49.0	348.2	3.8	246	*	Szurlies (2004)
Taimyr basalts, Siberia	−59.3	325.8	7.8	248		Walderhaug et al. (2005)
German Trias, Lower Buntstein	−50.6	345.6	3.3	249	*	Szurlies et al. (2003)
Taimyr Siberian Traps, Siberia	*−59.0*	*330.0*	*10.0*	*250*	X	2832
Siberian Traps, Siberia	−56.2	326.0	3.3	251		Gurevitch et al. (2004)
Kotuy River Siberian Traps, Siberia	−52.7	328.4	13.9	251		Pavlov et al. (2007)
Siberian Traps NSP1 pole	−56.4	321.7	2.1	251		Pavlov et al. (2007)
Sudetes sediments, Poland	*−50.0*	*343.0*	*5.0*	*251*	X,*	3161
Stolbovaya River Siberian Traps, Siberia	−53.3	330.2	5.3	251		Pavlov et al. (2007)
Big Nirundaiver intrusion, sediments, Siberia	−54.3	323.0	5.0	251		Pavlov et al. (2007)
Moyero River Siberian Traps, Siberia	−58.5	314.5	2.7	251		Gallet and Pavlov (1996); Pavlov et al. (2007)
Siberian Traps Mean recalculated, Siberia	−52.8	334.4	9.7	251		Kravchinsky et al. (2002), recalculated
Dome de Barrot red beds, France	−46.0	327.0	2.7	255	*	652

. . . continued

Formation	Plat	Plon	α_{95}	Age	Notes	Reference
Massif des Maures, France	−51.0	341.0	4.0	255	*	1408
Late Permian sediments, Urals	−45.6	350.2	3.5	260	*	Bazhenov et al. (2008)
Esterel sediments, France	*−47.0*	*331.0*	*5.0*	*261*	X,*	165
Brive Basin sediments, France	−49.0	343.0	4.0	261	*	3144
Permian red beds, Lodeve, France	*−53.0*	*331.0*	*0.0*	*264*	X,*	1207
Lodeve Basin, France	−49.0	334.0	1.5	264	*	1813
Upper Lodeve sandstone, France	*−47.0*	*336.0*	*4.6*	*264*	X,*	168
Saxonian red sandstone, France	*−51.0*	*324.0*	*4.0*	*264*	X,*	2361
Esterel extrusives, France	−51.5	322.0	6.1	264		165
Cracow volcanics B	−50.0	344.0	4.1	269		Nawrocki et al. (2008)
Lunner dikes, Norway	−51.0	343.0	2.5	271		Dominguez et al. (2011)
Lunner dikes, Norway	−53.0	344.0	5.9	271		3188, redated
Bohuslan dikes combined, Sweden	−51.0	345.0	8.6	275		1155
Scania melaphyre dikes, Sweden	−54.0	352.0	11.0	279		2222
Bohemian quartz porphyry, Germany	*−37.0*	*341.0*	*7.0*	*280*	X	3145
Mauchline lavas, Scotland	*−47.0*	*337.0*	*14.0*	*280*	X	3093
Bohemian Massif igneous, Germany	−42.0	346.0	10.0	280		2356
Oslo volcanics, Norway	*−47.0*	*337.0*	*1.0*	*281*	X	915
Ringerike lavas, Norway	−44.6	337.4	13.4	281		1830
Sarna alkaline intrusion, Sweden	*−38.0*	*346.0*	*6.9*	*281*	X	1735
Trachytes, Ukraine	−49.4	359.7	6.5	283		Yuan et al. (2011)
Moissey volcanics, France	−41.0	352.0	6.7	285		1205
Intrasudetic Basin volcanics, Poland	−43.0	352.0	3.2	285		3161
North Sudetic Basin sediments, Poland	*−44.0*	*4.0*	*5.1*	*285*	X,*	3161
Krkonose Basin oil shales, Czech Republic	*−40.0*	*346.0*	*2.0*	*285*	X,*	2444
Lower Lodeve sandstone	*−44.0*	*350.0*	*7.7*	*285*	X,*	168
Mount Hunneberg Sill, Sweden	*−38.0*	*346.0*	*6.3*	*285*	X	2211
North Sudetic Basin volcanics, Poland	*−42.0*	*354.0*	*8.1*	*285*	X	3161
Lodeve Basin, France	−42.0	349.0	2.0	285	*	1813
Lodeve B Component, France	*−49.0*	*342.0*	*17.0*	*285*	X,*	2454
Intrasudetic basin sediments, Poland	*−37.0*	*340.0*	*6.8*	*285*	X,*	3161
Krakow volcanics, Poland	*−43.0*	*345.0*	*7.9*	*285*	X	275
Bohemian red beds, Czech Republic	*−41.0*	*345.0*	*4.0*	*285*	X,*	167
Lower Silesia volcanics, Poland	*−40.0*	*352.0*	*13.2*	*285*	X	465, recalculated
Exeter Lavas, UK	−50.0	330.0	4.0	286		461
Black Forest volcanics, Germany	−49.0	356.0	5.9	286		170, recalculated
Exeter Lavas, UK	*−48.0*	*343.0*	*10.0*	*286*	X	411, recalculated
Black Forest rhyolites, Germany	*−42.0*	*353.0*	*1.0*	*286*	X	2941
Thuringer Forest sediments, Germany	*−41.5*	*340.0*	*5.8*	*287*	X,*	1792
Stabben Sill, Norway	*−32.0*	*354.0*	*2.4*	*291*	X	1540
Saar-Nahe volcanics, Germany	*−41.0*	*349.0*	*15.9*	*291*	X	712
Nahe volcanics, Germany	*−46.0*	*347.0*	*13.0*	*291*	X	940
Sudetic Mountain granitoids, Poland	−42.0	346.0	13.0	293		2446
Great Whin Sill, UK	*−44.0*	*339.0*	*4.8*	*294*	X	585
Hadrian's Wall-Pennines Sill and Hett Dike (Whin Sill), UK	*−32.9*	*347.1*	*3.5*	*294*	X	Liss et al. (2004)
Holy Island Sill and Dyke (Whin Sill), UK	*−35.4*	*346.8*	*6.3*	*294*	X	Liss et al. (2004)
Nideck-Donon volcanics, France	*−47.0*	*348.0*	*4.0*	*294*	X	1010
Lower Nideck volcanics, France	*−42.0*	*348.0*	*19.0*	*294*	X	174
Cracow volcanics A, Poland	−44.0	355.0	4.8	294		Nawrocki et al. (2008)
Alnwick Sill, High Green and St. Oswalds Chapel Dyke (Whin Sill), UK	*−47.1*	*337.1*	*8.1*	*294*	X	Liss et al. (2004)

. . . continued

Formation	Plat	Plon	α_{95}	Age	Notes	Reference
Scania dolerites, Sweden	−38.0	348.0	6.5	294		2222
Scania dolerite dikes, Sweden	−37.0	354.0	11.0	294		2211
Thuringer Forest volcanics, Germany	*−37.1*	*350.0*	*7.1*	*295*	X	1792
Silesia volcanics, Poland	*−43.0*	*354.0*	*13.6*	*296*	X	465
Arendal diabase dykes, Norway	*−42.5*	*339.6*	*7.1*	*297*	X	175
Ny-Hellesund sills, Norway	*−39.0*	*341.0*	*2.9*	*297*	X	626
Peterhead dyke, Scotland	−41.0	342.0	1.3	297		1535
Donets basin, Ukraine	*−43.0*	*345.0*	*3.0*	*297*	X,*	Iosifidi et al. (2010)
Svedlodarsk, Karamysh Fm, Donbas	*−48.4*	*349.8*	*2.4*	*299*	X,*	Meijers et al. (2010)
Mount Billinger sill, Sweden	−31.0	354.0	4.0	299		2211
Donets basin, Ukraine	*−42.0*	*359.0*	*4.0*	*301*	X,*	Iosifidi et al. (2010)
Debaltsevo Donbas, Ukraine	*−48.2*	*342.3*	*2.0*	*303*	X	Meijers et al. (2010)
Wackerfield dyke, England	*−49.0*	*349.0*	*3.0*	*303*	X	180
Queensferry sill, Scotland	*−38.3*	*354.0*	*5.2*	*305*	X	2447
Westphalian-Stephanian red beds, Czech Republic	*−38.0*	*343.0*	*9.0*	*305*	X,*	167
Tashkovska Donbas, Ukraine	*−38.4*	*339.5*	*2.9*	*312*	X	Meijers et al. (2010)
WEST GONDWANA:						
AMAZONIA						
Anari and Tapirapua Fms, Brazil	−65.5	250.3	3.8	197		3316
French Guyana dikes, Brazil	−81.2	235.1	4.0	198		3378
Bolivar dykes, Venezuela	*−66.9*	*245.6*	*4.9*	*203*	X	150
Dolerite dykes, Suriname	−82.0	320.0	10.0	232		701
Mitu Group red beds, Peru	−71.4	303.6	5.7	249	*	3524
Independencia Group	−80.7	7.0	6.6	260	i	Rapalini et al. (2006)
Multiple Fms., E. Cordillera, Bolivia	−81.8	344.2	3.5	280	*	Gilder et al. (2003)
Copacabana Group sediments, Peru	−68.2	321.3	5.2	280	*	Rakotosolofo et al. (2006)
Santa Fe Group, Brazil	−65.7	330.9	4.1	300	i	Brandt et al. (2009)
Itarare Subgroup, Tubarao Group, Brazil	*−57.0*	*357.0*	*11.2*	*310*	X,*	798
COLORADO						
Mendoza sediments and volcanics	−51.0	223.0	6.0	195		Iglesia-Llanos et al. (2006)
Los Colorados Mendoza	−81.8	298.3	7.6	216		Vizan et al. (2004)
Amana Fm, Paganzo Group, Argentina	*−83.0*	*317.0*	*7.0*	*240*	X,*	1132
Puesto Viejo Fm Volcanics, Mendoza	−76.0	312.4	7.3	245		Domeier et al. (2012)
Puesto Viejo Fm Sediments, Mendoza	−87.0	325.0	4.9	245	*	Domeier et al. (2012)
Sierra Chica, La Pampa	−80.1	348.6	3.3	263		Domeier et al. (2011a)
Upper Choiyoi Group, Mendoza	−73.7	315.6	4.1	264		Domeier et al. (2012)
Horcajo, Uspallata Basin, Argentina	−72.4	264.8	12.0	267		2475
Tambillos, Uspallate Basin, Argentina	−80.6	308.3	6.5	270		2475
De la Cuesta Fm., Famatina, Argentina	*−77.2*	*343.6*	*12.2*	*275*	X,*	Spagnuolo et al. (2008)
La Colina Fm, Paganzo	*−80.6*	*268.8*	*2.8*	*283*	X,*	Geuna and Escosteguy, (2004)
Middle Paganzo II, Los Colorados Lower Beds, Argentina	*−59.5*	*357.5*	*2.5*	*283*	X,*	620
La Colina Fm, Los Colorados 1, Argentina	*−74.0*	*313.0*	*3.1*	*283*	X,*	166
Cerro Colorado	−79.3	290.6	11.0	275	*	Geuna and Escosteguy (2004)
Rincon Blanco, Paganzo Basin, Argentina	−75.0	291.5	6.7	275	Com.	Geuna and Escosteguy (2004)
La Tabla Fm, Chile	−51.0	347.0	5.7	310		1420
Pular and Cas Fms, Chile	*−57.0*	*350.0*	*9.6*	*310*	X	1420

. . . continued

Formation	Plat	Plon	α_{95}	Age	Notes	Reference
La Colina, Las Mellizas, Paganzo, Argentina	−67.2	343.7	5.6	310		Geuna et al. (2010)
SOUTH AFRICA						
Red sandstone Fm, Zambia	*−68.0*	*50.5*	*4.6*	*222*	X,*	323
Cassanje Series, Angola	*−54.0*	*80.0*	*6.0*	*249*	X,*	1960
Karroo Basin	*−50.9*	*86.3*	*7.6*	*251*	X,*	De Kock and Kirschvink (2004)
K1 Dwyka Varves, Zimbabwe, Zambia, Tanzania	*−26.5*	*26.5*	*5.6*	*282*	X,*	435
Dwyka Group combined	−25.0	67.0	12.0	315	*	3489
MESETA						
Argana Flows. Morocco	−69.2	55.5	6.0	201		Ruiz-Martinez et al. (submitted)
Moroccan Intrusives, Morocco	*−71.0*	*36.0*	*7.0*	*201*	X	148
Central Atlantic Magmatic Province, Morocco	−73.0	61.3	19.0	201		Knight et al. (2004)
Taztot Trachyandesite, Morocco	*−38.7*	*56.8*	*4.6*	*273*	X	723
Chougrane red beds, Morocco	*−32.2*	*64.1*	*4.7*	*273*	X,*	723
Djebel Tarhat red beds, Morocco	*−24.0*	*63.8*	*7.8*	*273*	X,*	1080
Volcanics, Mechra ben Abou, Chougrane, Morocco	*−36.0*	*58.0*	*20.9*	*281*	X	1859
SOMALIA						
K3 beds, Galula coalfield, Tanzania	−46.0	40.0	5.0	257	*	324
NORTHWEST AFRICA						
Ighrem and Foum Zguid dykes, Morocco	−73.0	64.7	4.1	200		Palencia-Ortas et al. (2011)
Zarzaitine Fm, Algeria	−70.9	55.1	2.6	207	*	2932
Abadla Fm., Upper Unit, Algeria	−29.2	60.0	4.5	273	*	3275
Abadla Fm., Lower Unit, Algeria	−29.1	57.8	3.6	275	*	3275
Mezarif Basin sediments, Algeria	−29.3	56.4	3.4	275	*	Merabet et al. (2005)
Upper El Adeb Larache Fm, Algeria	*−38.5*	*57.5*	*2.8*	*287*	X,*	2540
Lower Tiguentourine Fm, Algeria	*−33.8*	*61.4*	*4.1*	*290*	X,*	2728
Merkala Fm., Tindouf Basin, Algeria	−32.4	56.6	2.3	304	*	Henry et al. (1999)
Lower El Adeb Larache Fm, Algeria	−28.7	55.8	3.5	307	*	2540
Illizi Basin sediments, Algeria	−28.3	58.9	4.6	309	*	3484
Reggane Basin, Harsi Bachir Fm, Algeria	−32.8	55.7	2.0	310	*	Derder et al. (2009)
Djebel Reouina Fm., Tindouf Basin, Algeria	−28.4	56.9	1.7	315	*	Merabet et al. (1999)
Oubarakat,El-Adeb Larache Fms, Algeria	−28.2	55.5	4.5	317	*	3481
Reggane Basin, Algeria	−26.6	44.7	5.3	320	*	3402
NORTHEAST AFRICA						
Upper Triassic Sediments, Southern Tunisia	*−54.9*	*43.3*	*11.5*	*222*	X,*	3020
Al Azizia Fm. Combined, Libya	−57.0	40.3	6.0	231	Com.	3408
Jebel Nehoud Ring Complex, Kordofan, Sudan	−40.8	71.3	6.0	280		3504
ARABIA						
Abu Durba sediments, SW Sinai, Egypt	−25.6	64.0	7.2	307	*	2784

The following criteria were applied in the pole selection (by Torsvik et al. (in submission)): to be included, a pole must (1) have a Q-factor of 3 or greater, (2) be tectonically coherent with a continental craton (an exception is made for the Colorado Plateau, where the poles are adjusted by a counterclockwise rotation of 5.4° (Bryan and Gordon, 1990)), (3) not be remagnetized, (4) have a reliably known age.
Poles added to or combined from the original compilation are listed in bold.
Plat/Plon = paleopole latitude/longitude. α_{95} = the semi-angle of the 95% cone of confidence about the mean magnetization direction (bold and underlined values are A_{95}, which is 95% cone of confidence about the mean pole). Age = estimated paleopole age in Ma (based on the timescale of Gradstein et al., 2004). Notes: X (with italicized line) = entry removed during filtering exercise of section 7.1. * = corrected for inclination shallowing by f=0.6 in section 7.3 and section 8. "i" = inclination shallowing correction applied by original authors. "r" = corrected for Colorado Plateau rotation (see above). References: Global Paleomagnetic Database reference number (Refno in: http://www.ngu.no/geodynamics/gpmdb/) or original reference information.

Table 5.2: Reconstruction parameters used or discussed in the text.

North America to Northwest Africa	**Lat**	**Lon**	**Angle**	**Reference**
Pangea A-1[ab]	67.6	346.0	74.8	Bullard et al. (1965)
Pangea A-2	57.3	339.0	89.0	Van der Voo and French (1974)
Pangea B	36.2	356.0	77.3	Morel and Irving (1981)
Labails et al. (2010) model[c]	64.3	345.3	78.0	Labails et al. (2010)
New reconstructions (inc. corrected, f=0.6)				
210 Ma	63.2	352.9	79.0	this paper
220 Ma	63.5	339.8	79.1	this paper
230 Ma	65.3	345.9	75.6	this paper
240 Ma	66.3	346.3	74.1	this paper
250 Ma	66.0	341.1	72.0	this paper
260 Ma	65.8	347.4	75.0	this paper
270 Ma	63.4	345.3	77.9	this paper
280 Ma	65.1	345.5	74.4	this paper
290 Ma	67.9	350.7	70.3	this paper
300 Ma	61.8	335.9	76.6	this paper
310 Ma	59.9	338.2	80.6	this paper
Europe to North America[a]	88.5	27.7	−38.0	Bullard et al. (1965)
Europe to North America (310-220 Ma)[bc]	78.6	161.9	−31.0	Alvey (2009)
Europe to North America (190 Ma)[bc]	69.0	154.8	−23.6	Torsvik et al. (in submission)
Greenland to Europe[a]	73.0	96.5	22.0	Bullard et al. (1965)
Greenland to Europe[bc]	65.1	126.1	18.9	Alvey (2009)
South America to Africa[a]	44.0	329.4	57.0	Bullard et al. (1965)
Amazonia to South Africa[bc]	50.0	327.5	55.1	Torsvik et al. (2009)
Colorado to South Africa[bc]	47.5	326.7	57.3	Torsvik et al. (2009)
Arabia to Africa[a]	36.9	18.0	−6.0	Bullard et al. (1965)
Arabia to South Africa[bc]	37.1	17.2	−8.9	Torsvik et al. (in submission)
Northwest Africa to South Africa[bc]	33.6	26.0	2.3	Torsvik et al. (in submission)
Northeast Africa to South Africa[bc]	40.5	298.6	−0.7	Torsvik et al. (in submission)
Somalia to South Africa[bc]	9.9	143.0	−0.2	Torsvik et al. (in submission)
Moroccan Meseta to Northwest Africa[c]	29.4	347.9	5.1	Labails et al. (2010)

[a,b,c]= parameter used in the construction of apparent polar wander paths in panel (a,b,c) of Fig. 17. European paleopoles <220 Ma are rotated to North America according to Euler poles interpolated from the 220 Ma and 190 Ma reconstruction poles.

Table 5.3: 310–210 Ma mean paleopoles for Laurussia and West Gondwana

Laurussia		**Raw Poles**			**Inc. Corrected (f=0.6)**		
Age	**N**	**Plat**	**Plon**	**A_{95}**	**Plat**	**Plon**	**A_{95}**
210	32	−64.2	50.3	2.1	−65.0	54.4	2.0
220	32	−57.8	47.2	2.3	−58.4	51.1	2.4
230	24	−52.3	47.4	2.8	−52.9	50.9	2.9
240	21	−47.4	51.8	4.0	−48.8	56.1	3.7
250	20	−43.8	59.0	3.9	−46.1	61.4	3.2
260	25	−43.0	59.4	2.3	−44.9	61.7	1.9
270	23	−39.1	58.7	2.8	−40.6	60.5	2.9
280	39	−33.2	58.0	2.6	−33.5	58.7	2.6
290	59	−30.8	55.9	2.1	−31.3	56.6	2.1
300	39	−31.0	54.2	2.9	−31.5	55.1	3.0
310	14	−31.7	48.6	6.1	−31.8	49.0	6.3
West Gondwana		**Raw Poles**			**Inc. Corrected (f=0.6)**		
Age	**N**	**Plat**	**Plon**	**A_{95}**	**Plat**	**Plon**	**A_{95}**
210	7	−66.6	61.6	6.0	−67.4	63.9	6.7
220	3	−59.0	53.5	15.9	−55.1	50.0	12.7
230	5	−57.3	54.5	9.5	−54.6	47.3	6.9
240	7	−53.0	62.5	6.7	−51.9	50.4	6.6
250	8	−50.9	65.7	7.3	−48.1	52.1	8.0
260	7	−50.4	62.6	8.5	−48.0	58.5	8.9
270	17	−41.3	62.8	5.7	−40.1	60.6	6.4
280	19	−37.5	60.1	5.8	−35.7	54.9	6.5
290	11	−40.1	56.9	8.0	−38.3	49.0	8.7
300	11	−30.1	56.5	3.7	−26.7	50.6	4.9
310	14	−28.9	56.3	3.3	−25.3	49.6	4.3

Mean poles were calculated by means of a 20 Myr moving window at 10 Myr intervals.
N = number of paleopoles used in the calculation of the mean pole.
Plat/Plon = paleopole latitude/longitude.
All poles are reported in South African coordinates, using the rotation parameters described in the caption of Fig. 17c (and listed in Table 2).
A_{95} = the semi-angle of the 95% cone of confidence about the paleopole.

References

Alvey, A. D. (2009). Using crustal thickness and continental lithosphere thinning factors from gravity inversion to refine plate reconstruction models for the Arctic and North Atlantic. *Ph.D thesis, University of Liverpool, U.K.*, 189 pp.

Anson, G. L., & Kodama, K. P. (1987). Compaction-induced inclination shallowing of the post-depositional remanent magnetization in a synthetic sediment. *Geophysical Journal of the Royal Astronomical Society*, 88, 673-692.

Arason, P., & Levi, S. (1990). Compaction and inclination shallowing in deep-sea sediments from the Pacific Ocean. *Journal of Geophysical Research*, 95, 4501-4510.

Arthaud, F., & Matte, P. (1977). Late Paleozoic strike-slip faulting in southern Europe and northern Africa: Result of a right-lateral shear zone between the Appalachians and the Urals. *Geological Society of America Bulletin*, 88, 1305-1320.

Bachtadse, V., Zaenglein, R., Tait, J., & Soffel, H. C. (2002). Palaeomagnetism of the Permo/Carboniferous (280 Ma) Jebel Nehoud ring complex, Kordofan, Central Sudan. *Journal of African Earth Sciences*, 35, 89-97.

Bazhenov, M. L., Grishanov, A. N., Van der Voo, R., & Levashova, N. M. (2008). Late Permian paleomagnetic data east and west of the Urals. *Geophysical Journal International*, 173, 395-408.

Bazhenov, M. L., & Shatsillo, A. V. (2010). Late Permian palaeomagnetism of northern Eurasia: Data evaluation and a single-plate test of the geocentric axial dipole model. *Geophysical Journal International*, 180, 136-146.

Bilardello, D., Jezek, J., & Kodama, K. P. (2011). Propagating and incorporating the error in anisotropy-based inclination corrections. *Geophysical Journal International*, 187, 75-84.

Bilardello, D., & Kodama, K. P. (2010a). Rock magnetic evidence for inclination shallowing in the Early Carboniferous Deer Lake Group red beds of western Newfoundland. *Geophysical Journal International*, 181, 275-289.

Bilardello, D., & Kodama, K. P. (2010b). Palaeomagnetism and magnetic anisotropy of Carboniferous red beds from the maritime provinces of Canada: Evidence for shallow palaeomagnetic inclinations and implications for North American apparent polar wander. *Geophysical Journal International*, 180, 1013-1029.

Bilardello, D., & Kodama, K. P. (2010c). A new inclination shallowing correction of the Mauch Chunk Formation of Pennsylvania, based on high-field AIR results:

Implications for the Carboniferous North American APW path and Pangea reconstructions. *Earth and Planetary Science Letters*, 299, 218-227.

Brandt, D., Ernesto, M., Rocha-Campos, A. C., & dos Santos, P. R. (2009). Paleomagnetism of the Santa Fé Group, Central Brazil: Implications for the late Paleozoic apparent polar wander path for South America. *Journal of Geophysical Research*, 114.

Briden, J. C., Smith, A. G., & Sallomy, J. T. (1971). The geomagnetic field in Permo-Triassic time. *Geophysical Journal of the Royal Astronomical Society*, 23, 101-117.

Bryan, P., & Gordon, R. G. (1990). Rotation of the Colorado Plateau: An updated analysis of paleomagnetic data, *Geophysical Research Letters*, 17, 1501-1504, doi:10.1029/GL017i010p01501.

Bullard, E., Everett, J. E., & Smith, A. G. (1965). The fit of continents around the Atlantic. *Philosophical Transactions of the Royal Society of London*, 258, 41-51.

Carey, S. W. (1958). The tectonic approach to continental drift, *in*: *Continental drift, a symposium*, 1956. University of Tasmania, 177-358.

Celaya, M. A., & Clement, B. M. (1988). Inclination shallowing in deep sea sediments from the North Atlantic. *Geophysical Research Letters*, 15, 52-55.

Courtillot, V., & Besse, J. (2004). A long-term octupolar component in the geomagnetic field? 0-200 million years B.P. Timescales of the paleomagnetic field. *American Geophysical Union - Geophysical Monograph*, 145, 59-74.

De Boer, J. (1963). The geology of the Vicentinian Alps (NE Italy), with special reference to their paleomagnetic history. *Geol. Ultraiectina*, 11.

De Boer, J. (1965). Paleomagnetic indications of megatectonic movements in the Tethys. *Journal of Geophysical Research*, 70, 931-944.

De Kock, M. O., & Kirschvink, J. L. (2004). Paleomagnetic constraints on the Permian–Triassic boundary in terrestrial strata of the Karoo Supergroup, South Africa: Implications for causes of the end-Permian extinction event. *Gondwana Research*, 7, 175-183.

Deamer, G. A., & Kodama, K. P. (1990). Compaction-induced inclination shallowing in synthetic and natural clay-rich sediments. *Journal of Geophysical Research*, 95, 4511-4529.

Dercourt, J., Zonenshain, L. P., Ricou, L. E., Kazmin, V. G., Le Pichon, X., Knipper, A. L., et al. (1986). Geological evolution of the Tethys belt from the Atlantic to

the Pamirs since the Lias. *Tectonophysics*, 123, 241-315.

Derder, M. E. M., Henry, B., Amenna, M., Bayou, B., Djellit, H., Guemache, M. A., & Hemmi, A. (2009). New structural implications for the central Sahara (Algeria), from the revisited Upper Carboniferous "Hassi Bachir" formation: Paleomagnetic constraints. *Tectonophysics*, 463, 69-76.

Dietz, R. S., & Holden, J. C. (1970). Reconstruction of Pangaea: Breakup and dispersion of continents, Permian to present. *Journal of Geophysical Research*, 75, 4939-4956.

Dietzel, G. F. L. (1960). Geology and Permian paleomagnetism of the Merano region, province of Bolzano, (N. Italy). *Geol. Ultraiectina*, 4.

Domeier, M., Van der Voo, R., Tohver, E., Tomezzoli, R. N., Vizan, H., Torsvik, T. H., & Kirshner, J. (2011a). New Late Permian paleomagnetic data from Argentina: Refinement of the apparent polar wander path of Gondwana. *Geochemistry, Geophysics, Geosystems*, 12, Q07002.

Domeier, M., Van der Voo, R., Denny, F. B. (2011b). Widespread inclination shallowing in Permian and Triassic paleomagnetic data from Laurentia: Support from new paleomagnetic data from Middle Permian shallow intrusions in southern Illinois (USA) and virtual geomagnetic pole distributions. *Tectonophysics*, 511, 38-52.

Domeier, M., Van der Voo, R., Tomezzoli, R. N., Tohver, E., Hendriks, B. W. H., Torsvik, T. H., Vizn, H., Dominguez, A. R. (2012). Support for an "A-type" Pangea reconstruction from high-fidelity paleomagnetic records for the Late Permian and Middle Triassic, *Journal of Geophysical Research*, in press.

Dominguez, A. R., Van der Voo, R., Torsvik, T. H., Hendriks, B. W. H., Abrajevitch, A., Domeier, M., Larsen, B. T., & Rousse, S. (2011). The ∼270 Ma paleolatitude of Baltica and its significance for Pangea models. *Geophysical Journal International* 186, 529-550.

Donohoo-Hurley, L. L., Geissman, J. W., & Lucas, S. G. (2010). Magnetostratigraphy of the uppermost Triassic and lowermost Jurassic Moenave Formation, western United States: Correlation with strata in the United Kingdom, Morocco, Turkey, Italy and the eastern United States. *Geological Society of America Bulletin* 122, 1936-1950.

du Toit, A. L. (1937). Our wandering continents: An hypothesis of continental drifting. Oliver & Boyd, London, U.K.

Evans, D. A. D. (2006). Proterozoic low orbital obliquity and axial-dipolar geomagnetic field from evaporite palaeolatitudes. *Nature*, 444, 51-55.

Evans, M. E. (1976). Test of the dipolar nature of the geomagnetic field throughout Phanerozoic time. *Nature*, 262, 676-677.

Gallet, Y., & Pavlov, V. (1996). Magnetostratigraphy of the Moyero River Section (North-Western Siberia): Constraints on geomagnetic reversal frequency during the early Palaeozoic. *Geophysical Journal International*, 125, 95-105.

Garces, M., Parés, J. M., & Cabrera, L. (1996). Further evidence for inclination shallowing in red beds. *Geophysical Research Letters*, 23, 2065-2068.

Gates, A. E., Simpson, C., & Glover, L. (1986). Appalachian Carboniferous dextral strike-slip faults: An example from Brookneal, Virginia. *Tectonics*, 5, 119-133.

Geuna, S. E., & Escosteguy, L. D. (2004). Palaeomagnetism of the Upper Carboniferous-Lower Permian transition from Paganzo Basin, Argentina. *Geophysical Journal International*, 157, 1071-1089.

Geuna, S. E., Escosteguy, L. D., Limarino, C. Ó. (2010). Paleomagnetism of the Carboniferous–Permian Patquía Formation, Paganzo Basin, Argentina: Implications for the apparent polar wander path for South America and Gondwana during the Late Palaeozoic. *Geologica Acta*, 8, 373-397.

Gilder, S., Chen, Y., Cogne, J., Tan, X., Courtillot, V., Sun Dongjiang, et al. (2003a). Paleomagnetism of Upper Jurassic to Lower Cretaceous volcanic and sedimentary rocks from the western Tarim Basin and implications for inclination shallowing and absolute dating of the M-0 (ISEA?) chron. *Earth and Planetary Science Letters*, 206, 587-600.

Gilder, S., Rousse, S., Farber, D., McNulty, B., Sempere, T., Torres, V., & Palacios, O. (2003b). Post-Middle Oligocene origin of paleomagnetic rotations in Upper Permian to Lower Jurassic rocks from northern and southern Peru. *Earth and Planetary Science Letters*, 210, 233-248.

Gradstein, F. M., Ogg, J. G., Smith, A. G., et al. (2004). A Geologic Time Scale 2004. *Cambridge Univ. Press*, Cambridge, U.K., 610 pp.

Guicherit, R. (1964). Gravity tectonics, gravity field, and paleomagnetism in NE-Italy, with special reference to the Carnian Alps. *Geol. Ultraiectina*, 14.

Gurevitch, E. L., Heunemann, C., Radko, V., Westphal, M., Bachtadse, V., Pozzi, J. P., & Feinberg, H. (2004). Palaeomagnetism and magnetostratigraphy of the PermianTriassic northwest central Siberian Trap Basalts. *Tectonophysics*, 379, 211-226.

Hallam, A. (1973). A revolution in the earth sciences: From continental drift to

plate tectonics. Clarendon Press, Oxford, U.K.

Hallam, A. (1983). Supposed Permo-Triassic megashear between Laurasia and Gondwana. *Nature*, 301, 499-502.

Henry, B., Merabet, N. E., Bouabdallah, H., & Maouche, S. (1999). New Lower Stephanian paleomagnetic pole for the Saharan Craton (Merkala Formation, Tindouf Basin, Algeria). *C. R. Acad. Sci. Paris, Sciences de la terre et des planètes*, 329, 161-166.

Hospers, J., & Van Andel, S. I. (1969). Palaeomagnetism and tectonics: A review. *Earth-Science Reviews*, 5, 5-44.

Iglesia-Llanos, M. P., Riccardi, A. C., & Singer, S. E. (2006). Paleomagnetic study of Lower Jurassic marine strata from the Neuquén Basin, Argentina: A new Jurassic apparent polar wander path for South America. *Earth and Planetary Science Letters*, 252, 379-397.

Iosifidi, A. G., Mac Niocaill, C., Khramov, A. N., Dekkers, M. J., & Popov, V. V. (2010). Palaeogeographic implications of differential inclination shallowing in Permo-Carboniferous sediments from the Donets Basin, Ukraine. *Tectonophysics*, 490, 229-240.

Irving, E. (1958). Rock magnetism: A new approach to the problems of problems of polar wandering and continental drift, *in: Continental drift, a symposium*, 1956. University of Tasmania.

Irving, E. (1967). Palaeomagnetic evidence for shear along the Tethys: Aspects of Tethyan biogeography. *Publication of the Systematics Association*, 7, 59-76.

Irving, E. (1977). Drift of the major continental blocks since the Devonian. *Nature*, 270, 304-309.

Irving, E. (2004). The case for Pangea B, and the Intra-Pangean Megashear. Timescales of the paleomagnetic field. *American Geophysical Union - Geophysical Monograph*, 145, 13-27.

Jackson, M. J., Banerjee, S. K., Marvin, J. A., Lu, R., & Gruber, W. (1991). Detrital remanence, inclination errors, and anhysteretic remanence anisotropy: Quantitative model and experimental results. *Geophysical Journal International*, 104, 95-103.

Jeager, J. C., & Irving, E. (1957). Paleomagnetism and reconstruction of Gondwanaland. *C. R. 3^{rd} Congr. Pacific and Indian Ocean Sciences*, 233-242, Imprimerie Officielle, Tananarive, Madagascar.

Johnson, C. L., & Constable, C. G. (1997). The time-averaged geomagnetic field: Global and regional biases for 0-5 ma. *Geophysical Journal International*, 131, 643-666.

Johnson, C. L., Constable, C. G., Tauxe, L., Barendregt, R., Brown, L. L., Coe, R. S., Layer, P. W., Mejia, V., Opdyke, N. D., Singer, B. S., Staudigel, H., & Stone, D. B. (2008). Recent investigations of the 0 to 5 Ma geomagnetic field recorded by lava flows. *Geochemistry Geophysics Geosystems*, 9, Q04032.

Kanasewich, E. R., Havskov, J., & Evans, M. E. (1978). Plate tectonics in the Phanerozoic. *Canadian Journal of Earth Sciences*, 15, 919-955.

Kelly, P., & Gubbins, D. (1997). The geomagnetic field over the past 5 million years. *Geophysical Journal International*, 128, 315-330.

Kent, D. V., & Smethurst, M. A. (1998). Shallow bias of paleomagnetic inclinations in the Paleozoic and Precambrian. *Earth and Planetary Science Letters*, 160, 391-402.

Kent, D. V., & Irving, E. (2010). Influence of inclination error in sedimentary rocks on the Triassic and Jurassic apparent pole wander path for North America and implications for Cordilleran tectonics. *Journal of Geophysical Research*, 115.

Kent, D. V., & Olsen, P. E. (2008). Early Jurassic magnetostratigraphy and paleolatitudes from the Hartford continental rift basin (eastern North America): Testing for polarity bias and abrupt polar wander in association with the Central Atlantic Magmatic Province. *Journal of Geophysical Research*, 113.

Kent, D. V., & Tauxe, L. (2005). Corrected Late Triassic latitudes for continents adjacent to the North Atlantic. *Science*, 307, 240-244.

King, R. (1955). The remanent magnetism of artificially deposited sediments. *Geophysical Journal International*, 7, 115-134.

Klitgord, K. D., & Schouten, H. (1986). Plate kinematics of the Central Atlantic. *in: The Geology of North America: The western North Atlantic Region*. P. R. Vogt, & B. E. Tucholke (Eds.), Geological Society of America, Boulder, CO (USA).

Knight, K. B., Nomade, S., Renne, R., Marzoli, A., Bertrand, H., & Youbi, N. (2004). The Central Atlantic magmatic province at the Triassic–Jurassic boundary; paleomagnetic and $^{40}Ar/^{39}Ar$ evidence from Morocco for brief, episodic volcanism. *Earth and Planetary Science Letters*, 228, 143-160.

Kodama, K. P. (2009). Simplification of the anisotropy-based inclination correction technique for magnetite- and haematite-bearing Rocks: A case study for the Car-

boniferous Glenshaw and Mauch Chunk Formations, North America. *Geophysical Journal International*, 176, 467-477.

Kravchinsky, A., Konstantinov, K. M., Courtillot, V., Savrasov, J. I., Valet, J. P., Cherniy, S. D., Mishenin, S. G., & Parasotka, B. S. (2002). Palaeomagnetism of East Siberian traps and kimberlites: two new poles and palaeogeographic reconstructions at about 360 and 250 Ma. *Geophysical Journal International*, 148, 1-33.

Labails, C., Olivet, J., Aslanian, D., & Roest, W. R. (2010). An alternative early opening scenario for the Central Atlantic Ocean. *Earth and Planetary Science Letters*, 297, 355-368.

Le Pichon, X., Sibuet, J-C., & Francheteau, J. (1977). The fit of the continents around the North Atlantic Ocean. *Tectonophysics*, 38, 169-209.

Le Pichon, X., & Fox, P. J. (1971). Marginal offsets, fracture zones, and the early opening of the North Atlantic. *Journal of Geophysical Research*, 76, 6294-6308.

Levi, S., & Banerjee, S. K. (1990). On the origin of inclination shallowing in redeposited sediments. *Journal of Geophysical Research*, 95, 4383-4389.

Liss, D., Owens, W. H. & Hutton, D. H. W. (2004). New palaeomagnetic results from the Whin Sill Complex: evidence for a multiple intrusion event and revised virtual geomagnetic poles for the Late Carboniferous for the British Isles. *Journal of the Geological Society*, London, 161, 927-938.

Livermore, R. A., Smith, A. G., & Vine, F. J. (1986). Late Palaeozoic to early Mesozoic evolution of Pangaea. *Nature*, 322, 162-165.

Lottes, A. L., & Rowley, D. B. (1990). Early and Late Permian reconstructions of Pangaea: Palaeozoic palaeogeography and biogeography. *Memoirs of the Geological Society of London*, 12, 383-395.

Løvlie, R., & Torsvik, T. H. (1984). Magnetic remanence and fabric properties of laboratory-deposited hematite-bearing red sandstone. *Geophysical Research Letters*, 11, 221-224.

McElhinny, M. W., & McFadden, P. L. (2000). Paleomagnetism: Continents and oceans. Academic Press, San Diego, CA, USA.

McElhinny, M. (2004). Geocentric axial dipole hypothesis: A least squares perspective. Timescales of the paleomagnetic field. *American Geophysical Union - Geophysical Monograph*, 145, 1-12.

McFadden, P. L. (2004). Is 600 myr long enough for the random palaeogeographic test of the geomagnetic axial dipole assumption? *Geophysical Journal International*, 158, 443-445.

Meert, J. G., Tamrat, E., & Spearman, J. (2003). Non-dipole fields and inclination bias: Insights from a random walk analysis. *Earth and Planetary Science Letters*, 214, 395-408.

Meijers, M. J., Hamers, M. F., van Hinsbergen, D. J., van der Meer, D. G., Kitchka, A., Langereis, C. G., et al. (2010). New Late Paleozoic paleopoles from the Donbas Foldbelt (Ukraine): Implications for the Pangea A vs. B controversy. *Earth and Planetary Science Letters*, 297, 18-33.

Merabet, N., Henry, B., Bouabdallah, H., & Maouche, S. (1999). Paleomagnetism of the Djebel Reouina Namurian Formation (Tindouf Basin, Algeria). *Studia Geophysica Et Geodaetica*, 43, 376-389.

Merabet, N., Henry, B., Kherroubi, A., & Maouche, S. (2005). Autunian age constrained by fold tests for paleomagnetic data from the Mezarif and Abadla Basins (Algeria). *Journal of African Earth Sciences*, 43, 556-566.

Mitra, R., & Tauxe, L. (2009). Full vector model for magnetization in sediments. *Earth and Planetary Science Letters*, 286, 535-545.

Morel, P., & Irving, E. (1981). Paleomagnetism and the evolution of Pangea. *Journal of Geophysical Research*, 86, 1858-1872.

Muttoni, G., Gaetani, M., Kent, D. V., Sciunnach, D., Angiolini, L., Berra, F., et al. (2009). Opening of the Neo-Tethys Ocean and the Pangea B to Pangea A transformation during the Permian. *GeoArabia*, 14, 17-48.

Muttoni, G., Kent, D. V., & Channell, J. E. T. (1996). Evolution of Pangea: Paleomagnetic constraints from the Southern Alps, Italy. *Earth and Planetary Science Letters*, 140, 97-112.

Muttoni, G., Kent, D. V., Garzanti, E., Brack, P., Abrahamsen, N., & Gaetani, M. (2003). Early Permian Pangea "B" to Late Permian Pangea "A". *Earth and Planetary Science Letters*, 215(3-4), 379-394.

Nawrocki, J., Fanning, M., Lewandowska, A., Polechonska, O., & Werner, T. (2008). Palaeomagnetism and the age of the Cracow volcanic rocks (S Poland). *Geophysical Journal International*, 174, 475-488.

Nüernberg, D., & Müeller, R. D. (1991). The tectonic evolution of the South Atlantic from Late Jurassic to present. *Tectonophysics*, 191, 27-53.

Palencia-Ortas, A., Ruiz-Martnez, V. C., Villalaín, J. J., Osete, M. L., Vegas, R., Touil, A., Hafid, A., McIntosh, G., van Hinsbergen, D. J. J., & Torsvik, T. H. (2011). A new 200 Ma paleomagnetic pole for Africa, and paleo-secular variation scatter from Central Atlantic Magmatic Province (CAMP) intrusives in Morocco (Ighrem and Foum Zguid dykes). *Geophysical Journal International*, 185, 1220-1234.

Pavlov, E., Courtillot, V., Bazhenov, M. L., & Veselovsky, R. V. (2007). Paleomagnetism of the Siberian Traps; new data and a new overall 250 Ma pole for Siberia. *Tectonophysics*, 443, 72-92.

Rakotosolofo, N. A., Tait, J. A., Carlotto, V., & Cardenas, J. (2006). Palaeomagnetic results from the Early Permian Copacabana Group, Southern Peru: Implication for Pangaea palaeogeography. *Tectonophysics*, 413, 287-299.

Rapalini, A. E., Fazzito, S., & Orue, D. (2006). A new Late Permian paleomagnetic pole for stable South America: The Independencia Group, eastern Paraguay. *Earth, Planets, and Space*, 58, 1247-1253.

Reynolds, R. L., Goldhaber, M. B., & Snee, L. W. (1997). Paleomagnetic and $^{40}Ar/^{39}Ar$ results from the Grant intrusive breccia and comparison to the Permian Downeys Bluff sill evidence for Permian igneous activity at Hicks Dome, southern Illinois Basin, *U.S. Geological Survey Bulletin*, 2094-G, 16 pp.

Rochette, P., & Vandamme, D. (2001). Pangea B: An artifact of incorrect paleomagnetic assumptions? *Annali Di Geofisica*, 44, 649-658.

Romm, J. (1994). A new forerunner for continental drift. *Nature*, 367, 407-408.

Ross, C. A. (1979). Late Paleozoic collision of North and South America. *Geology*, 7, 41-44.

Ruiz-Martínez, V. C., Torsvik, T. H., van Hinsbergen, D. J. J., & Gaina, C. (submitted). Earth at 200 Ma. *Earth and Planetary Science Letters*.

Sahabi, M., Aslanian, D., & Olivet, J. (2004). A new interpretation of the evolution of the Central Atlantic. *Comptes Rendus - Academie Des Sciences, Geoscience*, 336, 1041-1052.

Schaltegger, U., & Brack, P. (2007). Crustal-scale magmatic systems during intracontinental strike-slip tectonics: U, Pb and Hf isotopic constraints from Permian magmatic rocks of the Southern Alps. *International Journal of Earth Sciences*, 96, 1131-1151.

Smith, A. G., Hurley, A. M., & Briden, J. C. (1981). Phanerozoic paleocontinental

world maps. Cambridge Univ. Press, London, UK.

Smith, A. G., & Livermore, R. A. (1991). Pangea in Permian to Jurassic time. *Tectonophysics*, 187, 135-179.

Smith, A. G., & Hallam, A. (1970). The fit of the southern continents. *Nature*, 225, 139-144.

Snider-Pellegrini, A. (1858). La Création et ses mystères dévoilés. Frank and Dentu, Paris.

Spagnuolo, C., Rapalini, A., & Astini, R. (2008). Palaeomagnetic confirmation of Palaeozoic clockwise rotation of the Famatina Ranges (NW Argentina): Implications for the evolution of the SW margin of Gondwana. *Geophysical Journal International*, 173, 63-78.

Steinberger, B., & Torsvik, T. H. (2008). Absolute plate motions and true polar wander in the absence of hotspot tracks. *Nature*, 452, 620-623.

Sun, W. W., & Kodama, K. P. (1992). Magnetic anisotropy, scanning electron microscopy, and X-ray pole figure goniometry study of inclination shallowing in a compacting clay-rich sediment. *Journal of Geophysical Research*, 97, 19,599-19,615.

Swanson-Hysell, N. L., Maloof, A. C., Weiss, B. P., & Evans, D. A. D. (2009). No asymmetry in geomagnetic reversals recorded by 1.1-billion-year-old Keweenawan basalts. *Nature Geoscience*, 2, 713-717.

Symons, D. T. A., Bormann, R. E., & Jans, R. P. (1989). Paleomagnetism of the Triassic red beds of the lower Fundy Group and Mesozoic tectonism of the Nova Scotia Platform, Canada. *Tectonophysics*, 164, 13-24.

Symons, D. T. A., Kawasaki, K., & McCausland, J. A. (2009). The Yukon-Tanana terrane: Part of North America at ∼215 Ma from paleomagnetism of the Taylor Mountain batholith, Alaska. *Tectonophysics*, 465, 60-74.

Szurlies, M. (2004). Magnetostratigraphy; the key to a global correlation of the classic Germanic Trias; case study Volpriehausen Formation (middle Buntsandstein), central Germany. *Earth and Planetary Science Letters*, 227, 395-410.

Szurlies, M., Bachmann, G. H., Menning, M., Nowaczyk, N. R., & Kaeding, K. C. (2003). Magnetostratigraphy and high-resolution lithostratigraphy of the Permian–Triassic boundary interval in central Germany. *Earth and Planetary Science Letters*, 212, 263-278.

Tan, X., Kodama, K. P., Gilder, S., & Courtillot, V. (2007). Rock magnetic evidence for inclination shallowing in the Passaic Formation red beds from the Newark Basin

and a systematic bias of the Late Triassic apparent polar wander path for North America. *Earth and Planetary Science Letters*, 254, 345-357.

Tan, X., & Kodama, K. P. (2002). Magnetic anisotropy and paleomagnetic inclination shallowing in red beds: Evidence from the Mississippian Mauch Chunk Formation, Pennsylvania. *Journal of Geophysical Research*, 107, 17.

Tauxe, L., & Kent, D. V. (1984). Properties of a detrital remanence carried by haematite from study of modern river deposits and laboratory redeposition experiments. *Geophysical Journal of the Royal Astronomical Society*, 76, 543-561.

Tauxe, L., & Kent, D. V. (2004). A simplified statistical model for the geomagnetic field and the detection of shallow bias in paleomagnetic inclinations: Was the ancient magnetic field dipolar? Timescales of the paleomagnetic field. *American Geophysical Union - Geophysical Monograph*, 145, 101-115.

Tauxe, L., Kodama, K. P., & Kent, D. V. (2008). Testing corrections for paleomagnetic inclination error in sedimentary rocks: A comparative approach. *Physics of the Earth and Planetary Interiors*, 169, 152-165.

Torcq, F., Besse, J., Vaslet, D., Marcoux, J., Ricou, L. E., Halawani, M., et al. (1997). Paleomagnetic results from Saudi Arabia and the Permo-Triassic Pangea configuration. *Earth and Planetary Science Letters*, 148, 553-567.

Torsvik, T. H., Gaina, C., Steinberg, M. & Van der Voo, R. (2006). North Atlantic fits with implications for the Barents Sea. *Norwegian Geological Survey Industry Report*, 17 pp. (confidential).

Torsvik, T. H., Muller, R. D., Van der Voo, R., Steinberger, B., & Gaina, C. (2008). Global plate motion frames: Toward a unified model. *Reviews of Geophysics*, 46, 1-44.

Torsvik, T. H., Van der Voo, R., Preeden, U., Mac Niocaill, C., Steinberger, B., Doubrovine, P., van Hinsbergen, D. J. J., Domeier, M., Gaina, C., Tohver, E., Meert, J. G., McCausland, P. J., & Cocks, L. R. M. (submitted). Phanerozoic Polar Wander and Paleogeography. *Earth science reviews*.

Torsvik, T. H., Rousse, S., & Smethurst, M. A. (2009). A new scheme for the opening of the South Atlantic Ocean and the dissection of an Aptian salt basin. *Geophysical Journal International*, 183, 29-34.

Torsvik, T. H., & Van der Voo, R. (2002). Refining Gondwana and Pangea palaeogeography: Estimates of Phanerozoic non-dipole (octupole) fields. *Geophysical Journal International*, 151, 771-794.

Vai, G. B. (2003). Development of the palaeogeography of Pangaea from Late Carboniferous to Early Permian. *Palaeogeography, Palaeoclimatolology, Palaeoecology*, 196, 125-155.

Valet, J. P., & Herrero-Bervera, E. (2011). Time-averaged and mean axial dipole field. *in: The Earth's Magnetic Interior*, E. Petrovský et al. (eds.). IAGA Special Sopron Book Series 1, 131-137.

Van Bemmelen, R. W. (1966). On mega-undations: A new model for the Earth's evolution. *Tectonophysics*, 3, 83-127.

Van der Lingen, G. J., (1960). Geology of the Spanish Pyrenees, north of Canfranc, Huesca Province. *Estud. Geol.*, 16, 205-242.

Van der Voo, R. (1993). Paleomagnetism of the Atlantic, Tethys and Iapetus oceans. Cambridge University Press, Cambridge, U.K.

Van der Voo, R., & French, R. B. (1974). Apparent polar wandering for the Atlantic-bordering continents: Late Carboniferous to Eocene. *Earth-Science Reviews*, 10, 99-119.

Van der Voo, R., Mauk, F. J., & French, R. B. (1976). Permian–Triassic continental configurations and the origin of the Gulf of Mexico. *Geology*, 4, 177-180.

Van der Voo, R., & Torsvik, T. H. (2001). Evidence for Late Paleozoic and Mesozoic non-dipole fields provides an explanation for the Pangea reconstruction problems. *Earth and Planetary Science Letters*, 187, 71-81.

Van der Voo, R., & Torsvik, T. H. (2004). The quality of the European Permo-Triassic paleopoles and its impact on Pangea reconstructions. Timescales of the paleomagnetic field. *American Geophysical Union - Geophysical Monograph*, 145, 29-42.

Van Hilten, D. (1962). Presentation of paleomagnetic data, polar wandering, and continental drift. *American Journal of Science*, 260, 401-426.

Van Hilten, D. (1964). Evaluation of some geotectonic hypotheses by paleomagnetism. *Tectonophysics*, 1, 3-71.

van Vreumingen, M. J. (1993). The influence of salinity and flocculation upon the acquisition of remanent magnetization in some artificial sediments. *Geophysical Journal International*, 114, 607-614.

Vizán, H., Ixer, R., Turner, P., Cortes, J. M., & Cladera, G. (2004). Paleomagnetism of Upper Triassic rocks in the Los Colorados Hill section, Mendoza Province, Argentina. *Journal of South American Earth Science*, 18, 41-59.

Walderhaug, H. (1993). Rock magnetic and magnetic fabric variations across three thin alkaline dykes from Sunnhordland, western Norway; influence of initial mineralogy and secondary chemical alterations. *Geophysical Journal International*, 115, 97-108.

Walderhaug, H. J, Eide, E. A., Scott, R. A., Inger, S., & Golionko, E. G. (2005). Paleomagnetism and $^{40}Ar/^{39}Ar$ geochronology from the South Taimyr igneous complex, Arctic Russia; a Middle–Late Triassic magmatic pulse after Siberian flood-basalt volcanism. *Geophysical Journal International*, 163, 501-517.

Walper, J. L., & Rowett, C. L. (1972). Plate tectonics and the origin of the Caribbean Sea and the Gulf of Mexico. *Transactions of the Gulf Coast Association of Geological Societies*, 22, 105-116.

Wegener, A. (1915; 1922). Die Entstehung der Kontinente und Ozeane. On the Origin of Continents and Oceans, English translation of 3^{rd} edition by J. G. A. Skerl (1924), Methuen, London. 212 pp.

Weil, A. B., Van der Voo, R., & van der Pluijm, B. A. (2001). Oroclinal bending and evidence against the Pangea megashear: The Cantabria-Asturias Arc (northern Spain). *Geology*, 29, 991-994.

Weil, A. B., Yonkee, A., & Sussman, A. (2010). Reconstructing the kinematic evolution of curved mountain belts: A paleomagnetic study of Triassic red beds from the Wyoming salient, Sevier thrust belt, *Geological Society of America Bulletin*, 122, 3-23.

Westphal, M. (1977). Configuration of the magnetic field and reconstruction of Pangaea in the Permian Period. *Nature*, 267, 136-137.

Yuan, K., Van der Voo, R., Bazhenov, M. L., Bakhmutov, V., Alekhin, V., & Hendriks, B. W. H. (2011). Permian and Triassic Paleolatitudes of the Ukrainian Shield with Implications for Pangea Reconstructions. *Geophysical Journal International*, 184, 595-610.

Zijderveld, J. D. A. (1967). The natural remanent magnetizations of the Exeter Volcanic Traps (Permian, Europe). *Tectonophysics*, 4, 121-153.

Zijderveld, J. D. A. (1975). Paleomagnetism of the Esterel rocks. *Ph.D. Thesis, Univ. of Utrecht.*

Zijderveld, J. D. A., Hazeu, G. J. A., Nardin, M., & Van der Voo, R. (1970). Shear in the Tethys and the Permian paleomagnetism in the Southern Alps, including new results. *Tectonophysics*, 10, 639-661.

CHAPTER VI

Conclusions

In the following section, the primary findings of each chapter are summarized, with an emphasis on how they address the critical questions posed in the introduction of this dissertation: (1) Are there any indications of systematic bias in the present paleomagnetic data? (2) Do new, high-fidelity data significantly differ from older, lower-quality results? (3) What effect do these findings (1,2) have on the apparent configuration of Pangea? (4) What time-dependent paleogeography is derived from the highest-quality results? In the closing section, the principal conclusions and broader implications of this work are discussed, and avenues for future research are considered.

6.1 Summary of Results

Chapter II: A new Late Permian igneous-based paleopole from central Argentina is presented. The age of the studied volcanic rocks (∼263 Ma) is well-determined by SHRIMP U-Pb dating of zircons, and the age of magnetization acquisition is constrained by a positive tilt-test. Rock-magnetic experiments and statistical tests suggest that the magnetization is high-fidelity and representative of a time-averaged magnetic field. The position of the paleomagnetic pole is distinct from a preliminary result, and falls between the Late Permian APWP segments of Laurussia and

Gondwana. This implies that the observed late Permian separation of the APWPs is due to systemic bias in lower-quality paleomagnetic data, which currently dominate the South American dataset. To test this interpretation, a Permian–Middle Triassic compilation of quality-filtered South American paleomagnetic data are compared against the greater-Gondwana reference APWP and the APWP of Laurussia. The filtered South American APWP bisects the separation between the APWPs of greater Gondwana and Laurussia, corroborating the contention that the separation of the latter two is due, at least in part, to systemic data pathologies.

Chapter III: Building on the findings of chapter II, this chapter further explores the hypothesis that high-fidelity late Paleozoic–early Mesozoic paleomagnetic data will be in accord with the conventional Pangea model. The chapter presents and considers a new set of results from volcanic rocks of the Late Permian Upper Choiyoi Group and the Early–Middle Triassic Puesto Viejo Group, western Argentina. Results from a joint U-Pb and ^{40}Ar-^{39}Ar isotopic dating study offer reliable age estimates of ∼264 Ma and ∼245 Ma for the Upper Choiyoi and Puesto Viejo Groups, respectively. A magnetic anisotropy investigation, conducted parallel to the paleomagnetic study, allows for independent interpretation of the site-specific structure of the volcanic rocks, and for correction of the magnetization directions. Rock magnetic experiments and field stability tests demonstrate that the volcanic rocks are carrying effectively primary magnetizations, and two new paleomagnetic poles are calculated. These new paleopoles bisect the gap between the late Paleozoic–early Mesozoic segments of the reference APWPs of Laurussia and Gondwana, as observed for the paleopole presented in Chapter II. In an explicit test of the conventional Pangea reconstruction, these new paleopoles are compared with the global reference APWP of Torsvik et al. (2008), which assumes an A-type paleogeographic model. The new

paleopoles are in good accord with this reference APWP, implying that they are compatible with the conventional reconstruction, and that the previously documented discrepancy is an artifact due to systemic data pathologies. In support of the latter argument, this chapter also presents paleomagnetic data from volcaniclastic rocks of the Puesto Viejo Gr; the paleomagnetic pole derived from this data is far-removed from the global APWP, and is instead proximal to the APWP of Gondwana. Correspondingly, magnetic anisotropy measurements indicate that a significant shallow inclination bias is present in these rocks; a deviation which is being increasingly recognized in paleomagnetic records from typical clastic sedimentary rocks.

Chapter IV: Having recognized a prominent bias in the APWP of Gondwana (chapters II and III), this chapter considers the evidence for widespread bias in the complementary APWP of Laurentia. To first evaluate this possibility, a new paleomagnetic study is conducted on Middle Permian (∼270 Ma) shallow intrusive rocks in southern Illinois. Although no field tests are applicable, the observation of an exclusively reverse magnetization and its shallow direction are consistent with a Middle Permian acquisition. However, the resulting paleopole is found to have a distinctly higher paleolatitude than the Middle Permian segment of the reference APWP of Laurentia. Given that the latter is based almost exclusively on paleomagnetic results from clastic redbeds, it is hypothesized that the reference APWP is biased by widespread inclination shallowing. To test this notion, this chapter next presents results from a VGP distribution analysis on published Permian–Middle Triassic paleomagnetic records from Laurentia. Relative to the results from a statistical field model (TK03.GAD), the compiled VGPs from the Laurentian redbeds appear to have an excessively elongate distribution, specifically one that would be expected from rocks subjected to inclination shallowing. Quantitative estimates of this incli-

nation bias are made via the theoretical model. It is observed that correction for this bias, by application of the minimum estimated correction to the sedimentary-based paleomagnetic data, results in an improved agreement between the reference APWP and the new igneous-based paleopole. Moreover, with application of the inclination corrections, the reference APWP of Laurentia comes into greater accord with the APWP of Gondwana in a Pangea A-type reconstruction.

Chapter V: In the first part of this chapter, an exhaustive review of the historical development of the paleomagnetic Pangea problem is presented. With well-documented evidence (presented in the preceeding chapters) of (1) systematic bias in the published paleomagnetic data and (2) an improved agreement between the late Paleozoic–early Mesozoic paleomagnetic data of Laurentia and Gondwana with the use of quality-filters or inclination shallowing corrections, this chapter proceeds with a new and comprehensive paleomagnetic analysis of Pangea. This is conducted with the most up-to-date Late Carboniferous–Late Triassic paleomagnetic data from Laurussia and West Gondwana. To simplify the multivariate analysis, the role of data-quality, Euler parameters, and inclination shallowing are examined in isolation. Through a stepwise approach, it is shown that the paleomagnetic data can be reconciled with the conventional A-type paleogeographic model of Pangea by using recently improved Euler parameter estimates and high-quality paleomagnetic data (including correcting for inclination shallowing, where necessary). In lieu of specific (and unknown) inclination correction factors, an average correction is applied; a numerical exercise indicates that this average correction will yield a reasonably reliable result, assuming it is close to the "true" average of the (unknown) distribution of shallowing factors. Having confirmed that the paleomagnetic data can be reconciled with the conventional paleogeographic model of Pangea, this chapter then explores

the inverse problem of determining the best-fit Laurussia vs. Gondwana Euler parameters from the paleomagnetic data. The 310-210 Ma time-specific values are found to be A-type. The overarching conclusion is that neither alternative Pangea reconstructions nor time-dependent non-dipole geomagnetic fields need to be invoked in order to reconcile the paleogeographic model and the paleomagnetic data; the discrepancy can be entirely explained as an artifact of data pathologies.

6.2 Conclusions, Implications, and Future Work

Succinctly, the principal achievement of this dissertation is resolution of the long-standing discrepancy between late Paleozoic–early Mesozoic paleomagnetic data and a geologically-plausible reconstruction of Pangea. It is shown that the conventional A-type reconstruction is compatible with high-quality Late Carboniferous–Late Triassic paleomagnetic data with use of up-to-date Euler parameters. Significantly, this result implies that it is unnecessary to invoke a trans-continental megashear or substantial time-dependent non-dipole fields in the late Paleozoic–early Mesozoic in order to reconcile the paleomagnetic data and the paleogeographic model; the conventional A-type model and the GAD assumption are mutually acceptable. Of equal importance is the revelation of widespread bias in the late Paleozoic–early Mesozoic paleomagnetic data, both from Laurussia and Gondwana. Such bias, most notably due to inclination shallowing in typical clastic sedimentary rocks, is presumably also present in the paleomagnetic data of earlier times (and would be less easily recognized due to the absence of an independent paleogeographic reference), and could compromise the accuracy of paleolatitudinal estimates, if not corrected or accounted for. The findings of this dissertation should therefore act as a cautionary notice, in that it is here demonstrated that systemic data pathologies (that are likely to be

present in all but the highest-quality data, especially where derived from sedimentary rocks) can lead to serious paleogeographic problems.

Although the use of the highest-quality data has yielded congruent first-order APWPs of Laurussia and Gondwana in the late Paleozoic–early Mesozoic, the finer details of these APWPs are not yet well established. The validity of the final APWPs calculated in chapter V is ultimately dependent on the veracity of the chosen average inclination correction coefficient. There are still too few high-quality igneous-based poles (especially from Gondwana) to construct a reliable APWP by excluding the sedimentary-based results altogether. Future work is therefore needed to continue to refine these APWP estimates, with particular attention paid to the treatment of inclination corrections. It is critical that future paleomagnetic investigations of clastic sedimentary rocks assume that a shallow inclination bias is present, until it can be proven otherwise; "guilty until proven innocent" should become the *modus operandi* of sedimentary-based paleomagnetism. It is also worth noting that a minor shallow inclination bias was observed in some ignimbrites studied herein (chapter III), so it cannot always be safely assumed that igneous-based paleomagnetic data are free from systemic directional bias. In addition to the expectedly slow-pace of progress that formation-specific inclination corrections will bring, the average inclination corrections applied in this work may be revised as the true distribution of shallowing coefficients becomes more well-known.

The late Paleozoic–early Mesozoic paleomagnetic data from East Gondwana (not considered in this dissertation) remain discordant with respect to the data from West Gondwana and Laurussia. Given the predominance of sedimentary-based paleomagnetic data from East Gondwana, it would be rather surprising if this bias didn't play a significant role in this discrepancy. However, Gondwana's longitudinal

span complicates the overall effect of inclination shallowing on its disperse poles, and other variables such as local rotations or Euler parameters may be playing equally important roles in this unresolved problem.

Following from the conclusion that Pangea A is broadly tenable for the late Paleozoic–early Mesozoic, but that the APWPs of Laurentia and Gondwana are still in need of improvement, it is clear that there are details of the time-dependent paleogeography of Pangea that remain to be resolved. There are, of course, fundamental limitations on the resolution of paleomagnetic data, but with additional high-quality results, it should be possible to further address remaining questions of interest, such as: did the Laurussia vs. Gondwana Euler parameter(s) change through the Late Carboniferous–Late Triassic? Did it do so in a systematic way? Curiosities, such as the prominent bend in the APWPs at the Permian–Triassic boundary, also beg further definition, if not elucidation, through additional work.

Despite confirming that the GAD hypothesis can work with the conventional paleogeographic model of Pangea, important derivative questions remain about the structure of the paleomagnetic field in pre-Jurassic time. With regard to the context of this work, the complete expression of a time-averaged field remains one of the most critical unknowns. For example, the E/I technique is a powerful tool, but is predicated on a theoretical field structure (TK03.GAD) that needs verification or modification, according to observations of the time-averaged field in space and time. It is typically a tacit assumption that this field model is time-independent—in chapter IV it was used to coarsely evaluate data from the Permian and Triassic—but it remains to be demonstrated that this assumption is valid; reliable secular variation studies of pre-Jurassic magnetizations are badly needed.

APPENDICES

APPENDIX A

Complete geochronology data

The following data tables and figures present the complete geochronology data discussed in chapters II and III. Table A.1 presents the SHRIMP U-Pb data from the Sierra Chica, La Pampa Province, Argentina (see chapter II for details and sampling locations). Table A.2 presents the SHRIMP U-Pb data from the Upper Choiyoi and Puesto Viejo Groups of the San Rafael Block, Mendoza Province, Argentina (see chapter III for details and sampling locations). All SHRIMP U-Pb analyses were carried out by Eric Tohver at the University of Western Australia. Figure A.1 shows an example cathodoluminescence image of zircons selected for SHRIMP U-Pb analysis. Table A.3 presents the ^{40}Ar-^{39}Ar geochronology data from the Upper Choiyoi and Puesto Viejo Groups (see Chapter III); these analyses were carried out by Bart Hendriks at the Norwegian Geological Survey (NGU). Figure A.2 shows the complete ^{40}Ar-^{39}Ar geochronology results (except the examples shown in Chapter II).

Table A.1: Complete SHRIMP U-Pb data from the Sierra Chica

Sample/spot	$\%^{206}Pb_c$	ppm U	ppm Th	$^{232}Th/^{238}U$	ppm $^{206}Pb^*$	$^{206}Pb/^{238}U$ Age[1]	$^{206}Pb/^{238}U$ Age[2]	$^{206}Pb/^{238}U$ Age[3]	$^{207}Pb/^{206}Pb$ Age[1]	$^{208}Pb/^{232}Th$ Age[1]	%Disc.
Sierra Chica SC-D01											
SC-D01-12	0.94	102	137	1.38	3.69	262.5 ± 8.5	263.6 ± 8.6	264.0 ± 11.0	105 ± 210	256.0 ± 12	-60
SC-D01-3	-	163	191	1.21	5.78	263.5 ± 8.5	260.5 ± 8.4	259.0 ± 10.0	630 ± 170	283.0 ± 13	139
SC-D01-8	0.47	141	192	1.40	5.11	264.3 ± 7.3	264.6 ± 7.4	265.0 ± 9.6	220 ± 130	261.6 ± 9.6	-17
SC-D01-11	1.50	81	105	1.33	2.97	265.5 ± 8.2	264.2 ± 8.2	264.0 ± 11.0	434 ± 180	270.0 ± 12	64
SC-D01-4	0.39	309	561	1.87	11.20	265.9 ± 7.6	267.1 ± 7.7	267.0 ± 11.0	90 ± 65	262.0 ± 8.3	-66
SC-D01-10	0.59	269	466	1.79	9.83	266.8 ± 7.1	268.3 ± 7.3	269.0 ± 10.0	52 ± 76	260.5 ± 7.8	-80
SC-D01-7	-	265	411	1.60	9.67	269.3 ± 7.2	267.8 ± 7.2	268.1 ± 9.8	460 ± 99	273.0 ± 8.8	71
SC-D01-2	-	177	273	1.59	6.59	273.6 ± 7.5	272.6 ± 7.6	275.0 ± 10.0	399 ± 80	269.5 ± 9.1	46
SC-D01-9	-	146	324	2.29	5.58	280.9 ± 8.1	280.1 ± 8.1	277.0 ± 13.0	386 ± 120	288.8 ± 9.7	37
SC-D01-6[4]	-	149	141	0.98	5.62	278.5 ± 8.0	276.0 ± 8.0	276.6 ± 9.4	570 ± 71	290.0 ± 11	105
SC-D01-5[4]	2.72	39	41	1.09	1.44	261.9 ± 9.0	265.4 ± 8.7	273.0 ± 11.0	-311 ± 740	207.0 ± 24	-219
SC-D01-1[4]	0.73	97	103	1.10	3.83	288.7 ± 8.4	291.4 ± 8.6	292.0 ± 10.0	-75 ± 210	273.0 ± 13	-126
Sierra Chica SC-D03											
SC-D03-3	1.66	100	100	1.04	3.40	246.5 ± 8.8	246.9 ± 8.8	245.0 ± 11.0	181 ± 260	252.0 ± 14	-26
SC-D03-2	1.96	60	88	1.50	2.08	248.8 ± 7.6	252.5 ± 7.3	254.6 ± 9.8	-398 ± 600	229.0 ± 15	-260
SC-D03-4	2.04	47	54	1.17	1.65	250.5 ± 7.7	254.6 ± 7.7	256.9 ± 9.5	-476 ± 510	220.0 ± 15	-290
SC-D03-17	0.93	269	436	1.68	9.63	261.2 ± 7.0	263.3 ± 7.1	263.3 ± 9.8	-49 ± 130	255.0 ± 8	-119
SC-D03-12	-	95	138	1.49	3.39	261.6 ± 7.7	260.4 ± 7.7	259.0 ± 10.0	414 ± 94	271.6 ± 9.9	58
SC-D03-6	-	139	213	1.59	4.90	261.6 ± 7.4	259.8 ± 7.3	261.1 ± 9.9	493 ± 120	263.2 ± 9.2	88
SC-D03-5	0.04	332	558	1.74	11.90	263.6 ± 8.2	263.8 ± 8.2	262.0 ± 12.0	242 ± 66	268.0 ± 11	-8
SC-D03-8	1.88	97	165	1.76	3.54	264.1 ± 8.3	267.4 ± 7.9	261.0 ± 11.0	-266 ± 620	272.0 ± 16	-201
SC-D03-9	1.47	116	176	1.56	4.25	265.0 ± 11.0	267.0 ± 11.0	267.0 ± 15.0	-177 ± 400	257.0 ± 15	-167
SC-D03-13	0.24	338	470	1.44	12.30	265.7 ± 8.7	266.4 ± 8.8	265.0 ± 12.0	168 ± 130	266.0 ± 10	-37
SC-D03-14	0.56	192	223	1.20	7.00	266.0 ± 10.0	267.0 ± 10.0	266.0 ± 13.0	93 ± 120	265.0 ± 13	-65
SC-D03-16	2.57	62	121	2.00	2.33	267.0 ± 12.0	270.0 ± 12.0	277.0 ± 18.0	-102 ± 640	246.0 ± 17	-138
SC-D03-11	5.62	92	178	1.99	3.64	274.0 ± 16.0	276.0 ± 16.0	277.0 ± 25.0	-153 ± 750	266.0 ± 22	-156
SC-D03-15	1.32	78	144	1.91	2.95	274.5 ± 8.4	275.4 ± 8.1	275.0 ± 12.0	160 ± 430	273.0 ± 14	-42
SC-D03-10	-	301	744	2.55	11.30	277.4 ± 7.5	275.7 ± 7.5	273.0 ± 13.0	482 ± 88	285.3 ± 8.5	74
SC-D03-1[4]	-	55	67	1.26	1.85	251.0 ± 12.0	246.0 ± 12.0	244.0 ± 15.0	830 ± 190	280.0 ± 18	231
SC-D03-7[4]	0.03	753	339	0.47	73.10	690.0 ± 18.0	691.0 ± 18.0	690.0 ± 19.0	648 ± 18	689.0 ± 23	-6
Sierra Chica SC-D04											
SC-D04-2	2.92	37	71	2.00	1.29	250.6 ± 6.7	253.7 ± 6.2	258.4 ± 10.2	-282 ± 619	232.0 ± 14.0	-213
SC-D04-3	2.44	31	47	1.55	1.11	254.3 ± 6.1	252.8 ± 5.4	254.5 ± 8.1	460 ± 430	254.0 ± 19.0	81
SC-D04-4	0.93	126	170	1.39	4.47	258.2 ± 4.0	260.2 ± 4.1	260.3 ± 5.5	-53 ± 113	250.0 ± 8.0	-120
SC-D04-5	1.08	83	102	1.26	2.92	255.4 ± 4.6	255.7 ± 4.3	257.5 ± 5.7	212 ± 292	246.0 ± 13.0	-17
SC-D04-6	0.84	128	167	1.35	4.56	259.7 ± 4.4	260.2 ± 4.2	263.4 ± 5.6	185 ± 218	245.0 ± 10.0	-29
SC-D04-8	1.71	43	116	2.77	1.54	255.7 ± 5.8	257.5 ± 5.1	249.5 ± 11.0	-24 ± 562	265.0 ± 12.0	-109
SC-D04-10	2.30	65	182	2.87	2.22	243.9 ± 6.8	247.4 ± 6.1	242.3 ± 12.8	-401 ± 768	246.0 ± 11.0	-264

...continued

Sample/spot	$\%^{206}Pb^{c}$	ppm U	ppm Th	$^{232}Th/^{238}U$	ppm $^{206}Pb^{*}$	$^{206}Pb/^{238}U$ Age[1]	$^{206}Pb/^{238}U$ Age[2]	$^{206}Pb/^{238}U$ Age[3]	$^{207}Pb/^{206}Pb$ Age[1]	$^{208}Pb/^{232}Th$ Age[1]	%Disc.
SC-D04-11	3.04	48	141	3.00	1.71	252.1 ± 5.1	257.8 ± 4.9	265.0 ± 11.3	-883 ± 641	236.0 ± 9.0	-450
SC-D04-12	-3.01	49	56	1.17	1.71	263.7 ± 6.1	252.8 ± 4.8	255.9 ± 6.3	1319 ± 255	301.0 ± 25.0	400
SC-D04-13	1.34	56	157	2.91	1.99	257.9 ± 6.9	256.0 ± 4.7	260.6 ± 10.5	500 ± 634	254.0 ± 15.0	94
SC-D04-14	-0.20	52	145	2.86	1.86	262.0 ± 4.8	255.2 ± 4.8	255.9 ± 10.6	1002 ± 78	270.0 ± 9.0	282
SC-D04-15	3.18	56	86	1.59	2.07	263.5 ± 5.1	261.3 ± 4.8	263.1 ± 7.3	550 ± 246	265.0 ± 13.0	109
SC-D04-17	0.64	277	1075	4.01	9.91	261.0 ± 3.8	260.7 ± 3.8	268.6 ± 11.6	300 ± 102	256.0 ± 5.0	15
SC-D04-18	-1.46	55	109	2.05	1.92	261.0 ± 5.3	255.3 ± 4.7	254.1 ± 7.8	904 ± 229	277.0 ± 13.0	246
SC-D04-19	-1.01	29	51	1.80	1.00	253.7 ± 7.4	247.7 ± 7.3	254.0 ± 11.1	941 ± 135	253.0 ± 14.0	271
SC-D04-16[4]	6.61	29	63	2.26	1.06	252.8 ± 7.9	255.7 ± 5.6	250.1 ± 11.0	-221 ± 1166	258.0 ± 21.0	-188
SC-D04-7[4]	6.19	52	134	2.66	1.83	242.1 ± 6.4	251.8 ± 4.7	248.6 ± 9.8	-2636 ± 3609	232.0 ± 14.0	-1189
SC-D04-20[4]	1.86	28	38	1.41	1.05	273.3 ± 7.6	270.5 ± 6.2	274.3 ± 8.9	601 ± 517	269.0 ± 27.0	120

Table A.1 continued

Sample/spot	T.$^{238}U/^{206}Pb$	± %	T.$^{207}Pb/^{206}Pb$	± %	$^{238}U/^{206}Pb^{*1}$	± %	$^{207}Pb^{*}/^{206}Pb^{*1}$	± %	$^{207}Pb^{*}/^{235}U^{1}$	± %	$^{206}Pb^{*}/^{238}U^{1}$	± %	ErrCorr
Sierra Chica SC-D01													
SC-D01-12	23.83	3.3	0.0557	4.1	24.06	3.3	0.0481	9.0	0.276	9.6	0.0416	3.3	0.345
SC-D01-3	24.25	3.3	0.0513	3.7	23.97	3.3	0.0607	7.8	0.350	8.5	0.0417	3.3	0.388
SC-D01-8	23.78	2.8	0.0543	3.5	23.89	2.8	0.0505	5.5	0.292	6.2	0.0419	2.8	0.455
SC-D01-11	23.43	3.1	0.0675	4.2	23.79	3.2	0.0555	8.2	0.322	8.8	0.0420	3.2	0.359
SC-D01-4	23.66	2.9	0.0509	2.6	23.75	2.9	0.0478	2.8	0.278	4.0	0.0421	2.9	0.724
SC-D01-10	23.52	2.7	0.0518	2.7	23.66	2.7	0.0471	3.2	0.274	4.2	0.0423	2.7	0.650
SC-D01-7	23.54	2.7	0.0528	2.6	23.44	2.7	0.0562	4.5	0.330	5.2	0.0427	2.7	0.523
SC-D01-2	23.07	2.8	0.0544	3.6	23.06	2.8	0.0547	3.6	0.327	4.5	0.0434	2.8	0.619
SC-D01-9	22.55	2.9	0.0509	3.5	22.45	2.9	0.0543	5.4	0.334	6.2	0.0445	2.9	0.476
SC-D01-6[4]	22.81	2.9	0.0534	3.6	22.65	2.9	0.0591	3.3	0.360	4.4	0.0441	2.9	0.667
SC-D01-5[4]	23.46	3.3	0.0627	6.7	24.11	3.5	0.0410	29.0	0.232	29.0	0.0415	3.5	0.122
SC-D01-1[4]	21.67	3.0	0.0506	4.6	21.83	3.0	0.0447	8.8	0.282	9.3	0.0458	3.0	0.322
Sierra Chica SC-D03													
SC-D03-3	25.23	3.6	0.0630	3.8	25.65	3.7	0.0497	11.0	0.267	12.0	0.0390	3.7	0.316
SC-D03-2	24.91	2.9	0.0552	4.7	25.41	3.1	0.0393	23.0	0.213	23.0	0.0394	3.1	0.134
SC-D03-4	24.72	3.0	0.0548	6.4	25.24	3.1	0.0381	19.0	0.208	19.0	0.0396	3.1	0.160
SC-D03-17	23.96	2.7	0.0526	2.7	24.18	2.7	0.0451	5.2	0.257	5.9	0.0414	2.7	0.466
SC-D03-12	24.17	3.0	0.0545	4.2	24.15	3.0	0.0550	4.2	0.314	5.2	0.0414	3.0	0.580
SC-D03-6	24.29	2.8	0.0523	3.1	24.15	2.9	0.0570	5.4	0.326	6.1	0.0414	2.9	0.470
SC-D03-5	23.95	3.2	0.0513	2.1	23.96	3.2	0.0510	2.9	0.294	4.3	0.0417	3.2	0.739
SC-D03-8	23.46	3.0	0.0566	4.0	23.91	3.2	0.0410	24.0	0.239	25.0	0.0418	3.2	0.130
SC-D03-9	23.51	4.1	0.0547	4.4	23.86	4.2	0.0428	16.0	0.248	17.0	0.0419	4.2	0.251
SC-D03-13	23.71	3.3	0.0514	3.4	23.77	3.4	0.0494	5.4	0.287	6.3	0.0421	3.4	0.531
SC-D03-14	23.61	3.9	0.0524	3.2	23.75	3.9	0.0479	5.1	0.278	6.4	0.0421	3.9	0.603
SC-D03-16	23.00	4.5	0.0649	4.9	23.60	4.7	0.0440	26.0	0.258	26.0	0.0423	4.7	0.179
SC-D03-11	21.80	5.9	0.0888	3.2	23.10	6.1	0.0430	30.0	0.259	31.0	0.0434	6.1	0.197
SC-D03-15	22.68	3.0	0.0599	4.6	22.98	3.1	0.0493	18.0	0.295	19.0	0.0435	3.1	0.169
SC-D03-10	22.83	2.7	0.0538	2.6	22.74	2.8	0.0568	4.0	0.344	4.8	0.0440	2.8	0.569
SC-D03-1[4]	25.50	4.9	0.0576	4.9	25.20	5.0	0.0668	8.9	0.365	10.0	0.0396	5.0	0.486
SC-D03-7[4]	8.85	2.7	0.0615	0.8	8.85	2.7	0.0612	0.8	0.954	2.8	0.1130	2.7	0.953
Sierra Chica SC-D04													
SC-D04-2	24.49	2.5	0.0648	4.8	25.23	2.7	0.0411	24.3	0.220	24.4	0.0396	2.7	0.111
SC-D04-3	24.24	2.1	0.0756	4.9	24.85	2.5	0.0562	19.4	0.310	19.6	0.0402	2.5	0.126
SC-D04-4	24.24	1.6	0.0525	2.8	24.47	1.6	0.0451	4.6	0.250	4.9	0.0409	1.6	0.326
SC-D04-5	24.48	1.7	0.0590	3.3	24.75	1.8	0.0504	12.6	0.280	12.8	0.0404	1.8	0.145
SC-D04-6	24.12	1.6	0.0566	2.7	24.33	1.7	0.0498	9.4	0.280	9.5	0.0411	1.7	0.180
SC-D04-8	24.29	2.0	0.0594	4.8	24.71	2.3	0.0456	23.2	0.250	23.3	0.0405	2.3	0.100
SC-D04-10	25.34	2.5	0.0579	3.8	25.94	2.8	0.0392	29.4	0.210	29.6	0.0386	2.8	0.096

...continued

Sample/spot	T.^{238}U/^{206}Pb	± %	T.^{207}Pb/^{206}Pb	± %	^{238}U/^{206}Pb*[1]	± %	^{207}Pb*/^{206}Pb*[1]	± %	^{207}Pb*/^{235}U[1]	± %	^{206}Pb*/^{238}U[1]	± %	ErrCorr
SC-D04-11	24.31	1.9	0.0579	4.3	25.07	2.1	0.0329	22.2	0.180	22.3	0.0399	2.1	0.092
SC-D04-12	24.67	1.9	0.0620	4.4	23.95	2.4	0.0851	13.1	0.490	13.3	0.0418	2.4	0.176
SC-D04-13	24.18	1.8	0.0678	3.9	24.50	2.7	0.0572	28.8	0.320	28.9	0.0408	2.7	0.095
SC-D04-14	24.16	1.9	0.0710	3.9	24.11	1.9	0.0726	3.8	0.420	4.3	0.0415	1.9	0.437
SC-D04-15	23.20	1.8	0.0838	3.4	23.96	2.0	0.0585	11.3	0.340	11.5	0.0417	2.0	0.171
SC-D04-17	24.05	1.5	0.0574	1.8	24.20	1.5	0.0523	4.5	0.300	4.7	0.0413	1.5	0.318
SC-D04-18	24.55	1.8	0.0578	4.2	24.20	2.1	0.0692	11.1	0.390	11.3	0.0413	2.1	0.181
SC-D04-19	25.16	3.0	0.0625	5.5	24.91	3.0	0.0704	6.6	0.390	7.2	0.0401	3.0	0.414
SC-D04-16[4]	23.35	2.1	0.0956	4.4	25.00	3.2	0.0421	46.3	0.230	46.4	0.0400	3.2	0.068
SC-D04-7[4]	24.51	1.9	0.0701	3.8	26.13	2.7	0.0185	88.6	0.100	88.7	0.0383	2.7	0.030
SC-D04-20[4]	22.66	2.3	0.0747	5.0	23.09	2.9	0.0599	23.9	0.360	24.1	0.0433	2.9	0.119

Errors are 1σ; Pb_c and Pb* indicate the common and radiogenic portions, respetively

Error in Standard calibration was 0.92% (not included in above errors but required when comparing data from different mounts)

[1]Common Pb corrected using measured [2]04Pb

[2]Common Pb corrected by assuming ^{206}Pb/^{238}U-^{207}Pb/^{235}U age-concordance

[3]Common Pb corrected by assuming ^{206}Pb/^{238}U-^{208}Pb/^{232}Th age-concordance

*Analysis not used in final age calculation

"T."=total

Table A.2: Complete SHRIMP U-Pb data from the San Rafael Block

Sample/spot	$\%^{206}Pb_c$	ppm U	ppm Th	$^{232}Th/^{238}U$	ppm $^{206}Pb^*$	$^{206}Pb/^{238}U$ Age[1]		$^{206}Pb/^{238}U$ Age[2]		$^{206}Pb/^{238}U$ Age[3]		$^{207}Pb/^{206}Pb$ Age[1]		$^{208}Pb/^{232}Th$ Age[1]		%Dis.
"PV01d" (Upper Choiyoi Group)																
PV01d-20	0.49	152	88	0.60	5.4	258.7	±3.5	258.8	±3.4	259.0	±3.8	246.1	±172	255.6	±14.9	−5
PV01d-16	0.08	308	132	0.44	11.0	262.2	±2.9	261.5	±2.9	262.0	±3.1	362.0	±71	264.5	±9.1	38
PV01d-14	−0.04	543	318	0.61	19.4	263.0	±2.6	262.4	±2.6	263.8	±2.9	334.5	±40	254.6	±4.5	27
PV01d-19	0.52	279	170	0.63	10.1	263.5	±2.9	264.3	±3.0	265.3	±3.3	148.3	±78	246.6	±6.8	−44
PV01d-7A	0.38	351	138	0.41	12.7	263.9	±2.9	264.8	±2.8	264.8	±3.0	144.1	±124	250.9	±14.1	−45
PV01d-15	0.12	461	211	0.47	16.6	264.8	±2.7	264.7	±2.7	265.1	±2.9	283.1	±78	260.8	±8.8	7
PV01d-6A	0.39	546	396	0.75	19.9	267.1	±3.0	267.4	±2.9	267.1	±3.3	222.9	±94	266.9	±7.2	−17
PV01d-13A[4]	1.64	111	41	0.38	4.1	264.7	±4.5	268.5	±3.9	267.0	±4.2	−349.8	±520	227.2	±45.1	−232
PV01d-1A[4]	1.63	132	51	0.40	4.9	266.0	±3.8	269.3	±3.7	270.1	±4.0	−246.6	±237	201.4	±20.3	−193
PV01d-2A[4]	5.04	99	44	0.46	3.6	257.3	±6.5	260.8	±5.9	258.8	±6.9	−319.8	±794	237.5	±54.5	−224
PV01d-5A[4]	2.17	85	34	0.42	3.0	259.3	±4.4	262.6	±4.2	263.3	±4.5	−297.2	±395	197.4	±31.2	−215
PV01d-18[4]	1.82	98	60	0.63	3.5	259.6	±4.8	262.9	±3.9	263.6	±4.4	−289.6	±576	220.5	±31.3	−212
PV01d-17[4]	3.37	160	92	0.59	5.9	261.1	±4.0	264.3	±4.4	265.1	±4.5	−254.2	±687	220.1	±31.6	−197
PV03d (Puesto Viejo Group)																
PV03d-9	1.44	147	44	0.31	5.3	261.7	±4.2	262.9	±3.0	262.9	±3.2	85.0	±460	237.0	±64.0	−67
PV03d-8A	0.01	686	312	0.47	25.2	269.8	±1.8	269.6	±1.8	269.9	±2.0	303.0	±53	268.9	±8.1	12
PV03d-8	0.18	411	53	0.13	15.2	270.9	±2.1	270.9	±2.1	271.0	±2.2	272.0	±68	265.0	±22.0	0
PV03d-2A	−0.03	152	119	0.81	5.6	271.8	±3.0	270.4	±3.0	269.7	±3.5	446.0	±64	286.7	±7.4	64
PV03d-3A	0.60	32	21	0.67	1.3	283.0	±12.0	279.0	±10.0	281.0	±12.0	733.0	±610	306.0	±67.0	159
PV03d-06A[4]	3.60	403	77	0.20	11.9	211.0	±2.4	210.7	±1.9	210.0	±2.1	253.0	±290	241.0	±54.0	20
PV03d-1A[4]	2.17	694	288	0.43	23.1	240.0	±2.1	239.5	±1.7	239.6	±1.9	326.0	±200	246.0	±21.0	36
PV03d-4AA[4]	2.54	130	97	0.77	4.7	257.0	±3.6	262.3	±3.1	261.8	±3.6	−744.0	±550	220.0	±19.0	−390
PV03d-10[4]	1.40	48	22	0.48	9.3	1296.0	±24.0	1303.0	±25.0	1306.0	±25.0	1182.0	±140	1143.0	±120.0	−9
PV03d-4A[4]	0.09	455	113	0.26	87.5	1300.3	±7.7	1297.8	±8.3	1303.3	±8.0	1340.0	±20	1213.0	±16.0	3
PV06d (Puesto Viejo Group)																
PV06d-8	1.39	125	64	0.52	4.5	258.0	±3.3	260.2	±3.1	259.6	±3.4	−96.0	±290	238.0	±21.0	−137
PV06d-6	1.89	103	46	0.46	3.7	258.6	±3.7	261.7	±3.4	263.2	±3.7	−245.0	±340	196.0	±25.0	−195
PV06d-3A	1.52	221	122	0.57	7.9	258.7	±2.6	261.5	±2.6	262.3	±2.8	−189.0	±150	219.8	±9.9	−173
PV06d-4A	0.46	630	309	0.51	22.4	259.6	±1.8	259.3	±1.8	260.3	±2.1	307.0	±36	251.8	±9.8	18
PV06d-12	0.38	522	199	0.39	18.7	261.7	±1.9	262.1	±1.9	262.0	±2.0	198.0	±84	255.7	±9.5	−24
PV06d-11	1.20	100	59	0.61	3.6	262.8	±4.0	263.8	±3.5	264.8	±3.9	120.0	±310	243.0	±23.0	−54
PV06d-5A	0.48	274	118	0.45	9.9	264.5	±2.5	265.3	±2.4	266.0	±2.6	149.0	±130	243.0	±15.0	−44
PV06d-10	0.54	238	67	0.29	8.7	266.7	±2.7	267.4	±2.7	267.3	±2.8	172.0	±85	254.0	±12.0	−36
PV06d-7	−0.93	161	94	0.61	5.8	268.4	±4.4	265.2	±4.1	265.4	±4.5	648.0	±170	298.0	±20.0	142
PV06d-2A[4]	0.81	279	189	0.70	9.2	241.3	±3.8	242.9	±3.6	242.8	±4.1	−23.0	±240	229.0	±13.0	−110
PV06d-1A[4]	2.29	76	30	0.41	2.8	261.7	±5.4	265.8	±4.0	268.0	±4.3	−435.0	±840	165.0	±64.0	−266
PV06d-9[4]	1.58	114	88	0.79	4.0	250.6	±4.1	253.9	±3.6	253.7	±4.1	−312.0	±550	228.0	±22	−225

Table A.2 continued

Sample/spot	T.^{238}U/^{206}Pb	%	T.^{207}Pb/^{206}Pb	%	^{238}U/^{206}Pb*[1]	%	^{207}Pb*/^{206}Pb*[1]	%	^{207}Pb*/^{235}U[1]	%	^{206}Pb*/^{238}U[1]	%	Err. corr
"PV01d" (Upper Choiyoi Group)													
PV01d-20	24.30	1.3	0.055	2.9	24.42	1.4	0.051	7.5	0.289	7.6	0.041	1.4	0.18
PV01d-16	24.07	1.1	0.054	2.0	24.09	1.1	0.054	3.2	0.308	3.3	0.042	1.1	0.33
PV01d-14	24.03	1.0	0.053	1.8	24.02	1.0	0.053	1.8	0.305	2.0	0.042	1.0	0.49
PV01d-19	23.84	1.1	0.053	2.1	23.97	1.1	0.049	3.3	0.282	3.5	0.042	1.1	0.32
PV01d-7A	23.84	1.1	0.052	1.9	23.93	1.1	0.049	5.3	0.282	5.4	0.042	1.1	0.21
PV01d-15	23.82	1.0	0.053	1.7	23.84	1.0	0.052	3.4	0.300	3.6	0.042	1.0	0.29
PV01d-6A	23.55	1.1	0.054	1.6	23.64	1.1	0.051	4.1	0.295	4.2	0.042	1.1	0.27
PV01d-13A[4]	23.46	1.5	0.053	3.4	23.85	1.7	0.040	20.1	0.231	20.2	0.042	1.7	0.09
PV01d-1A[4]	23.35	1.4	0.055	3.1	23.74	1.5	0.042	9.4	0.242	9.5	0.042	1.5	0.15
PV01d-2A[4]	23.32	2.2	0.081	6.8	24.55	2.6	0.040	30.9	0.227	31.1	0.041	2.6	0.08
PV01d-5A[4]	23.84	1.6	0.058	3.7	24.37	1.7	0.041	15.5	0.231	15.6	0.041	1.7	0.11
PV01d-18[4]	23.89	1.5	0.056	3.5	24.34	1.9	0.041	22.6	0.232	22.7	0.041	1.9	0.08
PV01d-17[4]	23.38	1.3	0.069	12.1	24.19	1.6	0.042	27.1	0.237	27.2	0.041	1.6	0.06
PV03d (Puesto Viejo Group)													
PV03d-9	23.79	1.2	0.059	2.9	24.14	1.6	0.048	20.0	0.273	20.0	0.041	1.6	0.08
PV03d-8A	23.39	0.7	0.052	1.4	23.39	0.7	0.052	2.3	0.309	2.4	0.043	0.7	0.28
PV03d-8	23.26	0.8	0.053	1.8	23.30	0.8	0.052	2.9	0.306	3.1	0.043	0.8	0.26
PV03d-2A	23.23	1.1	0.056	2.9	23.22	1.1	0.056	2.9	0.331	3.1	0.043	1.1	0.36
PV03d-3A	22.13	3.8	0.069	5.6	22.27	4.4	0.064	29.0	0.390	29.0	0.045	4.4	0.15
PV03d-06A[4]	28.98	0.9	0.080	2.5	30.06	1.2	0.051	13.0	0.235	13.0	0.033	1.2	0.09
PV03d-1A[4]	25.79	0.7	0.070	1.3	26.36	0.9	0.053	8.7	0.277	8.8	0.038	0.9	0.10
PV03d-4AA[4]	23.96	1.2	0.055	3.0	24.59	1.4	0.035	20.0	0.194	20.0	0.041	1.4	0.07
PV03d-10[4]	4.43	2.0	0.091	2.7	4.49	2.0	0.079	6.9	2.440	7.2	0.223	2.0	0.29
PV03d-4A[4]	4.47	0.7	0.087	1.0	4.47	0.7	0.086	1.1	2.653	1.2	0.224	0.7	0.53
PV06d (Puesto Viejo Group)													
PV06d-8	24.15	1.2	0.056	3.7	24.49	1.3	0.044	12.0	0.249	12.0	0.041	1.3	0.11
PV06d-6	23.97	1.3	0.057	3.3	24.43	1.5	0.042	13.0	0.235	13.0	0.041	1.5	0.11
PV06d-3A	24.05	1.0	0.055	2.5	24.42	1.0	0.043	6.1	0.241	6.2	0.041	1.0	0.16
PV06d-4A	24.22	0.7	0.056	1.4	24.33	0.7	0.052	1.6	0.297	1.7	0.041	0.7	0.40
PV06d-12	24.05	0.7	0.053	2.1	24.14	0.8	0.050	3.6	0.286	3.7	0.041	0.8	0.20
PV06d-11	23.75	1.3	0.058	3.5	24.03	1.5	0.048	13.0	0.278	13.0	0.042	1.5	0.11
PV06d-5A	23.76	0.9	0.053	2.3	23.87	0.9	0.049	5.5	0.283	5.6	0.042	0.9	0.17
PV06d-10	23.54	1.0	0.054	2.3	23.67	1.0	0.050	3.6	0.288	3.8	0.042	1.0	0.28
PV06d-7	23.74	1.6	0.054	2.9	23.53	1.7	0.061	8.1	0.359	8.2	0.043	1.7	0.20
PV06d-2A[4]	26.01	1.5	0.052	2.7	26.22	1.6	0.046	10.0	0.240	10.0	0.038	1.6	0.16
PV06d-1A[4]	23.59	1.5	0.057	4.1	24.14	2.1	0.039	32.0	0.221	32.0	0.041	2.1	0.07
PV06d-9[4]	24.82	1.4	0.053	6.9	25.22	1.7	0.041	21.0	0.222	22.0	0.040	1.7	0.08

... continued

Sample/spot	T.^{238}U/^{206}Pb	%	T.^{207}Pb/^{206}Pb	%	^{238}U/^{206}Pb*[1]	%	^{207}Pb*/^{206}Pb*[1]	%	^{207}Pb*/^{235}U[1]	%	^{206}Pb*/^{238}U[1]	%	Err. corr

Errors are 1σ; Pb_c and Pb* indicate the common and radiogenic portions, respetively

Error in Standard calibration was 0.92% (not included in above errors but required when comparing data from different mounts)

[1]Common Pb corrected using measured [2]04Pb

[2]Common Pb corrected by assuming ^{206}Pb/^{238}U-^{207}Pb/^{235}U age-concordance

[3]Common Pb corrected by assuming ^{206}Pb/^{238}U-^{208}Pb/^{232}Th age-concordance

*Analysis not used in final age calculation

"T."=total

Figure A.1: Example cathodoluminescence image of zircons selected for SHRIMP U-Pb geochronologic analysis, showing their oscillatory zoning. From sample "PV01d".

Table A.3: Complete ^{40}Ar-^{39}Ar data from the San Rafael Block

Step	Power	^{40}Ar (V)	1σ	^{39}Ar (V)	1σ	^{38}Ar (V)	1σ	^{37}Ar (V)	1σ	^{36}Ar (V)	1σ
First Sample Batch											
Sample CCH Whole rock			$J: 0.00161930 \pm 0.000006001\sigma$			$D: 1.01008652 \pm 0.007338861\sigma$					
1	2.0	0.17302	0.00020	0.00174	0.00002	0.00028	0.00000	0.00001	0.00000	0.00010	0.00000
2	2.5	0.69544	0.00094	0.00711	0.00001	0.00049	0.00001	0.00003	0.00000	0.00017	0.00001
3	3.0	0.77947	0.00019	0.00865	0.00001	0.00038	0.00000	0.00003	0.00000	0.00011	0.00000
4	3.5	0.72110	0.00021	0.00814	0.00002	0.00031	0.00000	0.00004	0.00000	0.00007	0.00000
5	4.0	0.40171	0.00024	0.00490	0.00001	0.00037	0.00000	0.00005	0.00000	0.00011	0.00000
6	4.5	0.06649	0.00004	0.00093	0.00001	0.00015	0.00000	0.00002	0.00000	0.00007	0.00000
7	5.0	0.03263	0.00015	0.00040	0.00000	0.00012	0.00000	0.00002	0.00000	0.00005	0.00000
8	5.5	0.03927	0.00008	0.00053	0.00001	0.00013	0.00000	0.00003	0.00000	0.00007	0.00000
9	6.0	0.01480	0.00007	0.00017	0.00000	0.00006	0.00000	0.00001	0.00000	0.00002	0.00000
10	7.0	0.00924	0.00002	0.00013	0.00000	0.00003	0.00000	0.00000	0.00000	0.00001	0.00000
11	8.8	0.00936	0.00003	0.00007	0.00000	0.00002	0.00000	0.00001	0.00000	0.00003	0.00000
Sample PV04d K-feldspar			$J: 0.00171020 \pm 0.000006801\sigma$			$D: 1.01008652 \pm 0.007338861\sigma$					
1	2.0	0.26654	0.00021	0.00261	0.00001	0.00014	0.00000	0.00001	0.00000	0.00021	0.00000
2	2.5	1.62138	0.00028	0.01979	0.00001	0.00037	0.00000	0.00003	0.00000	0.00010	0.00000
3	3.0	2.06512	0.00031	0.02511	0.00003	0.00049	0.00001	0.00002	0.00000	0.00010	0.00000
4	3.5	1.71118	0.00026	0.02088	0.00003	0.00036	0.00000	0.00003	0.00000	0.00006	0.00000
5	4.0	1.50488	0.00051	0.01816	0.00003	0.00031	0.00001	0.00002	0.00000	0.00005	0.00000
6	4.7	0.75567	0.00059	0.00920	0.00003	0.00019	0.00000	0.00003	0.00000	0.00006	0.00000
7	5.4	0.15211	0.00004	0.00190	0.00001	0.00003	0.00000	−0.00001	0.00000	0.00000	0.00000
8	6.1	0.02935	0.00004	0.00036	0.00001	0.00001	0.00000	−0.00001	0.00000	0.00001	0.00000
9	6.8	0.03350	0.00002	0.00038	0.00001	0.00001	0.00000	−0.00001	0.00000	0.00001	0.00000
10	7.5	0.03514	0.00005	0.00040	0.00000	−0.00001	0.00000	−0.00002	0.00000	−0.00001	0.00000
11	8.2	0.01418	0.00001	0.00016	0.00000	0.00001	0.00000	−0.00001	0.00000	0.00000	0.00000
12	9.0	0.02294	0.00002	0.00022	0.00001	0.00001	0.00000	−0.00002	0.00000	0.00000	0.00000
13	10.0	0.00515	0.00003	0.00004	0.00000	−0.00001	0.00000	0.00000	0.00000	0.00001	0.00000
Sample PV06d Whole rock			$J: 0.00163620 \pm 0.000006101\sigma$			$D: 1.01008652 \pm 0.007338861\sigma$					
1	2.0	0.90538	0.00014	0.01130	0.00002	0.00071	0.00000	0.00001	0.00000	0.00031	0.00000
2	2.5	1.10992	0.00031	0.01412	0.00001	0.00040	0.00001	0.00001	0.00000	0.00007	0.00000
3	3.0	0.43454	0.00012	0.00603	0.00001	0.00034	0.00000	0.00000	0.00000	0.00007	0.00000
4	3.5	0.09478	0.00006	0.00183	0.00002	0.00028	0.00000	0.00002	0.00000	0.00012	0.00000
5	4.0	0.05601	0.00003	0.00115	0.00001	0.00021	0.00000	0.00001	0.00000	0.00010	0.00000
6	4.5	0.01140	0.00002	0.00018	0.00000	0.00004	0.00000	0.00001	0.00000	0.00003	0.00000
7	5.0	0.00647	0.00002	0.00009	0.00000	0.00003	0.00000	−0.00001	0.00000	0.00001	0.00000
8	5.5	0.00487	0.00004	0.00007	0.00000	0.00002	0.00000	0.00001	0.00000	0.00001	0.00000
9	6.0	0.00240	0.00003	0.00002	0.00000	0.00002	0.00000	0.00000	0.00000	0.00001	0.00000
10	7.0	0.00506	0.00003	0.00006	0.00000	0.00001	0.00000	0.00000	0.00000	0.00001	0.00000
Sample PV09d Amphibole			$J: 0.00163050 \pm 0.000006001\sigma$			$D: 1.01008652 \pm 0.007338861\sigma$					

...continued

Step	Power	^{40}Ar (V)	1σ	^{39}Ar (V)	1σ	^{38}Ar (V)	1σ	^{37}Ar (V)	1σ	^{36}Ar (V)	1σ
1	2.5	0.46105	0.00037	0.00478	0.00001	0.00260	0.00001	0.00379	0.00001	0.00086	0.00000
2	3.0	0.71474	0.00040	0.00717	0.00003	0.00153	0.00001	0.00551	0.00001	0.00033	0.00000
3	3.5	0.84899	0.00026	0.00895	0.00001	0.00085	0.00001	0.00449	0.00001	0.00028	0.00000
4	4.0	0.66797	0.00015	0.00711	0.00002	0.00077	0.00000	0.00457	0.00001	0.00022	0.00000
5	4.5	0.10632	0.00006	0.00128	0.00002	0.00014	0.00000	0.00083	0.00001	0.00002	0.00000
6	5.0	0.06638	0.00004	0.00074	0.00000	0.00007	0.00000	0.00055	0.00001	0.00002	0.00000
7	5.5	0.06294	0.00003	0.00070	0.00001	0.00009	0.00000	0.00058	0.00000	0.00001	0.00000
8	6.0	0.06317	0.00008	0.00077	0.00001	0.00006	0.00000	0.00072	0.00001	0.00001	0.00000
9	7.0	0.09010	0.00003	0.00107	0.00001	0.00009	0.00000	0.00156	0.00001	0.00002	0.00000
10	8.8	0.04920	0.00002	0.00056	0.00000	0.00003	0.00000	0.00154	0.00001	0.00001	0.00000
11	10.0	0.01167	0.00002	0.00013	0.00000	0.00001	0.00000	0.00047	0.00000	0.00000	0.00000
Sample PV09d K-feldspar			$J : 0.00162630 \pm 0.000006101\sigma$			$D : 1.01008652 \pm 0.007338861\sigma$					
1	2.0	0.01458	0.00006	0.00014	0.00000	0.00034	0.00000	0.00040	0.00001	0.00001	0.00000
2	2.5	0.07824	0.00006	0.00088	0.00001	0.00006	0.00000	0.00298	0.00001	0.00001	0.00000
3	3.0	0.14569	0.00004	0.00169	0.00001	0.00002	0.00000	0.00566	0.00001	0.00001	0.00000
4	3.5	0.13117	0.00004	0.00158	0.00001	0.00003	0.00000	0.00524	0.00001	−0.00001	0.00000
5	4.0	0.06010	0.00005	0.00068	0.00001	0.00000	0.00000	0.00247	0.00001	0.00000	0.00000
6	4.7	0.08198	0.00004	0.00101	0.00001	0.00002	0.00000	0.00312	0.00001	0.00000	0.00000
7	5.4	0.05440	0.00003	0.00064	0.00000	0.00000	0.00000	0.00200	0.00001	0.00000	0.00000
8	6.1	0.06737	0.00004	0.00085	0.00001	0.00001	0.00000	0.00261	0.00002	0.00001	0.00000
9	6.8	0.00928	0.00003	0.00009	0.00000	0.00000	0.00000	0.00037	0.00000	0.00000	0.00000
10	7.5	0.02917	0.00005	0.00033	0.00000	0.00001	0.00000	0.00107	0.00001	0.00001	0.00000
11	8.2	0.01663	0.00003	0.00018	0.00000	0.00000	0.00000	0.00079	0.00001	0.00001	0.00000
12	9.0	0.01426	0.00002	0.00014	0.00001	−0.00001	0.00000	0.00045	0.00001	0.00000	0.00000
13	10.0	0.01406	0.00002	0.00017	0.00000	0.00001	0.00000	0.00054	0.00001	0.00001	0.00000
Sample PV30d Whole rock			$J : 0.00161780 \pm 0.000006001\sigma$			$D : 1.01008652 \pm 0.007338861\sigma$					
1	2.0	0.35720	0.00018	0.00289	0.00000	0.00125	0.00000	0.00000	0.00000	0.00089	0.00001
2	2.5	0.75115	0.00018	0.01195	0.00002	0.00082	0.00001	0.00002	0.00000	0.00063	0.00000
3	3.0	0.72568	0.00009	0.01277	0.00002	0.00056	0.00000	0.00001	0.00000	0.00028	0.00000
4	3.5	0.60574	0.00006	0.01087	0.00002	0.00048	0.00001	0.00001	0.00000	0.00021	0.00000
5	4.0	0.38897	0.00015	0.00631	0.00001	0.00060	0.00000	0.00001	0.00000	0.00031	0.00001
6	4.5	0.11331	0.00011	0.00144	0.00001	0.00029	0.00000	0.00001	0.00000	0.00017	0.00000
7	5.0	0.06742	0.00004	0.00090	0.00000	0.00019	0.00000	0.00003	0.00000	0.00012	0.00000
8	5.5	0.06531	0.00005	0.00080	0.00001	0.00019	0.00000	0.00002	0.00000	0.00010	0.00000
9	6.0	0.02156	0.00004	0.00025	0.00000	0.00006	0.00000	0.00001	0.00000	0.00004	0.00000
10	7.0	0.01274	0.00003	0.00012	0.00000	0.00005	0.00000	0.00000	0.00000	0.00002	0.00000
11	8.8	0.00955	0.00002	0.00008	0.00000	0.00003	0.00000	0.00001	0.00000	0.00002	0.00000
Sample PV40d Biotite			$J : 0.00162490 \pm 0.000006001\sigma$			$D : 1.01008652 \pm 0.007338861\sigma$					
1	2.0	0.00981	0.00002	0.00007	0.00000	0.00005	0.00000	0.00000	0.00000	0.00001	0.00000
2	2.5	0.01994	0.00002	0.00019	0.00000	0.00008	0.00000	−0.00001	0.00000	0.00000	0.00000

...continued

Step	Power	^{40}Ar (V)	1σ	^{39}Ar (V)	1σ	^{38}Ar (V)	1σ	^{37}Ar (V)	1σ	^{36}Ar (V)	1σ
3	3.0	0.03777	0.00003	0.00039	0.00000	0.00019	0.00000	−0.00001	0.00000	0.00001	0.00000
4	3.5	0.02032	0.00006	0.00023	0.00000	0.00009	0.00000	0.00000	0.00000	0.00000	0.00000
5	4.0	0.01177	0.00002	0.00011	0.00000	0.00004	0.00000	0.00000	0.00000	0.00001	0.00000
6	4.5	0.00571	0.00002	0.00007	0.00000	0.00003	0.00000	0.00001	0.00000	0.00001	0.00000
7	7.0	0.00040	0.00003	0.00001	0.00000	−0.00001	0.00000	0.00000	0.00000	0.00000	0.00000
8	8.8	0.00077	0.00002	0.00001	0.00000	0.00000	0.00000	−0.00001	0.00000	−0.00001	0.00000
Sample PV40d K-feldspar			$J : 0.00163050 \pm 0.000006101\sigma$			$D : 1.01008652 \pm 0.007338861\sigma$					
1	2.0	0.52736	0.00033	0.00519	0.00002	0.00018	0.00000	0.00002	0.00000	0.00027	0.00000
2	2.5	2.71297	0.00157	0.02975	0.00001	0.00060	0.00001	0.00016	0.00000	0.00020	0.00000
3	3.0	3.40006	0.00187	0.03725	0.00006	0.00064	0.00000	0.00019	0.00000	0.00016	0.00000
4	3.5	2.16914	0.00036	0.02370	0.00001	0.00038	0.00001	0.00010	0.00000	0.00009	0.00000
5	4.0	2.32901	0.00045	0.02540	0.00003	0.00037	0.00001	0.00012	0.00000	0.00008	0.00000
6	4.7	1.41561	0.01138	0.01538	0.00014	0.00022	0.00000	0.00006	0.00000	0.00003	0.00000
7	5.4	0.90801	0.00020	0.00996	0.00002	0.00017	0.00000	0.00006	0.00000	0.00003	0.00000
8	6.1	0.61680	0.00023	0.00678	0.00002	0.00010	0.00000	0.00003	0.00000	0.00003	0.00000
9	6.8	0.44921	0.00006	0.00498	0.00001	0.00009	0.00000	0.00003	0.00000	0.00002	0.00000
10	7.5	0.07927	0.00008	0.00087	0.00001	0.00001	0.00000	0.00000	0.00000	0.00001	0.00000
11	8.2	0.07917	0.00007	0.00085	0.00001	0.00001	0.00000	0.00000	0.00000	0.00001	0.00000
12	9.0	0.05552	0.00003	0.00060	0.00000	−0.00001	0.00000	0.00001	0.00000	0.00002	0.00000
13	10.0	0.01634	0.00002	0.00016	0.00001	−0.00002	0.00000	0.00000	0.00000	0.00000	0.00000
Second Sample Batch											
Sample PV01d-2 K-feldspar			$J : 0.00589250 \pm 0.000016901\sigma$			$D : 1.00764665 \pm 0.007199771\sigma$					
1	441	0.03571	0.00005	0.00067	0.00000	0.00005	0.00001	0.00002	0.00001	0.00007	0.00001
2	669	2.02954	0.00015	0.00964	0.00001	0.00147	0.00001	0.00009	0.00001	0.00617	0.00002
3	771	0.43790	0.00056	0.01400	0.00001	0.00022	0.00001	0.00003	0.00000	0.00027	0.00001
4	840	0.58962	0.00059	0.02222	0.00009	0.00031	0.00001	0.00005	0.00001	0.00008	0.00001
5	906	0.81152	0.00088	0.03038	0.00004	0.00038	0.00001	0.00010	0.00001	0.00011	0.00001
6	975	1.14570	0.00088	0.04380	0.00005	0.00056	0.00000	0.00013	0.00000	0.00008	0.00001
7	1034	1.11434	0.00112	0.04257	0.00011	0.00053	0.00001	0.00012	0.00001	0.00007	0.00001
8	1095	1.90114	0.00374	0.07407	0.00006	0.00102	0.00002	0.00022	0.00001	0.00009	0.00001
9	1153	4.23337	0.00303	0.16372	0.00017	0.00197	0.00002	0.00045	0.00001	0.00012	0.00001
10	1183	5.87338	0.00319	0.22716	0.00020	0.00289	0.00002	0.00057	0.00001	0.00012	0.00001
11	1211	4.70501	0.00732	0.17919	0.00015	0.00227	0.00002	0.00051	0.00001	0.00007	0.00001
12	1276	0.90226	0.00084	0.03399	0.00012	0.00040	0.00001	0.00008	0.00000	0.00003	0.00001
13	1331	0.10333	0.00008	0.00358	0.00001	0.00004	0.00001	0.00004	0.00001	0.00005	0.00001
Sample PV02d K-feldspar			$J : 0.00589980 \pm 0.000017201\sigma$			$D : 1.00764665 \pm 0.007199771\sigma$					
1	433	0.03819	0.00001	0.00105	0.00001	0.00006	0.00001	0.00005	0.00001	0.00010	0.00001
2	588	1.99890	0.00080	0.00632	0.00001	0.00145	0.00000	0.00007	0.00001	0.00646	0.00001
3	655	0.20380	0.00069	0.00655	0.00004	0.00012	0.00000	0.00003	0.00000	0.00018	0.00000
4	705	0.22100	0.00034	0.00812	0.00006	0.00016	0.00000	0.00004	0.00000	0.00008	0.00000

...continued

Step	Power	^{40}Ar (V)	1σ	^{39}Ar (V)	1σ	^{38}Ar (V)	1σ	^{37}Ar (V)	1σ	^{36}Ar (V)	1σ
5	779	0.50200	0.00109	0.01387	0.00003	0.00032	0.00001	0.00007	0.00001	0.00058	0.00001
6	836	0.44694	0.00050	0.01795	0.00004	0.00027	0.00000	0.00007	0.00001	0.00011	0.00000
7	896	1.08755	0.00107	0.04427	0.00009	0.00055	0.00001	0.00018	0.00001	0.00015	0.00000
8	964	1.51336	0.00101	0.06211	0.00007	0.00080	0.00001	0.00026	0.00001	0.00010	0.00001
9	1022	1.08740	0.00078	0.04422	0.00007	0.00054	0.00001	0.00018	0.00001	0.00008	0.00001
10	1084	1.46155	0.00070	0.05951	0.00010	0.00077	0.00001	0.00028	0.00000	0.00010	0.00001
11	1153	3.62786	0.00159	0.15089	0.00001	0.00183	0.00002	0.00067	0.00001	0.00003	0.00000
12	1211	6.08594	0.00576	0.25351	0.00107	0.00331	0.00005	0.00099	0.00001	0.00007	0.00001
13	1276	0.46253	0.00483	0.01903	0.00009	0.00024	0.00001	0.00003	0.00001	0.00004	0.00001
14	1331	0.07702	0.00013	0.00267	0.00001	0.00003	0.00001	−0.00003	0.00001	0.00003	0.00001
Sample RA03d Biotite			$J : 0.00596740 \pm 0.000019101\sigma$			$D : 1.00764665 \pm 0.007199771\sigma$					
1	428	0.43035	0.00019	0.01459	0.00001	0.00156	0.00001	0.00009	0.00001	0.00022	0.00001
2	483	0.26426	0.00013	0.00940	0.00003	0.00136	0.00001	0.00010	0.00000	0.00011	0.00000
3	521	0.25252	0.00010	0.00845	0.00002	0.00142	0.00001	0.00007	0.00000	0.00013	0.00000
4	591	2.50798	0.00018	0.01651	0.00002	0.00457	0.00001	0.00007	0.00000	0.00710	0.00000
5	641	0.80743	0.00072	0.02640	0.00002	0.00555	0.00002	0.00004	0.00000	0.00035	0.00000
6	689	1.32058	0.00057	0.04315	0.00006	0.00896	0.00002	0.00005	0.00000	0.00064	0.00000
7	732	1.23330	0.00158	0.03950	0.00008	0.00803	0.00002	0.00003	0.00000	0.00064	0.00000
8	786	0.78134	0.00007	0.02953	0.00002	0.00573	0.00002	0.00005	0.00000	0.00006	0.00000
9	818	0.53561	0.00066	0.02014	0.00003	0.00389	0.00001	0.00001	0.00000	0.00004	0.00000
10	847	0.50621	0.00012	0.01892	0.00003	0.00357	0.00001	0.00002	0.00000	0.00006	0.00000
11	900	0.66637	0.00004	0.02485	0.00002	0.00473	0.00001	0.00003	0.00000	0.00008	0.00000
12	929	0.53860	0.00014	0.02006	0.00003	0.00370	0.00001	0.00003	0.00000	0.00007	0.00000
13	976	0.62161	0.00010	0.02306	0.00008	0.00441	0.00001	0.00007	0.00000	0.00006	0.00000
14	1024	0.95634	0.00052	0.03635	0.00008	0.00700	0.00002	0.00010	0.00000	0.00008	0.00000
15	1104	2.02027	0.00438	0.07704	0.00016	0.01433	0.00002	0.00025	0.00001	0.00010	0.00000
16	1154	0.33753	0.00012	0.01223	0.00002	0.00224	0.00001	0.00024	0.00000	0.00006	0.00000
17	1199	0.02325	0.00006	0.00043	0.00000	0.00013	0.00000	0.00018	0.00000	0.00004	0.00000
18	1264	0.03232	0.00009	0.00051	0.00001	0.00007	0.00000	0.00006	0.00000	0.00005	0.00000

Table A.3 continued

$\%^{40}Ar^*$	$\%^{39}Ar(k)$	$^{40}Ar^*/^{39}Ar(k)$	1σ	Date	1.96σ	K/Ca	1.96σ	Δdays
First Sample Batch								
Sample CCH Whole rock								
83.58	5.30	84.05890	1.14495	229.97	5.76	39.32167	12.00566	63.559
92.69	21.71	91.48797	0.75696	248.95	3.77	77.51168	11.77107	63.578
95.80	26.40	87.16491	0.65676	237.93	3.29	79.49076	15.02772	63.598
96.99	24.85	86.73857	0.68414	236.84	3.43	56.95479	5.89426	63.638
92.16	14.94	76.36229	0.62104	210.09	3.16	28.75453	2.59340	63.658
69.56	2.83	50.37457	0.87161	141.31	4.61	16.00919	3.76670	63.677
52.31	1.21	43.52606	1.95732	122.74	10.46	7.74378	3.05879	63.717
49.36	1.62	36.79509	1.60640	104.29	8.67	5.99923	0.95214	63.737
62.96	0.53	54.37694	3.64053	152.08	19.14	10.14172	7.97129	63.756
78.04	0.39	56.44565	4.72257	157.61	24.75	9.44542	18.52277	63.796
4.82	0.22	6.32607	8.80265	18.37	49.84	2.63382	1.94468	63.815
Sample PV04d K-feldspar								
77.12	2.63	79.67439	0.95203	230.20	5.06	77.88490	25.68101	53.525
98.05	19.95	81.10021	0.59524	234.06	3.16	208.77102	25.78953	53.545
98.35	25.31	81.66435	0.60314	235.59	3.20	500.17347	111.16573	53.565
98.72	21.04	81.71299	0.60512	235.72	3.21	276.95223	61.55488	53.606
98.77	18.30	82.65725	0.62204	238.27	3.29	309.59541	87.77331	53.626
97.67	9.28	80.96119	0.66028	233.68	3.50	109.82510	22.08131	53.645
100.36	1.91	81.24790	0.71303	234.46	3.78	−52.19038	15.90985	53.686
93.92	0.37	76.46378	1.44115	221.47	7.70	−16.26797	8.01583	53.706
93.81	0.38	83.94059	2.12678	241.73	11.23	−13.51000	5.34622	53.726
107.96	0.41	95.02943	1.86802	271.37	9.71	−5.99746	1.49778	53.767
107.89	0.16	95.28725	2.25993	272.05	11.74	−4.13179	1.17556	53.787
101.07	0.23	104.45496	2.77365	296.19	14.21	−4.20800	1.32837	53.806
66.46	0.04	84.35928	14.80233	242.86	78.14	7.30694	21.49619	53.847
Sample PV06d Whole rock								
90.00	32.42	72.81672	0.59252	202.85	3.06	364.66856	238.80261	64.218
97.85	40.53	77.64074	0.57472	215.51	2.95	410.10936	241.83118	64.237
94.88	17.30	69.05585	0.53984	192.91	2.80	−583.26604	762.57505	64.256
63.35	5.25	33.11236	0.72140	95.08	3.95	29.50309	9.73770	64.296
47.41	3.31	23.27361	1.08304	67.35	6.03	27.83266	9.19026	64.315
16.70	0.52	10.68604	3.56046	31.24	20.22	4.01148	1.82784	64.335
64.28	0.26	47.18848	3.72197	134.03	19.97	−5.15644	2.06254	64.374
64.44	0.20	46.60702	8.69603	132.43	46.69	2.45914	0.62851	64.394
28.10	0.06	30.93682	26.48310	88.98	145.68	−2.12367	2.78296	64.412
37.47	0.17	32.46759	5.44008	93.28	29.85	8.52861	16.74197	64.452
Sample PV09d Amphibole								

...continued

$\%^{40}Ar^*$	$\%^{39}Ar(k)$	$^{40}Ar^*/^{39}Ar(k)$	1σ	Date	1.96σ	K/Ca	1.96σ	Δdays
46.31	14.36	45.29285	1.53576	128.40	8.24	0.42381	0.01893	56.615
86.61	21.56	87.46692	0.83003	240.25	4.18	0.43785	0.01982	56.635
90.49	26.93	86.90637	0.70025	238.81	3.53	0.66947	0.02996	56.675
90.71	21.39	86.30963	0.72014	237.27	3.64	0.52296	0.02349	56.695
95.94	3.84	81.01968	1.21733	223.59	6.19	0.51350	0.02669	56.715
92.67	2.23	84.21628	1.11425	231.87	5.64	0.45553	0.02299	56.756
94.57	2.10	86.42662	1.29239	237.57	6.52	0.40202	0.01984	56.775
93.72	2.32	77.86531	1.13901	215.39	5.82	0.35666	0.01805	56.794
94.17	3.21	80.44837	0.95177	222.11	4.85	0.22957	0.01118	56.835
97.08	1.67	87.04939	1.31923	239.18	6.65	0.12078	0.00557	56.855
93.42	0.39	84.10045	3.01040	231.57	15.25	0.09330	0.00610	56.874
Sample PV09d K-feldspar								
76.84	1.67	82.37851	4.70086	226.57	23.81	0.12739	0.00901	52.340
95.90	10.49	87.62645	1.07186	240.08	5.39	0.10634	0.00489	52.359
98.32	20.18	86.94751	0.84639	238.34	4.26	0.10788	0.00491	52.379
102.89	18.85	87.68007	0.82468	240.22	4.15	0.10872	0.00492	52.419
101.21	8.11	91.84758	1.15707	250.87	5.78	0.09936	0.00484	52.440
100.65	12.05	83.90356	1.14297	230.50	5.78	0.11669	0.00567	52.459
101.69	7.72	87.73406	0.84169	240.36	4.23	0.11649	0.00530	52.500
97.26	10.12	79.32227	1.03087	218.65	5.24	0.11682	0.00555	52.520
94.54	1.12	95.75893	6.64882	260.82	33.05	0.09167	0.00596	52.540
92.77	3.91	84.72522	2.18900	232.62	11.05	0.10998	0.00566	52.581
85.36	2.14	81.11874	3.83467	223.31	19.46	0.08173	0.00532	52.601
94.52	1.61	102.26921	6.39032	277.25	31.47	0.10781	0.01102	52.620
80.26	2.02	68.34150	2.49364	189.92	12.89	0.11290	0.00758	52.661
Sample PV30d Whole rock								
28.68	5.97	35.80578	2.61959	101.48	14.15	−211.18079	207.16996	63.889
75.82	24.70	48.13874	0.56409	135.15	2.99	151.79272	26.73764	63.908
88.60	26.39	50.85145	0.43001	142.47	2.27	466.18646	343.27438	63.928
89.94	22.48	50.58142	0.40924	141.74	2.16	396.85186	98.81680	63.967
76.64	13.04	47.71241	0.58343	133.99	3.09	167.34746	60.09780	63.987
57.24	2.97	45.54123	1.04610	128.11	5.57	69.91261	23.05273	64.006
47.43	1.86	35.95858	1.32991	101.90	7.18	8.44205	1.13372	64.047
54.11	1.65	44.71955	1.36116	125.87	7.25	11.62415	2.34034	64.066
43.91	0.52	38.24298	2.75297	108.18	14.81	5.59960	0.88985	64.085
45.81	0.24	49.95916	5.27158	140.06	27.87	17.16906	16.85257	64.126
51.81	0.17	59.50933	7.23492	165.64	37.71	3.05308	1.50888	64.145
Sample PV40d Biotite								
67.70	6.46	97.17070	9.52537	264.19	47.21	6.04004	8.89780	54.747
101.27	17.42	109.59677	2.48959	295.34	12.13	−4.65281	2.61786	54.767

...continued

$\%^{40}Ar^*$	$\%^{39}Ar(k)$	$^{40}Ar^*/^{39}Ar(k)$	1σ	Date	1.96σ	K/Ca	1.96σ	Δdays
95.27	36.52	93.14485	1.12195	253.98	5.59	−22.74907	22.31806	54.786
105.46	21.53	94.10250	1.67555	256.41	8.34	26.80721	35.05122	54.827
82.78	9.93	92.81246	5.80765	253.13	28.96	−12.35195	16.15562	54.847
59.64	6.46	49.87482	8.59164	140.43	45.61	3.01210	1.49181	54.867
241.26	0.66	140.67390	46.16385	370.97	215.65	−0.81485	1.08943	54.988
359.25	1.04	253.58579	57.51637	621.79	233.77	−0.29635	0.10449	55.008
Sample PV40d K-feldspar								
85.04	3.22	87.32976	0.83957	239.90	4.23	90.01086	17.27679	52.716
97.70	18.49	89.97462	0.65984	246.69	3.31	67.75066	3.90154	52.736
98.44	23.16	90.72358	0.67896	248.60	3.41	72.95795	3.58853	52.756
98.64	14.73	91.16094	0.66496	249.72	3.33	85.40736	7.63490	52.797
98.78	15.79	91.46463	0.67382	250.50	3.38	77.65519	5.15752	52.817
99.21	9.56	92.18200	1.29313	252.33	6.47	96.46661	10.80376	52.836
98.90	6.19	91.08008	0.68977	249.52	3.46	56.53071	4.27991	52.877
98.38	4.21	90.38030	0.70616	247.73	3.54	91.20385	7.77196	52.897
98.48	3.09	89.74568	0.70982	246.10	3.57	69.50829	10.92997	52.917
96.20	0.54	88.80722	1.71381	243.69	8.62	–	–	52.958
97.28	0.53	91.38390	1.09717	250.29	5.50	102.87970	134.51202	52.978
90.52	0.38	84.00758	1.29041	231.33	6.54	36.49460	23.90265	52.997
105.11	0.10	109.04368	5.07106	294.90	24.80	−28.80049	56.49129	53.038
Second Sample Batch								
Sample PV01d-2 K-feldspar								
46.43	0.08	24.81621	2.32302	245.94	42.18	4.4060	2.3638	98.829
11.92	1.14	25.26466	5.25285	250.09	95.16	14.9269	1.7052	98.844
81.99	1.66	25.82782	0.27739	255.29	5.01	61.0625	14.7545	98.860
95.87	2.63	25.61975	0.22774	253.37	4.12	59.2118	11.0673	98.876
95.94	3.60	25.80634	0.19998	255.09	3.61	42.8500	6.8527	98.892
97.98	5.18	25.80694	0.19085	255.10	3.45	50.3959	3.8633	98.908
98.00	5.04	25.83155	0.20336	255.32	3.67	51.4353	6.3535	98.924
98.55	8.77	25.47226	0.19132	252.01	3.46	49.2897	3.1172	98.940
99.09	19.38	25.80003	0.18752	255.03	3.39	52.0475	2.7855	98.956
99.28	26.88	25.84982	0.18674	255.49	3.37	56.8474	3.1689	98.972
99.49	21.21	26.30581	0.19412	259.69	3.50	50.4544	2.6046	98.988
98.81	4.02	26.41466	0.21577	260.69	3.89	58.0810	4.8193	99.003
84.78	0.42	24.61977	0.53759	244.12	9.77	11.9577	2.7763	99.019
Sample PV02d K-feldspar								
22.60	0.15	8.24128	1.84117	85.56	36.59	2.9238	0.6652	97.832
6.32	0.92	20.15341	8.36408	202.46	155.77	12.3699	1.7059	97.848
74.19	0.95	23.23652	0.35463	231.52	6.50	35.6291	10.4717	97.864
88.89	1.18	24.37450	0.28878	242.13	5.26	27.0735	4.9845	97.880

...continued

$\%^{40}Ar^*$	$\%^{39}Ar(k)$	$^{40}Ar^*/^{39}Ar(k)$	1σ	Date	1.96σ	K/Ca	1.96σ	Δdays
66.51	2.01	24.24684	0.44589	240.94	8.13	29.0672	6.6365	97.896
93.09	2.60	23.34479	0.19446	232.53	3.56	39.2902	10.4895	97.911
95.95	6.42	23.73675	0.18201	236.19	3.33	36.4689	2.8989	97.927
98.00	9.00	24.04484	0.17750	239.06	3.24	35.5651	2.2643	97.943
97.79	6.41	24.21652	0.18613	240.66	3.39	35.4085	4.4546	97.959
97.89	8.62	24.20912	0.18004	240.59	3.28	30.8072	1.6054	97.975
99.62	21.87	24.11885	0.17285	239.75	3.15	33.1314	1.6535	97.990
99.55	36.74	24.06597	0.20121	239.26	3.67	37.4534	1.7355	98.006
97.51	2.76	23.86305	0.33658	237.37	6.15	111.4205	52.6513	98.022
88.62	0.39	25.73171	0.79779	254.70	14.43	–	–	98.038
Sample RA03d Biotite								
84.83	3.46	25.19890	0.26163	252.44	4.79	33.2318	7.0497	83.856
88.18	2.23	24.97672	0.24673	250.36	4.53	17.8275	1.2958	83.874
84.54	2.01	25.44563	0.27023	254.75	4.94	24.3959	3.0516	83.894
18.02	3.92	27.55596	3.51218	274.34	63.57	42.5791	3.8277	83.912
87.35	6.27	26.90507	0.22407	268.32	4.07	115.9900	21.2868	83.932
85.96	10.25	26.49205	0.22766	264.49	4.14	163.5046	20.1777	83.951
84.88	9.38	26.68897	0.24221	266.32	4.40	254.3362	51.0962	83.970
97.64	7.01	26.01556	0.18837	260.06	3.44	121.3240	16.0878	83.989
97.57	4.78	26.13511	0.19556	261.17	3.57	388.6968	229.1930	84.008
96.69	4.49	26.05263	0.19448	260.41	3.55	228.1687	84.4519	84.027
96.46	5.90	26.04978	0.19286	260.38	3.52	145.2465	26.6569	84.046
96.35	4.76	26.05804	0.19738	260.46	3.60	124.7347	24.2887	84.065
96.87	5.48	26.29687	0.21407	262.68	3.90	65.3602	8.0768	84.084
97.47	8.63	25.82692	0.19533	258.30	3.57	72.9468	5.5070	84.103
98.49	18.29	26.01064	0.20295	260.01	3.70	60.3137	3.5858	84.122
94.94	2.90	26.38637	0.21749	263.51	3.96	9.6103	0.4500	84.142
50.29	0.10	27.55209	2.21522	274.31	40.10	0.4569	0.0239	84.160
56.97	0.12	36.22416	2.45179	352.67	42.49	1.7273	0.1965	84.180

...continued

$\%^{40}Ar^*$	$\%^{39}Ar(k)$	$^{40}Ar^*/^{39}Ar(k)$	1σ	Date	1.96σ	K/Ca	1.96σ	Δdays
First Sample Batch:				**Second Sample Batch**:				
Standard: Tinto biotite, Date: 410.3 ± 0 (1σ)				Standard: Tinto biotite, Date: 410.3 ± 0 (1σ)				
($^{40}Ar/^{39}Ar$)k: 0.16770557 ± 0.0051266 (1σ)				($^{40}Ar/^{39}Ar$)k: 0.02787779 ± 0.00036379 (1σ)				
($^{38}Ar/^{39}Ar$)k: 0.01351957 ± 0.00012302 (1σ)				($^{38}Ar/^{39}Ar$)k: 0.01275115 ± 4.401e^{-05} (1σ)				
($^{37}Ar/^{39}Ar$)k: 5.266e^{-05} ± 2.48e^{-06} (1σ)				($^{37}Ar/^{39}Ar$)k: 4.138E-05 ± 2.07e^{-06} (1σ)				
($^{39}Ar/^{37}Ar$)Ca: 0.00152792 ± 4.457e^{-05} (1σ)				($^{39}Ar/^{37}Ar$)Ca: 0.00073592 ± 5.1e^{-06} (1σ)				
($^{38}Ar/^{37}Ar$)Ca: 0.20808278 ± 0.00439516 (1σ)				($^{38}Ar/^{37}Ar$)Ca: 0.00448043 ± 2.32e^{-05} (1σ)				
($^{36}Ar/^{39}Ar$)Ca: 0.00027791 ± 2.09e^{-05} (1σ)				($^{36}Ar/^{39}Ar$)Ca: 0.00015769 ± 4.48e^{-06} (1σ)				
($^{36}Cl/^{38}Cl$)k: 316 ± 0.0003 (1σ)				($^{36}Cl/^{38}Cl$)k: 316 ± 0.0003 (1σ)				
$^{40}Ar\lambda$: 5.5492e^{-10} ± 9.3e^{-13} (1σ)/a				$^{40}Ar\lambda$: 5.5492E-10 ± 9.3e^{-13} (1σ)/a				
$^{39}Ar\lambda$: 2.94e^{-07} ± 1.64052e^{-09} (1σ)/d				$^{39}Ar\lambda$: 2.94E-07 ± 1.64052e^{-09} (1σ)/d				
$^{37}Ar\lambda$: 0.000823 ± 1.118e^{-07} (1σ)/d				$^{37}Ar\lambda$: 0.000823 ± 1.118e^{-07} (1σ)/d				
D: Mass discrimination per AMU based on power law				D: Mass discrimination per AMU based on power law				
Δ days: time between end of irradation and analysis				Δ days: time between end of irradation and analysis				

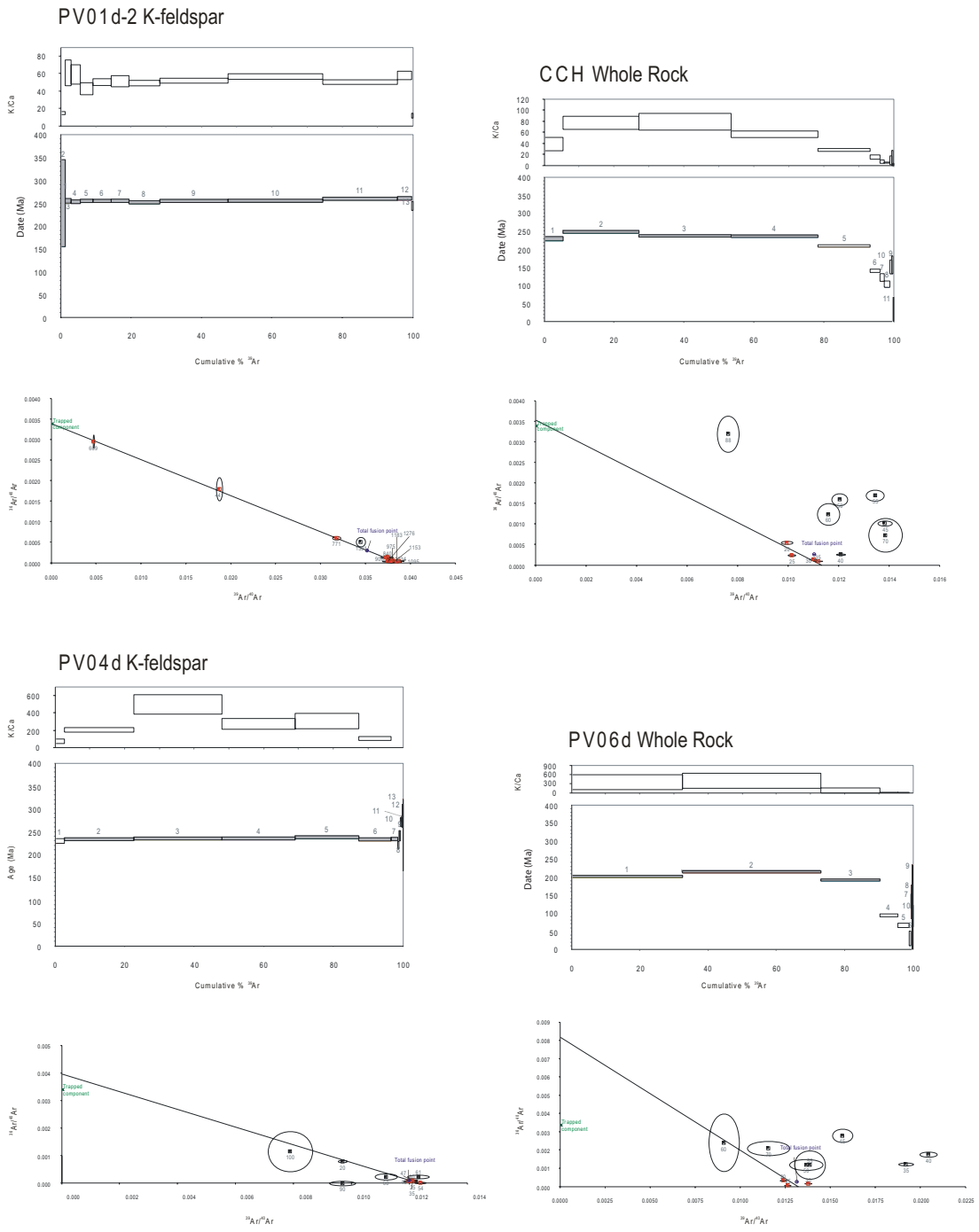

Figure A.2: Complete ^{40}Ar-^{39}Ar geochronology results from the San Rafael Block. Uppermost panels show K-Ca ratios as a function of released ^{39}Ar during stepwise heating (bars are plotted at 2σ error). Middle panels show the calculated date as a function of released ^{39}Ar during stepwise heating (bars are plotted at 2σ error). The numbers represent the heating step; the filled bars were used in the calculation of the plateau date. Lower panels show inverse isochron diagrams. Red symbols indicate the steps used in the inverse isochron calculation.

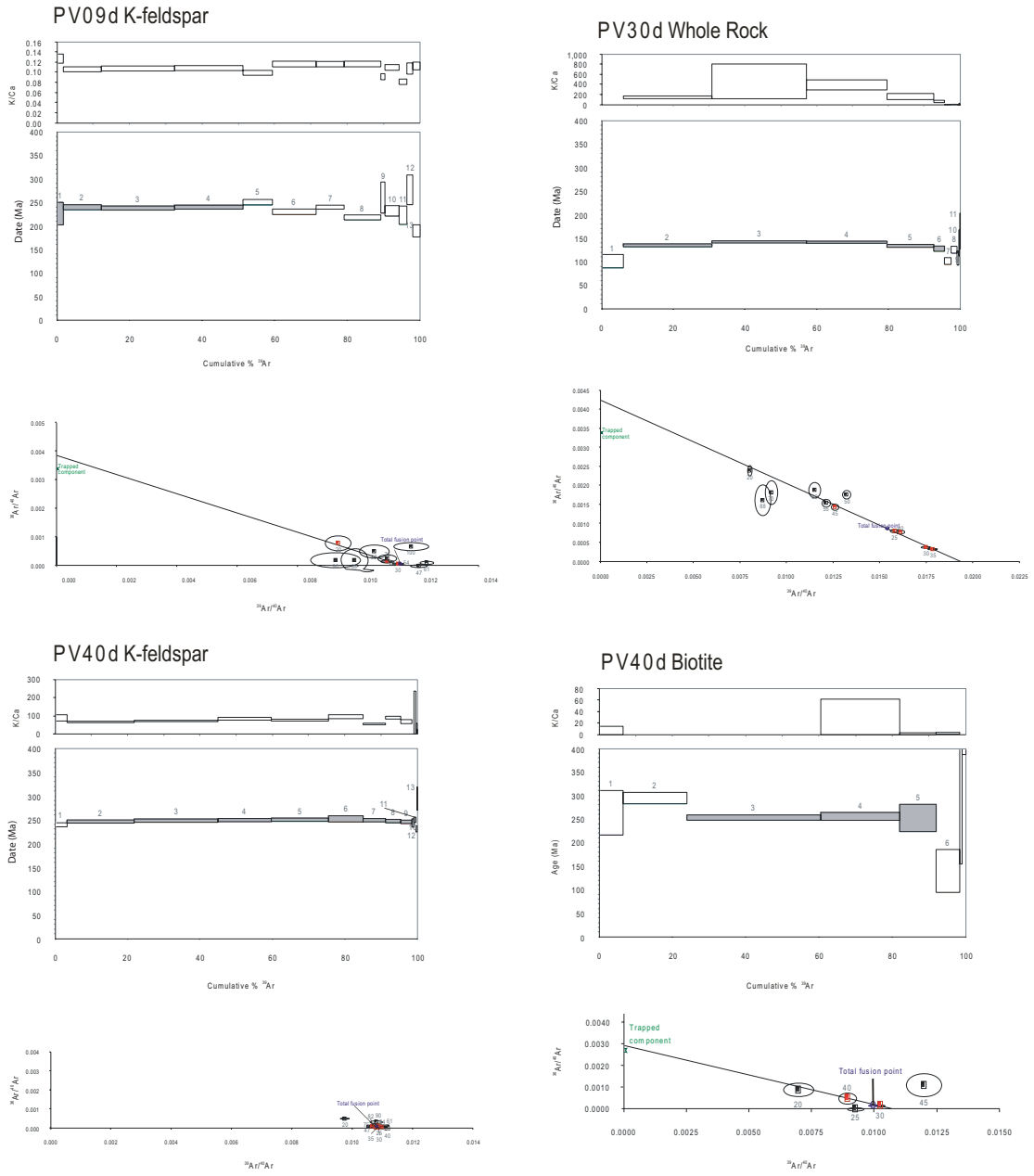

Figure A.3: Complete ^{40}Ar-^{39}Ar geochronology results (continued). Uppermost panels show K-Ca ratios as a function of released ^{39}Ar during stepwise heating (bars are plotted at 2σ error). Middle panels show the calculated date as a function of released ^{39}Ar during stepwise heating (bars are plotted at 2σ error). The numbers represent the heating step; the filled bars were used in the calculation of the plateau date. Lower panels show inverse isochron diagrams. Red symbols indicate the steps used in the inverse isochron calculation.

APPENDIX B

Descriptions of sampling sites and AMS interpretation of structural observations

Refer to Figs. 3.1 and 3.3 for the locations of the places and sites described below.

B.1 Cuesta de los Terneros

This area includes exposures of Puesto Viejo Gr. and Upper Choiyoi Gr. volcanic and sedimentary rocks. The Puesto Viejo Gr. is restricted to a narrow plateau at the southern end of the area (along route 144), where sites PV03–04, and PV20–26 were collected (Fig. B.1a). As described in the main text, these sites were collected along the eastern flank of the plateau, where it dips ∼22° to the west (Fig. B.1b). The AMS of these sites suggest the dip is secondary. The base of the Puesto Viejo sequence is marked by a thick basal conglomerate, which is cross-cut by normal faults. The orientation of the conglomerate is different than that of the sampled volcanic rocks above, and a steep normal fault may lie between them. The sequence between the conglomerate and the volcanic rocks is unfortunately concealed by talus and regolith.

The Puesto Viejo Gr. rocks lie unconformably on Upper Choiyoi Gr. volcanic rocks (mostly ignimbrites), which are exposed to the east and northeast of the Puesto Viejo Gr. plateau (Fig. B.1a). Bedding contacts indicate that sites CT02, 03, 05, 06, 07, 09, 10, 12, 13, 14, and 18 dip ∼15–20° to the SSE-SSW. The stratigraphically younger

sites (in the southern end of the area) generally exhibit an AMS with a sub-vertical K_{min} that is substantially steeper than the pole to the bedding plane (Fig. B.2a), suggesting that the dip pre-dates these volcanic rocks. The southernmost site, CT13, lies at the eastern base of the Puesto Viejo Gr. plateau, directly beneath the basal conglomerate. The dip of site CT13 is directed slightly more to the west than the other CT sites, perhaps due to the inferred normal fault that tilted the adjacent Puesto Viejo Gr. rocks. However, the pure west component of the resolved CT13 dip is only $\sim 5^\circ$ (whereas the Puesto Viejo Gr. rocks exhibited a dip of 22°). The CT13 AMS shows a sub-vertical K_{min} (steeper than the clearly tilted K_{min} of the Puesto Viejo Gr. rocks), and a magnetic lineation parallel to the dip; we therefore interpret the dip of this site to be primary.

Sites lower in the stratigraphic sequence (CT14 and CT18) exhibit AMS with prolate tendencies, in contrast to the oblate tendencies observed in the stratigraphically higher sites (Fig. C.2a). In the AMS of site CT14, the distribution of sample-level K_{min} and K_{int} estimates form a girdle perpendicular to the near-horizontal magnetic lineation (Fig. B.2b). Such a distribution is often associated with deformation, where the magnetic lineation is developed perpendicular to the principal regional stress (σ_1). This would imply that the lowest stratigraphic sites have experienced deformation that waned prior to emplacement of the stratigraphically higher sites. This interpretation is compatible with the timing of regional deformation; a waning San Rafael Orogenic Phase (SROP) is known to affect the Agua de los Burros Fm., but compressive deformation is not recognized in the younger Quebrada del Pimiento Fm. (Kleiman and Japas, 2009). Specifically, Kleiman and Japas (2009) have recognized a growth fold in the Agua de los Burros Fm. in Cuesta de los Terneros, implying that the nature of the bedding attitudes could be age-dependent (i.e. secondary in

the older rocks and primary in the younger rocks).

The stratigraphic relationship between CT02–03 and CT14 is not entirely clear, but the former may belong to the Cerro Carrizalito Fm., which is known to unconformably overlie the Agua de los Burros Fm. Flow contacts indicate that both sites (CT02–03) dip 20° to the SSW, as observed in the other CT sites. CT02 is a basal vitrophyre and its AMS is highly scattered. The AMS of overlying site CT03 is well-organized and consistent with deposition on a primary slope; a highly developed lineation is parallel to the dip (and roughly orthogonal to the inferred orientation of σ_1), and K_{min} and K_{int} are also well-defined (Fig. B.2c). Site CT04 was collected from a slumped block and a lack of bedding indicators prevent its restoration. Its scattered AMS similarly precludes restoration.

Sites CT15–17 were collected from tuffs of the Agua de los Burros Fm. that are locally structurally perturbed by an andesitic laccolith of the Quebrada del Pimiento Fm. The AMS of the tuff samples is poorly defined.

Sites PV38–39 were collected from a Puesto Viejo Gr. ignimbrite ∼8 km to the ESE of the Puesto Viejo Gr. plateau in Cuesta de los Terneros. This ignimbrite is separated from other Puesto Viejo Gr. rocks by exposures of Upper Choiyoi Gr. rocks and Neogene sedimentary rocks. Field observations suggest that the ignimbrite is dipping 15° to the SE, but the AMS of the ignimbrite reveals a well-defined magnetic foliation with a sub-vertical K_{min} (Fig. B.2d) that implies that no substantial post-emplacement tilting has affected this ignimbrite.

B.2 Atuel River area

Route 173 follows the Atuel River where it cuts through the Puesto Viejo Gr., exposing a thick sequence of volcaniclastic and sedimentary rocks, tuffs, and a promi-

nent ignimbrite. Sites PV15–19 and PV32–37 were collected from intercalated beds of red volcaniclastic rocks and white bands of unwelded tuff. The AMS of site PV15 (unwelded tuff) and sites PV16–18 (volcaniclastic rocks) is highly similar, characterized by a very weak magnetic foliation with a vertical pole (K_{min}) (Fig. B2e). This horizontal foliation implies that the sequence has not been substantially tilted since deposition, in agreement with the field observations that suggest that the beds are dipping $\leq 5°$.

Sites PV32–37 are ∼0.8 km WSW from, and stratigraphically above, sites PV15–19. The PV32–37 sampling profile roughly parallels the SW scarp of the basin bounding normal fault, and the beds exhibit a dip of 10° to the WNW. The AMS of the volcaniclastic rocks (PV33–36) and the tuffs (PV37) is again highly similar, showing an oblate shape with a K_{min} parallel to the pole of the bedding plane. A subsidiary lineation directed to the NNW may be related to the direction of primary flow, but it is not parallel to the current bedding dip. The AMS of the basal site, PV32, is dominated by this magnetic lineation (Fig. C.2a). We assume that the dominant magnetic foliation (in PV33–37) and the bedding normal K_{min} are features of deposition on a near-horizontal surface, and interpret the current bedding attitude to be secondary, likely due to displacement on the adjacent fault. Sites PV06–07 were collected near the sampling profile of sites PV32–37, from different horizons within a ∼10 m thick ignimbrite. Although AMS measurements were not made on the PV06–07 samples, the structural attitude of the ignimbrite clearly changes as it approaches the basin bounding fault, and we therefore assume its bedding orientation is secondary.

On the other (footwall) side of the fault, volcanic rocks of the Upper Choiyoi Gr. are exposed. Sites RA20–21 were collected from ignimbrites with prominent

fiamme that suggested the units were dipping 15° to the NE. The AMS of site RA20 yields an ambiguous result: a well-developed K_{min} is normal to the bedding plane inferred from fiamme orientations, but a statistically distinct (95% conf.) magnetic lineation is sub-parallel to the dip of the bedding. According to our simple model, this could either be due to deposition on a primary slope (where grain imbrication did not develop) or secondary tilting along a plane that coincides (by chance) with the orientation of the magnetic lineation (i.e. the lineation may have developed by primary flow that was unrelated to the current structure). Given the angle of dip (15°), and the proximity of these sites to a major normal fault–known to be active since deposition of the Upper Choiyoi Gr.-we assume their dip is secondary.

Sites RA08–09 were collected from an Upper Choiyoi Gr. ignimbrite located ∼4 km to the north of sites RA20–21. The stratigraphic relationship between these pairs of sites is not well established, but the RA08–09 ignimbrite has previously been assigned to the Cerro Carrizalito Fm. The RA08–09 ignimbrite exhibits a dip of 16° to the SSE, determined from flow contacts. The AMS of this ignimbrite exhibits no evidence of this structural orientation, rather showing a well-developed foliation with a vertical K_{min}. We interpret this to be a primary emplacement and compaction fabric, which implies that the bedding orientation is primary. It is interesting to note that this bedding orientation is identical to that observed in the Upper Choiyoi Gr. volcanic rocks to the northwest in Cuesta de los Terneros, and so may be related to a broad structure.

B.3 Valle Grande area

Another exposure of Puesto Viejo Gr. rocks can be found along route 173 near the Valle Grande Dam, ∼10 km to the southwest of the Puesto Viejo sequence

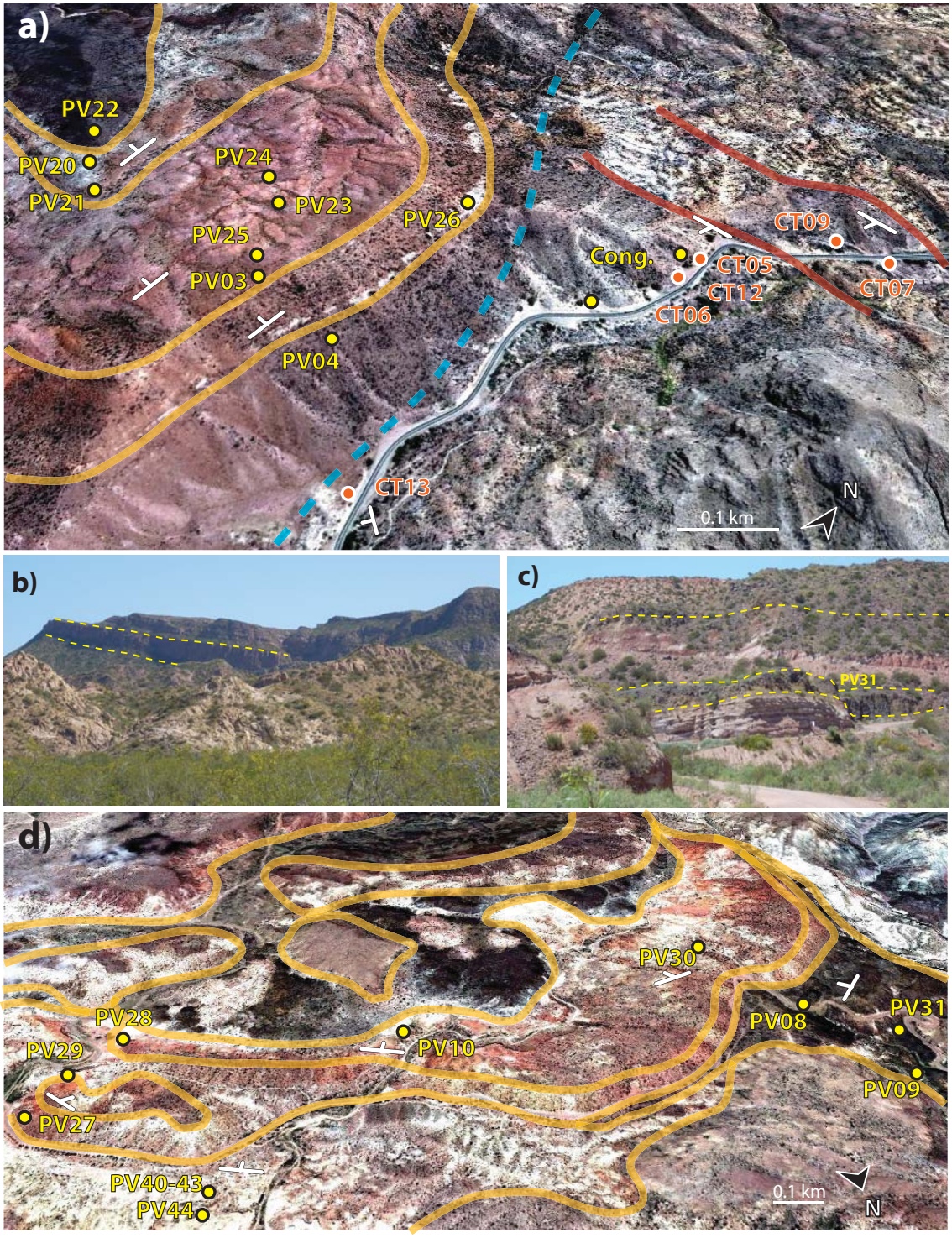

Figure B.1: Satellite imagery and photographs of San Rafael Block sampling areas. (a) Satellite imagery of part of the Cuesta de los Terneros area. Yellow (Red) sites and contacts belong to the Puesto Viejo Gr. (Upper Choiyoi Gr.). The blue dashed line is an inferred normal fault. (b) Field photograph showing the apparent dip (view is to the SE) of the Puesto Viejo Gr. sequence in Cuesta de los Terneros. (c) Field photograph showing the local dip of site PV31 (view is to the SSE). (d) Satellite imagery of part of the Valle Grande area.

described in the previous section. The stratigraphic relationship of the two sequences is obscured by Neogene sedimentary rocks. In the Valle Grande area, the Puesto Viejo Gr. is represented by a repeating sequence of sedimentary rocks, intercalated volcaniclastic rocks and unwelded tuffs, ignimbrites, and basalts (Fig. B.1d). Along the northern end of the exposure, the rocks exhibit a shallow dip ($\sim$5°) to the SSE-SSW. The specific direction of dip changes systematically from SSE in the west to SSW in the east, revealing a half-bowl-like structure. Similarly, the bedding contacts follow an arcuate form in map-view, convex away from the basin center.

Sites PV27 and PV40–44 were collected from medium-grained volcaniclastic rocks at the base of the sequence. The AMS of PV40–44 is highly similar, and shows a triaxial shape with a statistically distinct (95% conf.) and very well-defined magnetic lineation directed parallel to the dip (Fig. B.2f). These sites come from different stratigraphic horizons, separated by bands of unwelded tuff, and the lateral sampling profile spans $\sim$200 m. Due to this separation in time and space, the very well-organized triaxial AMS amongst the sites points to a well-developed and consistently-directed fluvial process. If the flow at the base of the Puesto Viejo Gr. sequence was consistently well-organized, and parallel to the modern bedding dip, it would imply that at least some component of the modern gradient was present at the time of deposition. Given that the modern dip is already shallow (7°), no substantial tilting/subsidence is likely to have occurred since the deposition of these rocks.

Sites PV08, 09, and 31 have been collected from a sequence of basalts that are $\sim$1.5 km west of sites PV40–44; the basalts are either stratigraphically above or temporally equivalent to the volcaniclastic sites. Sites PV08 and 09 exhibit shallow dips ($\leq$ 5°) to the SE. PV31 comes from a small fault block that is locally steeply dipping (20°) to the east (Fig. B.1c). The AMS of basalt is not expected to reflect

the same sedimentary-type (gravitational) settling and compaction fabrics commonly observed in ignimbrites. However, the K_{min} of PV09 is sub-vertical, whereas the poorly defined K_{min} of PV31 is oriented sub-parallel to the pole of the east-dipping bedding plane. In PV09, where the AMS exhibits a prolate tendency (Fig. C.2a), the magnetic lineation is directed to the SE, parallel to the direction of dip.

Stratigraphically above the basalts, sites PV10 and PV28–30 were collected from a thick ignimbrite, but across a strike-parallel profile ∼1.7 km long. The western-most site (PV30) exhibits a shallow dip ($\leq 5°$) to the SSE, the central site (PV10) a shallow dip to the SSW, and the eastern-most site (PV29) a $\leq 5°$ dip to the SW. Site PV28 was collected only ∼150 m from site PV29, but the two sites are separated by a local fault, and PV28 exhibits a relatively steeper dip of 25° to the SW. The AMS of these sites is highly scattered and cannot be used to infer the nature of the structural attitudes. Considering the strong, dip-parallel magnetic lineations observed in the volcaniclastic rocks at the base of the sequence, and the dip parallel K_{max} direction of site PV09, we interpret the shallow dip of the entire sequence to be effectively primary.

To the west of these sites, route 173 follows the Atuel River stratigraphically down-section and through the Upper Choiyoi Gr. Near the top of this sequence, sites RA03–05 and RA11–19 were collected from a homocline of ignimbrites and volcanic breccias, dipping 13° to the SE. As described in the main text, the AMS of sites RA13–19 is very consistent and suggests that the slope of the homocline predates the sampled volcanic rocks. In sites RA11–12, magnetic susceptibility is nearly isotropic and cannot be used to evaluate structural observations. In sites RA03-05, AMS was not measured. However, sites RA03–05 and RA11–12 lie between sites RA18–19 and RA13–17, so we adopt the same structural interpretations.

Sites RA01–02, and RA10 are located stratigraphically beneath, and ∼4 km to the SW of, RA18–19. Sites RA01–02 dip 8° to the NE; AMS measurements were not made on samples from these sites, and the dip is assumed to be secondary. Site RA10 is adjacent to a major fault, and despite being only ∼300 m from site RA02, exhibits a distinctly steeper dip of 17°, directed NE. The AMS of site RA10 shows a magnetic foliation with a pole normal to the bedding plane, implying that the dip is secondary.

Between the exposures of the Puesto Viejo Gr. in the Atuel River area and the Valle Grande area, two ignimbrites of the Upper Choiyoi Gr. were sampled (RA06–07). The stratigraphic relationship between sites RA06–07 and the other Upper Choiyoi Gr. sites is not known. Fiamme orientations indicate that RA06–07 are dipping 15° to the ESE. The AMS of these sites is characterized by a magnetic foliation parallel to the bedding plane. The coincidence of K_{min} and the bedding plane pole, and the lack of a well-developed magnetic lineation imply that the observed bedding attitude is a secondary structure. These sites are < 1 km from a major fault that cross cuts Upper Choiyoi Gr. rocks, and they may have been structurally perturbed by displacement upon it.

B.4 Old Puesto area

To the east of the Valle Grande area, sites PV02 and PV11–14 were collected from a sequence of Pueso Viejo Gr. volcanic and sedimentary rocks that lie in the same NNW-SSE trending basin as the Puesto Viejo Gr. sites collected in the Atuel River area. Sites PV02 and PV11 were collected from ignimbrites that lie just above a major basin bounding normal fault that locally strikes NW-SE. The ignimbrites exhibit a dip of ∼40° to the NE. Conformably above these ignimbrites, a poorly sorted

conglomerate is followed by a sequence of unwelded tuffs (PV12–13) intercalated with sedimentary rocks; these beds exhibit the same structural orientation as the ignimbrites beneath them. Above the tuffs, a conformable breccia is followed by an unconformable rhyolitic ignimbrite that appears to be oriented near-horizontally. The AMS of sites PV02 and PV11 indicates that the dip is secondary, as could be deduced by its high angle. The magnetic foliation is dominant and the K_{min} is normal to the bedding plane (i.e. inclined $\sim$40° from the vertical) (Fig. B.2g). The AMS of PV14 is also characterized by an oblate tendency, but K_{min} is oriented sub-vertically, corroborating the structural contrast discerned in the field (Fig. B.2h). We therefore infer that sites PV02 and PV11–13 were tilted after they were emplaced, likely due to displacement on the adjacent fault, and site PV14 was emplaced after tilting (faulting) ceased.

B.5 Rio Seco los Leones

70 km to the south of San Rafael, a sequence of ignimbrites, volcanic breccias, and intermediate intrusive rocks and lavas is exposed in an arroyo. Sites SL01–04 (ignimbrites) and SL05 (volcanic breccia) were collected from units that stratigraphically overlie the intermediate rocks. Following the assignment of the intermediate rocks to the Quebrada del Pimiento Fm., the sampled sites could belong to the Cerro Carrizalito Fm., as they have been previously assigned. The northernmost site, SL02, exhibits a dip of 20° to the WNW, whereas the other sites exhibit a similar dip to the SW-WSW. To the north of site SL02, the dip of the volcanic rocks is directed to the NW-NNW. This change in dip orientation is reflected by an arcuate ridge formed by the resistant ignimbrites. This arcuate structural form could be the remnant of a partly-dissected volcanic edifice. The AMS of sites SL01 and SL02 is

weak and poorly defined, and cannot be used to evaluate the local structure. Site SL03 shows a more well-defined triaxial AMS ellipsoid with an oblate tendency. The orientation of K_{min} is similar to the pole to the bedding plane, but is more inclined from the vertical. K_{max} is not statistically distinct (95% conf.), but appears to be well-clustered in a direction sub-parallel to the dip. The AMS of site SL04 is also weak, but notably exhibits a K_{min} that is sub-vertical, belying any substantial post-emplacement tilting. Given the structural form and the AMS results, we infer that the dip of these units is primary. Following the assumption that these units belong to the Cerro Carrizalito Fm., they should post-date SROP deformation.

References

Kleiman, L. E., & Japas, M. S. (2009) The Choiyoi volcanic province at 34°S-36° S (San Rafael, Mendoza, Argentina): implications for the late Palaeozoic evolution of the southwestern margin of Gondwana. *Tectonophysics*, 473, 283-299.

Figure B.2: Additional examples of anisotropy of magnetic susceptibility (AMS) data from the San Rafael Block. Results are presented in geographic coordinates. All symbols are projections onto the lower hemisphere. The left panels show the raw sample-level data. The center panels show 1000 bootstrapped eigenvectors (Constable and Tauxe, 1990) of the raw data. The gray lines depict the bedding attitude of the sites, as estimated from field-observations; the darker (lighter) line is a projection onto the lower (upper) hemisphere. The right panels show the relative eigenvalues (as cumulative distribution functions) associated with the eigenvectors: red = maximum (τ_{max}), blue = intermediate (τ_{int}), black = minimum (τ_{min}). The vertical dashed lines are the 95% confidence bounds on the eigenvalue estimates.

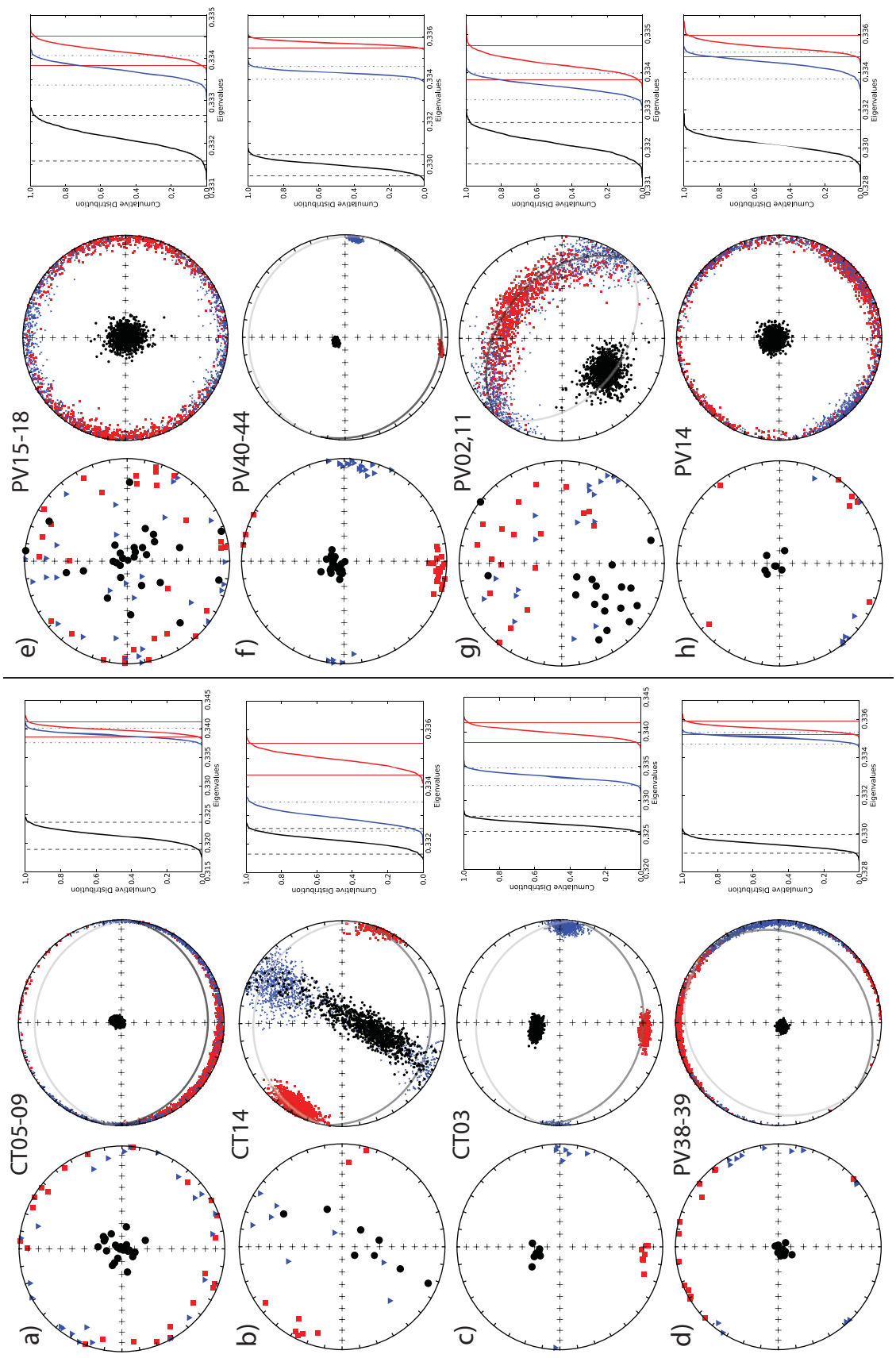
a)
CT05-09
b)
CT14
c)
CT03
d)
PV38-39
e)
PV15-18
f)
PV40-44
g)
PV02,11
h)
PV14
Cumulative Distribution
Eigenvalues

APPENDIX C

Supplementary magnetic fabric data

C.1 Anisotropy of Anhysteretic Remnant Magnetization (AARM)

AARM reveals the anisotropy of the low-coercivity minerals that are capable of maintaining a remanence. According to our rock-magnetic results, magnetite is the only significant low-coercivity magnetic phase present in the samples selected for AARM measurements. Importantly, AARM measurements on single-domain (SD) magnetite will not be subject to the so-called "inverse-effect" that is expected to affect AMS measurements on SD magnetite (Jackson, 1991). SD magnetite grains are magnetized along their long-axis, so they will yield a susceptibility of zero along this axis, and a maximum perpendicular to it. This results in an inversion in the simple relationship that is commonly assumed between AMS and grain orientation, where K_{max} is parallel to the long axis of the grain, and K_{min} is parallel to the short axis. The presence of SD grains can therefore compromise the physical interpretation of AMS, unless their contribution is recognized. AARM may therefore act as a more reliable proxy for the mean orientation of inequant magnetite grains, as well as a means to detect the presence of a significant SD grain population.

In sites PV20–24, PV38–39, and RA19 the AARM (Figs. C.1a–d) and AMS results exhibit very similar eigenvector orientations and relative eigenvalue distributions,

suggesting that SD grains do not significantly contribute to the AMS. The AARM of sites PV22 and PV28 is weak and poorly defined, as is the AMS of these sites.

C.2 Anisotropy of Thermal Remnant Mangetization (ATRM)

ATRM expresses the integrative anisotropy of all materials capable of carrying a remanence. These results differ from AMS in that they do not include contributions from diamagnetic or paramagnetic sources, and they differ from AARM in that high-coercivity magnetic phases also participate (assuming the Curie/Néel temperatures of all magnetic phases are exceeded during initial heating). Because hematite typically contributes more strongly to the total remanence of a sample than it does to its bulk susceptibility, ATRM may amplify the hematite sub-fabric, relative to its contribution to the AMS.

The ATRM of sites PV20–24 (Fig. C.1e) and PV38–39 (Fig. C.1g), which possess a negligible quantity of hematite according to the rock-magnetic experiments, is comparable to their corresponding AMS and AARM. In the hematite-dominated volcaniclastic rock samples from sites PV40–44 (Fig. C.1f) and RA19 (Fig. C.1h) the ATRM lacks the pronounced lineations evident in the corresponding AARM and AMS. This could be due to the enhancement of the hematite contribution relative to the magnetite signal; a weaker hematite lineation can be attributed to relatively ineffectual shape-effects, as the anisotropy of hematite is typically controlled by magnetocrystalline energy (Jackson, 1991). In RA19, the orientation of K_{min} is also more vertical than in the AMS or AARM, which may signify subtle differences in the orientation of the hematite and magnetite sub-fabrics. Interestingly, such a near-horizontal magnetic foliation in hematite would further validate our interpretation that the dip of site RA19 (and the neighboring sites) is primary.

C.3 Anisotropy of High-Field Magnetic Susceptibility (HF-AMS)

HF-AMS measurements were conducted to isolate paramagnetic + diamagnetic sub-fabrics. Because magnetite is saturated in the high-fields used in this technique, it does not yield an orientation-dependent signal, and its contribution can be easily subtracted. To extract the high-field contribution of hematite, the non-linear component of the high-field slope was removed according to the technique of Jackson and Solheid (2010). Unfortunately, as discussed in Jackson and Solheid (2010), this calculation is ill-conditioned, and a residual hematite signal almost invariably remains after the non-linear correction is applied, even in sites where the quantity of hematite appeared negligible according to the rock magnetic results. Because the linear parameters in this calculation are better determined, it appears that the most non-linear results are the least well corrected. As the hematite "hard" direction saturates last, the high-field slope associated with this orientation is the most non-linear. Consequently, the non-linear corrections typically yield an apparent inverse hematite fabric, where K_{max} is parallel to the hematite hard direction.

With this understanding, it is evident that samples from sites PV20–24 exhibit a HF-AMS (Fig. C.1i) comparable to the previously determined fabrics; the K_{max} of the HF-AMS broadly coincides with the K_{min} of the other anisotropy ellipsoids. Site PV03 has a smaller quantity of hematite than PV20–24 (but is from the same locality) and exhibits a HF-AMS (Fig. C.1j) where K_{int} corresponds to the K_{min} of the AMS/AARM ellipsoids. We interpret this result to be the mixing of the inverse (but now less dominant) hematite fabric and a normal paramagnetic + diamagnetic fabric that is similarly oriented. This could imply that the magnetite and hematite fabrics are broadly representative of the bulk petrofabric. Samples from sites PV38–

39 also exhibit a HF-AMS (Fig. C.1k) that is similar to the other magnetic fabrics isolated from these sites. The sample-level HF-AMS K_{min} axes are distributed in the horizontal plane, as the K_{max} axes are in the AMS/AARM results. The HF-AMS of site RA19 (Fig. C.1l) differs from the corresponding AMS in that the HF-AMS K_{max} is further inclined from the pole to the structural plane, relative to the AMS K_{min}. This is similar to the difference between the AMS and ATRM results, as discussed above, and may again highlight a minor difference in the orientation of the magnetite and hematite sub-fabrics in this site.

References

Jackson, M. (1991) Anisotropy of magnetic remanence: a brief review of mineralogical sources, physical origins, and geological applications, and comparison with susceptibility anisotropy. *Pure and Applied Geophysics*, 136, 1-28.

Jackson, M., & Solheid, P. (2010) On the quantitative analysis and evaluation of magnetic hysteresis data. *Geochemistry, Geophysics, Geosystems*, 11, Q04Z15.

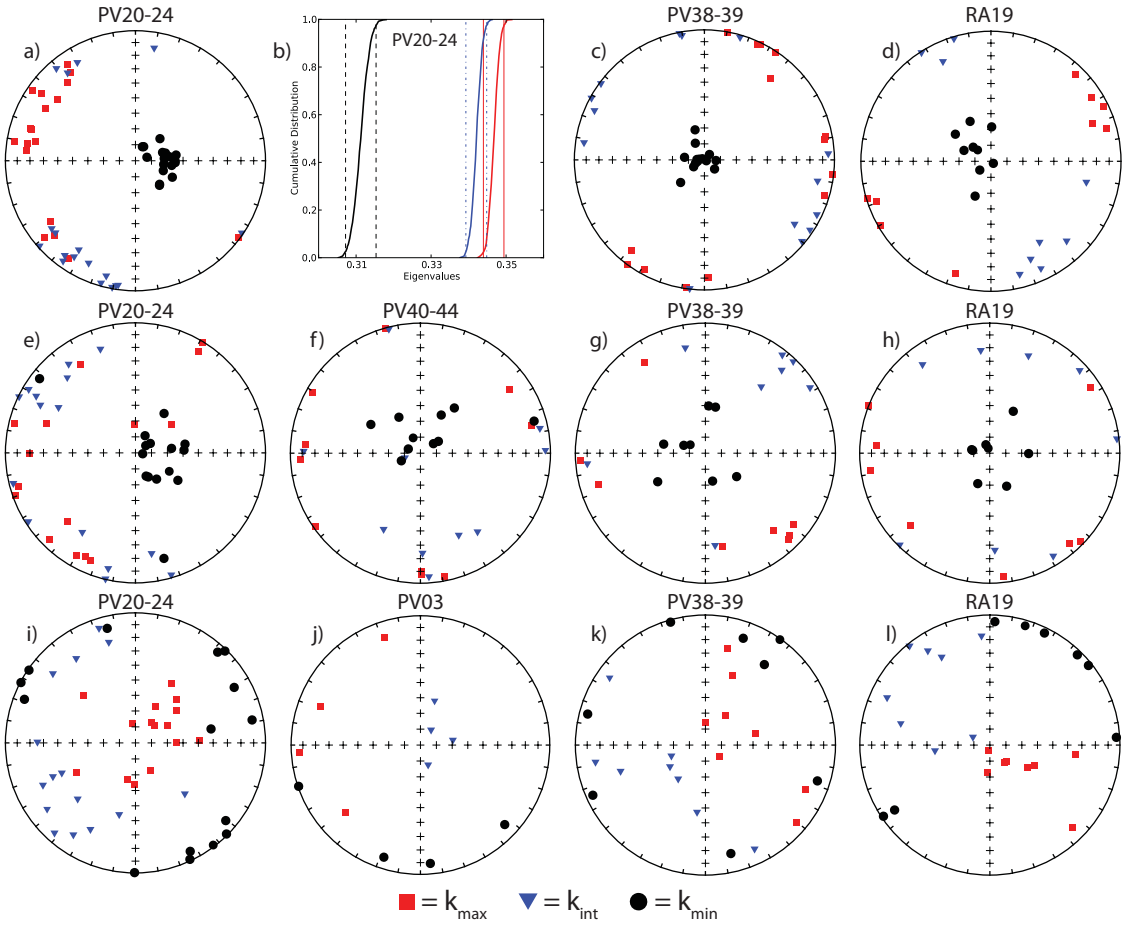

Figure C.1: Supplementary magnetic fabric analysis results from the San Rafael Block. (a–d) Anisotropy of anhysteretic remanent magnetization (AARM). (e–h) Anisotropy of thermal remanent magnetization (ATRM). (i–l) Anisotropy of high-field magnetic susceptibility (HF-AMS). All stereonets depict the raw data in geographic coordinates. All symbols are projections onto the lower hemisphere. (b) Relative eigenvalue distributions from (a); red = maximum eigenvalue (τ_{max}), blue = intermediate eigenvalue (τ_{int}), black = minimum eigenvalue (τ_{min}), dashed lines are the 95% confidence bounds on eigenvalue estimates.

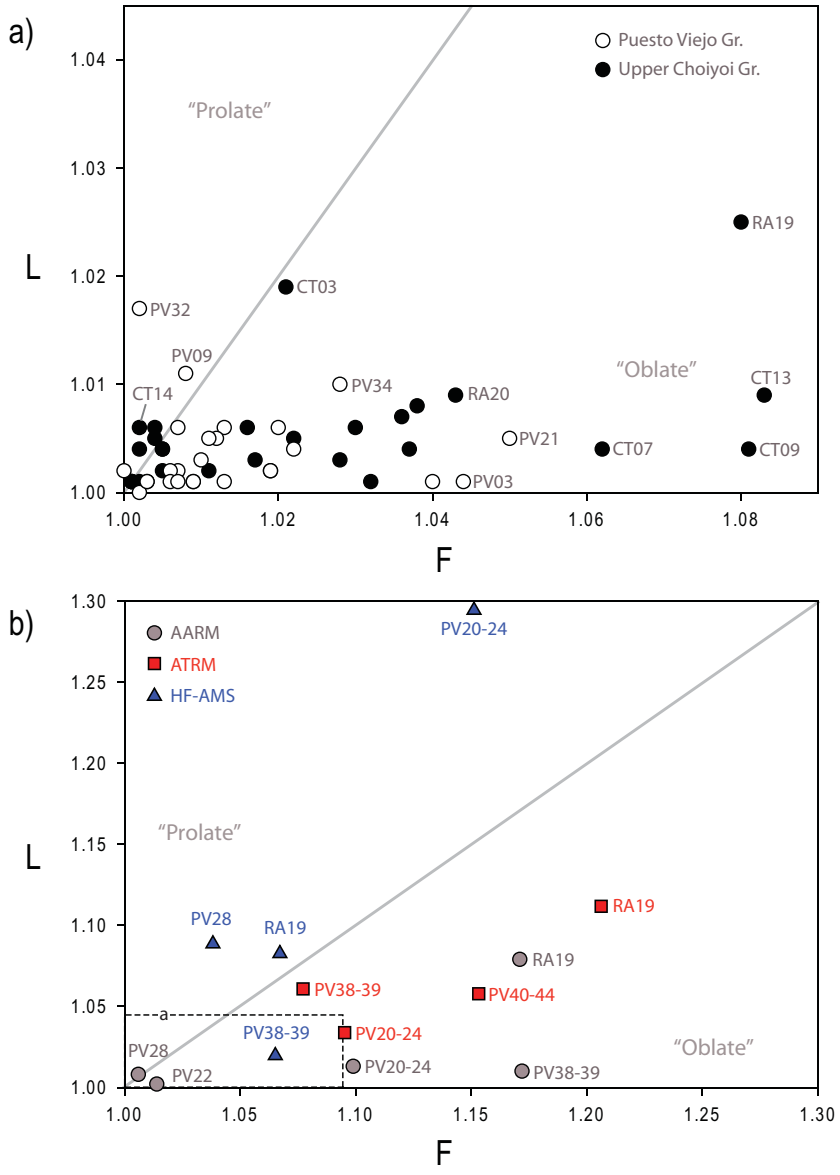

Figure C.2: Flinn diagrams of magnetic fabric data from the San Rafael Block. (a) AMS results and (b) AARM, ATRM, and HF-AMS results. Some of the most anisotropic results (sites) in panel a are labeled. For comparison, the dashed box in panel (b) shows the range of panel (a).